Springer Series in Measurement Science and Technology

Nicola Bowler

Eddy-Current Nondestructive Evaluation

Springer

Springer Series in Measurement Science and Technology

The Springer Series in Measurement Science and Technology comprehensively covers the science and technology of measurement, addressing all aspects of the subject from the fundamental principles through to the state-of-the-art in applied and industrial metrology, as well as in the social sciences. Volumes published in the series cover theoretical developments, experimental techniques and measurement best practice, devices and technology, data analysis, uncertainty, and standards, with application to physics, chemistry, materials science, engineering and the life and social sciences.

More information about this series at http://www.springer.com/series/13337

Nicola Bowler

Eddy-Current Nondestructive Evaluation

Springer

Nicola Bowler
Center for Nondestructive Evaluation,
Department of Materials Science and Engineering,
Department of Electrical and Computer Engineering
Iowa State University
Ames, IA, USA

ISSN 2198-7807 ISSN 2198-7815 (electronic)
Springer Series in Measurement Science and Technology
ISBN 978-1-4939-9627-8 ISBN 978-1-4939-9629-2 (eBook)
https://doi.org/10.1007/978-1-4939-9629-2

© Springer Science+Business Media, LLC, part of Springer Nature 2019
This work is subject to copyright. All rights are reserved by the Publisher, whether the whole or part of the material is concerned, specifically the rights of translation, reprinting, reuse of illustrations, recitation, broadcasting, reproduction on microfilms or in any other physical way, and transmission or information storage and retrieval, electronic adaptation, computer software, or by similar or dissimilar methodology now known or hereafter developed.
The use of general descriptive names, registered names, trademarks, service marks, etc. in this publication does not imply, even in the absence of a specific statement, that such names are exempt from the relevant protective laws and regulations and therefore free for general use.
The publisher, the authors and the editors are safe to assume that the advice and information in this book are believed to be true and accurate at the date of publication. Neither the publisher nor the authors or the editors give a warranty, expressed or implied, with respect to the material contained herein or for any errors or omissions that may have been made. The publisher remains neutral with regard to jurisdictional claims in published maps and institutional affiliations.

This Springer imprint is published by the registered company Springer Science+Business Media, LLC part of Springer Nature.
The registered company address is: 233 Spring Street, New York, NY 10013, U.S.A.

It is exciting and profound that mathematical physics can be used to calculate quantities of practical interest, that have a real impact on society in the context of inspections of aircraft, vehicles, bridges, nuclear power plants and other structures whose integrity is critical to human and environmental safety.

Excerpt from Chap. 5.

Dedicated to all those who have encouraged and inspired me, and especially to John, whose commitment to the truth drew me in.

Preface

This book is intended for senior undergraduate and graduate engineers and scientists, who need a deeper understanding of eddy-current nondestructive evaluation (EC NDE) that can be found in a guide for practitioners. It is written from the standpoint that despite powerful advances in computational electromagnetics, it is important to comprehend the physical principles at work in order to fully master methods of NDE. This book accompanies a course of the same name that has been developed at Iowa State University through support from the Center for Nondestructive Evaluation, and it is also intended to provide a reference and learning aid for nondestructive testing (NDT) engineers in industry and government laboratories.

Theoretical concepts from electricity and magnetism are used freely throughout this text and I am conscious of the fact that many professional test engineers have not taken senior-level courses in electromagnetics or may need to be reminded of the principles. When concepts, laws, and relationships are introduced in the text, I have tried to provide sufficient supporting explanation to aid those of you who may be meeting these for the first time.

The practice of eddy-current nondestructive testing grew, from the middle part of the twentieth century, following the vital impetus and pioneering achievements of Friedrich Förster and his colleagues. Förster laid foundations on which others have built. In the early years, eddy-current methods were used for metal sorting, hardness measurements, and the evaluation of heat treatments, detected through sensing electrical resistivity variations in the samples. These applications were followed quickly by the detection of cracks and corrosion. From the very beginning of these developments, it has been recognized that the introduction of new techniques, the improvement of existing methods, and the interpretation of measurements can benefit greatly from an understanding of the fundamental behavior of the electromagnetic fields. The aim of this book is to bring a knowledge of these fundamentals to new generations of engineers and scientists.

Eddy-current nondestructive evaluation is a commonly practiced method of electromagnetic NDT. The method has been a workhorse of metals characterization and defect detection for many decades, operating at frequencies typically ranging from a few kiloHertz to a few megaHertz. One survey estimated that the method is used in 10% of all NDT inspections. Other electromagnetic approaches, in particular, those that employ higher operating frequencies, are growing in usage in accordance with the expanding use of nonmetallic structural materials such as fiber-based composites. In this text, the discussion is limited to operating frequencies of the order of megaHertz and below, which means that microwave and teraHertz NDT, and magneto-optic imaging, remain outside the scope of this book.

My writing has been guided by four concepts. The work is intended to be visually appealing, with plenty of diagrams to aid comprehension (thanks go to: John Bowler, Adam Cich, Danielle Kimler, Ryan Williams, John Graham, Yi Lu, and Amin Gorji who have all contributed illustrations to this work). I have attempted to place the reported developments in the field of electromagnetic NDT in historical context, and I have tried to maintain a high level of clarity and transparency in the work by including many supporting references. A number of "back-of-the-envelope" example calculations and exercises are included. These are simple calculations that can be done by hand and impart a working knowledge of the connection between electromagnetic theory and the practical measurements described.

The text begins with a brief history of the development of eddy-current NDT, followed by introductions to electromagnetic induction and the basic process of eddy-current NDT, Chap. 1. In Chap. 2, the concept of the electromagnetic field is introduced, and the relationship between electric current and the magnetic field is described qualitatively in the context of an air-cored eddy-current coil near an unflawed metal test-piece. The skin effect and material parameters which affect it are discussed.

The influence of ferromagnetism on eddy-current inspection is profound. For the successful inspection of most steels or other types of ferromagnetic conductor, an understanding of the magnetization (and demagnetization) process is important. Chapter 3 provides an introduction to the process of magnetization in ferromagnetic materials and the meaning of permeability is explained.

The observed quantity in eddy-current NDT is the electrical impedance of the probe coil. Proper interpretation of the impedance allows the inspector to infer material property information, and to detect and characterize defects. Chapter 4 provides an introductory description of circuit theory that is relevant to EC NDE. Different contributions to the probe coil impedance are discussed. Continuing to build the background knowledge needed to more completely describe the electromagnetic behavior of a probe coil, and to become equipped to interpret the measured impedance, Chap. 5 describes the formation and various expressions of Maxwell's equations, from which the equations governing the electromagnetic fields can be formed. Further, expressions of interface conditions on the electromagnetic field are provided. The interface conditions are needed, along with the governing equations, to solve for the fields generated by eddy-current probe coils. They also provide the mathematical tools by which the influence on the impedance of the test-piece can be accounted for.

In Chap. 6, the many background elements considered in earlier chapters come together to allow a detailed illumination of the ways in which various factors affect the measured impedance of an eddy-current probe coil. This chapter embodies the core knowledge of eddy-current NDE insofar as detailing the response of an eddy-current probe to an unflawed test-piece of relatively simple shape. The effect of probe factors such as coil dimensions, construction with or without a ferrite core, and frequency of excitation current are considered. Test-piece factors conductivity, permeability, shape, and position relative to the coil are discussed. In particular, Chap. 6 initially conveys how to compute and interpret the impedance of a coil that is isolated from any test-piece and then introduces the effect of certain canonical test-piece geometries: e.g., the case of a surface coil positioned above a half-space conductor (i.e., a thick, flat conductor) and of a coil encircling a solid, circular–cylindrical rod. For the surface coil, the role of the ferrite core in enhancing inspections is described, along with sources of uncertainty in inspections due to, for example, unknown variations in the coil windings or accidental tilt of the probe during an inspection. The impedance plane diagram is introduced in absolute and normalized forms.

The inspection of test-pieces with more complex geometry, such as layered plates or tubes, is discussed in Chap. 7. The discussion includes the description of impedance plane diagrams for surface coils, encircling coils, and bobbin coils in relation to these test-pieces. The effect of the test-piece edge on the measured probe coil impedance is also described.

In Chap. 8, various probe configurations are discussed in the context of particular applications for which they are well suited. Common and more exotic configurations are included. Practically speaking, probes are often composed of more than one coil either for differential operation that is particularly effective in defect detection or so that each coil may be individually optimized for its role as drive or pick up coil. Some probes are of hybrid design, in which a drive coil induces eddy currents in the test-piece yet the signal is measured by another type of sensor, e.g., a Hall device or a giant magnetoresistive (GMR) sensor. Thin, flexible coils designed for in situ structural health monitoring, and array probes designed for rapid wide-area inspection, are also presented.

Having laid groundwork giving a detailed description of impedance signals due to *un*flawed test-pieces in prior chapters, attention is turned to the effect of defects on the impedance of an eddy-current probe coil, in Chap. 9. In keeping with the approach of this text, simple flaw shapes are considered with the intent of imparting comprehension of how the various characteristics of a defect (its size, shape, location, filler material, etc) influence the observed change in impedance of the eddy-current coil as it approaches the defect. Two regimes are considered: the “small flaw” regime, when the flaw is significantly smaller than the electromagnetic skin depth in the material, and the “thin-skin” regime, when a surface crack is significantly deeper than the electromagnetic skin depth. In these regimes, analytical solutions for the impedance change due to the defect can be derived and give a clear insight into the way in which the coil impedance changes in the presence of these and similar flaws.

Reflecting on a decade of university-based teaching in the field of NDE, and on decades-long conversations with industrial engineers responsible for NDT operations in aerospace, energy, and infrastructure engineering sectors, it is my view that the industrial need for well-educated NDT engineers remains strong. I offer this text to the NDT community in the hope that it will be useful in educating many NDT professionals now and for years to come. I extend my gratitude to Steve Burke and Buzz Wincheski for their comments on various parts of this text.

Ames, IA, USA
Nicola Bowler

Contents

Chapter 1
Introduction

Abstract This opening chapter begins with a brief history of the development of the field of eddy-current (EC) nondestructive evaluation (NDE), beginning with Faraday's discovery of the law of electromagnetic induction and including contributions of Henry, Hughes, and Förster. The role of the law of electromagnetic induction in EC NDE is described qualitatively and the principles via which a material defect may be detected are discussed. Finally, the parameters by which a simple EC surface coil may be described are introduced.

1.1 Introduction

A study conducted by the Institute of Metals [1] discovered that eddy-current nondestructive evaluation (EC NDE) accounts for approximately ten percent of NDE inspections. Other methods in common usage include inherently "visual" inspection methods such as liquid penetrant and magnetic particle testing (50%), ultrasonic, and X-ray methods (approximately 35%). The optimum method for a particular inspection depends on the nature of the specimen under test, and also on the information that is sought. Overviews of some of these methods can be found in [1, 2], but the primary focus of this text is eddy-current NDE.

Eddy-current NDE relies on the induction of electrical current in the part being tested. For this reason, it is used for the inspection of *metals*. Eddy-current NDE is useful for the determination of certain material properties and detection and characterization of inhomogeneities in metals. The method is fundamentally related to the electromagnetic properties of a test-piece. For this reason, it is commonly applied in metal sorting and identification, based on measurement of the metal conductivity, and in detection and characterization of defects in metal parts. These defects may be cracks, pits, dents, scratches, corrosion, heat-affected zones, and others. They may appear at the surface or below the surface. They are found in aerospace structures, nuclear power plant components, railroad tracks, pipelines, sheet metal, rods, and bars, to name a few.

Much early work in the field was done by Friedrich Förster [3], who developed practical eddy-current NDE techniques for many different test geometries, and also

N. Bowler, *Eddy-Current Nondestructive Evaluation*,
Springer Series in Measurement Science and Technology,
https://doi.org/10.1007/978-1-4939-9629-2_1

developed the theory and physics of the practice. The company he founded (Foerster Instruments, Inc.) is still a leading producer of eddy-current test instruments.

1.2 Historical Background

1.2.1 Michael Faraday

Michael Faraday (1791–1867, Fig. 1.1) was an English physicist and chemist. He came from a poor background and was largely self-educated. In 1821, he discovered the phenomenon of electromagnetic induction, which is one of the most far-reaching scientific discoveries of all time [5]. Like many other scholars of his time, Faraday was fascinated by the experiment of Hans Oersted in 1819 in which it was demonstrated that a compass needle could be deflected if brought near to a wire through which electric current was passing. Faraday set out to show, conversely, that electric current could be produced by a magnetic field. Faraday wound a coil of wire, connected to a battery, around one segment of an iron ring (circuit A in Fig. 1.2). An electric current could be made to pass through the wire by closing a switch. Another coil of wire was wound around a different segment of the iron ring (circuit B). On closing the switch in circuit A, a magnetic field was set up by the current flowing in coil A, magnetizing the iron ring. The magnetic field was concentrated in the high permeability iron, which acts as a magnetic circuit conveying the magnetic field to circuit B. The magnetic field created in the iron ring by coil A then coupled with coil B and induced a current to flow in circuit B. This secondary induced current was detected by deflection of the galvanometer. In this experiment, Faraday had invented the first transformer. His original ring is shown in Fig. 1.3.

Fig. 1.1 Michael Faraday, English physicist and chemist, 1791–1867 [4]

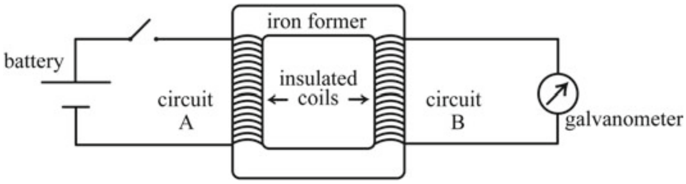

Fig. 1.2 Schematic diagram of Faraday's transformer

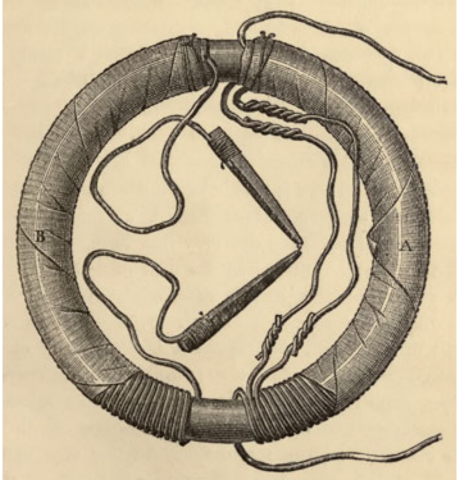

Fig. 1.3 Faraday's transformer [6]

One aspect of his experiment took Faraday by surprise. Rather than a steady flow of current in circuit B, as Faraday had expected, there was a transient current in response to the closing of the switch in circuit A, and another transient current in the opposite direction when the circuit was broken. In between, while the current was flowing steadily in circuit A, no current flowed in circuit B. To explain this, Faraday visualized magnetic field lines that sprang outward from coil A when the switch was closed and collapsed again as the circuit was broken. He hypothesized that electric current was induced in a conductor only when magnetic field lines moved across it. We now know that magnetic fields that vary in time and/or space are capable of inducing electric current flow in a nearby conductor.

Faraday continued to carry out significant experiments in electricity, inventing the first electric generator in 1831, probably the single greatest electrical discovery in history. He was also a tremendously popular lecturer in science for the general public, his lecturers being attended even by royalty and novelists of the time. Faraday lends his name to a unit measuring the quantity of electricity (1 Faraday ≡ 96,500 C) and to the unit of electrostatic capacitance, the Farad (F), named in his honor.

Fig. 1.4 Joseph Henry, American physicist, 1797–1878 [7]

1.2.2 Joseph Henry

A contemporary of Faraday, Joseph Henry (1797–1878, Fig. 1.4) was an American physicist who discovered the phenomenon of electromagnetic induction in 1820, before Faraday, but was unable to complete his experiments and publish his results in advance of Faraday due to a heavy teaching load. For this reason, Faraday receives the credit for the discovery [5]. In Henry's paper, however, he explained that the electric current in a coil can induce another current not only in another coil but in itself—the first description of the phenomenon of self-induction. The current observed in any coil is, therefore, a combination of the original current and the induced current. Joseph Henry made many further significant contributions to scientific and engineering advancement, especially in his role as the first secretary of the Smithsonian Institution, through which he encouraged worldwide communication of scientific discoveries. Upon his death, it was agreed that the unit of inductance should be named the Henry, in his honor.

1.2.3 David Hughes

Following the discovery of electromagnetic induction, nearly 50 years elapsed before further experiments suggested a path toward practical application of the phenomenon in materials testing. David Edward Hughes (1831–1900) was a Welsh experimental scientist and accomplished musician. He conducted some important experiments of relevance to EC NDE in 1879, when he showed that the properties of a current-carrying coil changed when the coil was placed in contact with metals of different conductivity and permeability. Here, lies the foundation for identification of metals and alloys by eddy-current testing, to be discussed in Chaps. 6 and 8.

1.2.4 Friedrich Förster

Following the work of Hughes, another 54 years passed before eddy-current technology was developed for industrial application. While working for the Kaiser Wilhelm Institute in Germany, 1933, Prof. Friedrich Förster played a very important role in adapting eddy-current technology for industrial use. He developed instruments for measuring conductivity and for sorting mixed ferrous components, among others, and contributed significantly to the understanding and interpretation of eddy-current signals, introducing the so-called "Förster diagram", which is related to the impedance-plane plots that will be described in this work. As mentioned above, Förster founded his own company (Foerster Instruments, Inc.) in 1948, a company whose business is based on eddy-current testing.

Many advances in the development of EC NDE were made in the 1950s and 1960s, in particular in the context of aviation and nuclear power industries. EC NDE is now a widely used and well-understood inspection technique for flaw detection and characterization as well as for materials property characterization. The development of EC NDE continues to be an active area of research in the present era. Research encompasses the design and realization of specialized probes for ever-more-challenging inspections, often assisted by computational modeling of the probe and its environment. Present-day research also focuses upon improving the interpretation of noisy signals, often with the goal of increasing inspection speed. Generally speaking, EC NDE plays an important role in improving safety, quality, and efficiency in aviation, transportation, infrastructure, and energy sectors.

1.3 Electromagnetic Induction

What happens when a time-varying electric current passes through a simple loop of wire held near a conductor such as a metal plate? As shown schematically in Fig. 1.5, the time-varying current flowing in the wire loop has the effect (somehow) of producing (actually, *inducing*) an electric current which flows in the metal plate. The current in the plate in some sense mirrors the applied current flowing in the wire loop, but flows in the opposite direction. These induced currents are known as eddy currents. The term "eddy current" was coined due to the analogy between vortex currents (eddies) in laminar fluid flow and the flow of these induced, circulating, electrical currents. In practice, eddy currents always flow in closed paths.

How are eddy currents induced? The answer lies in the phenomenon of electromagnetic induction, first observed experimentally by Faraday, who hypothesized the existence of the electric and magnetic fields in order to explain his observations.

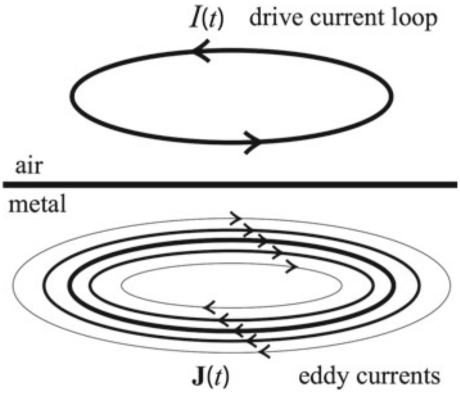

Fig. 1.5 Eddy currents induced in a metal part by a time-varying current loop in air. The eddy-current density in the conductor, $\mathbf{J}(t)$, is a vector field that is described in detail in Sect. 2.2

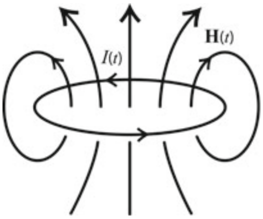

Fig. 1.6 Magnetic field associated with a time-varying current loop in air

The fact that the applied current is varying means that a magnetic field, denoted **H** with units Ampères per meter (A/m), is produced in the vicinity of the current loop, Fig. 1.6. This magnetic field is much like that in the vicinity of a stationary bar magnet, although here **H** varies with time whereas that associated with a bar magnet is static. The time-varying magnetic field couples with a nearby metal test-piece and, in turn, induces electric current in the metal. This phenomenon of electromagnetic induction forms the foundation of eddy-current nondestructive evaluation. The eddy currents that flow in the metal are themselves time-varying and produce their own associated magnetic field, $\mathbf{H}_{\mathrm{ec}}$. In an eddy current inspection, $\mathbf{H}_{\mathrm{ec}}$ couples with a sensor—sometimes the induction coil itself—and the signal is interpreted to obtain physical information about the test-piece.

The fact that EC NDE works on the principle of electromagnetic induction means that it is inherently a noncontact inspection method. One advantage of this is that a test-piece may be inspected for damage even when covered by a protective layer of paint or some other type of cladding, for example.

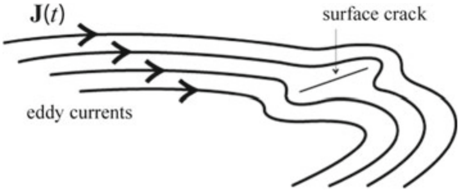

Fig. 1.7 Eddy currents disrupted by a surface defect. The eddy-current density $\mathbf{J}(t)$ is a vector field that is described in detail in Sect. 2.2

1.4 Eddy-Current Nondestructive Evaluation

Figure 1.5 shows eddy currents induced in an unflawed conductor. The existence of a defect such as a crack, some corrosion, a heat-affected zone or other inhomogeneity disrupts the flow of eddy currents, Fig. 1.7. In consequence, the magnetic field (Sect. 2.6) associated with the induced eddy currents, $\mathbf{H}_{\text{ec}}$, is also disrupted. The total magnetic field can be written as the sum of that from the drive coil, $\mathbf{H}^0$, and that "scattered" by the defect, $\mathbf{H}^{\text{s}}$:

$$\mathbf{H}_{\text{ec}}(t) = \mathbf{H}^0(t) + \mathbf{H}^{\text{s}}(t). \tag{1.1}$$

This disruption of the magnetic field may be detected by the inducing coil, or by another sensing or pick up coil specifically dedicated to measuring the flaw signal. A variety of defects can be detected in this way.

Note also that electromagnetic nondestructive evaluation methods can be used not only for flaw detection but also for the characterization of materials. With model-based or calibration methods it is possible to measure the electrical conductivity σ (or equivalently the resistivity $\rho = 1/\sigma$) of a metal, which is useful in identifying metal alloys. Thickness measurements can also be made under certain circumstances—useful when wall thinning due to corrosion is suspected. The distance between the coil and the metal part can be measured, which is useful for measuring the thickness of paint, for example.

1.5 Air-Cored Coil

The most basic eddy-current probe consists of a coil of wire wound on a nonconductive, nonmagnetic former, such as Delrin®. Such a coil is termed "air-cored" because the conductivity and permeability of the former are the same as those of air, to a close approximation. An image of such a coil, passing over a cracked test-piece, is shown in Fig. 1.8. Important parameters of the coil are its inner and outer radii, r_{i} and r_{o}, respectively, its length l, and number of turns (the number of loops of wire wound on the former) N. The minimum distance between the lower surface of the coil and the metal test-piece is determined by the thickness of the probe casing and is termed the probe "stand-off", s. A similar quantity is the coil "lift-off", h, usually

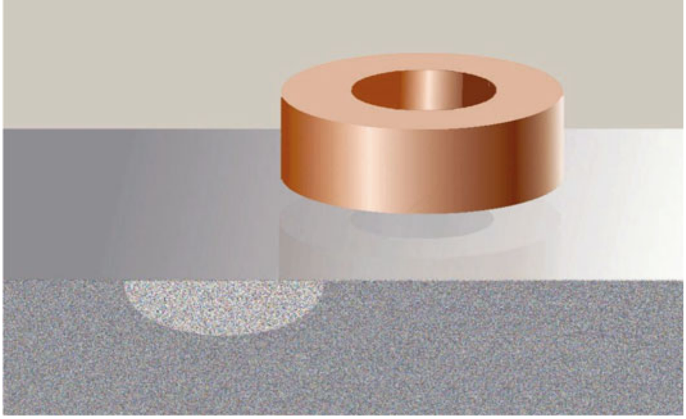

Fig. 1.8 Eddy-current coil passing over a test-piece with a surface crack

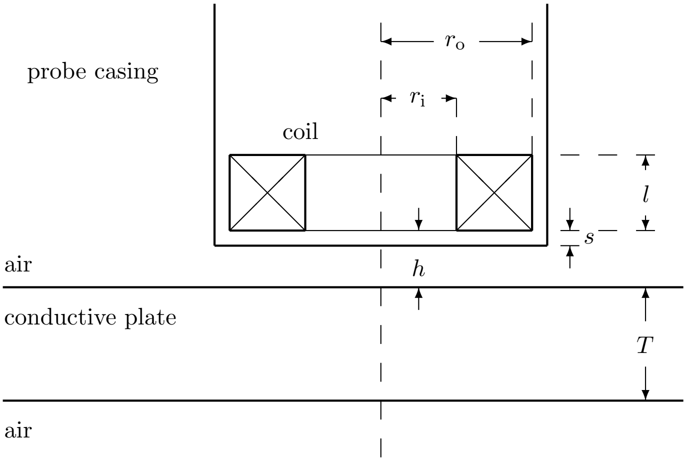

Fig. 1.9 Cross section through the axis of a circular, air-cored, eddy-current coil, positioned horizontally above a metal plate

defined to be the vertical distance between the lower surface of the coil windings and the metal test-piece. With this definition, $h \geq s$. A cross-sectional view of such a coil is shown schematically in Fig. 1.9. The coil parameters all affect the value of the coil impedance, Z, which is the quantity measured in a nondestructive eddy-current inspection and is generally a complex quantity. It is discussed in detail in Sect. 4.9. Z changes, for example, when a probe is placed on a metal sample from some distance away, and again when the probe moves near to a flaw in the metal. When the probe coil is sufficiently far from any metals that eddy currents are not induced by it, in practice, around 10 or 20 cm away depending on the coil, it is said to be *isolated* and its impedance has the symbol Z_0. For a sinusoidal (alternating current) excitation with angular frequency ω (Sect. 2.3), the component of Z_0 that is "in phase" with the variation of the exciting current is resistive, and the component that is "in quadrature" is inductive. This is represented in the following relationship:

$$Z_0 = R_0 + j\omega L_0 \tag{1.2}$$

where R_0 and L_0 are the d.c. resistance (Sect. 2.4) and inductance (Sect. 4.7) of the coil, respectively, and $j = \sqrt{-1}$. A theoretically "ideal" coil has $R_0 = 0$; it is a pure inductor:

$$Z_{\text{ideal}} = j\omega L_0. \tag{1.3}$$

In practice, the coil is usually made from a standard metal such as copper with finite resistance and, as the coil operating frequency increases, capacitance between the wires connecting the probe to any instrumentation, capacitance between the windings of the coil itself, and eddy currents in the wires themselves also exist. These effects, and a scheme by which corrections can be made for nonideal coil behavior, are discussed in detail in Chap. 8.

1.6 Summary

In this chapter, an introductory glance at the scope and history of EC NDE has been taken. In the next chapter, attention turns to visual representations and mathematical descriptions of the electromagnetic fields that Faraday conceptualized.

1.7 Exercises

1. On the same axes, sketch electric current (vertical) versus time (horizontal) for the currents flowing in circuits A and B of Faraday's transformer (Fig. 1.2) as the switch is first closed at time t_c and then opened at time t_o. Indicate the time points t_c and t_o on your plot. Remember that the current flowing in a circuit of this kind does not change instantaneously from "off" to "on" or vice versa, but has a finite transition time associated with its rise or fall.
2. Describe in your own words the phenomena observed, and the reasons for their occurrence, at each step of Faraday's experiment.

References

1. Cartz, L.: Nondestructive Testing: Radiography, Ultrasonics, Liquid Penetrant, Magnetic Particle, Eddy Current. ASM International, Materials Park (1995)
2. Jiles, D.C.: Introduction to the Principles of Materials Evaluation. CRC Press/Taylor & Francis Group, Boca Raton (2008)
3. McMaster, R.C., McIntire, P. (eds.), Mester, L.M. (tech. ed.): Nondestructive Testing Handbook: Electromagnetic Testing, vol. 4, 2nd edn. American Society for Nondestructive Testing, Columbus (1986)
4. Public domain image. http://en.wikipedia.org/wiki/Michael_Faraday. Accessed 2 July 2014
5. Asimov, I.: Asimov's Biographical Encyclopedia of Science and Technology. Pan Books, London (1975)
6. Public domain image. http://en.wikipedia.org/wiki/Transformer#mediaviewer/File:Faradays_transformer.png. Accessed 2 July 2014
7. Public domain image. http://en.wikipedia.org/wiki/Joseph_Henry#mediaviewer/File:Joseph_Henry_(1879).jpg. Accessed 2 July 2014

Chapter 2
Fields

Abstract In this chapter, the concept of the electromagnetic field is introduced in the context of current-carrying, possibly ferromagnetic, conductors. The electric current density, itself a vector field, is defined and related to electric current. Phasors are introduced and their usefulness for treating electrical systems whose current is alternating sinusoidally is described. The related material parameters, conductivity, and resistivity, are defined and discussed. The relationships between electric current, electric field, and magnetic field are introduced in relation to a line current. The relation of electromagnetic fields to power transfer is introduced. Magnetization field, the field of magnetic induction, and the permeability of a material are defined. The definition of the electromagnetic skin depth is provided, highlighting the material parameters that influence it. The consequences of the skin effect for EC NDE are discussed, utilizing the example of an air-cored eddy-current coil adjacent to an unflawed metal test-piece. For completeness, the electric displacement and polarization fields are also defined.

2.1 Introduction

What do we mean by an electric or magnetic "field"? A field is a way of referring to a spatial distribution of a certain quantity. Knowledge of field distributions is useful for predicting the behavior of physical systems. Faraday was the first to propose thinking of the universe as consisting of fields of various kinds. For example, knowledge of the form of the earth's gravitational field enables us to predict that an object will fall when dropped, and indeed what its velocity will be on impact with the ground. Similarly, knowledge of the forms of electric and magnetic fields allow us to predict the behavior of electric charges and currents when they interact with those fields.

In the previous chapter, it was mentioned that a time-varying current, flowing in a loop of wire, produces an associated magnetic field that is spatially similar to the field in the vicinity of a small bar magnet. A significant difference between them, however, is that the magnetic field associated with the time-varying current flow also fluctuates in time, whereas that associated with a bar magnet does not. On the other hand, a constant magnetic field similar to that produced by a bar magnet is produced

N. Bowler, *Eddy-Current Nondestructive Evaluation*,
Springer Series in Measurement Science and Technology,
https://doi.org/10.1007/978-1-4939-9629-2_2

by direct current flowing in a circular loop. In this chapter the relationship between the electric current flowing in the coil of an eddy-current probe, the magnetic field it produces, and the eddy currents induced in the conductive test-piece will be explored.

One characteristic of metals is the existence of conduction electrons which are free to move when an electro-motive force is present. The electro-motive force can be provided by a battery or AC power supply, for example. The conduction electrons are the carriers of electric current although, by historical accident, the conventional current I flows in the opposite direction to the flow of the negatively charged electrons. The unit of electric current is the Ampère (A), named after the French mathematician and physicist André Ampère (1775–1836). Within one week of the report of Oersted's experiment (Sect. 1.2.1), Ampère had formulated the right-hand rule (Sect. 2.6), in which the *direction* of deflection of a small bar magnet (e.g., a compass needle) in the vicinity of a current-carrying wire is specified [1]. In fact, it was in the formulation of the right-hand rule that it was incorrectly assumed that current flows from positive to negative poles, that is, that the charge carriers were positively charged.

2.2 Current Density

For the purpose of describing eddy currents in a conductor, it is more convenient to use the current density, $\mathbf{J}$, a vector field whose unit is Ampères per meter squared (Am^{-2}), rather than the current I. This is because eddy currents in a test-piece follow a path which offers the least electrical resistance to their flow. Their direction changes to accommodate the presence of resistive obstacles in the conductor, in the same way that smoothly flowing water separates to flow around a rock in a stream. This means that the direction as well as the magnitude of the eddy currents needs to be described, and this is best accomplished by the vector field $\mathbf{J}$. Examples of resistive obstacles in a conductor are cracks, pores, and regions of corrosion.

To begin to understand the relationship between I and $\mathbf{J}$, consider current flowing in a wire with cross-sectional area S, Fig. 2.1. In the case of direct current (DC), which does not vary with time, the current density in the wire is spatially uniform and the total current flowing in the wire is given by the product of the current density and the cross-sectional area of the wire:

$$I = JS. \tag{2.1}$$

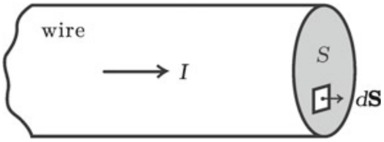

Fig. 2.1 Current I flowing in a wire with cross-sectional area S

In the case of time-varying current, however, the current density in the wire is generally not spatially uniform, and the current flowing in the wire is obtained by means of a surface integral.

$$I = \int_S \mathbf{J} \cdot d\mathbf{S}, \tag{2.2}$$

where $d\mathbf{S}$ is an element of surface area. The dot product ensures that the component of $\mathbf{J}$ that is normal to the surface S is the one that contributes to I. For refreshment on vector analysis, see Appendix 10.3.

Example: Uniform current density in a wire Determine the total current in a wire of radius 1 mm, placed along the z-axis, if $\mathbf{J} = (500/\pi)\hat{z}$ Am^{-2}.

Solution From (2.1), $I = JS = J\pi\alpha^2$ where α is the wire radius. Hence,

$$I = \frac{500}{\pi}\pi(10^{-3})^2 = 500 \times 10^{-6} = 0.5 \text{ mA}.$$

Example: Nonuniform current density in a wire The current density in a cylindrical conductor of radius α placed along the z-axis is $\mathbf{J} = 10\exp[-(1-\rho/\alpha)]\hat{z}$ Am^{-2}. Evaluate the current through the cross section of the conductor.

Solution From (2.2),

$$\begin{aligned} I &= \int \mathbf{J} \cdot d\mathbf{S} \\ &= \int_0^{2\pi}\int_0^{\alpha} 10\, e^{-(1-\rho/\alpha)}\hat{z} \cdot (\rho d\rho d\phi \hat{z}) \\ &= 10\int_0^{2\pi} d\phi \int_0^{\alpha} \rho\, e^{-(1-\rho/\alpha)} d\rho \\ &= \frac{20\pi}{e}\int_0^{\alpha} \rho\, e^{\rho/\alpha} d\rho \end{aligned}$$

Use of the standard integral [2, relation 4.2.55]

$$\int x e^{\beta x} dx = \frac{e^{\beta x}}{\beta^2}(\beta x - 1)$$

then gives $I = (20\pi/e)\alpha^2 = 23.11\alpha^2$ A.

2.3 Alternating Current and Phasor Representation

Direct current, produced by a battery, for example, flows steadily. The magnitude of the current, I, is constant as a function of time, as shown in Fig. 2.2. Alternating current is one form of time-varying current and often has a simple-harmonic waveform, as shown in Fig. 2.3.The current at any instant in time is given by

Fig. 2.2 Direct current $I(t) = I_0$

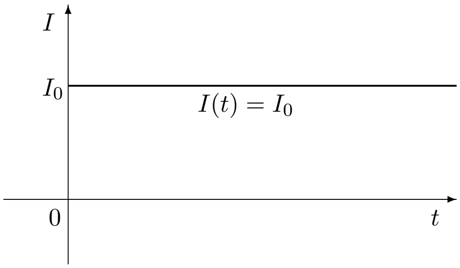

Fig. 2.3 Sinusoidal alternating current $I(t) = I_0 \cos(\omega t + \phi)$

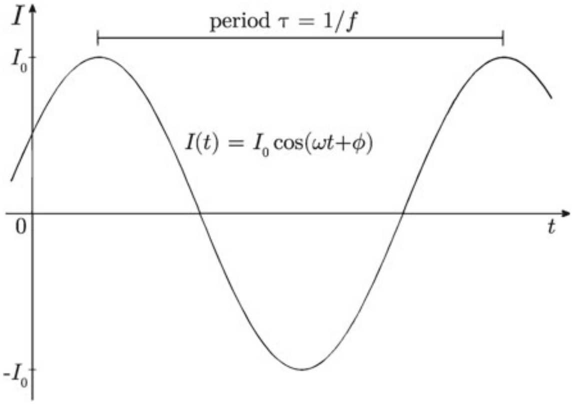

$$I(t) = I_0 \cos(\omega t + \phi) \tag{2.3}$$

where I_0 is the amplitude of the current, $\omega = 2\pi f$ is the angular frequency, t is time elapsed and ϕ is the phase of $I(t)$. It is popular to work in terms of the angular frequency ω (unit radian^{-1} or rad^{-1}) rather than the frequency f (unit Hertz, written Hz, or second^{-1}, written s^{-1}) because the period of the cosine function is 2π. In other words

$$\cos\alpha = \cos(\alpha + 2n\pi) \tag{2.4}$$

where n is an integer ... 2, 1, 0, 1, 2, ... Hence,

$$\cos(2\pi f t) = \cos[2\pi(f t + n)] \tag{2.5}$$

and the length of one cycle is defined by $f t = 1$ which means that the period of the oscillation τ (measured in seconds, s) is simply

$$\tau = \frac{1}{f}. \tag{2.6}$$

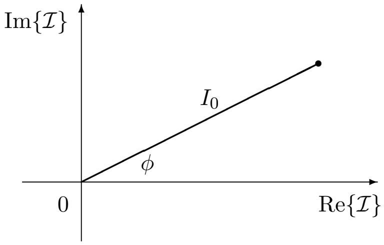

Fig. 2.4 Complex-plane representation of phasor $\mathcal{I} = I_0 \exp(j\phi)$

Note that sinusoidal alternating current, given in terms of the cosine function in (2.3), may equivalently be expressed in terms of the sine function $I(t) = I_0 \sin(\omega t + \phi + \pi/2)$. In this text, another representation will be used, in which

$$\begin{aligned} I(t) &= \mathrm{Re}\{\mathcal{I} \exp(j\omega t)\} \\ &= \mathrm{Re}\{I_0 \exp[j(\omega t + \phi)]\} \\ &= I_0 \mathrm{Re}[\cos(\omega t + \phi) + j \sin(\omega t + \phi)] \\ &= I_0 \cos(\omega t + \phi). \end{aligned} \tag{2.7}$$

In these equations, $j = \sqrt{-1}$, $\mathrm{Re}\{Z\}$ denotes the real part of Z,

$$\exp(j\alpha) = \cos\alpha + j \sin\alpha$$

is Euler's relationship and

$$\mathcal{I} = I_0 \exp(j\phi) \tag{2.8}$$

is the *phasor* representation of $I(t)$. $\mathcal{I}$ is a complex number representing a time-harmonic physical quantity. Note that, whereas, $I(t)$ is a real quantity that is a function of t, $\mathcal{I}$ is a complex quantity that does not depend on t. Phasor $\mathcal{I}$ is plotted in the complex-plane in Fig. 2.4. In this text, the complex time dependence $\exp(j\omega t)$ is used throughout rather than $\exp(-i\omega t)$, $i = \sqrt{-1}$, which is another convention. For revision of the complex-plane representation of a complex number, see Appendix 10.1.

The phasor notation of (2.7) is especially convenient because when the derivative with respect to time is taken, the factor $j\omega$ is brought down but the exponential term itself is unchanged and can often be subsequently canceled, simplifying the analysis. In other words, the conversion between the time derivative of $I(t)$ and its phasor form $\mathcal{I}$ is

$$\frac{\partial}{\partial t} I(t) \Leftrightarrow j\omega\mathcal{I}. \tag{2.9}$$

Example: Phasor addition Prove that the addition of two time-harmonic functions with the same frequency, $I(t) = I_0 \cos(\omega t + \phi)$ and $K(t) = K_0 \cos(\omega t + \psi)$ can be represented in phasor form by the sum $\mathcal{I} + \mathcal{K}$.

Solution

$$\begin{aligned}I(t) &= \mathrm{Re}\left\{\mathcal{I}e^{j\omega t}\right\}\\ K(t) &= \mathrm{Re}\left\{\mathcal{K}e^{j\omega t}\right\}\end{aligned}$$

and

$$I(t) + K(t) = \mathrm{Re}\left\{(\mathcal{I} + \mathcal{K})e^{j\omega t}\right\}.$$

Hence,

$$I(t) + K(t) \Leftrightarrow \mathcal{I} + \mathcal{K}.$$

Note that two phasors that represent time-harmonic functions with different frequencies *cannot* be summed in this way.

Example: Phasor multiplication Show that the product of two time-harmonic functions with the same frequency, $I(t) = I_0 \cos(\omega t + \phi)$ and $K(t) = K_0 \cos(\omega t + \psi)$ *cannot* be represented in phasor form by the product $\mathcal{I}\mathcal{K}$.

Solution

$$\begin{aligned}I(t)K(t) &= I_0 K_0 \cos(\omega t + \phi)\cos(\omega t + \psi)\\ &= \frac{1}{2} I_0 K_0 \left[\cos(2\omega t + \phi + \psi) + \cos(\phi - \psi)\right]\end{aligned}$$

from identity (10.13). This is the sum of two oscillations with different frequencies (2ω and 0), which means that the product $I(t)K(t)$ cannot be represented by a single phasor of any form.

Example: Phasor differentiation Prove relation (2.9).

Solution

$$\begin{aligned}\frac{\partial}{\partial t} I(t) &= \frac{\partial}{\partial t}\left[I_0 \cos(\omega t + \phi)\right]\\ &= -\omega I_0 \sin(\omega t + \phi)\\ &= -\omega I_0 \cos(\omega t + \phi - \pi/2)\\ &= \mathrm{Re}\left\{-\omega I_0 e^{j\omega t} e^{j\phi} e^{-j\pi/2}\right\}\\ &= \mathrm{Re}\left\{j\omega I_0 e^{j\omega t} e^{j\phi}\right\}\\ &= \mathrm{Re}\left\{j\omega \mathcal{I} e^{j\omega t}\right\}\end{aligned}$$

2.4 Conductivity and Resistivity

Different metals vary in their current-carrying ability. A measure of the ability of a material to convey electric current is its electrical *conductivity*, a parameter which is intrinsic to each material and arises in a metal from interactions between the conduction electrons and the crystal lattice. Also commonly used is the electrical *resistivity* of the material, which is its ability to impede (or resist) the passage of electric current. The resistivity is simply the reciprocal of the conductivity. In terms of current flowing in a wire, the DC resistance of the wire, R measured in Ohms (Ω), is proportional to the length of the wire, l, and inversely proportional to its cross-sectional area S, so that

$$R = \rho \frac{l}{S}. \tag{2.10}$$

The constant of proportionality, ρ, is the resistivity of the material out of which the wire is made. The units of ρ are Ohm meter (Ωm). Equivalently (2.10) can be written in terms of the material conductivity σ, measured in Siemens per meter (Sm^{-1}).

$$R = \frac{l}{\sigma S}, \tag{2.11}$$

where, evidently,

$$\sigma = \frac{1}{\rho}. \tag{2.12}$$

A higher value of conductivity is associated with better conductors than with poorer conductors. The conductivity of common metals varies by around two orders of magnitude. Copper is highly conductive and lends its name to the International Annealed Copper Standard (IACS), a measure of conductivity used to compare electrical conductors to a traditional copper-wire standard, in which 100% IACS represents conductivity 58 MSm^{-1}. Titanium, for example, has conductivity 1% IACS. The conductivities of selected metals are given in Table 2.1.

Electrical conductivity σ is essentially constant as a function of frequency for the electromagnetic inspection techniques discussed in this book, that operate up to frequencies of a few MHz. Conductivity is very sensitive, on the other hand, to variations in the temperature of a conductor [9]. Increasing the temperature of a conductor reduces its conductivity due to increased vibrations of the crystal lattice that impede the motion of the conduction electrons. Extensive tables of resistivity values at various temperatures are given in [6, 10]. Since conductivity values are commonly stated at 20 °C (degrees Celsius), measurements made at other temperatures must be corrected in order to properly analyze and sort metals, for example. The following formula for correcting for the effect of small temperature changes on the conductivity is given in [9, 11]:

$$\sigma(T_1) = \frac{\sigma(T_2)}{[1 + \alpha(T_1 - T_2)]}. \tag{2.13}$$

In (2.13), $\sigma(T_i)$ is conductivity in MS/m at temperature T_i in °C and α is the temperature coefficient of the material in °C^{-1}. The temperature coefficient for selected metallic elements is listed in Table 2.2 [11]. A detailed discussion on how to improve the accuracy of conductivity measurements made using EC NDE is provided in [9]. Two complementary methods of conductivity measurement, by EC NDE and by the

Table 2.1 Electrical conductivity of selected metals at 20 °C

Metal	Alloy	Conductivity, σ		Reference
		(MSm^{-1})	(% IACS)	
Aluminum, pure		35.38	61.00	[3]
Aluminum	2024	17.6	30.3	[4]
Brass	C26000	16.42	28.31	[5]
Bronze, commercial annealed		25.52	44.00	[3]
Chromium		5.10	8.80	[3]
Cobalt		16.01	27.60	[3]
Copper		58.00	100.00	[3]
Gold		40.60	70.00	[3]
Iron, pure		10.44	18.00	[3]
Nickel		14.62	25.20	[3]
Silver		68.03	117.3	[6]
Steel, Carbon	1018	5.18	8.93	[7]
Steel, Stainless	316	1.379	2.378	[5]
Steel, Spring	C1074/75	5.50	9.48	[5]
Titanium	Ti-6Al-4V	0.58	1.00	[8]
Tungsten		18.21	31.40	[3]
Zinc, commercial rolled		16.24	28.00	[3]

Table 2.2 Temperature coefficient for selected metallic elements at 20 °C [11]

Metal	Temperature coefficient ($\times 10^{-3}$ °C^{-1})
Aluminum	4.3
Copper	4.0
Gold	3.7
Iron	6.0
Nickel	5.9
Silver	3.8
Tungsten	4.4
Zinc	3.8

four-point potential drop method, are compared in [7]. The latter method is particularly useful for measuring the conductivity of ferromagnetic metals, where the eddy-current method commonly fails due to its inability to separate the effects of conductivity and permeability on the probe impedance except at frequencies typically lower than the operating range of most probes. Permeability is the parameter that describes the way in which a ferromagnetic material responds to an applied magnetic field and is described in Sect. 2.8.

Example: Temperature dependence of conductivity The aluminum alloy whose temperature coefficient is listed in Table 2.2 has conductivity 63.6% IACS at 25 °C. Evaluate the conductivity of this alloy at 20 °C.

Solution

$$\begin{aligned}\sigma(20\ ^\circ\mathrm{C}) &= \frac{\sigma(25\ ^\circ\mathrm{C})}{[1+\alpha\times(-5)]}\\ &= \frac{63.6}{[1-(0.0043\times 5)]}\\ &= 65.0\ \%\mathrm{IACS}.\end{aligned}$$

2.5 Electric Field

The fundamental source of an electrostatic field, or stationary electric field **E**, is a stationary electric charge. **E** has unit Volt per meter (V/m). Electric charges may be either positive, as in the case of a proton which resides in the atomic nucleus for example, or negative, as in the case of an electron. Static fields are not the concern of this text since EC NDE is founded on inherently dynamic processes, i.e., fields and their sources that vary with time.

When an electric current flows in a wire, or eddy currents are induced in a metal test-piece, there is an electric field associated with the moving electrons. The current I and current density $\mathbf{J}$ both exist only in the conductor because there are no conduction electrons in the region beyond the metal test-piece or coil. By contrast, the electric field is not spatially restricted to the region of the conductor alone, but exists everywhere. For example, the electric field in air due to an infinitesimally thin, long, straight wire (mathematically, the wire radius $\to 0$) carrying phasor current $\mathcal{I}$ in the z-direction is given by

$$\mathbf{E} = \hat{z}\,\frac{\mathcal{I}}{2\pi}j\omega\mu_0 \ln\rho, \qquad \rho > 0, \tag{2.14}$$

where the wire coincides with the z-directed axis of a cylindrical coordinate system of which ρ is the radial coordinate and μ_0 is the permeability of free space (Sect. 2.8). To discover how (2.14) is obtained, see Exercise 2 at the end of this chapter. This is just one example of the electric field external to a current-carrying body. In fact, it is also an example of the working of Faraday's Law of electromagnetic induction. The field expressed in (2.14) does not exist unless the current in the wire is time-varying. As you can see in (2.14), $\mathbf{E} \to 0$ if $\omega \to 0$. This is a consequence of the fact that the current flowing in the wire is the source of a magnetic field external to the wire, and it is actually the time variation in the magnetic field that in turn induces the electric field expressed in (2.14).

Inside the conductor, things are much simpler. There is a linear relationship between **J** and **E**, known as a constitutive relation. This particular constitutive relation is the "point form" of Ohm's Law, which will be discussed in more detail in Chap. 4. In an *isotropic* conductor, the conductivity is scalar which means that the electric field and the current density have the same direction at every point in the conductor. Ohm's Law is then stated as follows, with the magnitudes of **J** and **E** being proportional to one another and the constant of proportionality being σ:

$$\mathbf{J} = \sigma \mathbf{E}. \tag{2.15}$$

In the case of anisotropic conductivity such as exists in a carbon–fiber composite material it is necessary to express Ohms' Law as follows, wherein the conductivity $\overline{\overline{\sigma}}$ is a second-rank tensor:

$$\mathbf{J} = \overline{\overline{\sigma}} \cdot \mathbf{E} \qquad \text{and} \qquad \overline{\overline{\sigma}} = \begin{pmatrix} \sigma_{xx} & \sigma_{xy} & \sigma_{xz} \\ \sigma_{yx} & \sigma_{yy} & \sigma_{yz} \\ \sigma_{zx} & \sigma_{zy} & \sigma_{zz} \end{pmatrix}. \tag{2.16}$$

In this text, it is generally assumed that material properties are isotropic rather than changing with the direction of the applied field, which is true for most metals routinely inspected by EC NDE.

2.6 Magnetic Field

The fundamental source of a magnetic field **H** is *charge in motion*. A current flowing in a wire always has a magnetic field associated with it, regardless of whether the current is time-varying or flowing steadily. **H** has unit Ampère per meter (A/m). Continuing the discussion surrounding (2.14), the magnetic field in air due to an infinitesimally thin, long, straight wire carrying current $\mathcal{I}$ in the z-direction is given by

$$\mathbf{H} = \hat{\phi}\, \frac{\mathcal{I}}{2\pi\rho}, \qquad \rho > 0, \tag{2.17}$$

where ϕ is the azimuthal coordinate of the cylindrical system. (This is a demonstration of the right-hand rule of Ampère: If the right hand is wrapped around a conductor such that the thumb indicates the direction of current flow, here $\hat{z}$, then the direction in which the curling fingers point is the direction of the associated magnetic field, here $\hat{\phi}$.) To discover how expression (2.17) is obtained, see Exercise 2 at the end of this chapter. Unlike in the case of the electric field associated with this same wire, given in (2.14), note that there is no explicit frequency dependence (ω) in (2.17). In fact, a similar expression holds for direct current $I = I_0$ flowing in the same wire:

$$\mathbf{H} = \hat{\phi}\, \frac{I_0}{2\pi\rho}, \qquad \rho > 0 \tag{2.18}$$

whereas, as explained above, $\mathbf{E}$ expressed in (2.14) tends to zero when direct current flows in the wire. This is not to say, however, that there is no electric field external to a long straight wire carrying direct current I_0. In fact, the component of the electric field tangential to the wire surface must be continuous (see Sect. 5.6), which means that external to a DC current-carrying wire with axis parallel to the $\hat{z}$-direction, $\mathbf{E} = \hat{z}E_0$ is also $\hat{z}$-directed and is *constant* everywhere in space. Unlike the form expressed in (2.14), this constant term has no connection with the magnetic field.

The source of permanent magnetization in a ferromagnetic material lies in the orbital- and spin angular momentum of atomic electrons as described by quantum mechanics. So one can say, loosely, that the magnetic field due to a permanent magnet also originates with charge in motion. Ferromagnetism cannot, however, be fully explained in terms of classical physics. This type of magnetism is discussed in Sect. 2.8 and also in Chap. 3.

The existence of electric and magnetic fields external to a conductor is at the very heart of EC NDE. These are the fields that account for "action-at-a-distance" phenomena such as the attraction between two electric charges of opposite sign or the attraction between opposite poles of two permanent magnets. The fields store electromagnetic energy which is converted to kinetic energy (energy of motion) when such oppositely charged objects move toward each other. In the context of EC NDE, an EC drive coil is the source of an external electromagnetic field, which then couples into the metal test-piece and induces eddy currents there, whose current density can be determined from the electric field by means of (2.15).

2.7 Poynting Vector

It will be useful later on, Chap. 9, to have introduced the Poynting vector. The instantaneous power density, or Poynting's vector $\mathcal{P}$, has unit Watt-per-meter-squared (Wm^{-2}) and is given by

$$\mathcal{P} = \mathbf{E} \times \mathbf{H}. \tag{2.19}$$

When the fields vary sinusoidally, the average power per unit area $\overline{\mathcal{P}}$ can be computed as

$$\overline{\mathcal{P}} = \frac{1}{2}\mathrm{Re}\left(\mathbf{E} \times \mathbf{H}^*\right) \tag{2.20}$$

where $\mathbf{E}$ and $\mathbf{H}$ are now phasor representations of the time-harmonic fields in terms of their amplitudes and the superscript "$*$" indicates the complex conjugate. The average power $\overline{P}$ through a surface S is then

$$\overline{P} = \int_S \overline{\mathcal{P}} \cdot d\mathbf{S} = \frac{1}{2}\mathrm{Re}\int_S \left(\mathbf{E} \times \mathbf{H}^*\right) \cdot d\mathbf{S} \tag{2.21}$$

where the direction of the elemental surface $d\mathbf{S}$ gives the direction of power flow.

2.8 Permeability and Magnetic Induction

Ferromagnetic materials such as iron or iron-based alloys respond to the application of a magnetic field, such as that produced by alternating electric current flowing in an eddy-current coil, by becoming strongly magnetized. Such materials, especially steels, are commonly used in various structures and are routinely inspected using NDE methods. The ferromagnetism exhibited by these materials means that they interact with eddy currents in a way that is somewhat different from the interaction with non-ferromagnetic materials such as copper or aluminum. For this reason, ferromagnetic materials deserve special attention and will be dealt with in more detail in Chap. 3. Here, the concept of permeability is briefly introduced since it is needed in the discussion of the electromagnetic skin effect which follows.

When an applied magnetic field **H** interacts with a ferromagnetic material, **H** is augmented by the magnetization of the material, **M**, which also has units A/m in SI. In fact, **M** is related to **H** via the susceptibility χ, a material-dependent dimensionless parameter which embodies the strength of magnetization of the ferromagnet in response to the applied magnetic field,

$$\mathbf{M} = \chi \mathbf{H}. \tag{2.22}$$

Hence, the total magnetic field in the presence of a ferromagnet can be written

$$\mathbf{H} + \chi \mathbf{H} = (1 + \chi)\mathbf{H} = \mu_\mathrm{r} \mathbf{H}$$

where $\mu_\mathrm{r} = 1 + \chi$ is a material-dependent dimensionless parameter known as the relative permeability. Typically, χ is a function of **H** which means that μ_r is not constant for any particular ferromagnet but changes as the value of **H** changes. The relationship between **M** and **H** is inherently *nonlinear*.

When working with ferromagnetic materials, it is convenient to work in terms of the field of magnetic induction, **B**, whose unit is the Tesla (T), since **B** represents the combined effect of **H** and **M**. In the absence of magnetic material, there is a simple linear relationship between **B** and **H**;

$$\mathbf{B} = \mu_0 \mathbf{H}, \tag{2.23}$$

in which the parameter μ_0 is the permeability of free space with unit Henry per meter (H/m) and value $\mu_0 = 4\pi \times 10^{-7}$ H/m. In the presence of a ferromagnet,

$$\mathbf{B} = \mu_0(\mathbf{H} + \mathbf{M}). \tag{2.24}$$

By manipulating the above definitions, the following relationship can be obtained:

$$\mathbf{B} = \mu \mathbf{H} \tag{2.25}$$

where μ is the permeability of the material, unit H/m, and $\mu = \mu_0\mu_r$. For the reasons described in the discussion following (2.22), the relationship between **B** and **H** is also inherently nonlinear although, if the magnitude of the applied **H** field is not very large, **B** is approximately proportional to **H**. Relation (2.25) holds in the case that the material permeability is isotropic, as discussed in relation to conductivity, (2.15). In the case of a material that exhibits anisotropic permeability, a tensor form for permeability is required.

2.9 Electromagnetic Skin Effect

As mentioned in the discussion around (2.1), the current density inside a wire carrying DC current is spatially uniform. As the frequency increases, however, a phenomenon known as the electromagnetic skin effect comes into play. This phenomenon has the effect of confining the current to a thin skin near the surface of the conductor. The effect is observed in every conductor carrying AC current, whether it be the wires in the windings of the eddy-current coil, or the metal test-piece in which the eddy currents are induced. As the frequency of the alternating current flowing in the probe coil increases, the eddy-current density induced in the test-piece is confined to an increasingly thin layer (or "skin") near its surface. In other words, the depth of penetration of the eddy currents into the test-piece can be controlled by adjusting the frequency of the inspection. The fact that the depth of penetration can be varied in this way provides a tool for optimizing an electromagnetic inspection to a particular depth in the test-piece. For surface-breaking defects, it is best to work at higher frequencies for which the induced eddy currents are concentrated near the surface of the specimen. Inspection sensitivity is increased by concentrating the eddy currents in the vicinity of the flaw. For deep-lying flaws, lower frequencies are needed so that the eddy currents penetrate sufficiently far into the specimen to interact with the flaw.

An approximate guide to the depth of penetration of electric current flowing in a conductor is known as the electromagnetic skin depth, δ (m), given by the following formula:

$$\delta = \sqrt{\frac{2}{\omega\sigma\mu}} \tag{2.26}$$

which can also be expressed

$$\delta = \frac{1}{\sqrt{\pi f \sigma\mu}}. \tag{2.27}$$

In the definition of (2.26) and (2.27), δ is inversely proportional to the square root of the frequency of the alternating current exciting the eddy-current coil f, the electrical conductivity of the test-piece σ, and its magnetic permeability μ. This definition emerges from the analysis of a two-dimensional system in which eddy currents are excited in a half-space conductor (an infinitely deep conductor with a flat surface)

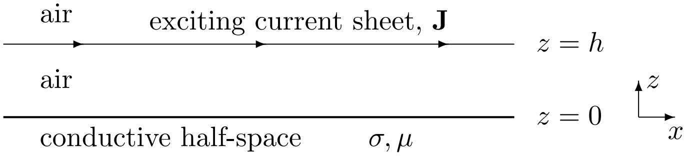

Fig. 2.5 Conductive half-space excited by a current sheet $\mathbf{J} = J(z)\hat{x}$

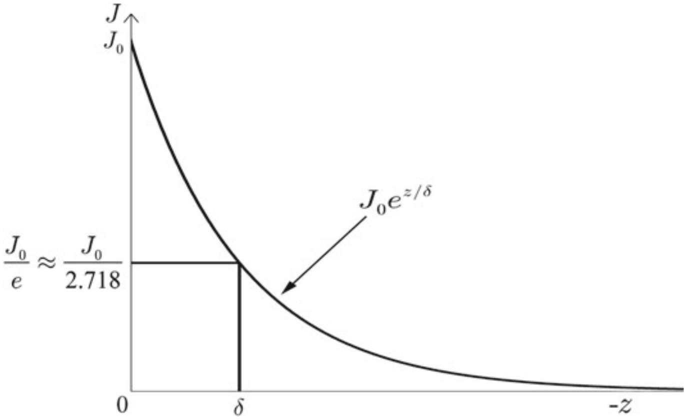

Fig. 2.6 Exponential decay of induced current density as a function of depth in a half-space conductor

by currents flowing in a thin sheet above the surface of the conductor, and parallel to it, as shown in Fig. 2.5. In this case, the magnitude of the eddy-current density in the test-piece falls off exponentially with depth from the surface:

$$J(z) = J_0 \exp(z/\delta), \qquad z < 0, \tag{2.28}$$

where $J_0 = J(0)$, as shown in Fig. 2.6. The value of electromagnetic skin depth versus frequency is plotted in Fig. 2.7 for various metals [12]. The derivation of (2.26)–(2.28) is presented in Sect. 6.3.1.

The value of δ is easy to compute for any given metal and serves as a useful guide to the depth of penetration of the electromagnetic field. In a real eddy-current measurement, however, the cylindrical geometry of a typical coil usually leads to lesser field strength, for a given depth in the test-piece, than a uniform field excitation, especially for a small probe. In Fig. 2.8 [3], eddy-current contours produced by a surface coil of the type shown in Figs. 1.8 and 1.9 are compared at three distinct frequencies. It is obvious that the depth of penetration of the eddy-current density decreases as the frequency increases.

Example: Electromagnetic skin effect What thickness of copper sheet, conductivity 58 MS/m, is needed to block 99% of incoming cellphone signal at 800 MHz?

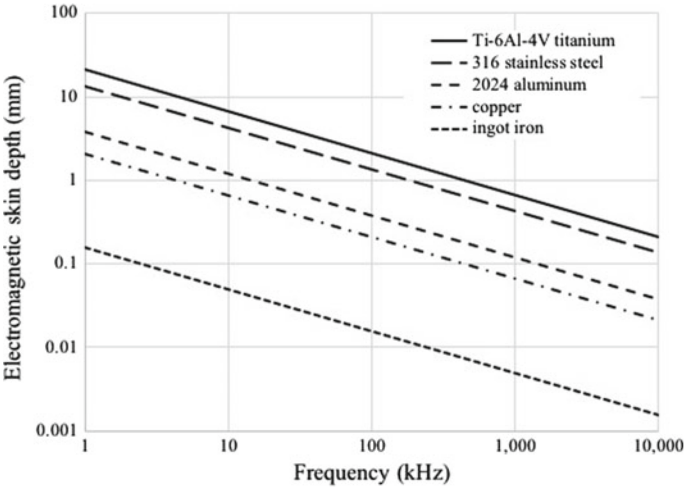

Fig. 2.7 Electromagnetic skin depth δ versus frequency for various metals at 20 °C, whose conductivities are given in Table 2.1. Relative permeability of 316 stainless steel is here taken to be $\mu_\mathrm{r} = 1.02$ [5] and that of ingot iron to be a representative value $\mu_\mathrm{r} = 1{,}000$, Table 3.2

Solution The electromagnetic wave carrying the cellphone signal also obeys a law of exponential decay in a metal similar to (2.28),

$$A(z) = A_0 e^{-|z/\delta|}.$$

When 99% of the signal is blocked,

$$\frac{A(z)}{A_0} = 0.01 = e^{-|z/\delta|}$$

and

$$-\frac{z}{\delta} = \ln(0.01) = -4.61$$

or $z = 4.61\delta$. Now, in copper at 800 MHz,

$$\delta = \frac{1}{\sqrt{\pi \times 800 \times 10^6 \times 58 \times 10^6 \times 4\pi \times 10^{-7}}} = 2.34\ \mu\mathrm{m},$$

using (2.27). Finally, the depth of copper that blocks 99% of incoming cellphone signal at 800 MHz is

$$z = 4.61 \times 2.34 = 10.8\ \mu\mathrm{m}.$$

The copper does not need to be very thick at all!

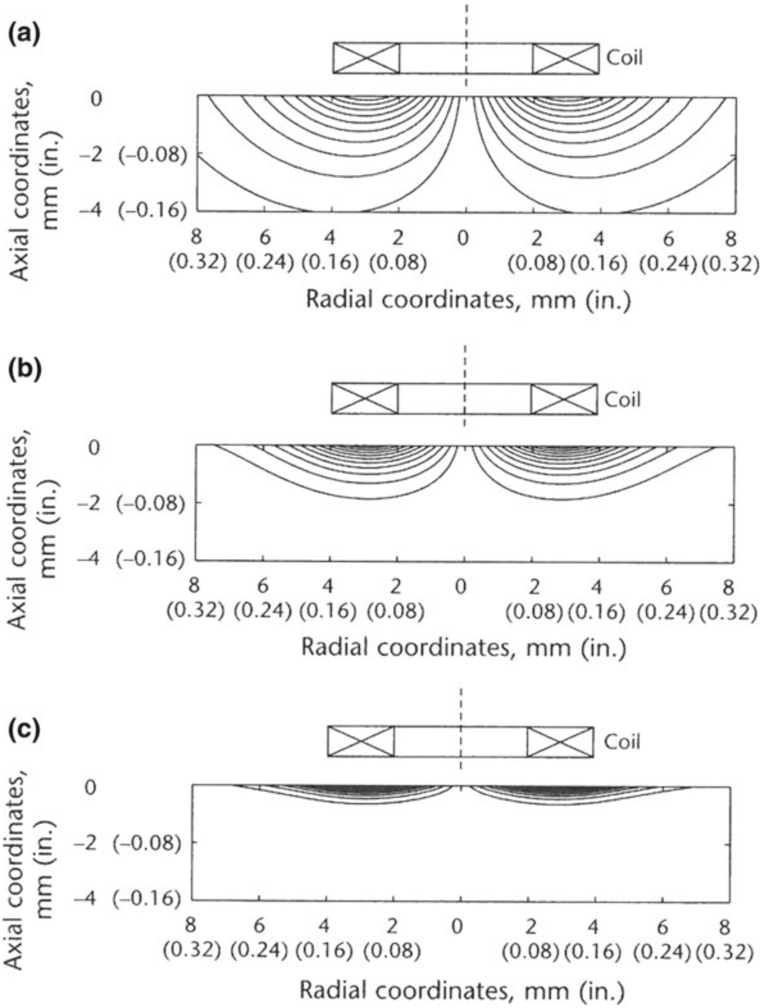

Fig. 2.8 Contours of eddy-current density $|J_\phi|$ induced by a surface coil at frequencies 1 kHz (**a**), 10 kHz (**b**) and 100 kHz (**c**). The probe parameters are $r_\mathrm{i} = 2$ mm, $r_\mathrm{o} = 4$ mm, $l = 1$ mm, $N = 800$ and $s = 1$ mm. The test-piece is a half-space ($T \rightarrow \infty$) with $\sigma = 35.4$ MS/m and $\mu_\mathrm{r} = 1$. The electromagnetic skin depth takes values $\delta = 2.7$, 0.85 and 0.27 mm in **a**, **b** and **c**, respectively. Reprinted with permission from the NDT Handbook: Electromagnetic Testing. Copyright © 2004, ASNT, Columbus, Ohio [3]

2.10 Polarization and Electric Displacement

We have now met three of the four electromagnetic fields, namely the electric field, **E**, the magnetic field, **H**, and the field of magnetic induction, **B**. The fourth is the *electric displacement*, **D**, measured in Coulombs per meter squared (C/m^2). **D** is also known as *electric flux density* because electric flux Ψ_e can be defined in terms of **D** as follows:

$$\Psi_\mathrm{e} = \int_S \mathbf{D} \cdot d\mathbf{S} \tag{2.29}$$

(compare with (4.16) that relates magnetic flux Ψ with magnetic induction **B**). For a dielectric material, **D** is related to **E** in a way that parallels the relationship between **B** and **H** for a magnetic material.

In EC NDE, we are dealing with metals, for which conductivity $\sigma \gg 1$ and relative permittivity $\epsilon_\mathrm{r} = 1$, rather than dielectrics (insulators) for which $\sigma \ll 1$ and $\epsilon_\mathrm{r} > 1$. This means that we do not rely heavily on the use of **D** in EC NDE. Nonetheless, occasionally we shall need to be aware of the meaning of **D** and for this reason the relations between **D**, **E** and the polarization **P** of a dielectric are summarized briefly here.

As we already know, there are free electrons available in a conducting material to conduct electricity when a force is applied. A dielectric material has no such free charges. Instead, at an atomic level in a dielectric, the negatively charged electron cloud is balanced by the positively charged atomic nuclei. On application of an external force, the charge clouds are not free to move in a macroscopic sense, but they do exhibit some degree of displacement from one another, so that an electric dipole is created. The displaced charges give rise to local dipoles whose moment is expressed

$$\mathbf{p} = Q\mathbf{d} \tag{2.30}$$

where **d** is the distance vector from $-Q$ to $+Q$ of the dipole.

On a macroscopic scale, over a collection of many atoms, it is useful to introduce the polarization vector field of a material, **P** measured in C/m^2, where **P** is the dipole moment per unit volume of the dielectric and is a measure of the intensity of polarization in the material. The electric displacement inside a material of polarization **P** is then

$$\mathbf{D} = \epsilon_0\mathbf{E} + \mathbf{P}. \tag{2.31}$$

For some dielectrics, **P** is proportional to the applied electric field and

$$\mathbf{P} = \chi_\mathrm{e}\epsilon_0\mathbf{E} \tag{2.32}$$

where χ_e is the (dimensionless) electric susceptibility of the material. If (2.32) is combined with (2.31), the constitutive relation

$$\mathbf{D} = \epsilon\mathbf{E} \tag{2.33}$$

is obtained, in which $\epsilon = \epsilon_0(1 + \chi_e) = \epsilon_0\epsilon_r$. Relation (2.33) implies that the material permittivity is isotropic, as discussed in relation to conductivity, (2.15). In the case of a material that exhibits anisotropic permittivity, a tensor form for permittivity is required.

2.11 Summary

In this chapter, the electromagnetic fields and the constitutive relations by which they are related to material properties have been introduced. The relative importance of these fields and material properties to the EC NDE method have been described. The conductivity of a material is of primary importance in EC NDE. The permeability of a ferromagnetic test-piece also strongly influences the signals measured in an EC inspection, as will be seen in Chap. 6. In the next chapter, a description of ferromagnetic phenomena is given that attempts to explain the origins of ferromagnetism and the mechanisms that underly it, which gives insight into the fact that the magnetic history of a test-piece can strongly affect the measured EC signals obtained from it.

2.12 Exercises

1. Obtain the phasor notation of the following time-harmonic functions, if possible.
   (i) $A(t) = 2\sin(\omega t) - 3\cos(\omega t)$,
   (ii) $C(t) = 4\cos(80\pi t - \pi/4)$,
   (iii) $D(t) = 2 - \cos(2\omega t)$,
   (iv) $I(t) = -7\sin(\omega t)$,
   (v) $U(t) = \sin(\omega t + \pi/4)\sin(\omega t + \pi/8)$,
   (vi) $V(t) = 5\cos(\omega t + \pi/3)$.
2. Obtain $C(t)$ in terms of ω from the following phasors.
   (i) $\mathcal{C} = 1 + 3j$,
   (ii) $\mathcal{C} = 3\,e^{j0.9}$,
   (iii) $\mathcal{C} = 2\,e^{j\pi/2} + 3\,e^{j0.7}$.
3. A coil is made of 150 turns of silver wire wound on a circular cylindrical core and carries current 0.1 A. If the mean radius of the turns is 6.5 mm and the diameter of the wire is 0.4 mm, (i) calculate the DC resistance of the coil (you may make the approximation that all the turns on the coil (windings) have the same radius as the mean radius) and (ii) calculate the current density in the wire.
4. Determine the total current in a wire of radius 1.6 mm placed along the z-axis if

$$\mathbf{J} = \frac{500}{\rho}\hat{z} \qquad \text{Am}^{-2}.$$

5. Given that the electrical conductivity of nickel is 14.62 MS/m at 20 °C, evaluate the electrical conductivity of nickel at 25 °C.
6. According to (2.13), sketch the dependence of conductivity on temperature. Rewrite (2.13) in terms of resistivity ρ and now sketch the dependence of ρ on temperature. Explain the features of your two sketches.
7. Using the data shown in Fig. 2.7, estimate the conductivities of graphite, titanium, and copper. Give your answers in terms of (a) MS/m and (b) % IACS. What additional piece of information do you need to determine the conductivity of ingot iron from this data? Conduct a little research to find this information and use it to (c) estimate the conductivity of ingot iron from the data shown in Fig. 2.7.

References

1. Asimov, I.: Asimov's Biographical Encyclopedia of Science and Technology. Pan Books, London (1975)
2. Abramowitz, M., Stegun, I.A. (eds.): Handbook of Mathematical Functions with Formulas. Graphs and Mathematical Tables. Dover, New York (1972)
3. Moore, P.O. (ed.), Udpa, S.S. (tech. ed.): Nondestructive Testing Handbook: Electromagnetic Testing, vol. 5, 3rd edn. American Society for Nondestructive Testing, Columbus (2004)
4. Bowler, N.: Theory of four-point alternating current potential drop measurements on a metal half-space. J. Phys. D: Appl. Phys. **39**, 584–589 (2006)
5. Bowler, N., Huang, Y.: Electrical conductivity measurement of metal plates using broadband eddy-current and four-point methods. Meas. Sci. Technol. **16**, 2193–2200 (2005)
6. Kaye, G.W.C., Laby, T.H.: Tables of Physical and Chemical Constants, 15th edn. Longman, London (1986)
7. Bowler, N., Huang, Y.: Model-based characterization of homogeneous metal plates by four-point alternating current potential drop measurements. IEEE T. Magn. **41**, 2102–2110 (2005)
8. Bowler, J.R., Bowler, N.: Theory of four-point alternating current potential drop measurements on conductive plates. Proc. R. Soc. Ser. A. **463**, 817–836 (2007)
9. Suhr, H., Guettinger, T.W.: Error reduction in eddy current conductivity measurements. British J. NDT. **35**, 634–638 (1993)
10. Lide, D.R. (ed.): CRC Handbook of Chemistry and Physics, 82nd edn. CRC Press, London (2001)
11. NDT Resource Center: The Collaboration for NDT Education, Iowa State University, Ames, Iowa, USA. http://www.ndt-ed.org (2014). Accessed 10 Oct 2017
12. McMaster, R.C., McIntire, P. (eds.), Mester, L.M. (tech. ed.): Nondestructive Testing Handbook: Electromagnetic Testing, vol. 4, 2nd edn. American Society for Nondestructive Testing, Columbus (1986)

Chapter 3
Ferromagnetic Materials

Abstract Ferromagnetic properties of materials exert a profound influence upon EC NDE. Successful interpretation of EC measurements on many steels or other types of ferromagnetic conductor requires an understanding of the magnetization (and demagnetization) processes that occur in ferromagnetic materials. This chapter builds upon the role of electric current as the fundamental source of the magnetic field to explain the phenomenon of magnetization, to describe hysteresis, and to show the nonlinear character of permeability. Energy arguments are invoked to explain the existence of ferromagnetic domains and domain processes are described. Methods of demagnetizing test-pieces to regularize them for EC inspection are suggested. Description of the role of low-conductivity ferromagnetic ceramics (ferrite cores) in EC coil construction is described in Chap. 6, Signals and Coils.

3.1 Introduction

Ferromagnets are materials that become strongly magnetized in response to an applied magnetic field, even retaining some magnetization when the applied magnetic field is removed. A naturally occurring ferromagnetic material is magnetite or lodestone, Fe_3O_4. Early records speak of a spoon-shaped compass formed from magnetite being used in Chinese ceremonies of the second century BCE. By the time of the seventh and eighth centuries CE, magnetized iron needles were being used by Chinese navigators; either floating in water in the form of a "wet" compass, placed on a pointed shaft as a "dry" compass, or suspended from a silk thread.

Elements of the periodic table that are ferromagnetic at room temperature are iron (Fe), nickel (Ni), and cobalt (Co). Their alloys and compounds are also often ferromagnetic. Some compounds, known as ferrites, are low-conductivity ferromagnetic materials. MnZn ferrite and its practical role in the construction of EC probe cores is discussed in Sect. 6.3.5 of this text.

In the context of EC NDE, ferromagnetic materials constitute a distinct material class because the EC probe impedance signal due to a ferromagnetic test-piece may be very different from that due to a non-ferromagnetic test-piece with the same conductivity. Recalling the normalized impedance-plane plot of Fig. 6.3, the reactance

N. Bowler, *Eddy-Current Nondestructive Evaluation*,
Springer Series in Measurement Science and Technology,
https://doi.org/10.1007/978-1-4939-9629-2_3

of the coil is reduced as it is brought near to the surface of a non-ferromagnetic test-piece (dashed lines). If the test-piece is ferromagnetic, however, the coil reactance may increase, as shown by the dotted lines. Most commonly, the ferromagnetic test-pieces encountered in EC NDE are *steels*, which are alloys of iron.

This chapter expands greatly on the brief introduction to permeability and magnetic induction given in Sect. 2.8 of this text. Nonetheless, even here I shall skim lightly over the deep and complicated topic of ferromagnetism. For a more detailed treatment, the interested reader is referred to Jiles' comprehensive yet accessible text [1] or to Cullity's classical work [2].

3.2 Fundamental Source of the Magnetic Field

Consider the schematic diagram of a bar magnet shown in Fig. 3.1. Such a magnet could be made from any ferromagnetic material. It is common knowledge that two such magnets, if their ends are brought together, will either repel or attract each other. Whether or not the force between the magnets is repulsive or attractive depends on the *polarity* of the magnets or the relative orientation of their *magnetic dipole moments*.

The magnetic dipole moment $\mathbf{m}$ of a bar magnet like the one depicted in Fig. 3.1 can be expressed

$$\mathbf{m} = P\,\mathbf{d} \tag{3.1}$$

where P is the pole strength and $\mathbf{d}$ is the vector length between the poles. $\mathbf{m}$ is directed from S toward N. This definition is analogous to that of the electrostatic dipole given in (2.30). By analogy with electrostatics, the definition in (3.1) suggests the existence of a magnetic monopole as the fundamental source of the magnetic field and leads to speculation that the magnetic monopole might play a role in magnetostatics that is similar to that of the electric charge in electrostatics. In fact, expression (3.1) is of limited use. The notion of magnetic poles remains popular in everyday thinking, and may be used to describe the interactions of long, thin bar magnets whose poles

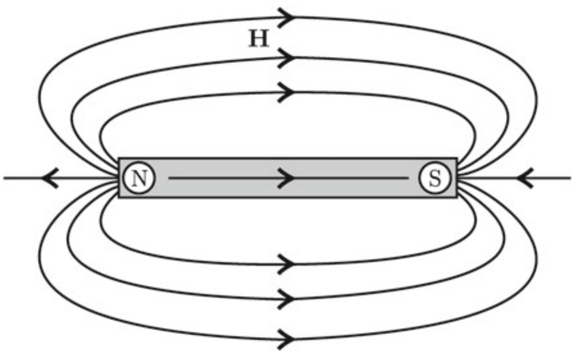

Fig. 3.1 By convention, the lines of magnetic field **H** originate at the north pole (N) and terminate at the south pole (S) of a simple bar magnet

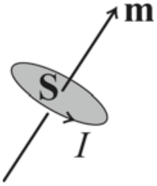

Fig. 3.2 Magnetic dipole moment **m** of a loop formed by current *I*

are well separated, but scientifically it is held that magnetic monopoles do not exist. One simple experiment that immediately shows a difficulty with the notion of the magnetic monopole is the following. If you try to isolate one pole of a bar magnet by, say, dividing the magnet in half, then immediately new poles are formed at the surface of division. Each half of the original magnet forms a new magnetic dipole with its own N and S poles.

What, then, is the fundamental source of the magnetic field? During the course of Ampère's experiments on electricity and magnetism, he discovered that the magnetic field of a small current loop is identical to that of a small bar magnet. This observation led Ampère to hypothesize that *all* magnetic effects are due to current loops, and that the magnetic effects in ferromagnetic materials such as iron are due to so-called *molecular currents*. These currents are now known to be quantum mechanical in origin, due to the orbital and spin angular momenta of atomic electrons. Ampère's insight was especially remarkable because it predated the discovery of the electron by about 100 years!

We are led to deduce, therefore, that the fundamental source of the magnetic field is not a magnetic monopole, but the motion of electrical charge or, equivalently, electric current. The magnetic dipole moment of a current loop, **m**, is defined to be the product of the current flowing in the loop, I, and the vector area of the loop, **S**;

$$\mathbf{m} = I\mathbf{S}. \tag{3.2}$$

This is shown schematically in Fig. 3.2. The units of **m** are Ampère-meter-squared (Am^2).

3.3 Magnetization

The application of a magnetic field **H** to a ferromagnetic material results in magnetization **M** (with SI unit A/m) of that material. Magnetization was introduced in Sect. 2.8 of this text. In fact, the application of a magnetic field to any material gives rise to a magnetization

$$\mathbf{M} = \chi\mathbf{H}, \tag{3.3}$$

where χ is the magnetic susceptibility of the material (dimensionless). There are several classes of magnetic material, but in ferromagnets (e.g., iron, cobalt, nickel,

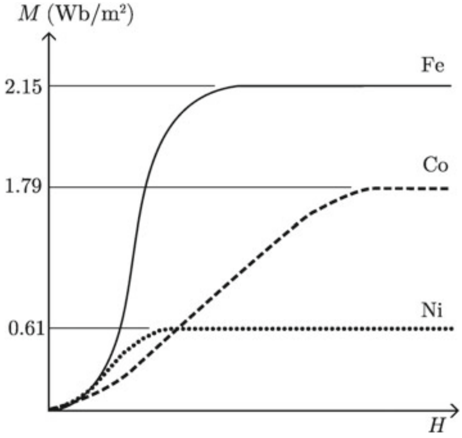

Fig. 3.3 Initial magnetization curves for several ferromagnetic metals. Note that the units of M differ between Fig. 3.3 and Table 3.1 by the factor μ_0

and their alloys) χ is positive, relatively large, and nonlinear, so that

$$\mathbf{M}(H) = \chi(H)\mathbf{H}. \tag{3.4}$$

One of the puzzles of ferromagnetism, eventually explained by domain theory (Sect. 3.6), was the very large magnetization that can occur on the application of a relatively small magnetic field. In fact, the resulting **M** can be of the order of a thousand times larger than the field of **H** applied to produce it!

The *initial magnetization curve* is the nonlinear response of a ferromagnetic material, initially in the demagnetized state, to an applied magnetic field. The demagnetized state is one in which the ferromagnet exhibits zero magnetization in the absence of an applied **H**, corresponding to the origin of Fig. 3.3. The demagnetized state, and methods for achieving it, will be discussed in more detail in Sects. 3.6 and 3.7 of this text. Initial magnetization curves for the ferromagnetic elements Fe, Co, and Ni are shown in Fig. 3.3. It can be seen that each element has a different value of saturation magnetization, M_0. The saturation magnetization is the maximum achievable value of M for a specific material, and is an intrinsic property of the material. Values of saturation magnetization for various ferromagnets are listed in Table 3.1. Note that the units of M differ between Fig. 3.3 and Table 3.1 by the factor μ_0. From the tabulated values of M_0 it can be seen that an alloy of two ferromagnetic elements often, but not always (as in the case of Permendur), yields a value of M_0 that lies between those of the individual elements.

Another feature of the magnetization curves shown in Fig. 3.3 is that the slope of the curve is different for each element. In consequence, Co requires significantly higher applied H to reach saturation than Fe and Ni. This feature is a consequence of the crystal structure of the material and, indeed, varies according to magnetization direction in the case of a single crystal material.

Table 3.1 Saturation magnetization (M_0) values for various ferromagnets [1]

Material	M_0 ($\times 10^6$ A/m)
Iron	1.71
Cobalt	1.42
Nickel	0.48
78 Permalloy (78% Ni, 22% Fe)	0.86
Supermalloy (80% Ni, 15% Fe, 5% Mo)	0.63
Permendur (50% Co, 50% Fe)	1.91

3.3.1 Rayleigh Law

In the region of the initial magnetization curve in which H is *low*, μ can be expressed

$$\mu(H) = \mu(0) + \nu H, \tag{3.5}$$

where ν is a nonzero constant. This leads to dependence of B on H given by

$$B(H) = \mu(0)H + \nu H^2. \tag{3.6}$$

These relationships were first noted by Lord Rayleigh. They permit construction of hysteresis loops and expressions for hysteresis loss and remanence in terms of ν and H [1]. The low-field region of the magnetization curve, for which these relationships hold, is highlighted in Fig. 3.4.

In EC NDE theory, often a linear relation between B and H in terms of the initial permeability is assumed. This relationship may be expressed as

$$B = \mu(0)H. \tag{3.7}$$

Comparison of (3.6) and (3.7) quickly reveals that the assumed relation (3.7) is only true in the asymptotic limit as $H \rightarrow 0$! On the other hand, incorporation of

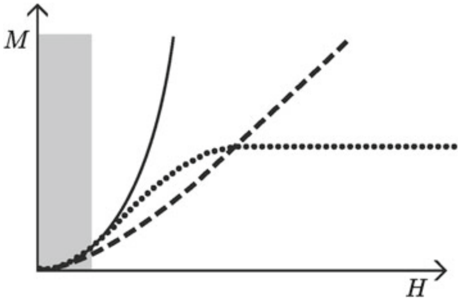

Fig. 3.4 Rayleigh region of the initial magnetization curve, indicated by the shaded region

full, nonlinear, ferromagnetic behavior into eddy current theory quickly leads to great complexity. The relationship (3.7) is straightforward to incorporate and gives reasonable results for many purposes. One consequence of neglecting the nonlinear magnetic behavior in EC modeling is some loss of accuracy in computing Z and ΔZ for ferromagnetic test-pieces. For example, results shown in [3] comparing computed and measured ΔZ for artificial rectangular defects in a flat test-piece show very good agreement for aluminum (within $\approx$5%), but poorer agreement for steel (within $\approx$20%).

3.4 Hysteresis

A magnetic hysteresis loop is the path traced by B as H is first reduced from its value at saturation, through zero, to a saturating value in the opposite direction, and then increased again through zero to saturation. A sketch of a typical hysteresis loop is shown in Fig. 3.5. The fact that the loop is not closed indicates that there is an energetically irreversible process occurring. The area of the loop is the work done by the magnetic field in magnetizing the material. The hysteresis loop is a common means of representing the bulk magnetic properties of a ferromagnetic material. It has certain characteristics that vary from material to material. One of these is the *coercivity*, H_c (A/m). Coercivity, or coercive field, is the reverse magnetic field needed to reduce the magnetization of a ferromagnetic sample to zero, once it has been magnetized to saturation. Remanence, B_r (T or Wb/m^2), is the field of magnetic

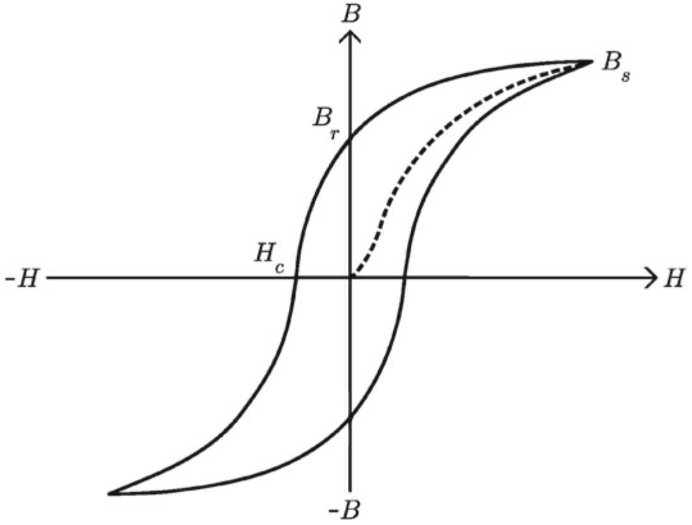

Fig. 3.5 Typical major hysteresis loop of a ferromagnetic material. The dashed line indicates the initial magnetization curve

induction exhibited by a ferromagnet on removal of the applied magnetizing field H, after the ferromagnet has been magnetized to saturation. It is important to note that the definitions of H_c and B_r involve the *major* hysteresis loop of a material, in which the material is magnetized to saturation. Smaller (minor) hysteresis loops may be obtained by cycling the applied magnetic field H to lower strengths, but the definitions of H_c and B_r relate only to the major hysteresis loop.

Various applications in which ferromagnets are used require different characteristics of the material, that may be deduced from the hysteresis loop. For example, the core of an electromagnet should exhibit low H_c and B_r so that the strength of the magnetization can be easily controlled. Materials for permanent magnets should have high B_r, so that they exhibit strong magnetization, and high H_c so that they are not easily demagnetized by stray fields. Ferromagnets for transformer cores must exhibit minimal losses in order to convert energy efficiently. Low loss in a ferromagnet is observable as a narrow hysteresis loop with relatively small area. Explanation of the processes that underly the hysteresis loop are given in Sect. 3.6 of this text.

3.5 Permeability

Magnetic permeability, μ measured in Henrys per meter (H/m), provides a measure of the ability of a material to augment the applied magnetizing field by its own magnetization. It relates the field of magnetic induction to **H** and **M** as follows

$$\begin{aligned} \mathbf{B}(H) &= \mu(H)\mathbf{H} && (3.8)\\ &= \mu_0[\mathbf{H} + \mathbf{M}(H)] && (3.9)\\ &= \mu_0[1 + \chi(H)]\mathbf{H}, && (3.10) \end{aligned}$$

from which it is evident that

$$\mu = \mu_0(1 + \chi). \tag{3.11}$$

This leads to the definition of relative permeability, μ_r (dimensionless), which is the ratio of the permeability of a specific material to that of free space,

$$\mu_\mathrm{r} = \frac{\mu}{\mu_0} = 1 + \chi. \tag{3.12}$$

Consider the initial magnetization curve of B versus H shown in Fig. 3.6, solid line. The permeability as a function of H, dashed line, can be obtained from the initial magnetization curve using the relation $\mu = B/H$. Other quantities that are in common usage are the differential permeability, defined

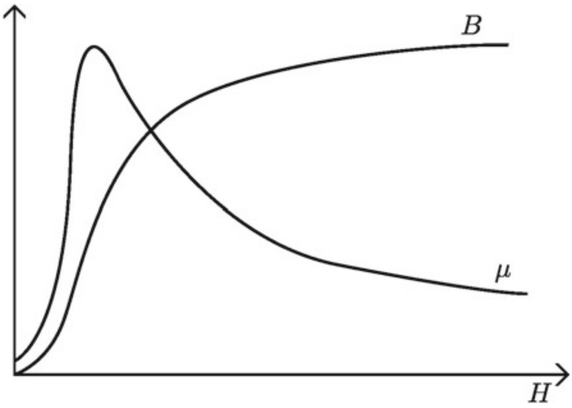

Fig. 3.6 Initial magnetization curve for B and associated permeability μ for a representative soft ferromagnetic material, e.g., annealed iron

Table 3.2 Relative initial permeability $\mu_{\mathrm{r,in}}$, relative permeability at 2 T magnetic induction $\mu_{\mathrm{r,2T}}$, and maximum relative permeability $\mu_{\mathrm{r,max}}$ for various ferromagnets [1, 4]. Relative permeability is dimensionless

Material	$\mu_{r,\mathrm{in}}$	$\mu_{\mathrm{r,2T}}$	$\mu_{\mathrm{r,max}}$
Iron (purified)		5,000	180,000
Armco iron	250		7,000
Nickel (wrought)	250		2,000
78 Permalloy (78% Ni, 22% Fe)		8,000	100,000
Supermalloy (80% Ni, 15% Fe, 5% Mo)		100,000	800,000
Permendur (50% Co, 50% Fe)		800	5,000

$$\mu' = \frac{dB}{dH} \tag{3.13}$$

and the initial permeability, defined as the slope B/H of the tangent to the initial magnetization curve as $H \to 0$

$$\mu_{\mathrm{in}} = \left.\frac{dB}{dH}\right|_{B=0,H=0} = \left.\frac{B}{H}\right|_{B\to 0,H\to 0}. \tag{3.14}$$

Some typical values of $\mu_{\mathrm{r,in}}$ are given in Table 3.2, together with values of maximum relative permeability $\mu_{\mathrm{r,max}}$ and relative permeability at 2 T magnetic induction field $\mu_{\mathrm{r,2T}}$. Note that μ varies as a function of H whereas μ_{in} and μ_{max} do not.

Comparing (3.8) and (3.4) it is clear that μ is to **B** what χ is to **M**. Correspondingly, the following definitions of differential and initial susceptibility mirror those for μ:

$$\chi' = \frac{dM}{dH}, \tag{3.15}$$

$$\chi_{\text{in}} = \left.\frac{dM}{dH}\right|_{M=0,H=0} = \left.\frac{M}{H}\right|_{M\to 0,H\to 0}. \tag{3.16}$$

3.6 Ferromagnetic Domains

In ferromagnets, permanent magnetic moments exist on the atomic scale. They do not rely on the presence of an external magnetic field for their existence, but rather their existence is explained by quantum-mechanical descriptions of spin and orbit of atomic electrons. Another definition of magnetization relates **M** to the magnetic dipole moment per unit volume in the material:

$$\mathbf{M} = \frac{\mathbf{m}}{V}. \tag{3.17}$$

The macroscopic properties of ferromagnets can be explained if long-range magnetic order (over many atoms) exists within the material. Such a region of long-range order is known as a *domain*. The dimensions of a typical domain are on the order of tens of microns. A domain in a ferromagnetic material is a region in which the individual atomic magnetic dipole moments are aligned parallel with one another. This means that the magnetization within a particular domain is essentially saturated, with $\mathbf{M} = \mathbf{M}_0$. The direction of magnetization generally varies from one domain to another, accounting for the fact that a ferromagnet may exhibit no remanent magnetization despite the fact that each domain is magnetized to saturation. In the demagnetized state, the vector sum of the magnetization over all domains is zero. Magnetization is then the process of rearranging the domains so that their magnetic moments are in alignment with each other and, ultimately, with the direction of applied **H**. The existence of domains within a bulk ferromagnetic sample explains the fact that a large magnetization M may be achieved by application of a relatively small H to a sample. The applied H does not create order throughout the sample but, rather, overcomes energy barriers to align domain magnetization vectors that already exist.

3.6.1 Why do Domains Form?

Materials in equilibrium occupy a state in which their free energy is minimized. If not, a change of some kind will occur until a local energy minimum is reached. A phase transition, such as from the solid to the liquid state, requires input of energy to effect the transformation. In a solid ferromagnet, minimization of quantum mechanical *exchange energy* occurs when neighboring atomic magnetic moments are aligned parallel with one another. So, minimization of exchange energy drives the magnetic ordering that occurs in ferromagnets. A ferromagnet does not just spontaneously magnetize throughout its entire volume, however, because although exchange energy is reduced, a fully ordered sample has large magnetostatic energy associated with it. In other words, there is a large external magnetic field associated with a fully ordered sample. We know this because the purpose of a simple bar magnet, which is normally magnetized to saturation and therefore fully ordered, is to have a large external magnetic field associated with it in order to interact strongly with other bodies. A schematic diagram of the external magnetic field due to a bar magnet is shown in Fig. 3.1. Domains, then, form in order to reduce the magnetostatic energy of the sample. Simply speaking, the magnetic state of the ferromagnet is determined by a balance between the exchange energy, the magnetostatic energy, and the energy cost associated with creating domain walls.

3.6.2 Domain Walls

The boundary between two domains consists of a region in which neighboring atomic magnetic moments cannot be perfectly aligned with one another but rotate, over many atoms, from the magnetization direction of one domain to that of its neighbor. An example of one type of domain wall is shown schematically in Fig. 3.7. Domain wall thickness varies according to material type, but is typically of the order of 100 nm, occurring on the scale of many atomic moments. In iron, **M** in neighboring domains switches direction by either 90° or 180°, due to the cubic crystal structure of iron. The walls that separate these domains are hence known as 90° (Néel) or 180° (Bloch) walls, respectively. Other ferromagnetic materials exhibit different characteristic arrangements of their domain structure, that are related to their crystal structure.

Fig. 3.7 Rotation of magnetic moments across a 180° Bloch wall

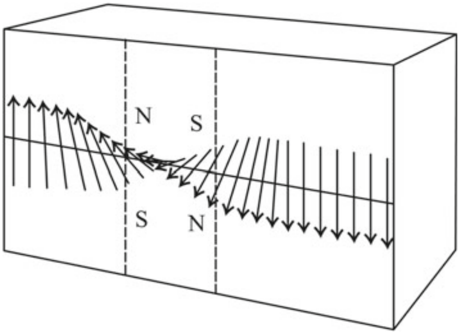

3.6.3 Domain Processes During Magnetization

When a magnetic field is applied to a ferromagnetic material, work is done by the magnetic field to reorient the domain magnetization directions to a direction more closely aligned with that of the applied field. There are several processes by which this occurs.

At low applied H-field strengths magnetic domains whose magnetization vector is directed in a direction similar to that of the applied field grow at the expense of domains whose magnetization direction is not similar to that of the applied field. The growth of one domain at the expense of another takes place by movement of the domain wall between them. Strictly, the atomic magnetic moments that are at the edge of a domain whose $\mathbf{M}$ vector is directed similarly to $\mathbf{H}$ rotate into alignment with $\mathbf{M}$. This process gives the appearance of domain wall movement. The process of domain wall movement is shown schematically in the first two insets of Fig. 3.8. At higher strengths of applied H, the restructuring of the domains continues until only a single domain exists, with magnetization direction similar to that of the applied field. This situation is shown in the third inset of Fig. 3.8. The magnetization of the single domain does not at first lie parallel to the direction of applied $\mathbf{H}$, because all ferromagnetic materials have one or more *easy axes* along which the magnetization vector will preferentially align and the directions of the easy axes are determined by the crystal structure of the particular material. For example, iron has body-centered cubic crystal structure and the six equivalent easy axes are in the directions of the cube edges $\langle 100 \rangle$ and similar. Cobalt, on the other hand, has a hexagonal close-packed crystal structure and there is only one easy axis, in the $\langle 0001 \rangle$ direction. For very high applied H, the magnetization direction rotates away from the easy axis to align fully with the direction of $\mathbf{H}$, as shown in the fourth inset in Fig. 3.8. This latter magnetization stage, in which $\mathbf{M}$ rotates, is reversible (anhysteretic), which means that when H is reduced from its saturating value the reorientation of $\mathbf{M}$ to realign with the easy axis

Fig. 3.8 Schematic showing domain rearrangement during magnetization

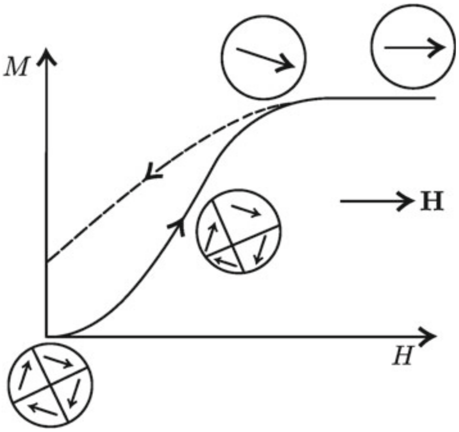

follows the same M-H curve as it did when H was increasing. On the other hand, motion of the domain walls is a hysteretic process because, simply speaking, domain walls are "pinned" at positions in which their local energy is minimized. Pinning sites are associated with inhomogeneities in the material such as impurities (small quantities of other elements dispersed in the crystal structure) and discontinuities in the crystal lattice (such as might occur at a grain boundary). Hysteresis loops such as the one shown in Fig. 3.5 are observed because it is necessary to supply energy to overcome domain wall pinning regardless of their direction of motion.

3.6.4 Hard and Soft Ferromagnets

Hard ferromagnetic materials, such as the permanent magnet material samarium-cobalt, are those with a high density of pinning sites. These materials require relatively high applied H to become magnetized; to provide sufficient energy to move the domain walls across multiple pinning sites. Hard ferromagnetic materials have relatively high H_c. Soft ferromagnetic materials such as iron, on the other hand, contain relatively few impurities and exhibit correspondingly low H_c. The motion of the domain walls is not smooth but occurs as a series of jumps from one pinning site to the next. In other words, as H is increased smoothly, B or M respond in a step-like manner because the increase in H produces no change in B or M while the domain wall is pinned, but then a sudden change is observed when the domain wall snaps away from one pinning site and moves to the next. This discontinuous motion is evidenced by looking closely at the hysteresis curve, which turns out to be made up of a sequence of steps rather than being a smooth curve, Fig. 3.9.

3.6.5 Evidence for the Existence of Domains

The existence of domains was first observed indirectly by Heinrich Barkhausen in 1919 in the form of audible clicks produced by a loudspeaker attached to a voltage

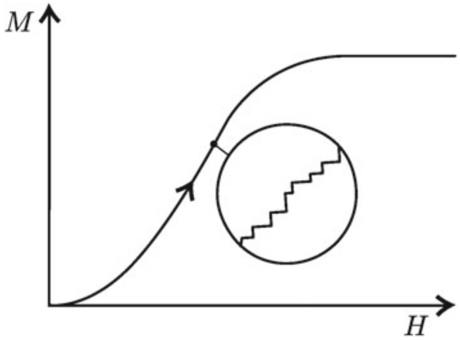

Fig. 3.9 Discontinuous changes in B as a function of H

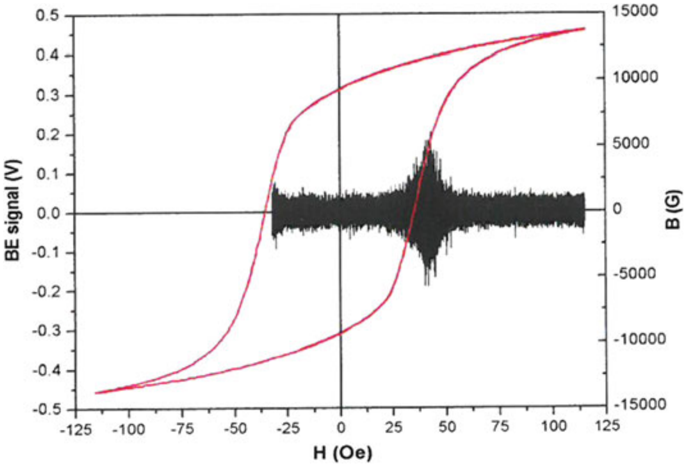

Fig. 3.10 One hysteresis cycle shown in terms of magnetic induction B. The Barkhausen effect (BE) signal overlays part of the hysteresis cycle [5, Fig. 8, used with permission]. Note, 1 Oersted (Oe) $=1000/(4\pi) \approx 79.58$ A/m and 1 Gauss (G) $=10^{-4}$ T

pick up loop wrapped around a ferromagnetic sample, as the sample was being magnetized. The discrete movements of the domain walls as they jump from one pinning site to another cause small, rapid changes in B that induce voltage pulses in the pick up coil, by Faraday's Law of induction. The loudspeaker in Barkhausen's experiment made it possible to observe these discrete changes in B. Today, Barkhausen "noise" can be recorded and analyzed digitally and is useful in some near-surface magnetic NDE applications. Figure 3.10 shows the increase in Barkhausen noise in a region of steepest slope of the hysteresis loop, which corresponds to a maximum in μ'.

Today, magnetic force microscopy (an adaptation of atomic force microscopy) permits direct imaging of ferromagnetic domains, with lateral resolution around 40 nm, but is limited to surface observations.

3.6.6 The Curie Temperature, T_C

Ferromagnetic ordering disappears at temperatures higher than the so-called *Curie temperature* T_C, at which a phase transition occurs. This is a temperature above which thermal agitation of the crystal lattice overcomes ferromagnetic ordering. Curie temperatures for some ferromagnetic materials are listed in Table 3.3. The fourth ferromagnetic element, Gadolinium, has not been mentioned until now because T_C for Ga is below room temperature and consequently, its applications are not widespread in the context of EC NDE.

Table 3.3 Curie temperatures for various ferromagnets [1]

Material	T_C (°C)
Iron	770
Cobalt	1130
Nickel	358
Gadolinium	20
Hard ferrites	400–700

3.7 Demagnetization

In the context of EC NDE, the process of demagnetization is important for controlled EC experiments on ferromagnetic samples. As mentioned in Sect. 3.3 of this text, the theory of EC NDE commonly assumes a linear relationship between B and H with the form of (3.7), which is most closely true in the asymptotic limit as $H \rightarrow 0$. For this reason, better agreement between EC theory and experimental data can be obtained by demagnetizing any magnetic sample that is to be the subject of an EC benchmark experiment. Or, if comparative electromagnetic measurements are to be made on ferromagnetic samples, it is better to remove the influence of magnetic history by demagnetizing them first.

In many cases, magnetization and demagnetization are performed by inserting the test-piece into a solenoid and appropriately adjusting the magnetic field that the solenoid produces. A solenoid is a long, air-cored coil whose axial magnetic field is given by $H_z = nI$ where n is the number of turns per unit length and I is the current flowing in the coil. H_z is approximately uniform over the cross section of the solenoid, when its length is much greater than its diameter. (A solenoid is the subject of Exercise 3 at the end of Chap. 6) For samples that are too large to fit inside a solenoid, a C-core magnetic can be moved over the surface of the sample, demagnetizing it at each location. To demagnetize a sample, the current flowing in the solenoid or other electromagnets is gradually reduced in amplitude while being cycled at a frequency sufficiently low to permit domain reordering to occur under the influence of the magnetic field that the electromagnet produces. As the applied H is reduced in amplitude, B also reduces as shown in Fig. 3.11 until, ultimately, the material reaches the demagnetized state characterized by $B = 0$.

Figure 3.12 shows the emergence of multiple domains as a sample of iron, initially saturated, is demagnetized. Notice how the magnetostatic field external to the iron is reduced as domains form during demagnetization. The triangular domains formed with 90° domain walls are known as *closure domains*. They act to eliminate the external magnetostatic field by "closing the loop" of $\mathbf{M}$ within the material.

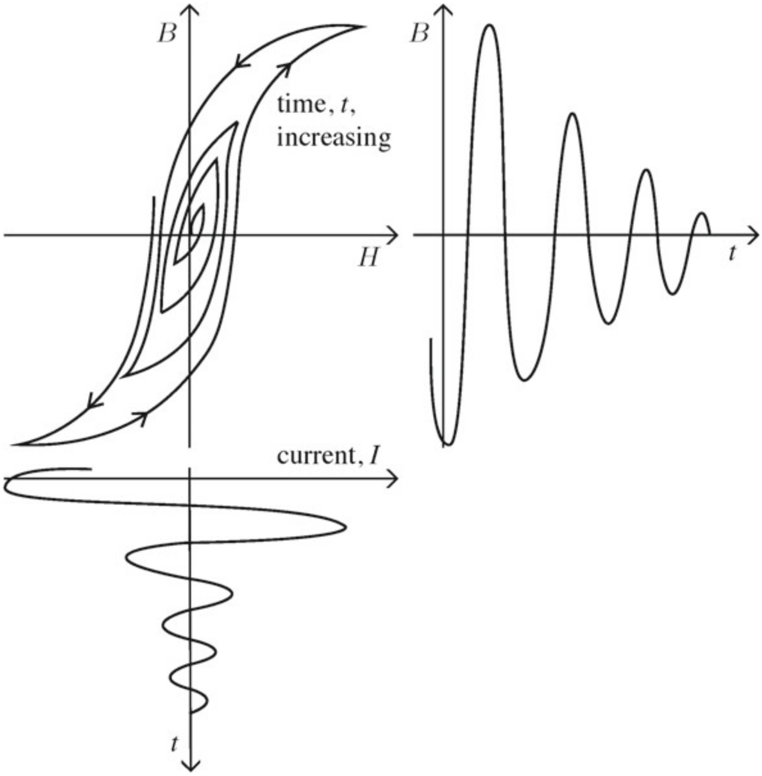

Fig. 3.11 The variation in applied current I in a solenoid enclosing a ferromagnetic sample as the sample is demagnetized. B cycles to zero as I and H (produced by I) cycle to zero

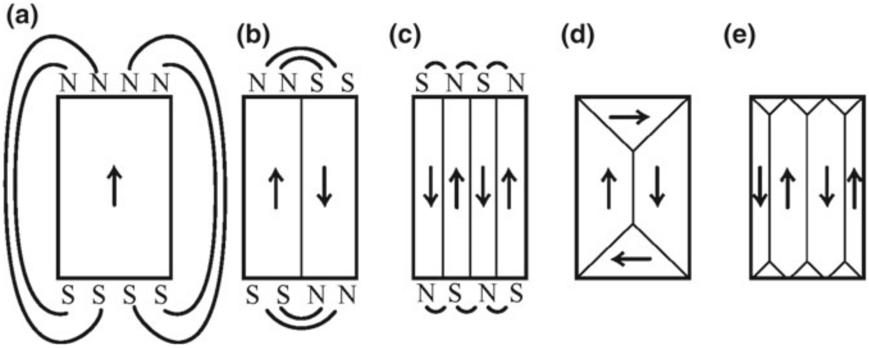

Fig. 3.12 Schematic diagram showing the emergence of domains as a saturated sample (a) is demagnetized (e). Iron forms domains of this kind since the cubic crystal structure support 90° and 180° domain walls

3.8 Summary

In this chapter, an introduction to ferromagnetic materials and their properties has been given. Ferromagnetic materials are important in EC NDE for both enhancing probe performance (Sect. 6.3.5) and because some test-pieces exhibit ferromagnetic behavior that influences the EC signal (Chaps. 6 and 9). A basic understanding of this topic is one of the building blocks that contributes to a complete understanding of EC NDE, that we are working toward. Similarly, the topic of the next chapter—electrical circuits—gives us a building block that helps us to understand the function of an EC coil and probe.

3.9 Exercises

1. Several devices exist for making quantitative measurements of magnetic field strength. These are known as magnetometers. Conduct a little research to find four examples of magnetometer and, in two sentences for each one, describe how they work.
2. Explain what is meant by the initial magnetization curve, mentioning the domain processes that occur along with it.
3. Discuss the reasons why magnetic ordering occurs in ferromagnets, explaining why a material does not usually spontaneously magnetize uniformly throughout its volume.
4. Give two pieces of evidence for the existence of ferromagnetic domains.
5. Explain the meaning of coercivity and remanence, and give their SI units.
6. For a typical hysteresis loop of B versus H, sketch the form of μ as a function of H. Where is μ maximum?

References

1. Jiles, D.C.: Introduction to Magnetism and Magnetic Materials, 2nd edn. CRC Press/Wiley, Boca Raton (1998)
2. Cullity, B.D., Graham, C.D.: Introduction to Magnetic Materials, 2nd edn. IEEE Press, Hoboken (2009)
3. Bowler, J.R., Harfield, N.: Evaluation of probe impedance due to thin-skin eddy-current interaction with surface cracks. IEEE T. Magn. **34**, 515–523 (1998)
4. Kaye, G.W.C., Laby, T.H.: Tables of Physical and Chemical Constants, 15th edn. Longman, London (1986)
5. Kinser, E.R.: Magnetic nondestructive characterization of case depth in surface-hardened steel. M.S. thesis, Iowa State University (2005)

Chapter 4
Circuits

Abstract The observed quantity in eddy-current nondestructive evaluation is the electrical impedance of the probe coil. Proper interpretation of the impedance allows the inspector to infer material property information, and to detect and characterize defects. This chapter provides an introductory description of circuit theory that is relevant to eddy-current nondestructive evaluation, describing resistors, capacitors, and inductors and the impedance of circuits in which they are combined. The concept of an equivalent electrical circuit for an eddy-current probe is introduced and the equivalent circuit is given in its simplest form.

4.1 Introduction

The process of induction of eddy currents in a metal test-piece, due to a time-varying electric current flowing in an eddy-current coil, is most clearly understood in terms of the electric and magnetic fields introduced in Chap. 2. It is helpful, on the other hand, to describe certain characteristics of an eddy-current coil in terms of electrical circuit theory. In this chapter, the circuit quantities *resistance*, *capacitance*, and *inductance* are introduced and the quantity that is actually measured in an eddy- current inspection, the *impedance* of the coil, is defined. Some simple circuit configurations are analyzed in order to prepare the way for discussion of a method of correcting for "non-ideal" coil behavior, to be given in Sect. 6.3.6. A fairly brief overview is given here. More detail can be found in [1].

4.2 Electromotance and Potential Difference

Electromotance (commonly but misleadingly known as "electromotive force" [2]) must be applied to a conductor to compel the conduction electrons to move. A battery, for example, provides a DC source of electromotance. Another way of expressing this is that the battery terminals maintain a difference in *electrical potential*, V, which has the unit Volt (V). When connected to an electrical circuit, the *potential difference*

N. Bowler, *Eddy-Current Nondestructive Evaluation*,
Springer Series in Measurement Science and Technology,
https://doi.org/10.1007/978-1-4939-9629-2_4

provided by the battery compels the conduction electrons to move. The electrons move because an electric field exists between two points of different potential and a charge Q, with unit Coulomb (C), in an electric field experiences force **F** given by the product of the charge and the electric field:

$$\mathbf{F} = Q\mathbf{E}. \tag{4.1}$$

The potential energy W required to move the charge Q from point A to point B is

$$W = -\int_A^B \mathbf{F} \cdot d\mathbf{l} = -Q\int_A^B \mathbf{E} \cdot d\mathbf{l}. \tag{4.2}$$

The potential difference between these two points, V_{BA}, is the potential energy per unit charge:

$$V_{BA} = -\int_A^B \mathbf{E} \cdot d\mathbf{l}. \tag{4.3}$$

4.3 Resistance

As described in Sect. 1.5, a simple eddy-current coil is formed by winding multiple turns of wire on a nonconductive former. One intrinsic parameter of any coil is its DC resistance. Consider a conductor whose ends are maintained at a potential difference V, as shown in Fig. 4.1. The resistance R of the conductor is defined as the potential difference per unit current:

$$R = \frac{V}{I}. \tag{4.4}$$

From the point form of Ohm's Law, (2.15), the resistance of the conductor can be derived. The applied electric field of Fig. 4.1 is uniform, since the fields are not varying with time, and its magnitude is given by

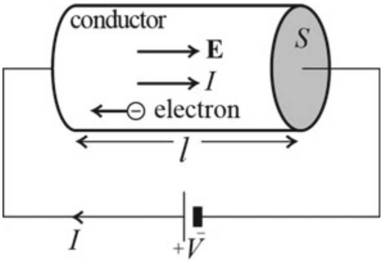

Fig. 4.1 A conductor with uniform cross section S under an applied electric field **E** due to the electromotance or potential difference V supplied to the circuit

$$E = \frac{V}{l}. \tag{4.5}$$

Since the conductor has uniform cross section and the current is DC, (2.1) holds. Combining (2.1), (2.15) and (4.5) gives

$$\frac{I}{S} = \sigma E = \frac{\sigma V}{l}.$$

From (4.4) it is now easy to see that (2.11) follows.

4.4 Capacitance

An eddy-current probe exhibits two forms of capacitance. One is *inter-winding capacitance* which arises from the fact that the windings of the coil are in close proximity to one another and separated by an insulating layer. The other is capacitance in the leads that connect the coil to the voltage source. Both of these sources of capacitance interfere with the operation of the probe, because their presence gives rise to an unwanted resonance in the probe circuit. This phenomenon will be described, and a method for correcting measured data to remove the effect of the probe resonance will be given, in Sect. 6.3.6.

A capacitor is formed by two conductors that carry equal and opposite charge, separated by an insulator (dielectric material). Broadly speaking, materials can be classified in terms of their conductivity σ and relative permittivity ϵ_r as either conductors (with $\sigma \gg 1$ and $\epsilon_\mathrm{r} = 1$) or dielectrics (with $\sigma \ll 1$ and $\epsilon_\mathrm{r} \gg 1$).

Consider a simple capacitor formed by two parallel conductive plates as shown in Fig. 4.2. The conductors are maintained at potential difference V given by

$$V = V_1 - V_2 = -\int_2^1 \mathbf{E} \cdot d\mathbf{l} \tag{4.6}$$

where $\mathbf{E}$ is the electric field between the capacitor plates. The capacitance, C, of the capacitor is defined as the ratio of the magnitude of the charge on one of the plates to the potential difference between them,

$$C = \frac{Q}{V}. \tag{4.7}$$

Capacitance can be regarded as a measure of how much electrical energy is stored by the capacitor. Equation (4.7) is useful for determining the capacitance of an ideal parallel-plate capacitor in which the plate separation d is much smaller than the dimensions of the plate. In this case, it is assumed that $\mathbf{E}$ is uniform in the gap between the capacitor plates, Fig. 4.2, and that the *fringing field* which leaks out at the edge of the capacitor plates is negligible. Then,

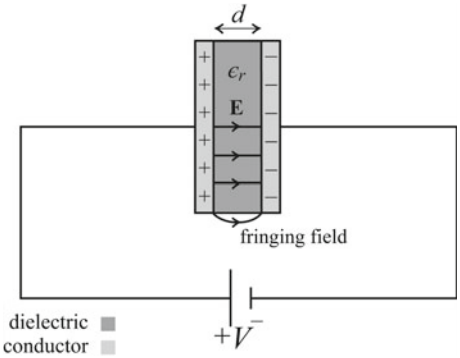

Fig. 4.2 A parallel-plate capacitor with plate area S, filled with a dielectric material with relative permittivity ϵ_r

$$C \approx \frac{\epsilon S}{d} \tag{4.8}$$

where ϵ is the permittivity of the dielectric filling the capacitor and S is the area of one of the identical plates. In fact, the ratio of the capacitance of an air-filled capacitor, C_0, compared with that of the same capacitor filled with dielectric, C, gives the relative permittivity of the dielectric:

$$\frac{C}{C_0} = \frac{\epsilon}{\epsilon_0} = \frac{\epsilon_0 \epsilon_r}{\epsilon_0} = \epsilon_r \tag{4.9}$$

where $\epsilon_0 = 8.854 \times 10^{-12}$ Farads per meter (F/m) is the permittivity of free space.

4.5 Discharge of a Capacitor Through a Resistor

Having defined resistance and capacitance, we are now in a position to consider a simple circuit formed by connecting a capacitor and resistor in series, as shown in Fig. 4.3. If the capacitor is given charge Q_0 at time $t = 0$, a potential difference $V = Q_0/C$ appears across the plates. In the absence of an electromotance, the capacitor discharges and current $I = dQ/dt$ flows through the circuit. At any time $t > 0$ therefore, the potential difference across the resistor is $R \times dQ/dt$. One of Kirchhoff's Laws of circuit theory (Kirchhoff's Voltage Law) states "The directed sum of the potential differences (voltages) around any closed loop is zero." Applying this law to the series RC circuit gives

$$R\frac{dQ(t)}{dt} + \frac{Q(t)}{C} = 0. \tag{4.10}$$

The solution of this equation shows that there is an exponential decay of charge with time,

Fig. 4.3 Capacitor C and resistor R connected in a series circuit

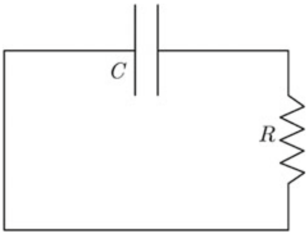

$$Q(t) = Q_0 \exp\left(-\frac{t}{RC}\right) \tag{4.11}$$

where $\tau = RC$ is known as the relaxation time of the RC circuit.

4.6 Forced Oscillation of an RC Circuit by Alternating Electromotance

If an electromotance of the form $V_0 \cos(\omega t + \phi)$ is now introduced into the circuit, as shown in Fig. 4.4, applying Kirchhoff's Law (stated in the previous section) gives

$$R\frac{dQ(t)}{dt} + \frac{Q(t)}{C} = V_0 \cos(\omega t + \phi). \tag{4.12}$$

The solution of this equation, characteristic of alternating currents, is easily obtained by writing the equation in phasor form:

$$j\omega R\mathcal{Q} + \frac{\mathcal{Q}}{C} = \mathcal{V} \tag{4.13}$$

where $\mathcal{Q}$ represents phasor charge, related to Q by $Q = \text{Re}\left\{\mathcal{Q}e^{j\omega t}\right\}$ as discussed in Sect. 2.3 and $\mathcal{V}$ represents phasor voltage, similarly. Then

Fig. 4.4 Capacitor C and resistor R connected in a series circuit with time-harmonic electromotance $V_0 \cos(\omega t + \phi)$

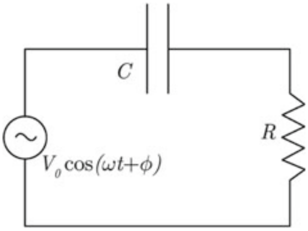

$$\mathcal{Q} = \frac{\mathcal{V}}{j\omega R + 1/C} \tag{4.14}$$

and the phasor current $\mathcal{I} = j\omega\mathcal{Q}$ is given by

$$\mathcal{I} = \frac{\mathcal{V}}{R + 1/(j\omega C)}. \tag{4.15}$$

Next we will define another circuit component, inductance, and see the interesting effect of introducing an inductance into the circuit—a resonance is created in the circuit at a particular frequency.

4.7 Inductance

The inductance of an eddy- current coil is its most important circuit property because it is the property that allows the coil to detect changes in its local magnetic field that arise due to perturbations of the eddy currents induced in the test-piece due to the presence of defects or inhomogeneities. To understand inductance, it is necessary to define magnetic flux. By analogy with the relationship between electric current I and current density $\mathbf{J}$, (2.2), magnetic flux Ψ is related to the field of magnetic induction $\mathbf{B}$ as

$$\Psi = \int_S \mathbf{B} \cdot d\mathbf{S}. \tag{4.16}$$

The unit of magnetic flux is the Weber (Wb) and, while the unit of $\mathbf{B}$ is the Tesla, $\mathbf{B}$ is also commonly quoted in Wb/m^2. One can conceive of a magnetic circuit in which Ψ is constrained to flow within a high-permeability material (e.g., a ferromagnet), by analogy with the way in which electrical current is confined within a high conductivity material (a conductor). Indeed, Faraday's transformer experiment relied upon this phenomenon to some extent (Sect. 1.2.1). The analogy has its limitations, however, because $\mathbf{B}$ easily "leaks" out of a material if μ_r is not especially large, unlike $\mathbf{J}$ which is confined strictly to the conductor.

In Chap. 2, the nature of the magnetic field produced by current flowing in a long, straight wire was discussed. If now a *closed* conducting path is considered, the current I produces a magnetic induction $\mathbf{B}$ that causes flux Ψ as defined in (4.16) to pass through the closed path. Further, if the circuit has N identical turns, the flux linkage λ can be defined as

$$\lambda = N\Psi. \tag{4.17}$$

If the relationship between I and $\mathbf{B}$ in the medium surrounding the circuit is linear, the flux linkage is proportional to the current producing it and $\lambda \propto I$. (The relationship between I and $\mathbf{B}$ is not linear in the case of a ferromagnetic material, as discussed in Chap. 3.) A constant of proportionality is introduced such that

$$\lambda = LI \tag{4.18}$$

where L is the *inductance* of the circuit. Inductance is measured in the unit Henry (H), after Joseph Henry (Sect. 1.2.2). From (4.17) and (4.18) the inductance of an inductor is defined as the ratio of the magnetic flux linkage to the current through the inductor:

$$L = \frac{\lambda}{I} = \frac{N\Psi}{I}. \tag{4.19}$$

Inductance can be regarded as a measure of how much magnetic energy is stored in an inductor.

Strictly, L is the *self*-inductance of an inductor since the flux linking the circuit is produced by the inductor itself. It is also possible to define mutual inductance, in which the flux linking the inductor is produced by a separate circuit. See, for example, [3].

An eddy-current coil with large self-inductance is desirable because the coil then responds more strongly to changes in the magnetic field in the vicinity of the coil. The probe is thus more sensitive to magnetic field variations caused by perturbations of the induced eddy-current density in a test-piece and, therefore, more sensitive to a defect or other feature that causes the perturbation. The self-inductance of an eddy-current coil is commonly increased in practice by winding the coil around a high-permeability ferrite core. This is discussed further in Sect. 6.3.5.

4.8 Forced Oscillation of an LRC Circuit by Alternating Electromotance

If an inductor is now introduced into the circuit, as shown in Fig. 4.5, a potential difference of $-L \times dI/dt$ appears across the inductor at any time $t > 0$. This can be shown by taking the derivative with respect to time of rearranged (4.19):

$$L\frac{dI}{dt} = \frac{d\Psi}{dt} = -V \tag{4.20}$$

where the final identity comes from Faraday's Law, given later in (5.1), Sect. 5.2. In this case, applying Kirchhoff's Law gives

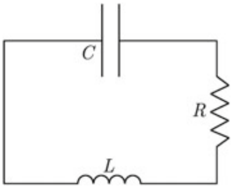

Fig. 4.5 Capacitor C, resistor R and inductor L connected in a series circuit

$$L\frac{d^2Q(t)}{dt^2} + R\frac{dQ(t)}{dt} + \frac{Q(t)}{C} = 0 \tag{4.21}$$

and, if an alternating electromotance $V(t) = V_0\cos(\omega t + \phi)$ is applied to the circuit,

$$L\frac{d^2Q(t)}{dt^2} + R\frac{dQ(t)}{dt} + \frac{Q(t)}{C} = V_0\cos(\omega t + \phi). \tag{4.22}$$

The solution of this equation, in phasor form, is

$$\mathcal{Q} = \frac{\mathcal{V}}{-\omega^2 L + j\omega R + 1/C} \tag{4.23}$$

and the corresponding current is

$$\mathcal{I} = \frac{\mathcal{V}}{R + j[\omega L - 1/(\omega C)]}. \tag{4.24}$$

4.9 Impedance

Now we define Z to be the complex impedance of the circuit, given by

$$Z = \frac{\mathcal{V}}{\mathcal{I}}. \tag{4.25}$$

The symbol "Z" was first introduced by Sir Oliver Heaviside (1850-1925, Fig. 4.6), an English physicist and electrical engineer who, despite being formally educated only to elementary level, made important advances in the application of mathematics to electrical circuits. His choice of mathematical notations and methods were often not celebrated by his peers, however, and for this reason, he was forced to publish his papers at his own expense [4]!

Returning to consideration of the series LRC circuit, the following expression for Z can now be obtained from (4.24) and (4.25);

$$Z = R + j\omega L + \frac{1}{j\omega C}. \tag{4.26}$$

In general, the real and imaginary parts of Z are given the symbols R and X and are known as the resistance and *reactance* of the circuit, respectively;

$$Z = R + jX. \tag{4.27}$$

In the specific example of the series LRC circuit, $X = \omega L - 1/(\omega C)$.

Fig. 4.6 Oliver Heaviside, English physicist and electrical engineer, 1850–1925 [5]

Impedance is a very important quantity in EC NDE! In most eddy- current inspections, the complex impedance of the probe is viewed by the inspector on an “impedance-plane plot” [1, 6], in which R is plotted on the horizontal (real) axis and X is plotted on the vertical (imaginary) axis. Variations in the impedance as a probe moves across a defective region in a test-piece, or from one material type to another, are manifested as movement in the impedance point on the complex plane.

Impedances connected in series or in parallel in a circuit can be manipulated in the same way as pure resistances;

$$Z = Z_1 + Z_2 + Z_3 + \ldots, \text{ series,} \tag{4.28}$$

$$\frac{1}{Z} = \frac{1}{Z_1} + \frac{1}{Z_2} + \frac{1}{Z_3} + \ldots, \text{ parallel.} \tag{4.29}$$

In the case of parallel impedances, it is more convenient to work in terms of the admittance, $Y = 1/Z$. Then

$$Y = Y_1 + Y_2 + Y_3 + \ldots, \text{ parallel.} \tag{4.30}$$

4.10 Frequency Response of an LRC Circuit

Consideration of (4.24) shows that the current amplitude varies as a function of frequency. If the alternating electromotance is maintained at constant amplitude for all frequencies, the current amplitude peaks when $\omega L = 1/(\omega C)$, for which

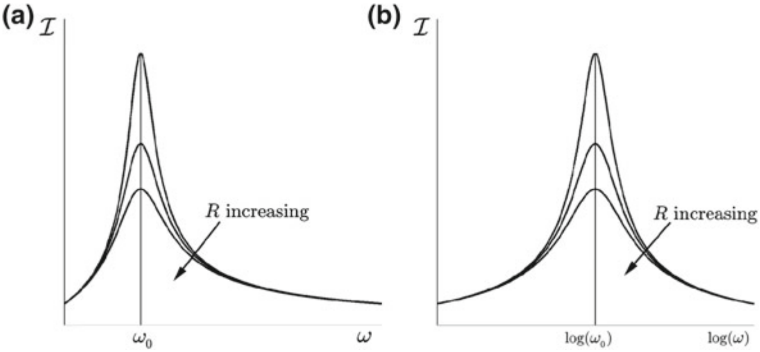

Fig. 4.7 Magnitude of current as a function of angular frequency, ω, for a series LRC circuit energized by an alternating electromotance whose amplitude is constant as a function of ω. The effects of varying R are shown on (**a**) linear and (**b**) logarithmic frequency scales

$$\omega = \omega_0 = \frac{1}{\sqrt{LC}} \tag{4.31}$$

and ω_0 is known as the resonance frequency of the circuit. If R increases, the curve becomes shallower and the peak height is reduced, as shown in Fig. 4.7.

The breadth of the peak is controlled by the quality, or Q-factor

$$\mathsf{Q} = \frac{\omega_0 L}{R} = \frac{1}{\omega_0 C R}. \tag{4.32}$$

Another type of resonant circuit is the subject of Exercise 3, at the end of this chapter.

4.11 Equivalent Electrical Circuit for an Eddy-Current Probe

An equivalent electrical circuit that accounts for the various contributions to the impedance of a real eddy-current probe is examined in Sect. 6.3.6 and is shown schematically in Fig. 6.15. It can be seen that the circuit representation is more complicated than any of those considered above. Nonetheless, under many circumstances it is reasonable to consider the impedance of an eddy-current probe to be described, to a first approximation, by the resistive and inductive contributions only. In other words, for a coil operating at a frequency well below its resonance frequency,

$$Z \approx R + j\omega L. \tag{4.33}$$

4.12 Summary

In this chapter, the three circuit quantities resistance, inductance, and capacitance have been introduced and their combination in various simple circuits has been developed to the point of defining impedance the quantity, that is measured in an EC inspection. The way in which the circuit components feature in the make-up of an EC probe has been outlined; resistance originates primarily in the resistivity of the wire of the coil windings, self-inductance arises from the coil's own time-varying magnetic flux changing in the vicinity of the coil's own windings, and capacitance arises from inter-winding effects. Acknowledging that in most cases an eddy-current coil impedance is given, to a good approximation, by the sum of resistive and inductive contributions only, (4.33), we turn in the next chapter to a discussion of the physical and mathematical framework that is needed to compute the probe impedance under various circumstances of practical significance. The framework that we need is provided by the field known as electromagnetism.

4.13 Exercises

1. If the ends of a cylindrical bar of carbon ($\sigma = 3 \times 10^4$ S/m) of radius 5 mm and length 8 cm are maintained at a potential difference of 9 V, find (a) the resistance of the bar, (b) the current through the bar.
2. The resistance per unit length of a long wire with a circular cross section and diameter 2 mm is 5.488 mΩ/m (milli-Ohm per meter). If a direct current of 40 mA flows through the wire, (a) find the conductivity of the wire; (b) identify the material of the wire: and (c) find the electric current density in the wire.
3. For the parallel resonance circuit shown in Fig. 4.8, in which L and R are in series with each other but in parallel with C, that is driven by alternating electromotance $V = V_0 \cos(\omega t + \phi)$, (a) express the impedance of the circuit, Z, in the form $R + jX$, (b) determine the resonance frequency ω_0 in terms of R, L and C, and (c) show that the current amplitude is *minimum* at resonance, rather than maximum as in the case of the series LRC circuit.

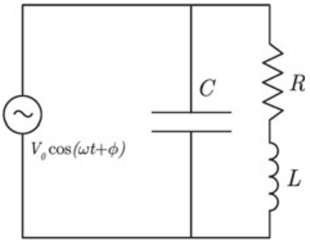

Fig. 4.8 Parallel resonance circuit in which L and R are connected in series with each other but in parallel with C, driven by alternating electromotance $V = V_0 \cos(\omega t + \phi)$

References

1. Blitz, J.: Electrical and Magnetic Methods of Nondestructive Testing. Adam Hilger, Bristol (1991)
2. Duffin, W.J.: Electricity and Magnetism. McGraw-Hill, London (1980)
3. Sadiku, M.N.O.: Elements of Electromagnetics, 4th edn. Oxford University Press, New York (2007)
4. Asimov, I.: Asimov's Biographical Encyclopedia of Science and Technology. Pan Books, London (1975)
5. Public domain image (2014). Accessed 2 July 2014
6. Hagemaier, D.J.: Fundamentals of Eddy Current Testing. American Society for Nondestructive Testing, Columbus(1990)

Chapter 5
Maxwell's Equations

Abstract To describe the electromagnetic behavior of an eddy-current probe coil, and with the goal of becoming equipped to interpret the measured impedance of an eddy-current coil, this chapter describes expressions of Maxwell's equations in full and under the quasi-static regime that is of direct relevance to eddy-current NDE. From Maxwell's equations, equations governing the electromagnetic fields can be expressed in various ways. Interface conditions on the electromagnetic field is also provided. The interface conditions are needed, along with the governing equations, to set up a bounded system of equations that can be solved for the fields generated by eddy-current probe coils. Similarly, suitable governing equations and appropriate interface conditions provide the mathematical framework by which the influence of a test-piece—with or without a defect—on the probe impedance can be described.

5.1 Introduction

James Clerk Maxwell (1831–1879, Fig. 5.1) was a Scottish mathematician and physicist [1]. Early in life, he showed signs of mathematical talent, contributing an original research article to the Royal Society of Edinburgh at the age of only fifteen years. When he was reluctantly appointed as professor of experimental physics at the University of Cambridge (UK) later in life, however, he was not a great success as a lecturer. His lectures were too difficult for most students to understand and typically attracted an audience of only three or four. In research, he was brilliant. Maxwell made significant contributions to the understanding and theoretical descriptions of several important physical phenomena, including the kinetic theory of gases. His crowning achievement was in the field of electromagnetics, in which he expressed in mathematical form Faraday's speculations on the existence and effects of magnetic lines of force (Faraday had very little mathematical knowledge, remember). Maxwell gathered a few relatively simple equations that described the various known phenomena of electricity and magnetism, and coupled them together. He revealed that electricity and magnetism could not exist separately from one another but, if one was found, then the other existed as well. The field of *electromagnetism* was born.

N. Bowler, *Eddy-Current Nondestructive Evaluation*,
Springer Series in Measurement Science and Technology,
https://doi.org/10.1007/978-1-4939-9629-2_5

Fig. 5.1 James Clerk Maxwell, Scottish mathematician and physicist, 1831–1879 [2]

Maxwell showed that the oscillation of an electric charge produced an electromagnetic field that radiated outwards from its source at constant speed. This constant speed turned out to be the speed of light so Maxwell suggested that light itself was electromagnetic radiation! In addition, since charges could oscillate at any frequency, it seemed to Maxwell that an entire spectrum of electromagnetic radiation should exist, of which visible light constituted only a small part. As time went on, the existence of various other parts of the electromagnetic spectrum has been verified. All of today's wireless technology, and myriad other practical devices and theoretical endeavors, are founded on the work of Maxwell.

In the context of EC NDE, Maxwell's equations can be used to describe mathematically the interactions of a probe field with a test-piece, even to the point of being able to predict the change in coil impedance due to various types of defect in a structure. This mathematics is the only way to accurately determine these kinds of interactions. It is exciting and profound that mathematical physics can be used to calculate quantities of practical interest, that have a real impact on society in the context of inspections of aircraft, vehicles, bridges, nuclear power plants, and other structures whose integrity is critical to human and environmental safety.

5.2 Faraday's Law

Faraday's law is the first of Maxwell's equations that we shall examine. Faraday discovered that the induced electromotance in a closed circuit is equal to the time rate of change of the magnetic flux linkage in the circuit:

$$V = -\frac{d\lambda}{dt} = -N\frac{d\Psi}{dt} \tag{5.1}$$

where $\lambda = N\Psi$ is the flux linkage, N is the number of turns in the circuit, and Ψ is the magnetic flux through each turn. The negative sign is due to Lenz's Law, and shows that the induced voltage acts in such a way as to oppose the flux change producing it. This means that the direction of current flow in the circuit is such that the magnetic field produced by the induced current opposes the change in the original magnetic field. One consequence of Lenz's Law in EC NDE is that the direction of circulation of the induced eddy currents is opposite to that of the current flowing in the inducing coil.

From (5.1) a point form of Faraday's Law can be derived. First, express the right-hand-side of (5.1) in terms of the magnetic induction field **B**, by replacing Ψ with the surface integral given in (4.16). For $N = 1$,

$$V = -\frac{d}{dt}\int_S \mathbf{B}\cdot d\mathbf{S}, \tag{5.2}$$

where S is an open surface bounded by path C that describes the circuit of interest, such as the circular path made by a loop of wire. The path is closed but permits a discontinuity in **E** integrated around that path. The discontinuity is mathematically necessary, to represent the practical incorporation of a voltage source into a drive circuit, or to allow for the measurement of a potential drop induced in a pick up circuit. Imagine a closed loop of wire whose ends are connected via a twisted pair to the termini of a variable voltage source, or to a voltmeter. The loop is closed, but a voltage drop exists across the ends of the wire. Expressing the voltage in terms of the line integral of **E**, just mentioned, gives

$$\oint_C \mathbf{E}\cdot d\mathbf{l} = -\frac{d}{dt}\int_S \mathbf{B}\cdot d\mathbf{S} \tag{5.3}$$

Noting that it is the magnetic induction field **B** that is varying with time, rather than the loop area, we obtain

$$\oint_C \mathbf{E}\cdot d\mathbf{l} = -\int_S \frac{\partial \mathbf{B}}{\partial t}\cdot d\mathbf{S}. \tag{5.4}$$

Next apply Stokes' Theorem, Sect. 10.3.6, to the left-hand-side of (5.4). Stokes' Theorem requires that **E** has continuous derivatives on S but this condition does not exclude the possibility that its line integral ($V = \int \mathbf{E}\cdot d\mathbf{l}$) is discontinuous—a point whose necessity was just described. The application of Stokes' Theorem yields

$$\int_S \nabla\times\mathbf{E}\cdot d\mathbf{S} = -\int_S \frac{\partial \mathbf{B}}{\partial t}\cdot d\mathbf{S}. \tag{5.5}$$

For these two integrals to be equal, their integrands must be equal and, consequently,

$$\nabla\times\mathbf{E} = -\frac{\partial \mathbf{B}}{\partial t}. \tag{5.6}$$

Expression (5.6) is Faraday's Law in point form, and is also one of Maxwell's equations. This relation is at the heart of EC NDE, describing the fact that a time-varying field of magnetic induction, produced by an eddy- current coil, produces an electric field (and hence induces eddy currents) in a metal test-piece nearby.

5.3 Maxwell–Ampère Law

The second of Maxwell's equations that we shall examine is the Maxwell–Ampère Law. This relation was born out of a deficiency that Maxwell perceived in Ampère's circuital theorem. Beginning with the latter, Ampère's circuital theorem states that the line integral of the *magnetostatic* field **H** around a closed path is equal to the net current I enclosed by the path,

$$\oint \mathbf{H} \cdot d\mathbf{l} = I. \tag{5.7}$$

To obtain Ampère's circuital theorem in point form, apply Stokes' Theorem to the left-hand-side of (5.7) and relate I to the current density as in (2.2). Then

$$\int_S \nabla \times \mathbf{H} \cdot d\mathbf{S} = \int_S \mathbf{J} \cdot d\mathbf{S} \tag{5.8}$$

and hence

$$\nabla \times \mathbf{H} = \mathbf{J}. \tag{5.9}$$

This relation is known as Ampère's law and tells us that the magnetostatic field **H** is not conservative, but that **J** is its *source*. (The curl, $\nabla \times$, of a conservative field is identically zero.)

Maxwell recognized that Ampère's Law is incomplete for time-varying fields, because it violates the requirement that current be continuous. For more detail, see [3]. Adding displacement current density $\mathbf{J}_d = \partial \mathbf{D}/\partial t$ to the conduction current density **J** already present in (5.9) gives

$$\nabla \times \mathbf{H} = \mathbf{J} + \frac{\partial \mathbf{D}}{\partial t}, \tag{5.10}$$

which is Maxwell's equation (based on Ampère's circuital theorem) for a time-varying field. Displacement current

$$I_d = \int_S \frac{\partial \mathbf{D}}{\partial t} \cdot d\mathbf{S}$$

is the "current" that flows in a dielectric (between the plates of a capacitor, for example).

The main relevance of the Maxwell–Ampère law to EC NDE is that it enables description of the magnetic fields associated with (i) the electric current flowing in an eddy-current coil and (ii) the eddy currents flowing in a test-piece.

5.3.1 Quasi-static Regime

Despite the fact that eddy currents must be induced by a *time-varying* field associated with the current flowing in an eddy-current drive coil, it turns out that the displacement current can be neglected in most EC NDE analyses. The following argument shows why this is the case.

The total current density in any conductor is the sum of the conduction current density and the displacement current density, given by

$$\mathbf{J} + \mathbf{J}_d = \left(\sigma + \epsilon \frac{\partial}{\partial t}\right) \mathbf{E}$$

where Ohm's Law (2.15) and constitutive relation (2.33) have been used to form the above expression. In phasor form, for sinusoidal time variation of the fields, the above sum can be expressed as $(\sigma + j\omega\epsilon)\mathbf{E}$. For typical metals tested by EC NDE, σ is on the order of 10 MS/m and the maximum frequency employed is around 10 MHz. Therefore,

$$|\mathbf{J}| \sim 10^7 |\mathbf{E}|$$

and

$$|\mathbf{J}_d| \sim 2\pi \times 10^7 \times 8.85 \times 10^{-12} |\mathbf{E}| \sim 10^{-3} |\mathbf{E}|$$

This means that $|\mathbf{J}| \gg |\mathbf{J}_d|$ and displacement current can be neglected even for the highest frequencies most commonly employed in EC NDE, to a very good approximation. Under these circumstances, EC NDE operates in a *quasi-static* regime in which

$$\nabla \times \mathbf{H} \approx \mathbf{J}. \tag{5.11}$$

This relation is obviously equivalent to Ampère's Law, although we should keep in mind that strictly Ampère's Law applies only to magnetostatic fields. The field produced by an EC coil is necessarily time-varying in order for eddy currents to be induced in a test-piece at all and the term "*quasi*-static" is used to remind us of this fact.

As a related point of interest, radio-frequency EC technology that operates up to 100 MHz has been developed in recent years for inspection of lower conductivity materials such as carbon–fiber-based composites [4] and ceramic–matrix composites. As inspection frequency increases and conductivity of the test-piece decreases it is clear from the above discussion that the quasi-static approximation becomes less accurate and, for very low conductivity materials (insulators) it is the displacement current that dominates [5].

5.4 Gauss' Law

The third of Maxwell's equations that we shall consider is Gauss' Law. Gauss' Law states that the total electric flux Ψ_e through any closed surface is equal to the total charge enclosed by that surface, Q_enc.

$$\Psi_\mathrm{e} = \oint_S \mathbf{D} \cdot d\mathbf{S} = Q_\mathrm{enc} \tag{5.12}$$

Further,

$$Q = \int_V \rho_v dV$$

where ρ_v is volume charge density (electric charge per unit volume at a point) measured in Coulombs per meter cubed (C/m^3) and V is the volume enclosed by surface S. Hence,

$$\oint_S \mathbf{D} \cdot d\mathbf{S} = \int_V \rho_v dV \tag{5.13}$$

and, applying the divergence theorem (also of Gauss, (10.48)) to the left-hand side of (5.13) yields

$$\int_V \nabla \cdot \mathbf{D}\, dV = \int_V \rho_v dV \tag{5.14}$$

from which the point form of Gauss' Law is obtained:

$$\nabla \cdot \mathbf{D} = \rho_v. \tag{5.15}$$

In other words, the strength of divergence of **D** from a point is determined by the electric charge per unit volume at that point. Relation (5.15) allows **D**, or **E** by (2.33), to be determined easily for many symmetric distributions of charge, but note that the relation always holds irrespective of the particular shape of the charge distribution.

5.5 Gauss' Law for Magnetic Fields

The fourth and final equation of Maxwell that we shall consider is Gauss' Law for magnetic fields; the counterpart of the equation examined in the previous section (Sect. 5.4) for electric fields. Unlike for **D**, the magnetic induction field **B** has no sources or sinks. This is a consequence of the fact that the fundamental source of the magnetic field is charge in motion, which always gives rise to a magnetic dipole rather than individual "magnetic charges". To derive Gauss' Law for magnetic fields, we can follow a development similar to that in the previous section, but now there is no "charge" enclosed in surface S and

$$\Psi = \oint_S \mathbf{B} \cdot d\mathbf{S} = \int_V \nabla \cdot \mathbf{B}\, dV = 0. \tag{5.16}$$

At a point,

$$\nabla \cdot \mathbf{B} = 0 \tag{5.17}$$

and we see that **B** is solenoidal (divergenceless). This means that the lines of **B** are always closed loops.

5.5.1 *Magnetic Vector Potential*

The form of Gauss' Law as written in (5.17) invites the definition of the magnetic vector potential **A** such that

$$\mathbf{B} = \nabla \times \mathbf{A} \tag{5.18}$$

since, according to identity (10.44), the divergence of the curl of any vector is zero. One reason for defining the magnetic vector potential is that it is easier, for some configurations, to solve a problem in terms of the magnetic vector potential than in terms of the magnetic induction field itself. In this text, **A** is employed in the derivation of the analytical expression for **B** at all points in space due to a current loop in free space, Sect. 6.3.2.

5.6 Interface Conditions on the Electromagnetic Field

In later sections of this text, we shall see how Maxwell's equations may be manipulated to provide governing equations for the electromagnetic field in the vicinity of an eddy-current coil. When an eddy-current coil is brought near to a metal test-piece, the electromagnetic field due to the coil penetrates the conductor, and the field exists in more than one material (air and metal) at the same time. The conductor surface is a *boundary* or *interface* between the two dissimilar media, and the electromagnetic field obeys certain conditions there. These conditions are known as *boundary conditions* or *interface conditions*. In order to solve the governing equations and obtain a mathematical description of the electromagnetic field in a region of space occupied by more than one medium, we need to know the interface conditions that the fields must obey. The conditions on the four field quantities **E**, **D**, **H** and **B**, and on the

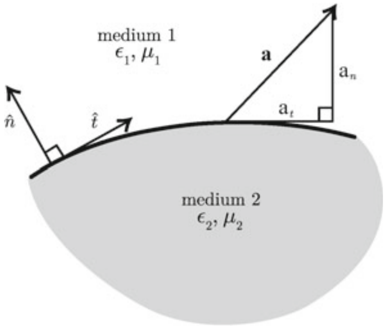

Fig. 5.2 A vector field **a** at the interface between two media with different dielectric and magnetic properties. The unit vectors normal ($\hat{n}$) and tangential ($\hat{t}$) to the interface are shown, along with the normal and tangential components of **a**

current density **J**, are presented in this section but not derived. For a derivation, see [3] or any standard undergraduate textbook on electricity and magnetism.

Consider a vector field that is oriented arbitrarily with respect to a boundary between two media, as shown in Fig. 5.2.

Electric Field It can be shown that *the tangential component of* **E** is continuous at the boundary. This means that the tangential component of **E** does not change as the boundary is traversed. Expressing this mathematically,

$$(\mathbf{E}_1 - \mathbf{E}_2) \times \hat{n} = 0 \qquad \text{or} \qquad E_{1t} - E_{2t} = 0. \tag{5.19}$$

In (5.19), the subscripts 1 and 2 refer to the two media and the subscripts n and t refer to the normal and tangential components of the vector at the interface, respectively.

Electric Displacement If ρ_s is the surface density of free charge placed deliberately on the interface, then it can be shown that *the jump* (discontinuity) *in the normal component of* **D** *at the boundary is equal to the free surface charge density on the boundary*:

$$(\mathbf{D}_1 - \mathbf{D}_2) \cdot \hat{n} = \rho_s \qquad \text{or} \qquad D_{1n} - D_{2n} = \rho_s. \tag{5.20}$$

Magnetic Field If $\mathbf{K} = K\hat{t}$ is a surface current measured in A/m that flows on the boundary, then *the jump in the tangential component of* **H** *at the boundary is equal to the surface current*:

$$(\mathbf{H}_1 - \mathbf{H}_2) \times \hat{n} = \mathbf{K} \qquad \text{or} \qquad H_{1t} - H_{2t} = K. \tag{5.21}$$

Magnetic Induction *The normal component of* **B** *is always continuous across a boundary*:

$$(\mathbf{B}_1 - \mathbf{B}_2) \cdot \hat{n} = 0 \qquad \text{or} \qquad B_{1n} - B_{2n} = 0. \tag{5.22}$$

Current Density From (5.19) with Ohm's law (2.15) the following boundary condition on the tangential component of the current density can be obtained:

Table 5.1 Interface conditions on the electromagnetic field and current density. The density of free surface charge at the boundary is represented by ρ_s (C/m^2). The surface current density at the boundary is K (A/m). In most cases of relevance to EC NDE, ρ_s and K are zero

Vector field	Tangential component	Normal component
Electric field, **E**	$E_{1t} - E_{2t} = 0$	$\epsilon_1 E_{1n} - \epsilon_2 E_{2n} = \rho_s$
Electric displacement, **D**	$D_{1t}/\epsilon_1 - D_{2t}/\epsilon_2 = 0$	$D_{1n} - D_{2n} = \rho_s$
Magnetic field, **H**	$H_{1t} - H_{2t} = K$	$\mu_1 H_{1n} - \mu_2 H_{2n} = 0$
Magnetic induction, **B**	$B_{1t}/\mu_1 - B_{2t}/\mu_2 = K$	$B_{1n} - B_{2n} = 0$
Current density, **J**	$J_{1t}/\sigma_1 - J_{2t}/\sigma_2 = 0$	$J_{1n} - J_{2n} = 0$

$$J_{1t}/\sigma_1 - J_{2t}/\sigma_2 = 0. \tag{5.23}$$

The normal component of the current density is continuous at the boundary:

$$J_{1n} - J_{2n} = 0. \tag{5.24}$$

Looking at continuity conditions (5.20) and (5.21), a parallel with Maxwell's equations (5.15) and (5.9) can be seen. In volumetric space, the volume charge density ρ_v gives rise to divergence in **D** as expressed in (5.9), whereas surface charge density ρ_s at an interface gives rise to a jump in D_n across the interface, (5.20). The behavior stems from the fact that ρ_v and ρ_s are *sources* of **D**. Similarly, the existence of a surface current **K** at a boundary gives rise to a jump in H_t across the boundary as expressed in (5.21), whereas the volume current density **J** gives rise to a circulating magnetic field, (5.9). Currents **J** and **K** are sources of **H**.

The constitutive relations (2.25) and (2.33) can be used with the above interface conditions (5.19)–(5.22) to obtain a full set of conditions on both the normal and tangential components of all four vector fields. These are given, along with conditions on the normal and tangential components of the current density **J**, in Table 5.1. Commonly, no surface charge density exists at a boundary and $\rho_s = 0$ in the above relations. Then, D_n is continuous at the boundary. Similarly, there is often no surface current at a boundary and $K = 0$. Then, H_t is continuous at the boundary.

Example: Interface conditions on the electric field The electric field just outside a cylindrical rod whose axis lies along the z-axis is given by $\mathbf{E}_2 = 60\hat{z}$ V/m. The conductivity of the rod is 46 MS/m. Find the current density in region 1, just inside the rod.

Solution: In a cylindrical coordinate system, the tangential component of the electric field at the rod surface is $\mathbf{E}_t = E_\phi \hat{\phi} + E_z \hat{z}$. Hence, $E_{1z} = E_{2z}$ and $J_z = \sigma E_{1z} = \sigma E_{2z} = 46 \times 10^6 \times 60 = 2.76 \times 10^9$ A/m^2.

Example: Interface conditions on the magnetic field Two extensive homogeneous isotropic ferrites (which can support no surface currents) meet on the plane $z = 0$.

For $z > 0$, $\mu_{\rm r1} = 100$ and for $z < 0$, $\mu_{\rm r2} = 20$. A uniform magnetic field $\mathbf{H}_1 = 5\hat{x} - 2\hat{y} + 3\hat{z}$ A/m exists for $z \geq 0$. Find $\mathbf{H}_2$ for $z \leq 0$.

Solution: $\mathbf{H}_2$ is also uniform. Considering first the component of the field normal to the boundary, in the z-direction, $\mu_1 H_{1\rm z} = \mu_2 H_{2\rm z}$ which means that

$$H_{2\rm z} = \frac{\mu_{\rm r1}}{\mu_{\rm r2}} H_{1\rm z} = \frac{100}{20} \times 3 = 15 \text{ A/m}.$$

Tangential to the boundary, in the absence of free surface currents, $H_{1t} = H_{2t}$. Hence

$$\mathbf{H}_{1t} = 5\hat{x} - 2\hat{y} = \mathbf{H}_{2t}.$$

Putting the tangential and normal components of the field together gives the solution

$$\mathbf{H}_2 = 5\hat{x} - 2\hat{y} + 15\hat{z} \text{ A/m}.$$

5.7 Summary

In this chapter, the equations of Maxwell have been described and their relation to EC NDE has been discussed. For ease of reference, Maxwell's equations in both differential and integral form are collected together in Table 5.2. It should be noted that, in most cases of relevance to EC NDE, the quasi-static approximation can be assumed, which means that $|\mathbf{J}| \gg |\partial \mathbf{D}/\partial t|$ and $\nabla \times \mathbf{H} \approx \mathbf{J}$. In conductors, it is also generally the case that $\rho_v = 0$. In this way, two of the four Maxwell's equations are simplified in their application to EC NDE.

The boundary conditions that govern the behavior of the electromagnetic fields and the current density at the interface between two media have also been described in this chapter and are summarized in Table 5.1. Again, some simplification is generally possible in problems of relevance to EC NDE. In particular, it is usually the case that ρ_s and K are zero in the treatment of EC boundary-value problems.

The stage is now set for proceeding to develop governing equations and boundary conditions which can be solved to compute quantities of relevance to EC NDE. This is the task to which we turn in the next chapter.

Table 5.2 Maxwell's equations in differential and integral form. ρ_v is volume density of free charge (C/m^3). $\mathbf{J}$ is current density (A/m^2). In most cases of relevance to EC NDE, $\nabla \times \mathbf{H} \approx \mathbf{J}$ and $\rho_v = 0$

Law	Differential form	Integral form
Faraday's law	$\nabla \times \mathbf{E} = -\frac{\partial \mathbf{B}}{\partial t}$	$\oint_C \mathbf{E} \cdot d\mathbf{l} = -\frac{d}{dt}\int_S \mathbf{B} \cdot d\mathbf{S}$
Maxwell–Ampère law	$\nabla \times \mathbf{H} = \mathbf{J} + \frac{\partial \mathbf{D}}{\partial t}$	$\oint_C \mathbf{H} \cdot d\mathbf{l} = \int_S \left(\mathbf{J} + \frac{\partial \mathbf{D}}{\partial t}\right) \cdot d\mathbf{S}$
Gauss' law	$\nabla \cdot \mathbf{D} = \rho_v$	$\oint_S \mathbf{D} \cdot d\mathbf{S} = \int_V \rho_v dV$
Gauss' law for magnetic fields	$\nabla \cdot \mathbf{B} = 0$	$\oint_S \mathbf{B} \cdot d\mathbf{S} = 0$

5.8 Exercises

1. A long, cylindrical conductor has radius a and carries current I uniformly distributed over its cross section. Use Ampère's law to show that, *inside* the conductor, $H_\phi = I\rho/(2\pi a^2)$, $\rho < a$, where ρ and ϕ are coordinates of a cylindrical system whose axis coincides with the axis of the conductor.
2. Beginning with Maxwell's equations, derive
   (a) the magnetic field in air due to an infinitesimally thin, long, straight wire carrying current $\mathcal{I}$ in the z-direction

   $$\mathbf{H} = \hat{\phi}\frac{\mathcal{I}}{2\pi\rho}, \qquad \rho > 0,$$

   where ρ and ϕ are coordinates of the cylindrical system and
   (b) the electric field in air due to the same infinitesimally thin wire

   $$\mathbf{E} = \hat{z}\,\frac{\mathcal{I}}{2\pi} j\omega\mu_0 \ln\rho, \qquad \rho > 0,$$

   previously given in (2.17) and (2.14), respectively.
3. Explain what is meant by the *quasi-static regime* in the context of EC NDE. At frequencies used in EC NDE, for what class of materials is this (a) a good approximation and (b) a poor approximation?
4. If a **B**-field is specified everywhere by $B_x = ky$, $B_y = -kx$, $B_z = 0$, k being constant, find an expression for the current density $\mathbf{J}$ which would give rise to it.
5. The electric field just outside a cylindrical rod whose axis lies along the z-axis is given by $\mathbf{E} = 15\hat{z}$ V/m. The conductivity of the rod is 43 MS/m. Find the current density just inside the rod.
6. Two extensive homogeneous isotropic ferrites (which can support no surface currents) meet on the plane $z = 0$. For $z > 0$, $\mu_{r1} = 50$ in medium 1 and for $z < 0$, $\mu_{r2} = 5$ in medium 2. A uniform magnetic field $\mathbf{H}_1 = 3\hat{x} - 4\hat{y} + 2\hat{z}$ A/m exists for $z \geq 0$. Find $\mathbf{H}_2$ for $z \leq 0$.

References

1. Asimov, I.: Asimov's Biographical Encyclopedia of Science and Technology. Pan Books, London (1975)
2. Public domain image. http://en.wikipedia.org/wiki/Michael_Faraday. Accessed 2 July 2014
3. Sadiku, M.N.O.: Elements of Electromagnetics, 4th edn. Oxford University Press, New York (2007)
4. Heuer, H.: Review on quality assurance along the CFRP value chain - Non-destructive testing of fabrics, preforms and CFRP by HF radio wave techniques. Compos. B-Eng. **77**, 494–501 (2015)
5. Gäbler, S., Heuer, H., Heinrich, G.: Measuring and imaging permittivity of insulators using high-frequency eddy-current devices. IEEE Trans. Instrum. Meas. **64**, 2227–2238 (2015)

Chapter 6
Signals and Coils

Abstract This is a pivotal chapter in which the many background elements introduced in earlier chapters are drawn together to show how various factors affect the observed impedance of an eddy current probe coil. This chapter focuses on fundamental knowledge in eddy-current NDE, detailing the response of eddy-current probes to unflawed test-pieces of relatively simple shape. The analysis begins with the simplified case of a current sheet and half-space conductor, from which the definition of the electromagnetic skin depth emerges. Semi-analytic calculations of coil impedance are given for a coil in free space and in the vicinity of a conductor, including cases of surface and tangent coils in the vicinity of a conductive half-space and encircling or bobbin coils in the vicinity of cylindrical conductors or bore holes, respectively. The effect of important probe factors—coil dimensions, construction with or without a ferrite core, and frequency of excitation current—are discussed. Test-piece factors—conductivity, permeability, shape, and position relative to the coil—are also discussed. Sources of uncertainty in inspections due to, for example, unknown variations in the coil windings or accidental tilt of the probe during an inspection are described. The impedance-plane diagram is introduced in absolute and normalized forms.

6.1 Introduction

The purpose of this chapter is the presentation of electromagnetic theory that underlies the observed impedance of an eddy-current coil. Two important configurations are considered, from which the impedance of most eddy current probe types can be obtained. These are (i) the configuration in which a coil is oriented such that its axis is perpendicular to the surface of the test-piece (a "surface" or "normal" coil) and (ii) that in which the coil axis is ideally aligned with the axis of the test-piece, as in the case of an encircling coil or bobbin probe. In both configurations, a simple current loop is considered first and the impedance of a coil with N turns is obtained later by superposition. This chapter presents, therefore, the theoretical building blocks from which the impedance of multi-coil probes such as *differential*, *driver pick up*, *plus-point*, *array* and *hybrid* probes can be calculated. These are discussed in Chap. 8.

N. Bowler, *Eddy-Current Nondestructive Evaluation*,
Springer Series in Measurement Science and Technology,
https://doi.org/10.1007/978-1-4939-9629-2_6

The test-pieces described in this chapter are also limited to the simplest possible; the homogeneous half-space and the long rod or bore hole. A half-space is an idealized shape with a flat surface that is, in practice, sufficiently large that the coil fields are not measurably perturbed by the edges or back surface of the sample. Similarly, the long rod and bore hole are sufficiently long that end effects are not observed by the coil. Eddy-current coil response to a spherical conductor has been examined by a few authors [1–3] but the spherical test piece geometry appears to be of lower practical relevance than flat and rod-like geometries, and is not discussed explicitly in this text. More complex test-piece geometrical configurations, in particular those involving layered and truncated media, are considered in Chap. 7.

Prior to considering two-dimensional problems of circular coils interacting with various test-pieces, the one-dimensional configuration of a half-space conductor excited by a *uniform current sheet* is treated in Sect. 6.3.1. The solution for this one-dimensional configuration is important because it reveals the definition of the electromagnetic skin depth, introduced in Sect. 2.9. It is also helpful for the reader to understand the solution for the electromagnetic field in the one-dimensional configuration before moving to that for the more complex two-dimensional configurations.

In Sect. 6.3.2, two methods for calculating the magnetic field due to a circular current loop in air is described. These are interesting but not essential to the development of probe interactions with a test-piece given in Sect. 6.3.3. From the solution for the circular current loop, a solution for a multi-turn coil may be obtained in a straightforward way by superposing N such loops, as shown in Sect. 6.3.4. Building on the discussion of the multi-turn coil, the improvement in coupling to the test-piece that can be obtained by use of a ferrite core is considered in Sect. 6.3.5. The treatment of the surface coil concludes with a discussion of significant sources of noise, such as coil tilt and nonideal coil behavior due to inter-winding capacitance and finite resistance of the windings, Sect. 6.3.6. A method for correcting for nonideal behavior of an absolute probe coil is presented that is particularly useful for reducing uncertainty in benchmark experiments.

Section 6.4 provides a discussion of the impedance due to a tangent coil, whose axis is tangential to the surface of the test-piece. Tangent coils find special application as plus-point probes, in which two tangent coils are combined (Sect. 8.5). The solution by which the impedance of a tangent coil can be calculated is a limiting case of the solution for a tilted coil, Sect. 6.3.6.

In Sects. 6.5 and 6.6, the theoretical description of other commonly employed configurations, in which the coil axis is parallel to the axis of the test-piece, are presented. Again, from the solution for the circular current loop, that for a multi-turn coil may be obtained by superposition. The configuration is relevant to test scenarios such as a coil encircling a cylindrical rod and a bobbin coil inspecting the interior of a bore hole or tube. In these systems of cylindrical symmetry, two sources of geometrical uncertainty exist; coil tilt and *wobble*. As in the case of the surface coil, tilt occurs when the coil axis tilts through a finite angle with respect to the axis of the test-piece—here either a rod or a bore hole. Wobble occurs when the coil axis is laterally displaced from the axis of the test-piece. Both of these effects are important to understand because they lead to signal noise that might obscure a genuine indication from a defect or other feature.

6.2 Coil Impedance

The impedance of an eddy current coil, Z, defined in Sect. 4.9, is the quantity measured in an EC NDE inspection. In Chaps. 2 and 4, we have discussed the fact that the impedance of an eddy current coil is determined by the value of its resistance, capacitance, and inductance. For the purposes of EC NDE, the inductance is the most important of these since it is the circuit quantity that represents the presence of the magnetic field in the coil, and in EC NDE it is this magnetic field that couples with the part under test and induces eddy currents in it. An *ideal* eddy-current coil would be a pure inductor with inductance L and impedance

$$Z_{\text{ideal}} = j\omega L. \tag{6.1}$$

A real coil, however, exhibits resistance R and capacitance C in addition to inductance. Resistance of a real coil arises due to the finite resistivity of the wire used in the coil windings and cables. Coil capacitance makes a significant contribution to the probe impedance when the frequency of operation of the probe is increased to a value that depends upon the particular construction of the coil, i.e., its number of turns and geometrical parameters. The source of C is the close proximity (to each other) of the coil windings and connecting wires. Thus, while L is the quantity of real interest in EC NDE, R and C cannot be eliminated in a real probe and contribute to its impedance.

6.2.1 Isolated Coil Impedance, Z_0

The impedance of an *isolated* coil, Z_0, is the value of impedance of a coil when it is remote from the test-piece or any other metal. It is also referred to as the impedance of the coil *in air*. In general, $Z_0 = R_0 + jX_0$, where R_0 and X_0 are the resistance and reactance of the isolated coil, (4.27). The value of Z_0 is primarily determined by the number of turns on the coil, its shape and dimensions.

If R_0 and stray capacitances associated with the probe are considered to be negligible, which is often approximately true for frequencies well below the resonant frequency of the coil, then $Z_0 \approx j\omega L_0 = jX_0$ where L_0 is the DC inductance of the coil. This is an “ideal” case for EC NDE because the useful interaction between an EC probe and a test-piece is mediated by inductance, as mentioned above.

Other measurements of coil impedance, when the coil field interacts with a test-piece, are often normalized with respect to $\text{Im}\{Z_0\} = X_0$.

6.2.2 *Coil Impedance in the presence of a Conductor, Z, and the Impedance-Plane Plot*

When a coil is moved from "air" (its isolated position) to the surface of a conductor, its impedance changes from Z_0 to Z. The precise value of Z depends on geometrical effects such as the proximity and orientation of the coil with respect to the test-piece, and the test-piece parameters conductivity and permeability.

In a typical EC inspection, impedance data are displayed in the form of a two-dimensional plot in which the real and imaginary parts of the coil impedance are displayed on orthogonal axes. An inspector observes the locus of points traced on the instrument display as the probe is moved in relation to the test-piece.

The impedance-plane plot sketched in Fig. 6.1 shows several possibilities for the change in coil impedance $Z = R + jX$ as the coil is moved from air to either a non-ferromagnetic or a ferromagnetic metal test-piece. These curves may be explained qualitatively as follows. When a probe is moved from isolation (air) to the surface of a non-ferromagnetic metal test-piece, its resistance increases whereas its reactance decreases, as indicated by the symbol Z_{n-f} in Fig. 6.1. The effective coil resistance increases in response to the fact that eddy currents are now flowing in the nearby test-piece, extracting energy from the probe and effectively increasing its resistance. The coil reactance decreases, on the other hand, due to the fact that the eddy currents induced in the test-piece circulate in a direction opposite to the direction of current flow in the coil, by Lenz's Law. Consequently, the magnetic induction field associated with the coil current is effectively reduced by the opposing magnetic induction field associated with the eddy currents, resulting in an overall reduction of the inductance of the coil. Example lift-off curves that are generated as an isolated coil is moved to the surface of a slab of bronze, at three different frequencies, are shown as broken lines in Fig. 6.2. Similar curves could be plotted as the probe moves from the air

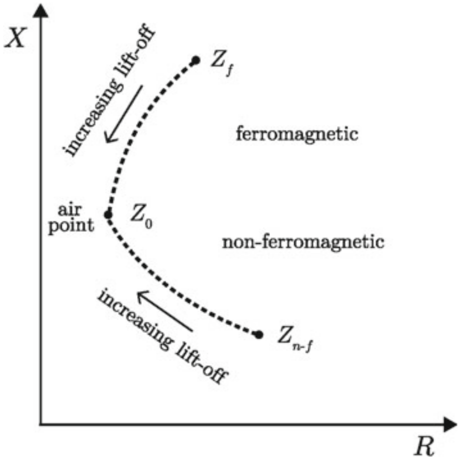

Fig. 6.1 Possible changes in coil impedance as the coil is moved from the air point, where it is isolated from any conductive material and exhibits impedance Z_0, to ferromagnetic and non-ferromagnetic conductors where its impedance becomes Z_f and Z_{n-f}, respectively

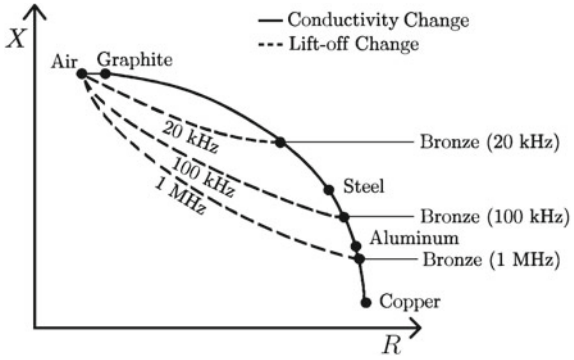

Fig. 6.2 Impedance-plane diagram for a surface coil, showing the air point at which the coil is remote from any test-piece, and impedance values (•) obtained when the coil is in contact with the surface of various metals. The coil operates at 20 kHz except where indicated. Broken lines (- - -) represent the impedance as a function of lift-off from the surface of a bronze test-piece, at three different frequencies

point to the surface of other types of metal, some of which are indicated in the figure. For any particular coil, the path of the lift-off curve that is observed depends on the test-piece conductivity and permeability and on the frequency of the inspection. Note that one practical use of lift-off curves are for determining the thickness of nonconductive, non-ferromagnetic, surface coatings on a metal substrate. Examples of such coatings are paints and lacquers.

Considering now the case of a probe moving from isolation to the surface of a ferromagnetic metal test-piece, indicated by point Z_f in Fig. 6.1, the increase in coil resistance is explained in the same way as for the case of the non-ferromagnetic test-piece, discussed above. The observed *increase* in inductance is, however, opposite in sign to the change observed in the case of non-ferromagnetic test material. This observation is explained by the fact that the strength of the magnetic induction field associated with the coil itself now increases when the coil nears the test-piece, due to the fact that the coil field is strengthened by the ferromagnetism of the test-piece (Chap. 3). The magnetic induction field associated with the induced eddy currents still opposes that of the coil, but the increased strength of the coil field dominates, resulting in an overall increase in the inductance of the coil.

Quite commonly, especially in the case of *calculated* impedance, values of resistance and reactance are plotted that are normalized with respect to the reactance of the isolated coil. In other words, the horizontal and vertical axes display the real and imaginary parts, respectively, of

$$\frac{Z}{X_0} = \frac{R - R_0}{X_0} + j\frac{X}{X_0}. \tag{6.2}$$

It is useful to be familiar with this form of data presentation because in several aspects it appears different to the impedance-plane plots of Figs. 6.1 and 6.2. Notice also that the real part of the isolated coil impedance, R_0, is subtracted from R prior to normalization with respect to X_0. This means that, as the lift-off increases, the curves tend toward the value of the probe impedance in air which is indicated by $Z_0/X_0 = 0 + j1$, Fig. 6.3. This point is the air point, on the normalized Z-plane plot. If we were to extrapolate the solid lines in Fig. 6.3 to higher frequencies, they

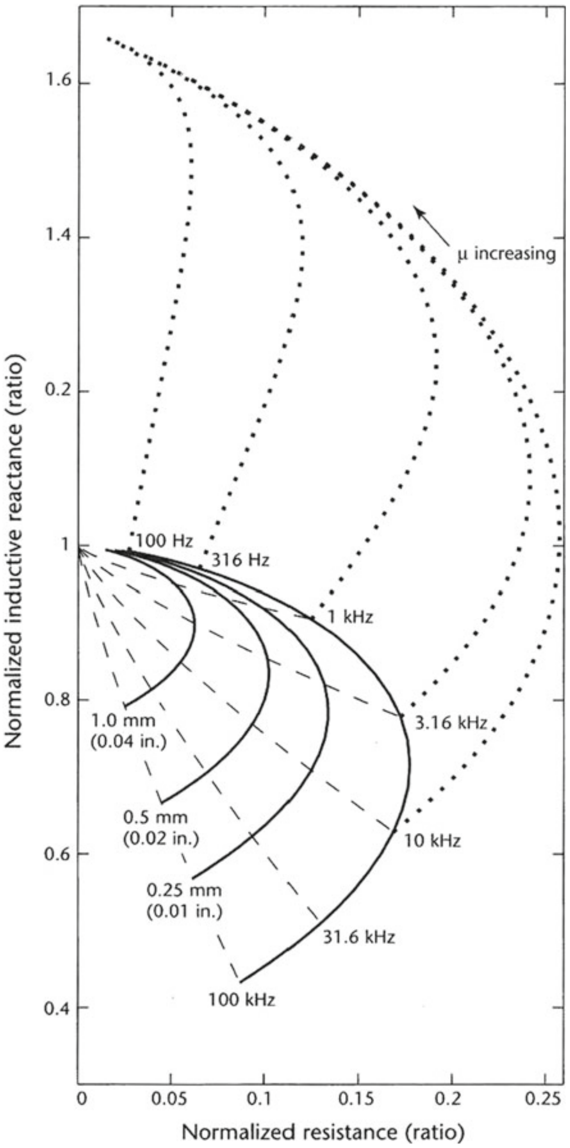

Fig. 6.3 Normalized impedance-plane diagram for a surface coil. Normalized inductive reactance $= X/X_0$ and normalized resistance $= (R - R_0)/X_0$. Solid lines (——) represent the complex impedance of the probe as a function of frequency. Broken lines (- - -) represent the impedance as a function of lift-off. Dotted lines $(\cdot\ \cdot\ \cdot)$ indicate the influence of permeability of the specimen on the probe impedance. The point given by the coordinates (0, 1) is the air point. For the particular impedance values shown in this plot, the probe parameters are $r_\mathrm{i} = 2$ mm, $r_\mathrm{o} = 4$ mm, $l = 1$ mm and $N = 800$, and the test-piece is a half-space $(T \to \infty)$ with $\sigma = 35.4$ MS/m and $\mu_\mathrm{r} = 1$. Reprinted with permission from the NDT Handbook: Electromagnetic Testing. Copyright ©2004, ASNT, Columbus, Ohio [4]

would approach the vertical axis at different points. In fact, in the high- frequency regime, the curves can be described asymptotically by the relation

$$\frac{X}{X_0} = \frac{R - R_0}{X_0} + c, \tag{6.3}$$

which is the equation of a straight line with unit slope and intercept c on the axis of X/X_0. The value of c is given by the ratio X/X_0 in the asymptotic (high-frequency) limit and provides an indication of the strength of coupling between the probe coil and the test-piece. The larger the value of $|c|$, the stronger the coupling between the probe and the test-piece.

6.2.3 Coil Impedance Change Due to a Flaw, ΔZ

When a coil is moved from a position on an unflawed region of a test-piece, to a region where the presence of a defect perturbs the induced eddy currents, there is a change in the impedance of the coil; ΔZ. This impedance change is defined as

$$\Delta Z = Z - Z_{\text{flaw}}, \tag{6.4}$$

where Z is the impedance when the coil is on the test-piece but far from a flaw, and Z_{flaw} is the impedance of the coil in the vicinity of a flaw.

An example of the magnitude of impedance change obtained as a coil scans over a slot in a metal plate is shown in Fig. 6.4 [5].

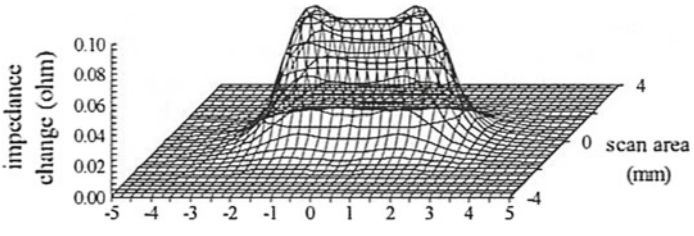

Fig. 6.4 Magnitude of the impedance change, $|\Delta Z|$, obtained by two-dimensional scanning of an eddy current probe over a through-slot in a metal plate. The physical and geometrical parameters of the probe, plate, and defect are given in Table 6.1. Reprinted from Badics, Z., Kojima, S., Matsumoto, Y., Aoki, K., Nakayasu, F.: Comparison of different "Matrix Multisensor" ECT probe designs by three-dimensional electromagnetic modeling. In: Collins, R., Dover, W.D., Bowler, J.R., Miya, K. (eds.) Nondestructive Testing of Materials. Studies in Applied Electromagnetics and Mechanics, vol. 8, pp. 13–20. IOS Press, Amsterdam (1995), p. 18, Fig. 2 [5], with permission from IOS Press

Table 6.1 Probe, plate, and defect parameters for the impedance change plotted in Fig. 6.4 [5]. The probe is formed from two square, printed-circuit coils—one driver and one pick up—separated by a 0.2-mm-thick substrate. The pick up coil contacts the test-piece. The test-piece is nuclear power plant steam generator tube material, of type and thickness not specified in the original paper. The flaw is an electro discharge machined (EDM) notch

Coil parameters		Value	Flaw parameters		Value
d_o	Outer dimension (mm)	2.00	l	Length (mm)	3.0
d_i	Inner dimension (mm)	0.72	w	Width (mm)	0.2
s	Coil stand-off (mm)	0.0	d	Depth	Through-wall
h	Probe lift-off (mm)	0.1			
n	Number of turns	40			
f	Inspection frequency (kHz)	200			

Many more examples, and techniques for calculating ΔZ due to various types of defect, are given in Chap. 9. The primary objective of the present chapter is to describe how Z is computed for various probe types when the probe interacts with an unflawed specimen.

6.3 Surface Coil

A surface coil is defined as one whose axis is parallel with the direction of the unit vector normal to the surface being inspected. An air-cored surface probe is shown schematically in Fig. 1.9. Surface coils can also be used to evaluate test-pieces with more complicated geometry, such as the interior of a borehole or tube, as shown in Fig. 6.5. Note that the axis of the coil in this configuration is still perpendicular to the surface under test. Many different designs of surface probes exist, for different inspection needs. Surface probes often operate in *absolute mode*, Sect. 8.2, meaning that the signal obtained in a measurement is simply the value of the coil impedance itself. *Differential* and *driver pick up* surface probes are also common, described in Sects. 8.3 and 8.4, respectively.

A normalized impedance-plane diagram obtained for a surface coil located above a conductive half-space is shown in Fig. 6.3. In practice, a small part of the impedance-plane plot is displayed by an oscilloscope (or *eddyscope*). It is common practice, in an eddy-current inspection, to "rotate" the display so that the change in Z due to lift-off variation appears horizontally on the eddyscope display. Then, indications due to flaws and other features can be easily distinguished from noise due to lift-off variations or tilt angle of the probe, as it scans the test-piece.

Fig. 6.5 Sectional view of the interior of a bore hole or tube inspected by a rotary surface coil. Note that the coil axis is parallel with the direction of the unit vector normal to the surface being inspected, here the $\hat{\rho}$-direction. In practice, the coil would be mounted in a rotary probe (not shown here) in order to inspect the entire interior surface of the borehole via a helical path

Considering the impedance-plane plot of Fig. 6.3, the solid curves represent the complex impedance of the probe as a function of frequency. Each solid curve is for a different value of the probe lift-off, as marked. The broken lines show the impedance as a function of lift-off from the conductor surface. In Fig. 6.3 the coupling (see discussion in Sect. 6.2.2) is clearly the strongest for the case in which the coil is nearest to the test-piece (the lift-off is the smallest) - a result that happily agrees with common sense! Impedance-plane plots such as this one can be computed or obtained by experimentation for various coil and test-piece configurations. Looking ahead to two other examples; it is shown in Fig. 6.14 that coupling increases when a coil is filled with a ferrite core and, for a coil encircling a rod, Fig. 6.23, coupling increases as the space between the coil and rod decreases, i.e., as the fill factor increases.

In Fig. 6.2, as well as the effect of lift-off discussed earlier, the effect on the Z-plane plot of changes in conductivity of the test-piece is shown. Note, the impedance change due to a change in probe lift-off, and the impedance change due to a change in conductivity, are more clearly distinguished at the higher frequencies shown because there is a greater angle between their effects in the Z-plane than at lower frequencies. At lower frequencies (such as 100 Hz in Fig. 6.3) it is very difficult to differentiate between lift-off and conductivity changes in Z. This kind of observation shows how impedance-plane plots can be used to guide the choice of inspection parameters, such as the frequency of coil operation, to optimize the sensitivity of an inspection for its particular purpose.

6.3.1 Excitation of a Half-Space Conductor by a Uniform Current Sheet

Having examined Maxwell's equations and the interface conditions on the electromagnetic field in Chap. 5, we are in a position to solve a problem—our first—in which an exciting current flowing *near to* a metal test-piece induces currents *in* the metal. The geometry that we shall consider is the simplest one possible; a uniform current sheet parallel to an infinitely deep (so-called *half-space*) conductor, as shown in Fig. 2.5. In this case the properties of the half-space conductor are assumed linear, isotropic and homogeneous, i.e., σ and μ_r are everywhere scalar and constant. This is a one-dimensional problem because the fields vary only in the direction perpendicular to the conductor surface, the z-direction. The solution of Maxwell's equations for this system will reveal the definition and meaning of the electromagnetic penetration depth introduced in Sect. 2.9. This problem is also a useful introduction to the more complex, two-dimensional, problem of the excitation of a half-space conductor by a circular coil, which will be considered in Sects. 6.3.3 and 6.3.4.

This is an artificial problem in the sense that no real coil is an infinite current sheet, but the solution obtained here may be applicable to real systems under certain circumstances. For example, parallel windings of a coil around a wide, thick plate give rise to an approximately uniform current sheet in regions sufficiently far from the edges. Second, a surface coil wound on a cylindrical former produces a current density that appears uniform on a scale somewhat less than the coil diameter, as shown in Fig. 6.6. Further, some coils are purposely designed to induce an eddy current density that is approximately uniform over a prescribed region of the surface of a test-piece [6].

Fig. 6.6 A large-diameter coil shows a region of approximately uniform current density **J** on a scale somewhat smaller than the coil diameter

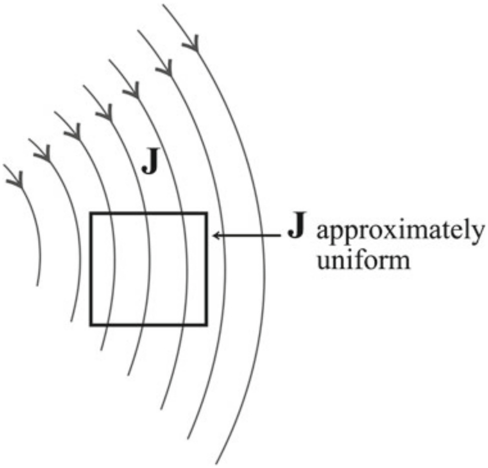

Governing Equation

We will begin by manipulating Maxwell's equations to obtain an equation which *governs* the behavior of the electric field in the system shown in Fig. 2.5. First, write down the phasor forms of Faraday's Law and the quasi-static Maxwell–Ampère Law as follows:

$$\nabla \times \mathbf{E} = -j\omega \mathbf{B}, \tag{6.5}$$

$$\nabla \times \mathbf{H} = \mathbf{J}. \tag{6.6}$$

Now write $\mathbf{J}$ as a sum of the current density in the source coil, $\mathbf{J}_\mathrm{s}$, and the eddy-current density induced in the test-piece, $\mathbf{J}_\mathrm{ec}$. Then,

$$\nabla \times \mathbf{H} = \mathbf{J}_\mathrm{s} + \mathbf{J}_\mathrm{ec}. \tag{6.7}$$

Take the curl of Faraday's Law, (6.5), substitute for $\mathbf{B}$ by means of constitutive relation (2.25) for isotropic permeability and then use (6.7) to obtain

$$\nabla \times \nabla \times \mathbf{E} = -j\omega\mu \left(\mathbf{J}_\mathrm{s} + \mathbf{J}_\mathrm{ec}\right). \tag{6.8}$$

Make the substitution $\mathbf{J}_\mathrm{ec} = \sigma\mathbf{E}$, (2.15), and employ vector identity (10.46) to obtain

$$\nabla\nabla \cdot \mathbf{E} - \nabla^2\mathbf{E} = -j\omega\mu \left(\mathbf{J}_\mathrm{s} + \sigma\mathbf{E}\right). \tag{6.9}$$

In the case of zero free volume charge, $\rho_v = 0$ and $\nabla \cdot \mathbf{D} = \epsilon\nabla \cdot \mathbf{E} = 0$. That is, $\nabla \cdot \mathbf{E} = 0$ and

$$\left(\nabla^2 - j\omega\mu\sigma\right)\mathbf{E} = j\omega\mu\mathbf{J}_\mathrm{s}. \tag{6.10}$$

This is the governing equation for the electric field. In actual fact it is valid for any geometrical configuration of current source $\mathbf{J}_\mathrm{s}$ and conductive test-piece, not only for the one-dimensional system that we are considering at the moment, Fig. 2.5. By similar steps it can be shown that the magnetic field obeys the governing equation

$$\left(\nabla^2 - j\omega\mu\sigma\right)\mathbf{H} = -\nabla \times \mathbf{J}_\mathrm{s}. \tag{6.11}$$

(The derivation of this equation is the subject of Exercise 1 at the end of this chapter.)

Focusing now on the one-dimensional system shown in Fig. 2.5, in which a uniform current sheet in the plane $z = h$ excites a half-space conductor that occupies $z < 0$, identify

$$\mathbf{J}_\mathrm{s} = \mathcal{I}\delta(z - h)\hat{x} \tag{6.12}$$

where $\mathcal{I}$ is the phasor amplitude of the alternating current being carried in the sheet at $z = h$. The delta function, $\delta(x)$, can be viewed as the derivative of the Heaviside step function $H(x)$. The delta function displays the following fundamental properties:

$$\int_{-\infty}^{\infty} f(x)\delta(x-x_0)dx = f(x_0), \tag{6.13}$$

$$\int_{x_0-\epsilon}^{x_0+\epsilon} f(x)\delta(x-x_0)dx = f(x_0), \qquad \epsilon > 0, \tag{6.14}$$

$$\delta(x-x_0) = 0, \qquad x \neq x_0. \tag{6.15}$$

In the context of (6.12), the delta function indicates that the current is confined to an infinitesimally thin sheet at $z = h$. Noting that the only variation in the fields is as a function of z, and that $\mathbf{E} = E_x\hat{x}$ must be x-directed as is the source $\mathbf{J}_\text{s}$, allows us to write a simplified form of (6.10) as follows:

$$\left(\frac{d^2}{dz^2} - k^2\right) E_x(z) = j\omega\mu\mathcal{I}\delta(z-h), \tag{6.16}$$

where we have identified

$$k^2 = j\omega\mu\sigma \tag{6.17}$$

and k will turn out to be a complex wavenumber which controls the propagation and absorption, or loss, of the electromagnetic field in the test-piece. By convention, we require that k is obtained by taking the root of k^2 that has positive real part. That is,

$$k = \sqrt{\frac{\omega\mu\sigma}{2}}(1+j). \tag{6.18}$$

Equation (6.16) is a simple one-dimensional differential equation. Solve it by writing down separate equations for the current source region, $z > 0$, and the conductor region, $z < 0$. These equations recognize the current source at $z = h$, located in a region that is otherwise nonconductive (air), and the conductive nature of the test-piece in the negative half-space.

$$\frac{d^2E_x(z)}{dz^2} = j\omega\mu\mathcal{I}\delta(z-h), \;\; z > 0, \tag{6.19}$$

$$\left(\frac{d^2}{dz^2} - k^2\right) E_x(z) = 0, \;\; z < 0. \tag{6.20}$$

Solution

In the conductor, the general solution for $E_x(z)$ is of the form

$$E_x(z) = E_0[e^{jkz} + Ce^{-jkz}] \tag{6.21}$$

where E_0 is the magnitude of the electric field at the conductor surface. Physically, the field cannot grow as distance from the source current increases (as $z \to -\infty$), so $C = 0$ and

$$E_x(z) = E_0e^{jkz}. \tag{6.22}$$

This solution reveals that the eddy-current density in this setup decays exponentially as a function of depth into the conductor. Substituting for k from (6.18) into (6.22) gives

$$E_x(z) = E_0 e^{(1+j)z/\delta} \tag{6.23}$$

where the electromagnetic skin depth, or penetration depth, is defined as

$$\delta = \sqrt{\frac{2}{\omega\mu\sigma}}. \tag{6.24}$$

This quantity was introduced in Sect. 2.9. The current density in the metal obeys the same form as the electric field since they are related linearly by the conductivity of the conductor via Ohm's law (2.15), so

$$J_x(z) = J_0 e^{(1+j)z/\delta}, \tag{6.25}$$

where J_0 is the magnitude of the current density at the conductor surface. It was noted in Sect. 2.9, and shown in Fig. 2.6, that the amplitude of the current density declines exponentially as a function of distance into the conductor. From (6.25), we see now that there is a linear phase change in J_x as a function of z. For example, at $z = -\delta$, $\arg(J_x)$ is -1 radian so the phase of J_x at the surface is 1 radian in advance of that at $z = -\delta$.

6.3.2 *Circular Current Loop in Air*

Analysis of the electromagnetic behavior of a circular current loop can form the basis of treatment of a finite eddy current "pancake" coil with multiple windings. In this section, two derivations of the field of magnetic induction, **B**, due to a circular current loop in air are given. These are interesting, and one method (that uses the Biot–Savart Law) can be applied to solve other similar problems. Both methods rely, however, on symmetry about the plane of the loop and consequently are not useful for deriving an expression for the electric field due to an eddy-current surface coil interacting with a test-piece. This more important configuration is treated in Sect. 6.3.3.

Biot–Savart Law

The Biot–Savart Law relates magnetic induction field **B** to the electric current which is the source of **B**. For current I flowing in a conductor as shown in Fig. 6.7,

$$d\mathbf{B} = \frac{\mu_0 I}{4\pi}\frac{d\mathbf{l} \times \hat{\imath}_r}{r^2} \tag{6.26}$$

in differential form, or,

Fig. 6.7 Schematic diagram showing one configuration for application of the Biot–Savart Law

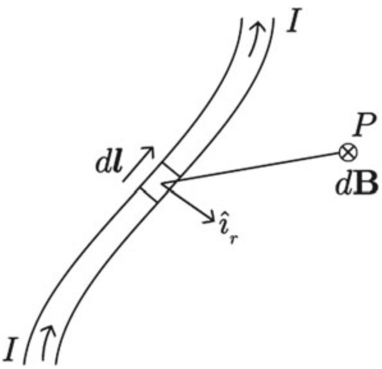

Fig. 6.8 Schematic diagram showing configuration for derivation of **B** at the center of a current loop, using the Biot–Savart Law

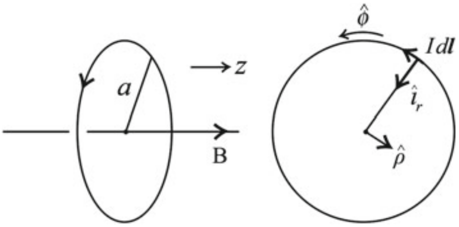

$$\mathbf{B} = \frac{\mu_0 I}{4\pi} \int \frac{d\mathbf{l} \times \hat{\imath}_r}{r^2}. \tag{6.27}$$

In these equations, $Id\mathbf{l}$ represents an infinitesimal current element. Each element makes a contribution $d\mathbf{B}$ to $\mathbf{B}$ at a field point P located at distance r from the current element. The element of magnetic induction field $d\mathbf{B}$ is directed perpendicular to the directions of both the current element $Id\mathbf{l}$ and that of the radius vector $\hat{\imath}_r$, in accordance with the vector product between them. In order to express $\mathbf{B}$ due to a wire made up of many elements $d\mathbf{l}$, the contribution of the individual elements is summed, which amounts to integrating over the length of the current wire, as expressed in (6.27). The direction of the magnetic induction field follows the right-hand rule and arises from the vector product contained within (6.26) and (6.27).

The current elements that feature in the Biot–Savart Law are assumed to be constrained, as if the current was flowing in a wire. This means that the Biot–Savart Law does not lend itself to calculation of the secondary magnetic induction field associated with the eddy currents themselves, $\mathbf{B}_{\text{ec}}$, because the eddy currents are distributed and best represented by a spatially varying current density $\mathbf{J}_{\text{ec}}$. To express $\mathbf{B}_{\text{ec}}$ for a particular test geometry, which may also include a defect of some kind, it is necessary to solve governing equations of the electromagnetic field for the particular setup, which can be derived from Maxwell's equations.

Example: Derivation of B at the center of a current loop, using the Biot–Savart Law Consider a circular current loop radius a carrying current I, as shown in Fig. 6.8.

In a cylindrical system with coordinates (ρ, ϕ, z) and axis coinciding with the axis of the current loop, $\hat{\imath}_r \equiv -\hat{\rho}$ and $d\mathbf{l} \equiv \rho\, d\phi\, \hat{\phi}$. Consequently,

$$\begin{aligned}\mathbf{B} &= \frac{\mu_0 I}{4\pi}\int_0^{2\pi}\frac{\rho\, d\phi\, \hat{\phi}\times(-\hat{\rho})}{\rho^2}\\ &= \hat{z}\frac{\mu_0 I}{4\pi}\int_0^{2\pi} d\phi\\ &= \hat{z}\frac{\mu_0 I}{2a}.\end{aligned} \tag{6.28}$$

This result may be generalized readily to obtain an expression for $\mathbf{B}$ along the entire axis of the wire—see Exercise 2 at the end of this chapter. The limitations of the Biot–Savart Law may quickly be seen by considering a field point off the axis, however. In this case, the distance between the current element and field point, r, varies as contributions from the various current elements around the loop are considered and we observe that the Biot–Savart Law is useful for obtaining simple analytical expressions for $\mathbf{B}$ only in a limited set of geometrical configurations. It may be used to evaluate $\mathbf{B}$ numerically in more complex configurations, however.

Magnetic Vector Potential

In [7], there is a beautiful derivation of the analytical expression for $\mathbf{B}$ at all points in space due to a current loop in free space. The derivation is reproduced in this section but, first, the theoretical reasoning that defines the magnetic vector potential $\mathbf{A}$ according to the Coulomb gauge is presented. The potential $\mathbf{A}$ was introduced in Sect. 5.5.1. It is employed in the derivation given in [7] and also in the seminal works of C. V. Dodd and W. E. Deeds that consider the response of a pancake coil near a conductive test-piece [8, 9], to be presented in Sects. 6.5 and 6.6 of this text. Despite the fact that the original solutions were written in terms of A_ϕ, the solutions are given in Sects. 6.5 and 6.6 in terms of E_ϕ directly, via (6.44).

In the absence of magnetic materials, the Maxwell–Ampère Law may be written

$$\nabla \times \mathbf{B} = \mu_0 \mathbf{J} \tag{6.29}$$

and, as usual,

$$\nabla \cdot \mathbf{B} = 0. \tag{6.30}$$

These governing equations will be solved by introducing the magnetic vector potential $\mathbf{A}$ such that

$$\nabla^2 \mathbf{A} = -\mu_0 \mathbf{J} \tag{6.31}$$

with the condition that $\mathbf{A}$ is *regular* at ∞. (A function is said to be regular in a particular region if it is analytic and single-valued in that region. A complex function is analytic in a particular region if it is differentiable at every point in that region.)

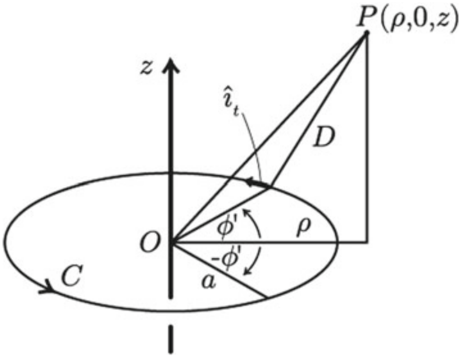

Fig. 6.9 Configuration used in solving for the vector potential, **A**, due to a current loop following path C

Equation (6.31) is obtained by choosing the gauge condition $\nabla \cdot \mathbf{A} = 0$, which is known as the Coulomb gauge. Equation (6.31) has solution

$$\mathbf{A}(\mathbf{r}) = \frac{\mu_0}{4\pi} \int_{\text{all space}} \frac{\mathbf{J}(\mathbf{r}')}{|\mathbf{r} - \mathbf{r}'|} dV' \tag{6.32}$$

where the prime denotes the source coordinates. Next, replace the volume integral in (6.32) with a line integral over path C as follows.

$$\mathbf{A}(\mathbf{r}) = \frac{\mu_0 I}{4\pi} \int_{\text{C}} \frac{d\mathbf{l}'}{|\mathbf{r} - \mathbf{r}'|} \tag{6.33}$$

If C is the loop shown in Fig. 6.9, then $d\mathbf{l}' = a\,\hat{\imath}_t\,d\phi' = a\,\hat{\phi}\,d\phi'$, $D^2 = |\mathbf{r} - \mathbf{r}'|^2 = a^2 + \rho^2 + z^2 - 2a\rho\cos\phi'$ and, noting that $\mathbf{A}$ is independent of ϕ,

$$\mathbf{A}(\rho, z) = \hat{\phi}\frac{\mu_0 I}{4\pi} \int_{\text{C}} \frac{a}{D} d\phi'. \tag{6.34}$$

Symmetry shows that the contributions of two current elements positioned symmetrically with respect to $\phi = 0$ sum to give a vector whose direction is perpendicular to the plane, since the parallel components sum to zero. The same argument applies for all planes of $\phi =$ constant which means that (i) $\mathbf{A}$ is $\hat{\phi}$-directed (as already written in the previous equation) and (ii) the magnitude of $\mathbf{A}$, denoted A, can be obtained by projecting components from two symmetric elements onto their plane of symmetry and integrating around half the loop C:

$$A_\phi(\rho, z) = \frac{\mu_0 I}{4\pi} \int_0^\pi \frac{2a\cos\phi'}{(a^2 + \rho^2 + z^2 - 2a\rho\cos\phi')^{1/2}} d\phi'. \tag{6.35}$$

This expression may be rewritten by introducing the elliptic modulus, k, defined below. Note, the elliptic modulus is not the same as the complex wavenumber introduced in (6.16)–(6.18) although it shares the same symbol.

$$k = \left[\frac{4a\rho}{(a+\rho)^2 + z^2} \right]^{1/2}$$

giving

$$A_\phi(\rho, z) = \frac{\mu_0 I}{k\pi} \left(\frac{a}{\rho} \right)^{1/2} \left[\left(1 - \frac{k^2}{2} \right) K - E \right]. \tag{6.36}$$

In (6.36), K and E are complete elliptic integrals of the first and second kinds defined by

$$K(k) = \int_0^{\pi/2} \frac{d\theta}{(1 - k^2 \sin^2\theta)^{1/2}} \tag{6.37}$$

$$E(k) = \int_0^{\pi/2} (1 - k^2 \sin^2\theta)^{1/2} d\theta. \tag{6.38}$$

Magnetic Induction

In [7, Sect. 6.1], it is shown that $\mathbf{B} = \nabla \times \mathbf{A}$, as given in (5.18), making it possible to calculate $\mathbf{B}$ via the auxiliary quantity $\mathbf{A}$. Taking the curl of (6.32) gives

$$\begin{aligned} \mathbf{B}(\mathbf{r}) &= \frac{\mu_0}{4\pi} \int_{\text{all space}} \nabla \times \frac{\mathbf{J}(\mathbf{r}')}{|\mathbf{r} - \mathbf{r}'|} \, dV' && (6.39) \\ &= \frac{\mu_0}{4\pi} \int_{\text{all space}} \left[\nabla \frac{1}{|\mathbf{r} - \mathbf{r}'|} \times \mathbf{J}(\mathbf{r}') \right] dV' && (6.40) \\ &= -\frac{\mu_0}{4\pi} \int_{\text{all space}} \frac{(\mathbf{r} - \mathbf{r}') \times \mathbf{J}(\mathbf{r}')}{|\mathbf{r} - \mathbf{r}'|^3} \, dV' && (6.41) \end{aligned}$$

where identity (10.45), Sect. 10.3, has been used and it has been observed that the curl of $|\mathbf{r} - \mathbf{r}'|^{-1}$ is identically zero. Equation (6.41), unlike the Biot–Savart Law, is a mathematical expression of Ampère's Law.

From this expression, the components of the magnetic induction field $\mathbf{B}$ can be calculated and are given as follows—see Exercise 4 at the end of this chapter:

$$B_r(\rho, z) = \frac{\mu_0 I}{2\pi} \frac{z}{\rho[(a+\rho)^2 + z^2]^{1/2}} \left[-K + \frac{a^2 + \rho^2 + z^2}{(a-\rho)^2 + z^2} E \right] \tag{6.42}$$

$$B_z(\rho, z) = \frac{\mu_0 I}{2\pi} \frac{1}{[(a+\rho)^2 + z^2]^{1/2}} \left[+K + \frac{a^2 - \rho^2 - z^2}{(a-\rho)^2 + z^2} E \right] \tag{6.43}$$

Electric Field

Finally, for a time-harmonic current excitation of the form $e^{j\omega t}$, Faraday's Law may be written as in (6.5). Then, using (5.18), it is found that

$$\mathbf{E} = -j\omega\mathbf{A}. \tag{6.44}$$

Equation (6.44) indicates a simple linear relationship between the magnetic vector potential and the electric field. From this relationship we see that, for a time-harmonic excitation, the solution for the electromagnetic field due to a circular current loop presented in this section could be equally well formulated in terms of **E**.

6.3.3 Circular Current Loop above a Half-Space Conductor

In their seminal work published in 1968, C. V. Dodd and W. E. Deeds derived an analytical solution for the impedance of a surface coil located above a planar conductor with its axis perpendicular to the conductor surface [8]. Initially, a current loop with infinitesimal cross section was considered. Ultimately, a semi-analytical expression for the impedance of a coil with finite cross section was obtained, for the coil located above a two-layer planar conductor, and for a similar coil encircling a two-layer conductive rod. Later, a similar solution was published for a coil coaxial with an arbitrary number of cylindrical conductors [9]. The latter solution can represent the response of a coil encircling a layered rod, or within a borehole, or a combination of these.

These different cases are treated in this text as follows. In this section the case of the current loop and half-space conductor is considered. In Sects. 6.3.4, 6.5.1 and 6.5.2, the coil and half-space conductor, the current loop and cylindrical conductor, and the coil and cylindrical conductor are considered. Layered conductors are treated in Chap. 7.

Dodd and Deeds' original solution was formulated in terms of **A** although relation (6.44) prompts formulation in terms of **E**, which is what we will do here. Once the solution for **E** has been obtained, the voltage in the coil can be obtained by integrating the electric field around the coil windings. The impedance can then be obtained by means of relation (4.25).

Governing Equation for E

Consider a filamentary circular current loop, radius a, height h above a planar conductor with conductivity σ, Fig. 6.10. The conductor in this case is non-ferromagnetic. As in Sect. 6.3.2, the system is axially symmetric so that the current density in the loop may be expressed

$$\mathbf{J}_\mathrm{s} = J_{\mathrm{s}\phi}\hat{\phi} \tag{6.45}$$

which immediately implies that

$$\mathbf{E} = E_\phi\hat{\phi}. \tag{6.46}$$

In this derivation it is also assumed that the conductor is linear, isotropic and homogeneous such that constitutive relations (2.25) and (2.33) hold. The consequence of this assumption in the case of a ferromagnetic conductor is that the relations to be developed are strictly accurate only for low applied **H**, due to the assumption of a linear relationship between **B** and **H**. The restriction of low applied **H** is not

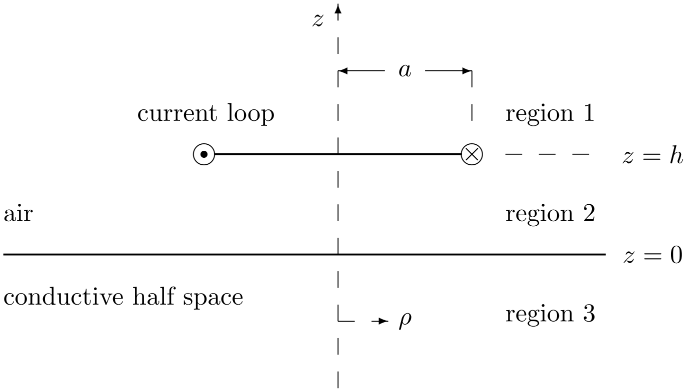

Fig. 6.10 Cross section through the axis of a circular, infinitesimal current loop, positioned horizontally above a metal half-space

required in the case of non-ferromagnetic conductors. A more detailed discussion of the nonlinear behavior of ferromagnetic materials is given in Chap. 3.

As noted above, the solution can be formulated in terms of the electric field. In fact, since the system is cylindrically symmetric, only the $\hat{\phi}$-component of the field is needed, as noted in (6.46). From Maxwell's equations, the governing equation for **E** is as given in (6.10) but here **E** has only an azimuthal component and

$$\nabla^2 \mathbf{E} = \left(\nabla^2 - \frac{1}{\rho^2}\right) E_\phi \hat{\phi}. \tag{6.47}$$

To obtain (6.47), (10.29) has been applied, noting that derivatives with respect to ϕ vanish due to axial symmetry. Expanding $\nabla^2 E_\phi$ by use of (10.28) and inserting into (6.10) gives

$$\left(\frac{\partial^2}{\partial\rho^2} + \frac{1}{\rho}\frac{\partial}{\partial\rho} - \frac{1}{\rho^2} + \frac{\partial^2}{\partial z^2} - k^2\right) E_\phi = j\omega\mu J_{\mathrm{s}\phi} \tag{6.48}$$

where $k^2 = j\omega\mu\sigma$. For phasor current $\mathcal{I}$ flowing in an infinitesimal coil that may be described mathematically by delta functions at $\rho = a$ and $z = h$, as depicted in Fig. 6.10, $J_{\mathrm{s}\phi} = \mathcal{I}\delta(\rho - a)\delta(z - h)$ and

$$\left(\frac{\partial^2}{\partial\rho^2} + \frac{1}{\rho}\frac{\partial}{\partial\rho} - \frac{1}{\rho^2} + \frac{\partial^2}{\partial z^2} - k^2\right) E_\phi = j\omega\mu\mathcal{I}\delta(\rho - a)\delta(z - h). \tag{6.49}$$

This is the equation governing the electric field due to a circular current loop with axis perpendicular to a half-space conductor, in the quasi-static regime.

Solution for E

The solution of (6.49) will be found by the method of separation of variables. Everywhere *off* the current loop, (6.49) may be written as

$$\left(\frac{\partial^2}{\partial\rho^2}+\frac{1}{\rho}\frac{\partial}{\partial\rho}-\frac{1}{\rho^2}+\frac{\partial^2}{\partial z^2}-k_i^2\right)E_\phi^i=0, \tag{6.50}$$

where $k_i^2=j\omega\mu_i\sigma_i$. The sub- or superscript i may take values 1, 2, and 3, and refers to regions above the loop ($z>h$), below the loop but above the conductor ($0<z<h$), and inside the conductor ($z\leq 0$), respectively, as labeled in Fig. 6.10.

Suppose the solution is variable-separable, of the form $E_\phi^i(\rho,z)=R(\rho)Z_i(z)$. The form of (6.50) indicates that the radial part of the solution does not change from one region to another, so $R(\rho)$ needs no subscript. Substitute this form into (6.50) and divide by $R(\rho)Z_i(z)$ to obtain

$$\frac{1}{R(\rho)}\frac{\partial^2R(\rho)}{\partial\rho^2}+\frac{1}{\rho R(\rho)}\frac{\partial R(\rho)}{\partial\rho}-\frac{1}{\rho^2}+\frac{1}{Z_i(z)}\frac{\partial^2Z_i(z)}{\partial z^2}-k_i^2=0. \tag{6.51}$$

Variables have now been separated; terms in (6.51) depend either on ρ or on z. This means that (6.51) can be separated into two equations by introducing a variable of separation, κ, in the following way:

$$\frac{1}{R(\rho)}\frac{\partial^2R(\rho)}{\partial\rho^2}+\frac{1}{\rho R(\rho)}\frac{\partial R(\rho)}{\partial\rho}-\frac{1}{\rho^2}=-\kappa^2 \tag{6.52}$$

$$\frac{1}{Z_i(z)}\frac{\partial^2Z_i(z)}{\partial z^2}-k_i^2=\kappa^2. \tag{6.53}$$

Equation (6.52) is a first-order Bessel equation with general solution

$$R(\rho)=\int_0^\infty \alpha(\kappa)J_1(\kappa\rho)d\kappa, \tag{6.54}$$

where $J_1(u)$ is the Bessel function of the first kind, of order 1, and $\alpha(\kappa)$ is a function of the continuous variable κ whose form is determined according to the boundary conditions of the system. A term containing $Y_1(u)$, the Bessel function of the second kind, of order 1, is not needed because there is no source at $\rho=0$. A discussion of the properties of Bessel functions is given in the Appendix, Sect. 10.4. Since κ is a continuous variable, the electric field is obtained by integrating over the range of κ. Write (6.53) as

$$\frac{\partial^2Z_i(z)}{\partial z^2}-\gamma_i^2Z(z)=0 \tag{6.55}$$

where $\gamma_i = \sqrt{\kappa^2 + k_i^2}$ and the root with positive real part is taken. The general solution of (6.55) contains terms of the form $e^{\gamma_i z}$ and $e^{-\gamma_i z}$. Hence, combining with (6.54), the general solution of (6.51) may be written as

$$E_\phi^i(\rho, z) = R(\rho)Z_i(z) = \int_0^\infty \left[A_i(\kappa)e^{\gamma_i z} + B_i(\kappa)e^{-\gamma_i z}\right] J_1(\kappa\rho)d\kappa \tag{6.56}$$

where $\alpha(\kappa)$ has been incorporated into $A_i(\kappa)$ and $B_i(\kappa)$. Consider in turn each of the three regions labeled in Fig. 6.10. In region 1, above the current loop,

$$E_\phi^1(\rho, z) = \int_0^\infty B_1(\kappa)e^{-\kappa z} J_1(\kappa\rho)d\kappa. \tag{6.57}$$

In region 2, below the current loop but above the half-space,

$$E_\phi^2(\rho, z) = \int_0^\infty \left[A_2(\kappa)e^{\kappa z} + B_2(\kappa)e^{-\kappa z}\right] J_1(\kappa\rho)d\kappa, \tag{6.58}$$

and in region 3, the conductor,

$$E_\phi^3(\rho, z) = \int_0^\infty A_3(\kappa)e^{\gamma_3 z} J_1(\kappa\rho)d\kappa. \tag{6.59}$$

The coefficients are now determined by applying interface conditions (5.19) and (5.21) between regions 1, 2, and 3 (see Exercise 5 at the end of this chapter). Note that imposing continuity of the tangential component of the electric field (E_ϕ) is straightforward at both interfaces, whereas the presence of the coil filament comes into play in application of the condition on the tangential component of the magnetic field (H_ϕ). In fact, the resulting interface conditions on E_ϕ are

$$E_\phi^1(\rho, h) = E_\phi^2(\rho, h), \tag{6.60}$$

$$\left.\frac{\partial}{\partial z} E_\phi^1(\rho, z)\right|_{z=h} = \left.\frac{\partial}{\partial z} E_\phi^2(\rho, z)\right|_{z=h} + j\omega\mu\mathcal{I}\delta(\rho - a), \tag{6.61}$$

$$E_\phi^2(\rho, 0) = E_\phi^3(\rho, 0), \tag{6.62}$$

$$\left.\frac{\partial}{\partial z} E_\phi^2(\rho, z)\right|_{z=0} = \left.\frac{\partial}{\partial z} E_\phi^3(\rho, z)\right|_{z=0}. \tag{6.63}$$

Finally, the following expressions for E_ϕ^i are obtained:

$$E_\phi^1(\rho, z) = -\frac{1}{2} j\omega\mu_0\mathcal{I}a \int_0^\infty J_1(\kappa a)J_1(\kappa\rho)e^{-\kappa(h+z)}\left[e^{2\kappa h} + \frac{(\kappa - \gamma)}{(\kappa + \gamma)}\right] d\kappa, \tag{6.64}$$

$$E_\phi^2(\rho, z) = -\frac{1}{2} j\omega\mu_0 \mathcal{I} a \int_0^\infty J_1(\kappa a) J_1(\kappa\rho) e^{-\kappa h} \left[e^{\kappa z} + \frac{(\kappa - \gamma)}{(\kappa + \gamma)} e^{-\kappa z} \right] d\kappa, \tag{6.65}$$

$$E_\phi^3(\rho, z) = -j\omega\mu_0 \mathcal{I} a \int_0^\infty J_1(\kappa a) J_1(\kappa\rho) e^{-\kappa h + \gamma z} \frac{\kappa}{(\kappa + \gamma)} d\kappa. \tag{6.66}$$

In these equations, $\gamma_3 = \sqrt{\kappa^2 + j\omega\mu_3\sigma_3}$ is replaced by $\gamma = \sqrt{\kappa^2 + j\omega\mu_0\sigma}$ for simplicity, where the root with positive real part is taken and, as before, ω is angular frequency, $\mu_0 = 4\pi \times 10^{-7}$ H/m is the permeability of free space and σ is the conductivity of the test-piece.

An efficient way of evaluating the integrals in the above equations for E_ϕ is to truncate the domain of the electric field at a particular value of r, far from the loop, where it has decayed to approximately zero. Truncating at approximately ten times the coil radius usually gives sufficient accuracy. Then, the integral can be written in terms of a summation based on the set of zeros of the function $J_1(u)$. This technique is used extensively in [10] and references therein.

Calculation of Z

Now that the solution for **E** has been obtained, (6.64)–(6.66), the self-induced voltage in the current filament can be obtained by integrating **E** around the filament. The impedance can then be obtained by means of relation (4.25); $Z = \mathcal{V}/\mathcal{I}$. In general, the voltage induced by field **E** in a current filament is, in phasor form,

$$\mathcal{V} = -\int \mathbf{E} \cdot d\mathbf{l}, \tag{6.67}$$

where the path of the integral follows the current loop. In the case of the axially symmetric single loop shown in Fig. 6.10,

$$\mathcal{V} = -a \int_0^{2\pi} E_\phi(a, h) d\phi = -2\pi a E_\phi(a, h) \tag{6.68}$$

and $\mathcal{V}$ can be obtained immediately by inserting $E_\phi(a, h)$ from either (6.64) or (6.65) into (6.68). Dividing by $\mathcal{I}$ then gives the self-induced impedance of the current filament, Z^δ,

$$Z^\delta = j\omega\mu_0\pi a^2 \int_0^\infty [J_1(\kappa a)]^2 \left[1 + \frac{(\kappa - \gamma)}{(\kappa + \gamma)} e^{-2\kappa h} \right] d\kappa. \tag{6.69}$$

Examining (6.69) it is seen that Z^δ depends on the frequency of operation ω, the coil cross-sectional area πa^2, its position with reference to the sample, h, and the sample conductivity σ. The above relation has been derived on the assumption of a non-ferromagnetic test-piece, but if the conductor is ferromagnetic then

$$Z^\delta = j\omega\mu_0\pi a^2 \int_0^\infty [J_1(\kappa a)]^2 \left[1 + \frac{(\mu_\mathrm{r}\kappa - \gamma)}{(\mu_\mathrm{r}\kappa + \gamma)} e^{-2\kappa h}\right] d\kappa, \tag{6.70}$$

with $\gamma = \sqrt{\kappa^2 + j\omega\mu_0\mu_\mathrm{r}\sigma}$, and Z^δ depends also on the relative permeability μ_r of the test-piece. By letting $h \to \infty$ the impedance of an isolated current filament, Z_0^δ, can be obtained readily:

$$Z_0^\delta = j\omega\mu_0\pi a^2 \int_0^\infty [J_1(\kappa a)]^2 d\kappa. \tag{6.71}$$

From (6.70), the self-inductance L of the coil can be obtained via (6.1). Similarly, the inductance L_0 of the isolated coil can be obtained from (6.71).

Comparing (6.71) with (6.70) allows the contribution to Z^δ from the test-piece to be identified, as follows:

$$Z^\delta = Z_0^\delta + j\omega\mu_0\pi a^2 \int_0^\infty [J_1(\kappa a)]^2 \frac{(\mu_\mathrm{r}\kappa - \gamma)}{(\mu_\mathrm{r}\kappa + \gamma)} e^{-2\kappa h} d\kappa. \tag{6.72}$$

6.3.4 Coil above a Half-Space Conductor

The impedance of a coil with finite cross section, shown in Fig. 6.11, is of more practical importance than that for the current loop obtained in the previous section, but can be obtained from it by the following process of superposition.

Electric Field

By the process of linear superposition, the fields due to n filamentary loops may be summed to obtain the total field due to a coil with n turns, $\mathbf{E}^T$, assuming that the current in each loop has the same phase and amplitude;

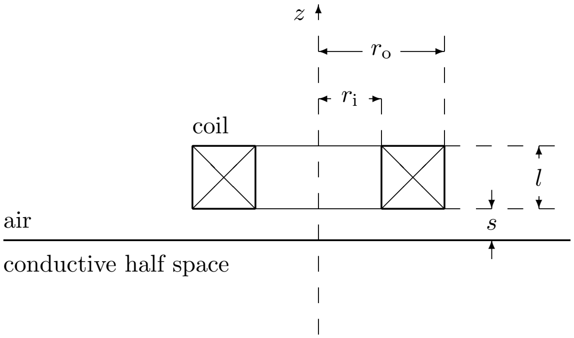

Fig. 6.11 Cross section through the axis of a circular, air-cored, eddy-current coil, positioned horizontally above a conductive half-space

$$\mathbf{E}^T(\rho, z) = \sum_{i=1}^{n} E(\rho, z|a_i, h_i) \tag{6.73}$$

where $E(\rho, z|a_i, h_i)$ is the electric field produced by the ith filamentary loop at (a_s, h_s). It is convenient to write this summation as an integral over the cross section of the coil. To do this, the superposition of the n δ-function coils must be approximated by a continuous current density $\mathbf{J}_\text{s}(a_\text{s}, h_\text{s})$ over the coil cross section and

$$\mathbf{E}^T(\rho, z) = \int_{\text{coil cross section}} \mathbf{E}(\rho, z|a_\text{s}, h_\text{s}) dS, \tag{6.74}$$

where $\mathbf{E}(\rho, z|a_\text{s}, h_\text{s})$ is the electric field produced by the equivalent current density $\mathbf{J}_s$ in the coil and the subscript s indicates that this is the *source* current density. The variables a_s and h_s are, then, continuous variables in the radial and vertical directions, respectively. For a coil with rectangular cross section and parameters as shown in Fig. 6.11,

$$\mathbf{E}^T(\rho, z) = \int_s^{s+l} \int_{r_\text{i}}^{r_\text{o}} \mathbf{E}(\rho, z|a_\text{s}, h_\text{s}) da_\text{s} dh_\text{s}. \tag{6.75}$$

As an example of applying the process of linear superposition consider the electric field in the region above the coil. This corresponds to region 1 in the case of the circular current loop treated in Sect. 6.3.3 and shown in Fig. 6.10. Taking the result for $E_\phi^1(\rho, z)$ in the case of the δ-function coil, (6.64), and inserting that into integral (6.75) gives

$$\begin{aligned} E_\phi^{T,1}(\rho, z) = -\frac{1}{2} j\omega\mu_0\mathcal{I} \int_0^\infty J_1(\kappa\rho) \Bigg\{ \int_{r_\text{i}}^{r_\text{o}} a_\text{s} J_1(\kappa a_\text{s}) da_\text{s} \times \\ \int_s^{s+l} e^{-\kappa(h_\text{s}+z)} \left[e^{2\kappa h_\text{s}} + \frac{(\kappa-\gamma)}{(\kappa+\gamma)} \right] dh_\text{s} \Bigg\} d\kappa, \end{aligned} \tag{6.76}$$

where the order of integration has been reversed. Consider first the integral over a_s.

$$\int_{r_\text{i}}^{r_\text{o}} a_\text{s} J_1(\kappa a_\text{s}) da_\text{s} = \frac{1}{\kappa^2} J(\kappa r_\text{i}, \kappa r_\text{o}) \tag{6.77}$$

where

$$J(x_1, x_2) = \int_{x_1}^{x_2} x J_1(x) dx = \frac{\pi}{2} x \left[J_0(x)\mathbf{H}_1(x) - J_1(x)\mathbf{H}_0(x) \right]_{x_1}^{x_2} \tag{6.78}$$

and $\mathbf{H}_n$ denotes the Struve function of order n. Guidance on computing $J(x_1, x_2)$ efficiently has been provided in [10]. Now consider terms in (6.76) that depend on h_s:

$$\int_{s}^{s+l} e^{-\kappa(h_s+z)} \left[e^{2\kappa h_s} + \frac{(\kappa-\gamma)}{(\kappa+\gamma)} \right] dh_s. \tag{6.79}$$

Integrating over this variable is easily accomplished analytically such that, finally,

$$E_{\phi}^{T,1}(\rho, z) = -\frac{1}{2} j\omega\mu_0 \mathcal{I} \int_{0}^{\infty} \frac{1}{\kappa^3} J(\kappa r_i, \kappa r_o) J_1(\kappa\rho) e^{-\kappa z} \left[e^{\kappa s}(e^{\kappa l} - 1) - e^{-\kappa s} \frac{(\kappa-\gamma)}{(\kappa+\gamma)} (e^{-\kappa l} - 1) \right] d\kappa. \tag{6.80}$$

Expressions for $E_{\phi}^{T,i}$, in other regions, may be obtained in a similar manner.

Voltage in a Surface Coil near a Half-Space Conductor

The total voltage induced in a coil of n turns is

$$\mathcal{V} = -2\pi \sum_{i=1}^{n} a_i E_{\phi}(a_i, h_i), \tag{6.81}$$

in which $2\pi a_i$ is the circumferential length and h_i is the height above the half-space of the ith current loop, and $E_{\phi}(a_i, h_i)$ is the electric field of that loop. It is convenient to approximate this summation by an integral over a turn density of N turns per unit cross-sectional area of the coil. To do this it will be assumed that there is a constant number of turns per unit cross-sectional area of the coil, such that

$$N = \frac{n}{l(r_o - r_i)} \tag{6.82}$$

where the notation of Fig. 6.11 is employed. Then,

$$\mathcal{V} = -\frac{2\pi n}{l(r_o - r_i)} \int_{s}^{s+l} \int_{r_i}^{r_o} a_s E_{\phi}(a_s, h_s) da_s dh_s. \tag{6.83}$$

Z for Surface Coil near a Half-Space Conductor

An expression for the impedance of the surface coil near a half-space conductor is now calculated using relation (4.25); $Z = \mathcal{V}/\mathcal{I}$, with $\mathcal{V}$ given by (6.83). Note, the current density of the source in the case of the finite coil is $J_s = n\mathcal{I}/[l(r_o - r_i)]$, not to be confused with $J_s = \mathcal{I}\delta(\rho - a)\delta(z - h)$ as for the infinitesimal current loop. This must be reflected in the expression for E_{ϕ} since **E** and **J** are related according to the point form of Ohm's Law, relation (2.15). Effectively, $\mathcal{I}$ in E_{ϕ} as expressed in (6.64) or (6.65) should be replaced by $n\mathcal{I}/[l(r_o - r_i)]$ in the case of the finite coil so that

$$Z = -\frac{2\pi n^2}{l^2(r_o - r_i)^2} \int_{s}^{s+l} \int_{r_i}^{r_o} a_s E_{\phi}(a_s, h_s) da_s dh_s. \tag{6.84}$$

Now the integrals with respect to a_s and h_s may be evaluated by inserting $E_\phi(a_\mathrm{s}, h_\mathrm{s})$ into (6.84). To do this, the integral over h_s is split into regions within the coil below and above h_s. In the region above h_s the expression for $E^1_\phi(\rho, z)$ is inserted whereas in the region below h_s the expression for $E^2_\phi(\rho, z)$ is used. Explicitly,

$$Z = -\frac{2\pi n^2}{l^2(r_\mathrm{o} - r_\mathrm{i})^2} \int_{r_\mathrm{i}}^{r_\mathrm{o}} a_\mathrm{s} \left[\int_s^{h_\mathrm{s}} E^2_\phi(a_\mathrm{s}, h_\mathrm{s}) dh_\mathrm{s} + \int_{h_\mathrm{s}}^{s+l} E^1_\phi(a_\mathrm{s}, h_\mathrm{s}) dh_\mathrm{s} \right] da_\mathrm{s}. \tag{6.85}$$

Inserting expressions for $E^1_\phi(\rho, z)$ and $E^2_\phi(\rho, z)$, the following integrals with respect to a_s and h_s emerge:

$$Z = \frac{j\omega\mu_0\pi n^2}{l^2(r_\mathrm{o} - r_\mathrm{i})^2} \int_0^\infty \int_{r_\mathrm{i}}^{r_\mathrm{o}} [a_\mathrm{s} J_1(\kappa a_\mathrm{s})]^2 \, da_\mathrm{s} \int_s^{s+l} \left[1 + \frac{(\kappa - \gamma)}{(\kappa + \gamma)} e^{-2\kappa h_\mathrm{s}} \right] dh_\mathrm{s} d\kappa, \tag{6.86}$$

assuming that the current in each loop has the same phase and amplitude.

Treating the integrals in (6.86) as outlined in (6.77)–(6.79) gives the following expression for the impedance of an air-cored surface coil of finite cross section near a conductive half-space:

$$\begin{aligned} Z = \frac{j\omega\mu_0\pi n^2}{l^2(r_\mathrm{o} - r_\mathrm{i})^2} \int_0^\infty \frac{J^2(\kappa r_\mathrm{i}, \kappa r_\mathrm{o})}{\kappa^5} \Bigg(2l + \frac{1}{\kappa} \Big\{ 2e^{-\kappa l} - 2 \\ + [e^{-2\kappa(l+s)} + e^{-2\kappa s} - 2e^{-\kappa(l+2s)}] \left(\frac{\gamma - \kappa}{\gamma + \kappa} \right) \Big\} \Bigg) d\kappa. \end{aligned} \tag{6.87}$$

Note, Z depends on the frequency of operation of the probe, ω, the coil dimensions, r_i, r_o and l, the *square* of the number of turns, n^2 (as in the case of the long solenoid, Exercise 3 at the end of this chapter), the coil position with reference to the sample, s, and the sample conductivity, σ. If the conductive half-space is also ferromagnetic, with relative permeability μ_r, then $\gamma = \sqrt{\kappa^2 + j\omega\mu_0\mu_\mathrm{r}\sigma}$ and the last term in (6.87) is $(\gamma - \mu_\mathrm{r}\kappa)/(\gamma + \mu_\mathrm{r}\kappa)$.

By letting $s \to \infty$ in (6.87), the following expression for the impedance of an isolated coil is obtained,

$$Z_0 = \frac{2j\omega\mu_0\pi n^2}{l^2(r_\mathrm{o} - r_\mathrm{i})^2} \int_0^\infty \frac{J^2(\kappa r_\mathrm{i}, \kappa r_\mathrm{o})}{\kappa^5} \left(l + \frac{e^{-\kappa l} - 1}{\kappa} \right) d\kappa. \tag{6.88}$$

From relation (6.87), the self-inductance of the loop L can be deduced via relation (6.1). Similarly, from (6.88) the inductance of the isolated loop L_0 can be obtained. Taking (6.87) and (6.88) together, the contribution to the coil impedance of the test-piece can be isolated.

$$Z = Z_0 + \frac{j\omega\mu_0\pi n^2}{l^2(r_\mathrm{o} - r_\mathrm{i})^2} \int_0^\infty \frac{J^2(\kappa r_\mathrm{i}, \kappa r_\mathrm{o})}{\kappa^6} [e^{-2\kappa(l+s)} + e^{-2\kappa s} - 2e^{-\kappa(l+2s)}] \left(\frac{\gamma - \kappa}{\gamma + \kappa} \right) d\kappa. \tag{6.89}$$

Evaluation of (6.87), or of (6.89) with (6.88), for particular coil parameters r_i, r_o, l and n^2 allows calculation of impedance values such as those plotted as an impedance-plane plot in Fig. 6.2, in which the effect of different material conductivities, and of coil frequency, are illustrated. The impedance-plane plot of Fig. 6.3 illustrates the effect of varying frequency, lift-off and permeability although for this figure the impedance is plotted in normalized form, as Z/X_0.

6.3.5 *Ferrite Core*

The strength of coupling between an eddy-current surface probe and the test-piece can be increased by winding the coil around a ferrite core, rather than a purely dielectric material such as machinable plastic. Ferrite cores are commonly used for increasing the signal-to-noise ratio of a particular coil configuration. A schematic diagram of a coil wound around a ferrite core is shown in Fig. 6.12. The ferrite strengthens the magnetic flux density within the coil in proportion to the permeability of the ferrite, (2.25) and (4.16), and consequently strengthens the electromagnetic coupling between the probe coil and the test-piece. Ferrites are low conductivity but high-permeability ferromagnetic materials. It is important that the core material has low conductivity because, if it were conductive, eddy currents would be induced by the coil in the core, as well as in the test-piece. The eddy currents induced in a conductive core would have the counterproductive effect of *reducing* the eddy-current density in the test-piece, which must be avoided.

Manganese zinc (MnZn) ferrite is commonly used in eddy-current probe cores and in transformer cores, where it is also desirable to minimize energy losses that would reduce the efficiency of the transformer. The initial relative permeability of MnZn ferrite is on the order of 1,000. The resistivity of MnZn ferrite is a function of temperature and frequency. Resistivity is reduced as temperature increases, and as frequency increases. Example values of the resistivity of MnZn ferrite are given in Table 6.2.

Fig. 6.12 Cross section through the axis of a circular, ferrite-cored, eddy-current coil

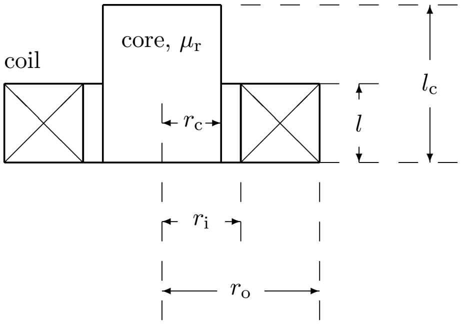

Table 6.2 Resistivity as a function of frequency for MnZn ferrites [11]

Frequency (MHz)	Resistivity (Ωm)
0.1	≈2
1	≈0.5
10	≈0.1
100	≈0.01

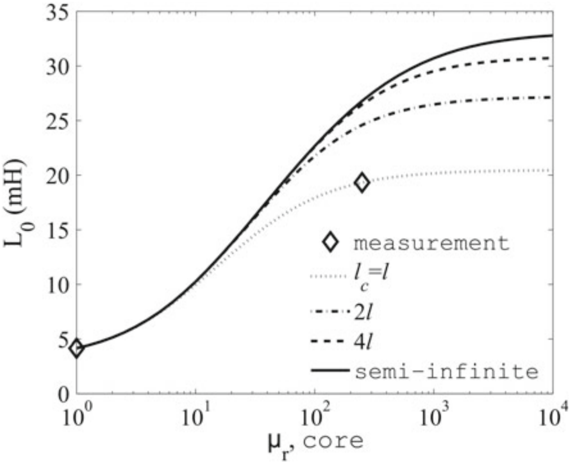

Fig. 6.13 Self-inductance of an isolated ferrite-cored coil as a function of μ_r of the core, for core lengths $l_c = l, 2l, 4l$ and for a semi-infinite core

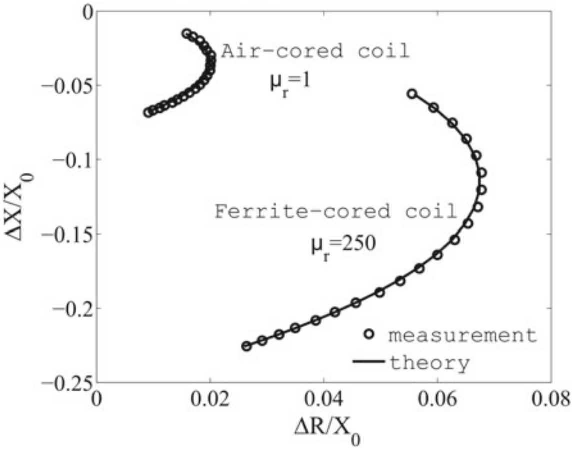

Fig. 6.14 Normalized impedance-plane diagram comparing Z for an air-cored and a ferrite-cored coil above a conductive half-space, where $\Delta X = X - X_0$ and $\Delta R = R - R_0$

Theodoulidis [12] and Lu et al. [13] have analyzed the impedance of a ferrite-cored coil utilizing the truncated region eigenfuction expansion (TREE) method, Sect. 7.3.1. Using this approach, the curves presented in Figs. 6.13 and 6.14 have been calculated. Parameters of the coil, core and conductive half-space used to obtain the calculated data plotted in Figs. 6.13 and 6.14 are given in Table 6.3. In Fig. 6.13 the self-inductance of an isolated ferrite-cored coil is plotted as a function of the relative permeability of the ferrite, and for various core lengths. It can be seen that

Table 6.3 Parameters for the numerical calculations whose data are presented in Fig. 6.13 and Fig. 6.14. Note that the core length and test-piece parameters are relevant only to Fig. 6.14

Coil parameters		Value	Ferrite core parameters		Value
r_o	Outer radius (mm)	10.275	r_c	Core radius (mm)	3.880
r_i	Inner radius (mm)	5.025	l_c	Core length (mm)	29.95
l	Length (mm)	18.180			
s	Coil stand-off (mm)	2.650	Test-piece parameters		
h	Probe lift-off (mm)	0.590	σ	Conductivity ($\mathrm{MSm^{-1}}$)	20.40
n	Number of turns	776	μ_r	Relative permeability	1

L_0 increases rapidly at first, as $\mu_{r,\mathrm{core}}$ increases, but the improvement is only slight as $\mu_{r,\mathrm{core}}$ increases above about 100. Similarly, there is a rapid increase in L_0 as the core length is doubled with respect to the coil length, but lesser improvement is obtained as the core length is doubled again and then made semi-infinite.

Figure 6.14 reveals the enhancement in Z and coupling parameter c, (6.3), when a ferrite core with $\mu_r = 250$ is inserted into the coil. One way of thinking about the effect of the ferrite core on the coupling between the coil and the test-piece is that the introduction of a ferrite core into a surface coil has an effect similar to that of moving the coil windings closer to the test-piece.

6.3.6 Sources of Uncertainty

Nonideal Coil Behavior

It has been discussed in previous sections that an ideal eddy-current coil would be a pure inductor. The inductance of the coil is the important circuit property as far as inducing current in a test-piece is concerned, and in detecting perturbations in the magnetic field associated with the induced eddy currents, due to the presence of defects. The behavior of a real coil is not that of a pure inductor, due in part to the fact that the current flowing in an eddy-current coil is not uniformly distributed over the cross section of the coil. The current is restricted to flow within the coil windings and, in fact, near the surface of the windings for higher frequency excitations (a consequence of the skin effect). These geometrical restrictions on the current density causes the coil to exhibit inter-winding capacitance. In addition, a real eddy-current coil exhibits finite DC resistance due to the resistivity of the metal constituting the coil windings, usually copper. Additional perturbations to the current density in the coil arise from irregularity in the windings. Capacitance in the leads connecting the probe to the power source also makes a significant contribution to the probe impedance at higher frequencies.

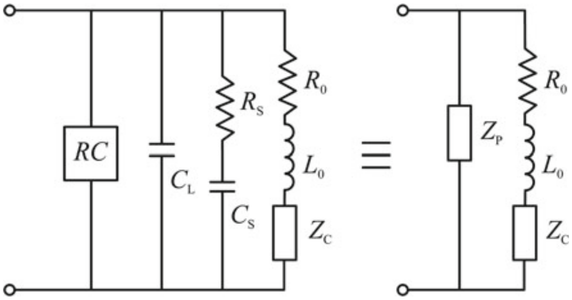

Fig. 6.15 Equivalent electrical circuit for an eddy current probe coil. R_0 and L_0 represent the DC resistance and inductance of the probe coil, respectively. Z_C is the impedance due to coupling with an external conductor (the test-piece). R_S and C_S represent stray resistance and capacitance, respectively, in the coil windings. C_L accounts for capacitance in the leads connecting the probe with the power source. Any other unspecified contributions to the impedance of the electrical circuit are represented by RC. In the right-hand figure, all parallel circuit components are lumped together in one parallel impedance, Z_P [14]

An equivalent circuit that takes into account these various contributions to the impedance of a real eddy current probe is shown schematically in Fig. 6.15 [14]. This circuit is more complicated than those considered in Chap. 4 but one familiar feature is that due to the presence of capacitive elements in parallel with series inductance and resistance, the probe resonates at a certain frequency f_0. Resonance manifesting in measured R and L is shown in Fig. 6.16 for one particular coil [14]. The value of f_0 depends on the values of the different circuit components in each individual coil, but f_0 on the order of hundreds of kHz is typical for an eddy-current coil. In order to avoid large uncertainties in precision eddy current measurements, a rule of thumb is that the operating frequency of a probe should be less than one-third of the resonance frequency.

In a routine EC inspection, the nonideal behavior of an EC coil is assumed to be negligible provided that it is operated at a frequency sufficiently far below f_0. For benchmark experiments in EC research, however, whose purpose is to provide data that validates a new theoretical treatment of a particular EC inspection, agreement between theory and experiment is sought to within a few percent. Under these circumstances it is essential to correct for the nonideal behavior of the coil. A procedure by which corrections for the nonideal coil behavior can be made was published by Harrison, Jones, and Burke in 1996 [14]. To follow this procedure for an eddy-current coil is in fact to *characterize* that coil since, during the correction procedure, *effective* values for the coil's outer radius and stand-off are determined. Essential steps in the correction procedure are explained in the following two paragraphs for an air-cored surface coil above a metal plate. The procedure is not restricted to this probe and test-piece configuration, however, but may be adapted to work for other canonical configurations for which impedance formulas are available [10].

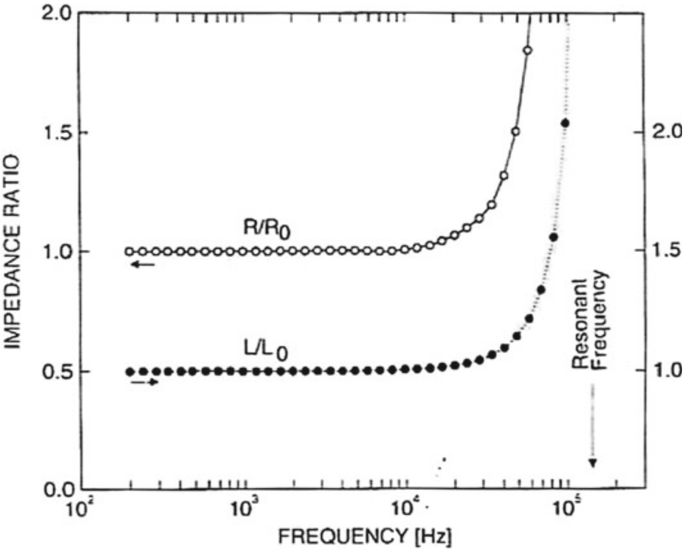

Fig. 6.16 Resistance and inductance of a coil, normalized with respect to the DC values, are shown as a function of operating frequency. Resonance is observed at 142 kHz for this particular coil [14]. With kind permission from Springer Science and Business Media: *J. Nondestr. Eval.*, vol. 15, 1996, p. 26, Benchmark problems for defect size and shape determination in eddy-current nondestructive evaluation, D. J. Harrison, L. D. Jones, and S. K. Burke, Fig. 4. Original caption: Isolated coil inductance and resistance as a function of frequency. Deviations from the DC values are due to nonideal coil behavior. The isolated coil resonant frequency is indicated by an arrow

Correction for DC Coil Resistance and Stray Capacitance Following the method described in [14], the first step in making corrections for nonideal coil behavior is to adjust experimental impedance measurements to eliminate the effects of stray capacitance and DC resistance of the coil. The ideal admittance, obtained from the DC values of coil resistance and inductance, R_0 and L_0 respectively, is

$$Y_{\text{ideal}} = \frac{1}{Z_{\text{ideal}}} = \frac{1}{R_0 + j\omega L_0}. \tag{6.90}$$

Writing Y_0 as the experimentally measured admittance in air, where

$$Y_0^{\text{exp}} = \frac{1}{Z_0^{\text{exp}}}, \tag{6.91}$$

and subtracting Y_{ideal} gives the admittance of the equivalent parallel network, Y_{P}, where

$$Y_{\text{P}} = Y_0^{\text{exp}} - Y_{\text{ideal}}. \tag{6.92}$$

Denoting the uncorrected impedance of the coil, measured with the coil over the conductive plate, by $Z_{\mathrm{U}}^{\mathrm{exp}}$ (with associated admittance $Y_{\mathrm{U}}^{\mathrm{exp}}$), the corrected impedance $Z_{\mathrm{C}}^{\mathrm{exp}}$ is obtained by subtracting the effect of the parallel circuit,

$$Z_{\mathrm{C}}^{\mathrm{exp}} = \frac{1}{Y_{\mathrm{U}}^{\mathrm{exp}} - Y_{\mathrm{P}}}. \tag{6.93}$$

The corrected impedance change in the coil due to the plate, $\Delta Z_{\mathrm{C}}^{\mathrm{exp}}$, is therefore

$$\Delta Z_{\mathrm{C}}^{\mathrm{exp}} = Z_{\mathrm{C}}^{\mathrm{exp}} - Z_{\mathrm{ideal}}. \tag{6.94}$$

In the case that this correction procedure is not followed, the impedance change in the coil due to the plate is given by

$$\Delta Z_{\mathrm{U}}^{\mathrm{exp}} = Z_{\mathrm{U}}^{\mathrm{exp}} - Z_{\mathrm{ideal}}. \tag{6.95}$$

Effective Coil Parameters and Determination of Plate Conductivity Calculating the self-inductance of an isolated EC coil using (6.88) and (6.1), with macroscopically measured coil dimensions r_{i}, r_{o} and l as inputs, yields a value for L_0 that is typically a few percent higher than the value measured using an impedance analyzer or other instruments [15]. The discrepancy can be explained by arguing that the measured value of r_{o} overestimates the equivalent value for an ideal coil, since it represents the outermost extent of the windings of a nonuniform current distribution. An equivalent but uniform current distribution would occupy a smaller volume than the real, nonuniform current distribution in the coil. Perfect agreement between the calculated and measured values of L_0 can be obtained by introducing an effective value for the coil outer radius, $r_{\mathrm{o}}^{\mathrm{eff}} < r_{\mathrm{o}}$. In the correction procedure, the value of $r_{\mathrm{o}}^{\mathrm{eff}}$ is determined by varying its value in the calculation of L_0 until agreement with the measured value is achieved.

Again due to nonuniformity of the current density in the coil, it is anticipated that the measured stand-off of the coil will be smaller than that of an ideal coil for which other parameters are identical. The coil impedance Z depends strongly on s which means that this subtle effect is important if precise results are sought. An effective value of the coil stand-off may be determined by minimizing the root mean square (RMS) error between the experimentally measured impedance of the coil on a metal plate, and values calculated using (6.87). The RMS error, ε, is computed from the following relation, in which the superscript "exp" denotes experimentally measured values, and "thry" denotes theoretically calculated values. N is the number of frequency points.

$$\varepsilon^2 = \frac{1}{N}\sum_{j=1}^{N}\left\{\left[\frac{\Delta R_j^{\mathrm{exp}}(f_j) - \Delta R_j^{\mathrm{thry}}(f_j)}{\Delta R_j^{\mathrm{exp}}(f_j)}\right]^2 + \left[\frac{\Delta L_j^{\mathrm{exp}}(f_j) - \Delta L_j^{\mathrm{thry}}(f_j)}{\Delta L_j^{\mathrm{exp}}(f_j)}\right]^2\right\} \tag{6.96}$$

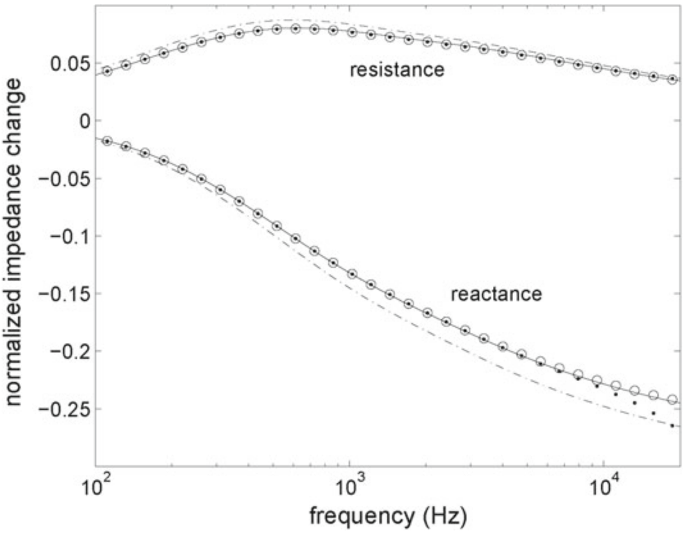

Fig. 6.17 Change in coil impedance due to a brass plate, normalized to the ideal isolated coil reactance $X_0 = \omega L_0$. Circles (o) represent experimental data corrected for nonideal coil behavior. Dots (·) represent uncorrected experimental data. Solid lines (—) represent theory with effective parameters. Broken lines (- - -) represent theory with measured parameters [15]. From: Bowler, N., Huang, Y.: Electrical conductivity measurement of metal plates using broadband eddy-current and four-point methods. Meas. Sci. Technol. **16**, 2193-2200 (2005), Fig. 2. ©IOP Publishing. Reproduced with permission. All rights reserved

At the same time, the conductivity of the plate is permitted to vary until ε is minimized. The probe stand-off and plate conductivity may be found simultaneously since ε shows well-defined minima with respect to variations in both of these parameters [14], especially at higher frequencies, Fig. 6.2.

In Fig. 6.17, the corrected experimental data, $\Delta Z_\mathrm{C}^{\mathrm{exp}}$ of (6.94), and uncorrected experimental data, $\Delta Z_\mathrm{U}^{\mathrm{exp}}$ of (6.95), are shown for normalized coil impedance change of a surface coil on a brass plate. For full details of this study see [15]. Also shown in Fig. 6.17 are curves calculated using (6.87) with measured and effective parameters. The improvement in agreement between theory and experiment after making corrections for DC coil resistance and stray capacitance, and refining coil parameters r_o and s, is dramatic. In Table 6.4, effective parameters obtained by this procedure for measurements on brass and stainless steel plates are compared with dimensions measured using digital calipers and conductivities measured using a Zetec MIZ-21A eddy-current instrument [15]. Notice that the effective outer radius is slightly smaller, and the effective stand-off is slightly greater, than values measured with calipers. This is in keeping with the initial hypothesis that an equivalent but uniform current distribution occupies a smaller volume than the real, nonuniform current distribution in the coil. The uncertainties in the effective value of s and in the fitted value of σ, quoted in Table 6.4, were assumed to be given by the RMS error ε, as defined in

Table 6.4 Measured and effective (or fitted) parameters. Lengths were measured using digital calipers at appropriate stages during fabrication of the coil. Conductivity σ was measured using a Zetec MIZ-21A eddy-current instrument

Parameter		Measured	Effective (geometric) and fitted (material)
r_{o}	Outer radius (mm)	11.84 ± 0.01	11.43 ± 0.06
s	Stand-off (mm)		
	Brass	1.00 ± 0.04	1.06 ± 0.03
	Stainless steel	1.00 ± 0.04	1.01 ± 0.02
σ	Conductivity (MSm^{-1})		
	Brass	16.2 ± 0.3	16.6 ± 0.4
	Stainless steel	0.7 ± 0.3	1.31 ± 0.02

(6.96), for each plate. Regarding the significant difference between the measured and fitted values of σ in stainless steel, given in Table 6.4, an independent measurement of conductivity by a four-point alternating current potential drop method on the same sample gave result 1.369 ± 0.007 MSm^{-1} [15].

Geometrical Sources of Uncertainty

Probably the most significant source of uncertainty in impedance measurements made using an EC probe operating in absolute mode is the variation in distance between the probe coil and the test-piece that may occur as the probe scans the object surface. For a flat test-piece, this variation in probe and part separation may be described as a variation in the probe lift-off and is often termed *lift-off noise*. Such impedance changes are indicated in the impedance-plane plot of Fig. 6.3 which may be calculated using the theory of Dodd and Deeds [8], Sect. 6.3.4.

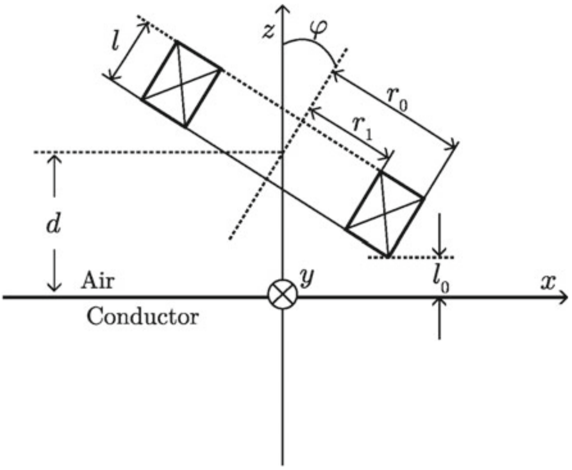

Fig. 6.18 Schematic diagram of surface EC coil whose axis is tilted at angle φ with respect to the direction normal to the test-piece surface

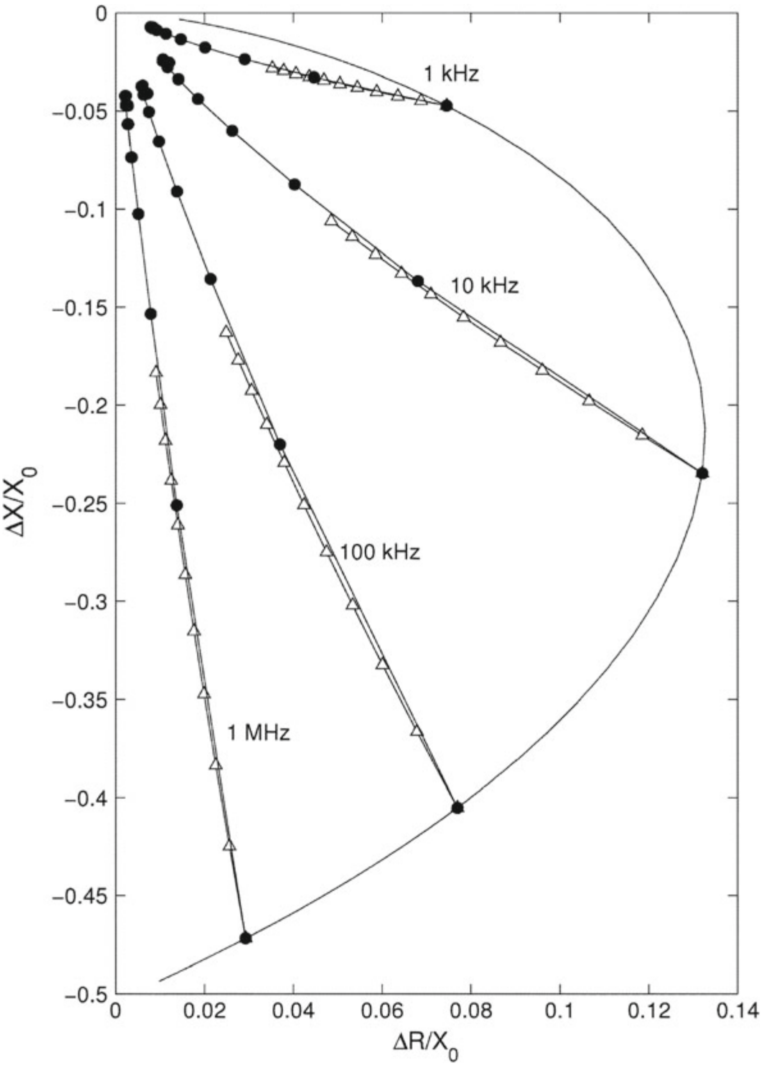

Fig. 6.19 Normalized impedance-plane plot as a function of coil tilt angle φ. Coil and test-piece parameters for the calculation are listed in Table 6.5. Note that in the axis labels ΔX here is equivalent to X and ΔR here is equivalent to $R - R_0$ as defined in (6.2). Reproduced with permission from IEEE: *IEEE Trans. Magn.*, vol. 41, 2005, p. 2453, Analytical model for tilted coils in eddy-current nondestructive inspection, T. Theodoulidis, Fig. 8. Original caption: Impedance change display showing tilt (•) and lift-off curves (△) in steps of 10° and 0.1 mm, respectively. The arc-shaped curve is produced by varying excitation frequency at zero lift-off and zero tilt angle

Table 6.5 Parameters for the numerical calculations whose data are presented in Figs. 6.19 and 6.20

Coil parameters		Value
r_{o}	Outer radius (mm)	4
r_{i}	Inner radius (mm)	2
l	Length (mm)	2
h	Lift-off (mm)	1
n	Number of turns	400
Test-piece parameters		
σ	Conductivity (MSm^{-1})	18.72
μ_{r}	Relative permeability	1

A similar source of noise in the signal of an absolute surface probe is *tilt* of the probe axis through an angle φ with respect to the direction normal to the surface of the test-piece, as shown schematically in Fig. 6.18. Tilt commonly occurs when a probe is scanned in contact with the test-piece because the friction between the probe and test-piece drags upon the probe base, causing the probe to tilt toward the direction of motion. In the context of Fig. 6.18 this would mean that the probe is being moved to the right. Theodoulidis analyzed the impedance of a tilted probe [16] and produced the impedance-plane plot shown in Fig. 6.19 for a coil and test-piece whose parameters are listed in Table 6.5. From the figure, it can be seen that the frequency response of Z at a particular angle of tilt gives rise to the same kind of curve that we are familiar with from the impedance-plane plot for the normal coil, Fig. 6.3. In Fig. 6.19, increasing the angle of tilt has a very similar effect on Z as increasing lift-off, which is also plotted.

In Fig. 6.20, eddy current amplitude and streamlines are plotted for a coil tilted at 0, 30, 60 and 90° with respect to the normal to the test-piece surface. It can be seen that the induced eddy currents become concentrated in the region directly below the coil edge for $\varphi = 90°$. This is the tangent coil configuration, which will be discussed further in Sect. 6.4.

Another source of uncertainty in impedance measurements is the presence of geometrical features in the test-piece, close to the inspection region. Examples of these are edges, joints, rivets, metal support structures and rapid changes in geometry such as corners. At worst, signals from these features completely mask the signal from the sought defect, rendering it undetectable. Often it is necessary to adjust the inspection frequency and choice of probe in order to minimize the signal from geometrical features that may mask the presence of defects. Coil impedance changes due to certain geometrical features are discussed in detail in Sect. 7.3.

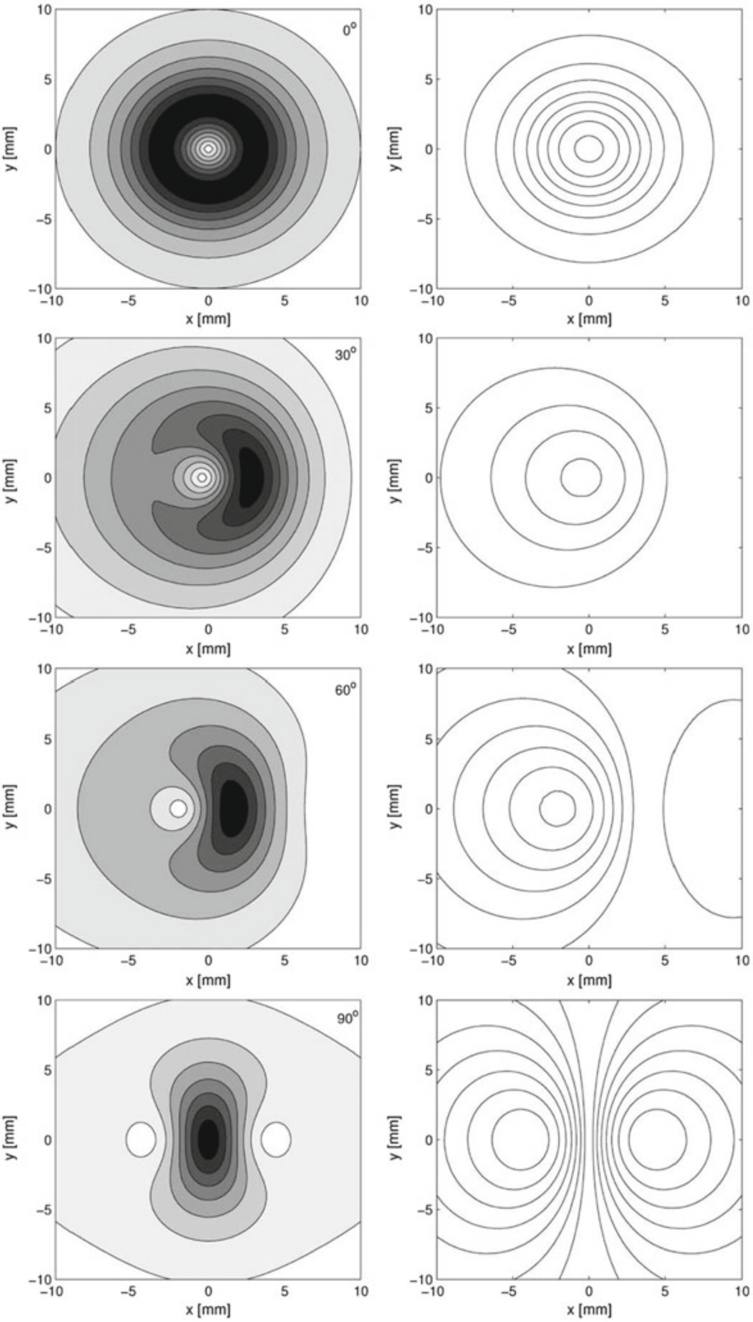
0°
30°
60°
90°
x [mm]
y [mm]
−10
−5
0
5
10

◀**Fig. 6.20** Eddy-current amplitude (left) and streamlines (right) by a coil tilted clockwise at 0 (top), 30, 60 and 90° (bottom) to the test-piece surface. Coil and test-piece parameters for the calculation are listed in Table 6.5. Reproduced with permission from IEEE: *IEEE Trans. Magn.*, vol. 41, 2005, p. 2451, Analytical model for tilted coils in eddy-current nondestructive inspection, T. Theodoulidis, Fig. 6. Original caption: Amplitude contours (left) and streamlines (right) of eddy currents induced on the surface of a conductive half-space by a cylindrical coil at various tilt angles. Coil rotation is clockwise

6.4 Tangent Coil

The tangent coil is oriented such that its axis lies parallel with the surface of the test-piece, as shown in Fig. 6.21. This is equivalent to tilting the axis of a surface coil through $\varphi = 90°$, Fig. 6.18. Referring to Fig. 6.20 it can be seen that the current density in the test-piece below a single tangent coil is concentrated below the coil windings, and is largely unidirectional in that region. Tangent coils are much less widely used than surface coils due to their significantly poorer coupling with the test-piece, but they find special application in plus-point probes, which combine two tangent coils. The plus-point probe is discussed in Sect. 8.5.

The solution by which the impedance of a tangent coil can be calculated is a limiting case of the solution for a tilted coil, which has been analyzed by Theodoulidis as mentioned in Sect. 6.3.6. Due to the lesser practical importance of the tangent coil configuration, when compared with the surface- and encircling-coil configurations, the full theoretical details of the impedance calculation for the tangent coil are not provided here. It can be observed from Fig. 6.19, however, that the calculated normalized impedance change is reduced by a factor of approximately 10 when a coil is tilted through 90° from the surface- to the tangent coil configuration. The interested reader is referred to [10] and [16] for further information.

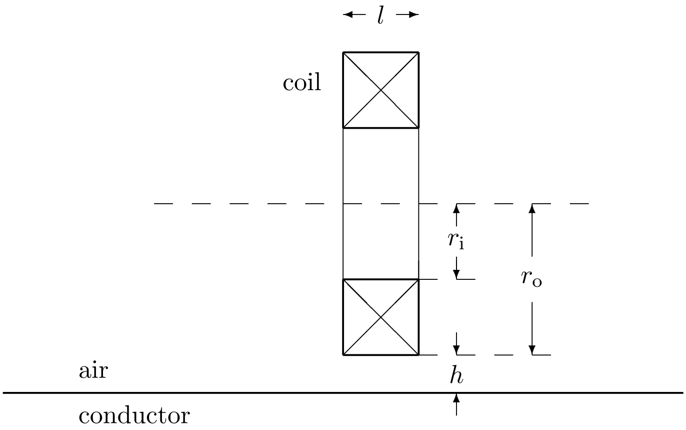

Fig. 6.21 Cross section through the axis of a circular, air-cored, eddy-current tangent coil, positioned above a conductive half-space

6.5 Encircling Coil

Encircling coils couple strongly with rod-like specimens, inducing eddy currents that flow in an azimuthal direction (circularly) around the rod. The probe is designed such that the test-piece may be passed through the middle of the coil, as shown in Fig. 6.22.

The cylindrical test-piece geometry was studied extensively by Friedrich Förster during the 1940s and beyond. Förster was a visionary who, during a study of ferromagnetic properties of metals in 1937, observed the influence of the earth's magnetic field on a test coil. This led Förster to develop highly sensitive measuring equipment for magnetic fields, the scientific basis for which was put into place in the 1950s and earned him the Victor de Forest Award in 1957. A summary of Förster's work relevant to the encircling coil is given in [17, Sect. 5: Analysis of encircling coil tests of wire, rods and bars].

In contrast with the surface coil and test-piece geometry, there is no lift-off associated with the encircling coil. Instead, the *fill factor*, η, indicates the fraction of the cross-sectional area of the coil that is occupied by the test object:

$$\eta = \left(\frac{\rho_1}{r_\mathrm{i}}\right)^2, \tag{6.97}$$

where ρ_1 is the radius of the cylindrical test-piece and r_i is the inner radius of the encircling coil. If the encircling coil is concentric with the test-piece, then the fill factor is an indicator of the strength of coupling between the coil and the test-piece. In Fig. 6.23, an example impedance-plane plot for a coil encircling a long, non-ferromagnetic, cylindrical rod is shown. Note that this impedance-plane diagram is

Fig. 6.22 Cross section through the axis of a circular coil with finite cross section, coaxial with a solid metal circular cylinder (test-piece)

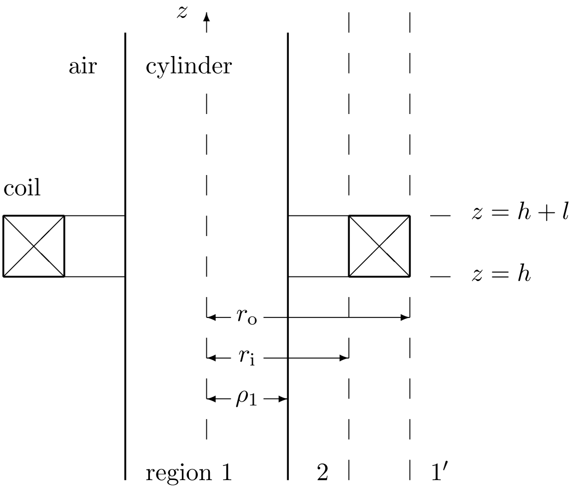

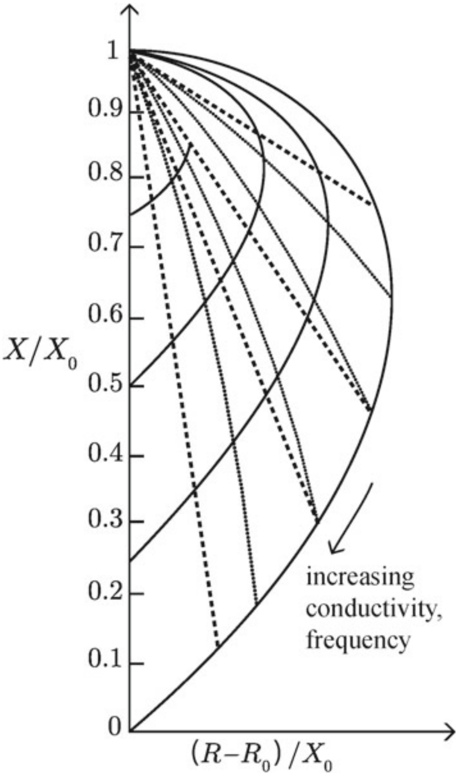

Fig. 6.23 Normalized impedance-plane plot for a coil with inner radius r_i encircling a cylindrical, non-ferromagnetic test-piece with radius ρ_1. Solid lines (——) represent the complex impedance of the probe as a function of rod conductivity, σ, or frequency, f. Broken lines (- - -) represent the effect of increasing the radius of the encircling coil r_i. Dotted lines ($\cdots$) indicate the effect of changing the sample radius ρ_1

presented in a form in which the data is normalized with respect to the reactance of the isolated coil, X_0. Comments made around (6.2) on the general shape of the normalized impedance-plane plot for a surface coil above a half-space conductor, Fig. 6.3, are applicable here. Figure 6.23 allows us to predict the way in which the coil impedance changes if either the sample diameter varies or a coil with different diameter is used. The outer curved solid line shows the locus of impedance values of a coil when it is tight to the test-piece (when the test-piece fills the coil and $\eta = 1$). The arrow indicates the way in which the impedance changes as either the test-piece conductivity or the frequency of the test are increased. From any fixed point on the outer solid curve, defined by particular values of frequency and conductivity, the dashed lines show how the impedance of the coil changes ($|Z|$ decreases) as the coil diameter increases, and the dotted lines show how $|Z|$ decreases as the diameter of the test-piece decreases.

In Fig. 6.24, an example impedance-plane plot for a coil encircling a long, ferromagnetic, cylindrical rod is shown. As for Fig. 6.23, this impedance-plane diagram is presented in a form in which the data is normalized with respect to the reactance of the isolated coil, X_0. Again, the arrow indicates the way in which the impedance changes as either the test-piece conductivity or the frequency of the test is increased.

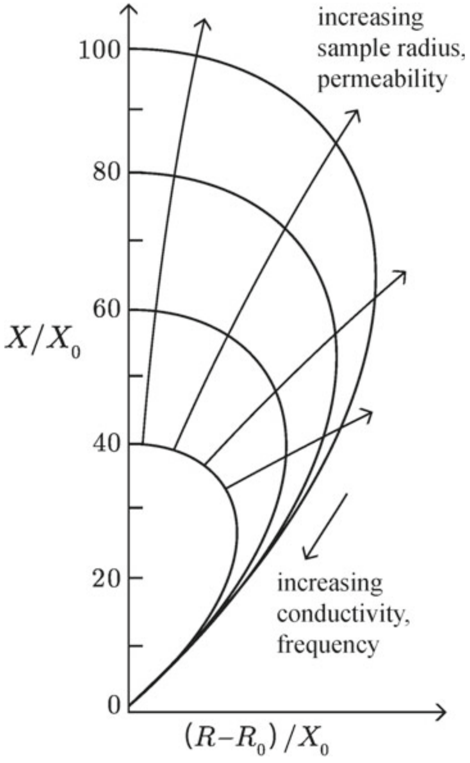

Fig. 6.24 Normalized impedance-plane plot for a coil with inner radius r_i encircling a cylindrical, ferromagnetic test-piece with radius ρ_1. Solid lines (——) represent the complex impedance of the probe as a function of rod conductivity, σ, or frequency of the test, f. Arrows (→) represent the effect of increasing the radius of the test-piece ρ_1, or the test-piece relative permeability [17]

A major difference between these curves and those for the case of non-ferromagnetic rods is that the magnitudes of both the real and imaginary components of the coil impedance, for ferromagnetic rods, are increased in proportion to $\mu_r \gg 1$. Note that the air point, corresponding to the absence of any test-piece, is still found at (0, 1) as in Fig. 6.23 but the scale of the impedance change due to the ferromagnetic test-piece is much larger than for the non-ferromagnetic case for the reasons just mentioned. When the fill factor is reduced, the real and imaginary components of the coil impedance are reduced in direct proportion to the reduction in the fill factor. This means that a change in impedance due to reduction in fill factor cannot be separated from a change due to reduction in test-piece permeability. Fortunately, however, this common direction is usually at a large phase angle compared with changes due to cracks and other longitudinal discontinuities, allowing the latter to be detected. Finally, when the fill factor $\eta = 1$ the intercept of the impedance locus with the vertical axis gives an approximate value for the relative permeability μ_r of the rod.

In a similar manner to the developments presented in Sects. 6.3.3 and 6.3.4, for the circular current filament and the coil above a half-space conductor, electromagnetic analysis of a circular current filament and a coil encircling a solid cylindrical conductor are presented in the following sections. Formulas are developed by which the value of coil impedance can be calculated using relevant input parameters. Impedance-plane diagrams such as that shown in Fig. 6.23 can be plotted by evaluating the formulas obtained.

6.5.1 Circular Current Loop Encircling a Solid Cylindrical Conductor

Governing Equation for E

Consider a filamentary circular current loop, radius a, exterior to a cylindrical conductor with radius ρ_1 and conductivity σ, Fig. 6.25. The conductor in this case is non-ferromagnetic. As in Sect. 6.3.3, the system is axially symmetric so that the current density in the loop is entirely azimuthal, (6.45), immediately implying that the electric field is also purely azimuthal, (6.46). Again, it is assumed that the conductor is linear, isotropic and homogeneous such that constitutive relations (2.25) and (2.33) hold. Formulating the solution in terms of the electric field, (6.48) is obtained as before. Arbitrarily assigning the plane of the current loop to be $z = h$, the following governing equation for the electric field due to a circular current loop coaxial with a circular conductive cylinder is obtained in the quasi-static regime;

$$\left(\frac{\partial^2}{\partial\rho^2} + \frac{1}{\rho}\frac{\partial}{\partial\rho} - \frac{1}{\rho^2} + \frac{\partial^2}{\partial z^2} - k^2\right) E_\phi = j\omega\mu\mathcal{I}\delta(\rho - a)\delta(z - h). \tag{6.98}$$

Solution for E

The solution of (6.98) will be found by the method of separation of variables. Everywhere *off* the current loop, (6.98) may be written

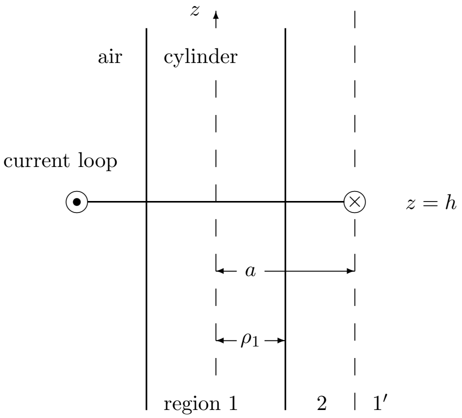

Fig. 6.25 Cross section through the axis of a circular, infinitesimal current loop, coaxial with a solid metal cylinder

$$\left(\frac{\partial^2}{\partial\rho^2}+\frac{1}{\rho}\frac{\partial}{\partial\rho}-\frac{1}{\rho^2}+\frac{\partial^2}{\partial z^2}-k_i^2\right)E_\phi^i=0, \tag{6.99}$$

where $k_i^2 = j\omega\mu_i\sigma_i$. The sub- or superscript i may take values $1, 2$ and $1'$, and refers to regions within the metal cylinder ($\rho < \rho_1$), outside the cylinder but within the current filament ($\rho_1 < \rho < a$), and exterior to the current filament ($\rho \geq a$), respectively, as labeled in Fig. 6.25.

Suppose the solution is of the form $E_\phi^i(\rho, z) = R_i(\rho)Z(z)$. The longitudinal part of the solution, $Z(z)$, does not change from one region to another so needs no subscript. (Note that this case is complementary to the case of the planar conductor, Sect. 6.3.3, in which the subscript attaches to the longitudinal part of the solution.) Substitute this form into (6.99) and divide by $R_i(\rho)Z(z)$ to obtain

$$\frac{1}{R_i(\rho)}\frac{\partial^2 R_i(\rho)}{\partial\rho^2}+\frac{1}{\rho R_i(\rho)}\frac{\partial R_i(\rho)}{\partial\rho}-\frac{1}{\rho^2}+\frac{1}{Z(z)}\frac{\partial^2 Z(z)}{\partial z^2}-k_i^2=0. \tag{6.100}$$

Variables have been separated, i.e., terms in (6.100) depend either on ρ or on z. This means that (6.100) can be separated into two equations by introducing a variable of separation, κ, in the following way:

$$\frac{1}{R_i(\rho)}\frac{\partial^2 R_i(\rho)}{\partial\rho^2}+\frac{1}{\rho R_i(\rho)}\frac{\partial R_i(\rho)}{\partial\rho}-\left(\frac{1}{\rho^2}+k_i^2\right)=\kappa^2 \tag{6.101}$$

$$\frac{1}{Z(z)}\frac{\partial^2 Z(z)}{\partial z^2}=-\kappa^2. \tag{6.102}$$

The general solution for (6.102) is conveniently written

$$Z(z)=A(\kappa)\sin\kappa(z-h)+B(\kappa)\cos\kappa(z-h)=B(\kappa)\cos\kappa(z-h) \tag{6.103}$$

where $A(\kappa)$ and $B(\kappa)$ are functions of the continuous variable κ. I have immediately put $A(\kappa) = 0$ due to the symmetry of the system about the plane of the current filament, $z = h$. The form of $B(\kappa)$ will be determined by other boundary conditions. The differential equation (6.101) governing the radial term has the following general solution,

$$R_i(\rho)=C_i(\kappa)I_1(\gamma_i\rho)+D_i(\kappa)K_1(\gamma_i\rho) \tag{6.104}$$

where $I_1(u)$ and $K_1(u)$ are the modified Bessel functions of the first and second kinds of order 1, respectively (see Sect. 10.4), and $\gamma_i = \sqrt{\kappa^2 + k_i^2}$ where the root with positive real part is taken. Note, the sign of κ^2 has been switched in (6.101) and (6.102), compared with (6.52) and (6.53), to preserve the definition of γ_i. One important consequence of this is that the general solution (6.103) is written in terms of the sine and cosine dependence on the spatial variable z, rather than in terms of an exponential dependence on z as in the equivalent general solution for the current loop above a half-space conductor, (6.56). For similar reasons the general solution (6.104) is written in terms of modified Bessel functions rather than Bessel functions as in (6.54). Since κ is a continuous variable, the electric field is obtained by integrating over the range of κ. Hence, combining (6.103) with (6.104), the general solution of (6.100) may be written

$$E_\phi^i(\rho, z) = R_i(\rho)Z(z) = \int_0^\infty [C_i(\kappa)I_1(\gamma_i\rho) + D_i(\kappa)K_1(\gamma_i\rho)] \cos\kappa(z-h)\,d\kappa, \tag{6.105}$$

where $B(\kappa)$ has been incorporated into $C_i(\kappa)$ and $D_i(\kappa)$. Considering in turn each of the three regions labeled in Fig. 6.25, in region 1—the conductor,

$$E_\phi^1(\rho, z) = \int_0^\infty C_1(\kappa)I_1(\gamma_1\rho)\cos\kappa(z-h)\,d\kappa. \tag{6.106}$$

In region 2, between the current loop and the conductor,

$$E_\phi^2(\rho, z) = \int_0^\infty [C_2(\kappa)I_1(\kappa\rho) + D_2(\kappa)K_1(\kappa\rho)]\cos\kappa(z-h)\,d\kappa, \tag{6.107}$$

and in region 1′, beyond the current loop,

$$E_\phi^{1'}(\rho, z) = \int_0^\infty D_{1'}(\kappa)K_1(\kappa\rho)\cos\kappa(z-h)\,d\kappa. \tag{6.108}$$

The coefficients are now determined by applying interface conditions between regions 1, 2 and 1′ in a process analogous to that resulting in (6.60)–(6.63) in Sect. 6.3.3. In particular,

$$E_\phi^1(\rho_1, z) = E_\phi^2(\rho_1, z), \tag{6.109}$$

$$\left.\frac{\partial}{\partial\rho}E_\phi^1(\rho, z)\right|_{\rho=\rho_1} = \left.\frac{\partial}{\partial\rho}E_\phi^2(\rho, z)\right|_{\rho=\rho_1}, \tag{6.110}$$

$$E_\phi^2(a, z) = E_\phi^{1'}(a, z), \tag{6.111}$$

$$\left.\frac{\partial}{\partial\rho}E_\phi^2(\rho, z)\right|_{\rho=a} = \left.\frac{\partial}{\partial\rho}E_\phi^{1'}(\rho, z)\right|_{\rho=a} + j\omega\mu\mathcal{I}\delta(z-h). \tag{6.112}$$

Finally, the following expressions for E_ϕ^i are obtained:

$$E_\phi^1(\rho, z) = -\frac{j\omega\mu_0\mathcal{I}a}{\pi}\int_0^\infty K_1(\kappa a)I_1(\gamma_1\rho)\frac{1}{\rho_1^2 D}\cos\kappa(z-h)\,d\kappa, \tag{6.113}$$

$$E_\phi^2(\rho, z) = -\frac{j\omega\mu_0\mathcal{I}a}{\pi}\int_0^\infty K_1(\kappa a)\left\{I_1(\kappa\rho) + \left[\frac{I_1(\gamma_1\rho_1)}{\rho_1^2 D} - I_1(\kappa\rho_1)\right]\frac{K_1(\kappa\rho)}{K_1(\kappa\rho_1)}\right\}\cos\kappa(z-h)\,d\kappa, \tag{6.114}$$

$$E_\phi^{1'}(\rho, z) = -\frac{j\omega\mu_0\mathcal{I}a}{\pi}\int_0^\infty K_1(\kappa a)K_1(\kappa\rho)\left\{\frac{1}{K_1(\kappa\rho_1)}\times\right.$$
$$\left.\left[\frac{I_1(\gamma_1\rho_1)}{\rho_1^2 D} - I_1(\kappa\rho_1)\right] + \frac{I_1(\kappa a)}{K_1(\kappa a)}\right\}\cos\kappa(z-h)\,d\kappa, \quad (6.115)$$

in which

$$D = \frac{1}{\rho_1}\left[\kappa I_1(\gamma_1\rho_1)K_0(\kappa\rho_1) + \gamma_1 I_0(\gamma_1\rho_1)K_1(\kappa\rho_1)\right]. \quad (6.116)$$

One method for evaluating the integrals in the above equation is mentioned in this text following (6.66).

Calculation of Z

As developed in Sect. 6.3.3 for a current filament above a half-space conductor, the self-induced voltage in the current filament coaxial with a cylindrical rod can be computed by integrating **E**, (6.114) or (6.115), around the current loop. By analogy with (6.68), and dividing by phasor current $\mathcal{I}$ to give impedance, (4.25), the impedance is then obtained by means of

$$Z^\delta = -\frac{2\pi a}{\mathcal{I}}E_\phi(a, h). \quad (6.117)$$

Inserting $E_\phi(a, h)$, determined from either (6.114) or (6.115) into (6.117) yields the self-induced impedance of the current filament, Z^δ:

$$Z^\delta = 2j\omega\mu_0 a^2\int_0^\infty [K_1(\kappa a)]^2\left\{\frac{1}{K_1(\kappa\rho_1)}\left[\frac{I_1(\gamma_1\rho_1)}{\rho_1^2 D} - I_1(\kappa\rho_1)\right] + \frac{I_1(\kappa a)}{K_1(\kappa a)}\right\}d\kappa. \quad (6.118)$$

We see that Z^δ depends on the frequency of operation ω, the coil cross-sectional area a^2, its position with reference to the sample, ρ_1, and the sample conductivity σ. The above relation has been derived on the assumption of a non-ferromagnetic test-piece, but if the conductor is in fact ferromagnetic then γ_1 should be replaced by $\gamma_1'/\mu_{\mathrm{r1}} = \sqrt{\kappa^2 + j\omega\mu_0\mu_{\mathrm{r1}}\sigma_1}/\mu_{\mathrm{r1}}$, and Z^δ depends also on the relative permeability of the test-piece, μ_{r1}. From relation (6.118) the self-inductance L of the filament can be easily obtained via relation (6.1). Lastly, the impedance of the completely isolated current filament (in the absence of a test-piece), Z_0^δ, can be obtained by letting $\sigma_1 \to 0$ in (6.118), i.e., $\gamma_1 \to \kappa$, to obtain

$$Z_0^\delta = 2j\omega\mu_0 a^2\int_0^\infty K_1(\kappa a)I_1(\kappa a)\,d\kappa. \quad (6.119)$$

Comparing (6.119) with (6.118) allows us to separate out the contribution to Z^δ from the test-piece, as follows.

$$Z^{\delta} = Z_0^{\delta} + 2j\omega\mu_0 a^2 \int_0^{\infty} \frac{[K_1(\kappa a)]^2}{K_1(\kappa\rho_1)} \left[\frac{I_1(\gamma_1\rho_1)}{\rho_1^2 D} - I_1(\kappa\rho_1) \right] d\kappa. \tag{6.120}$$

Lastly, as a point of interest, by comparing result (6.119) with (6.71) it can be deduced that

$$\int_0^{\infty} K_1(x) I_1(x) dx = \frac{\pi}{2} \int_0^{\infty} [J_1(x)]^2 dx.$$

6.5.2 Coil Encircling a Solid Cylindrical Conductor

Following a process of superposition, the results for the current loop encircling a solid cylindrical conductor, obtained in the previous section, can be extended to obtain the impedance of a coil with finite cross section, shown in Fig. 6.22. Much of this development is similar to that given in Sect. 6.3.4, for a surface coil with finite cross section positioned above a half-space conductor.

Electric Field

Assuming as before that the current in each loop has the same phase and amplitude, the electric field due to a coil encircling a solid cylindrical conductor can be written, similarly to (6.75);

$$\mathbf{E}^T(\rho, z) = \int_h^{h+l} \int_{r_\mathrm{i}}^{r_\mathrm{o}} \mathbf{E}(\rho, z | a_\mathrm{s}, h_\mathrm{s}) da_\mathrm{s} dh_\mathrm{s} \tag{6.121}$$

wherein a_s and h_s are continuous variables in the radial and vertical directions within the coil cross section.

Voltage in a Coil Encircling a Cylindrical Rod

The total voltage induced in a coil of n turns is given by (6.81) in which $2\pi a_i$ is the circumferential length and h_i is, in this case, the height of the ith current loop above the plane $z = 0$, Fig. 6.22. $E_\phi(a_i, h_i)$ is the electric field of the ith current loop. Replacing the summation by an integral over the cross section of the coil, an equation similar to (6.83) is obtained wherein the notation of Fig. 6.22 is employed:

$$\mathcal{V} = -\frac{2\pi n}{l(r_\mathrm{o} - r_\mathrm{i})} \int_h^{h+l} \int_{r_\mathrm{i}}^{r_\mathrm{o}} a_\mathrm{s} E_\phi(a_\mathrm{s}, h_\mathrm{s}) da_\mathrm{s} dh_\mathrm{s}. \tag{6.122}$$

Z for a Coil Encircling a Cylindrical Rod

Following a development similar to that for (6.84), the following equation for impedance of a coil encircling a cylindrical rod is obtained:

$$Z = -\frac{2\pi n^2}{l^2(r_\mathrm{o} - r_\mathrm{i})^2} \int_h^{h+l} \int_{r_\mathrm{i}}^{r_\mathrm{o}} a_\mathrm{s} E_\phi(a_\mathrm{s}, h_\mathrm{s}) da_\mathrm{s} dh_\mathrm{s}. \tag{6.123}$$

Now the integrals with respect to a_s and h_s may be evaluated by inserting $E_\phi(a_\mathrm{s}, h_\mathrm{s})$ into (6.123). To do this, the integral over a_s is divided into two, covering coil regions within and beyond a_s. In the region within a_s the expression for $E_\phi^2(\rho, z)$ is inserted whereas in the region beyond a_s the expression for $E_\phi^{1'}(\rho, z)$ is used. Explicitly,

$$Z = -\frac{2\pi n^2}{l^2(r_\mathrm{o} - r_\mathrm{i})^2} \int_h^{h+l} \left[\int_{r_\mathrm{i}}^{a_\mathrm{s}} a_\mathrm{s} E_\phi^2(a_\mathrm{s}, h_\mathrm{s}) da_\mathrm{s} + \int_{a_\mathrm{s}}^{r_\mathrm{o}} a_\mathrm{s} E_\phi^{1'}(a_\mathrm{s}, h_\mathrm{s}) da_\mathrm{s} \right] dh_\mathrm{s}. \tag{6.124}$$

Inserting expressions for $E_\phi^2(\rho, z)$ and $E_\phi^{1'}(\rho, z)$ into (6.124) and changing the order of integration, the following integrals with respect to a_s and h_s emerge:

$$\begin{aligned} Z = \frac{2j\omega\mu_0 n^2}{l^2(r_\mathrm{o} - r_\mathrm{i})^2} \int_0^\infty \int_h^{h+l} \int_{r_\mathrm{i}}^{r_\mathrm{o}} a_\mathrm{s}^2 \{ K_1(\kappa a_\mathrm{s}) I_1(\kappa a_\mathrm{s}) \\ + \frac{[K_1(\kappa a_\mathrm{s})]^2}{K_1(\kappa \rho_1)} \left[\frac{I_1(\gamma_1 \rho_1)}{\rho_1^2 D} - I_1(\kappa \rho_1) \right] \right\} \cos \kappa (h_\mathrm{s} - h)\, da_\mathrm{s} dh_\mathrm{s} d\kappa, \end{aligned} \tag{6.125}$$

assuming that the current in each loop has the same phase and amplitude. Integration with respect to h_s is straightforward and yields the following.

$$\begin{aligned} Z = \frac{2j\omega\mu_0 n^2}{l^2(r_\mathrm{o} - r_\mathrm{i})^2} \int_0^\infty \int_{r_\mathrm{i}}^{r_\mathrm{o}} \frac{a_\mathrm{s}^2}{\kappa} \{ K_1(\kappa a_\mathrm{s}) I_1(\kappa a_\mathrm{s}) \\ + \frac{[K_1(\kappa a_\mathrm{s})]^2}{K_1(\kappa \rho_1)} \left[\frac{I_1(\gamma_1 \rho_1)}{\rho_1^2 D} - I_1(\kappa \rho_1) \right] \right\} \sin \kappa l \, da_\mathrm{s} d\kappa. \end{aligned} \tag{6.126}$$

Recognizing that (6.126) can be written as the sum of the impedance of the isolated coil, Z_0, and a term representing the effect of the conductor, the following is obtained.

$$Z = Z_0 + \frac{2j\omega\mu_0 n^2}{l^2(r_\mathrm{o} - r_\mathrm{i})^2} \int_0^\infty \int_{r_\mathrm{i}}^{r_\mathrm{o}} \frac{a_\mathrm{s}^2}{\kappa} \frac{[K_1(\kappa a_\mathrm{s})]^2}{K_1(\kappa \rho_1)} \left[\frac{I_1(\gamma_1 \rho_1)}{\rho_1^2 D} - I_1(\kappa \rho_1) \right] \sin \kappa l \, da_\mathrm{s} d\kappa, \tag{6.127}$$

where

$$Z_0 = \frac{2j\omega\mu_0 n^2}{l^2(r_\mathrm{o} - r_\mathrm{i})^2} \int_0^\infty \int_{r_\mathrm{i}}^{r_\mathrm{o}} \frac{a_\mathrm{s}^2}{\kappa} K_1(\kappa a_\mathrm{s}) I_1(\kappa a_\mathrm{s}) \sin \kappa l \, da_\mathrm{s} d\kappa. \tag{6.128}$$

Finally, the expression for Z can be simplified by expressing the integral with respect to a_s as follows.

$$\int_{\mathrm{r_i}}^{r_\mathrm{o}} [a_\mathrm{s} K_1(\kappa a_\mathrm{s})]^2 da_\mathrm{s} = \frac{1}{\kappa^4} K^2(\kappa r_\mathrm{i}, \kappa r_\mathrm{o}) \tag{6.129}$$

where

$$K^2(x_1, x_2) = \int_{x_1}^{x_2} [x K_1(x)]^2 dx. \tag{6.130}$$

This integral must be evaluated numerically but allows us to write the following expression for the impedance of a coil of finite cross section coaxial with and encircling a solid cylindrical conductor.

$$Z = Z_0 + \frac{2j\omega\mu_0 n^2}{l^2(r_\mathrm{o} - r_\mathrm{i})^2} \int_0^\infty \frac{K^2(\kappa r_\mathrm{i}, \kappa r_\mathrm{o})}{\kappa^5} \frac{1}{K_1(\kappa\rho_1)} \left[\frac{I_1(\gamma_1\rho_1)}{\rho_1^2 D} - I_1(\kappa\rho_1) \right] \sin\kappa l \, d\kappa. \tag{6.131}$$

As already noted in Sect. 6.3.4, Z depends on the probe's frequency of operation, ω, the coil dimensions, r_i, r_o and l, the square of the number of turns, n^2, the coil position with reference to the sample—here specified by r_i and r_o, and the sample conductivity, σ. Evaluation of (6.131) for particular coil and sample parameters allows impedance-plane diagrams such as that shown in Fig. 6.23 to be developed. The frequency-dependent curves shown in Fig. 6.23 are obtained by varying ω and the fill factor-dependent curves by varying r_i or ρ_1 in (6.131).

6.5.3 Sources of Uncertainty

In a system of cylindrical symmetry, such as a coil encircling a cylindrical conductor, two sources of geometrical uncertainty exist; coil tilt and wobble. Tilt occurs when the coil axis tilts through a finite angle with respect to the axis of the test-piece and has been analyzed in detail by Theodoulidis and Skarlatos [18]. Wobble occurs when the coil axis is laterally displaced from the axis of the test-piece and has been analyzed by Theodoulidis [19] in the case of a bobbin coil (Sect. 6.6.1).

6.6 Bobbin Coil

Bobbin coils offer effective coupling with the interior of tube-like specimens. A bobbin coil is oriented with its axis parallel to the axis of the cylindrical cavity (e.g., a tube interior or a bore hole) in a test-piece and is designed to be threaded through it. Bobbin probes are very commonly used in differential mode for optimum defect detection, as discussed in Sect. 8.3. One application in which bobbin probes are commonly used is in the inspection of nuclear power plant steam generator tubes. Threading a bobbin probe through a tube offers shorter inspection time than using a rotating surface probe, which is common in borehole inspection, Fig. 6.5. A schematic diagram of a bobbin coil coaxial with a borehole is shown in Fig. 6.26.

In a definition analogous to that given in (6.97) for the encircling coil geometry, the fill factor of the bobbin coil, η_b, is defined as follows, with reference to the notation of Fig. 6.26.

$$\eta_b = \left(\frac{r_\mathrm{o}}{\rho_1} \right)^2. \tag{6.132}$$

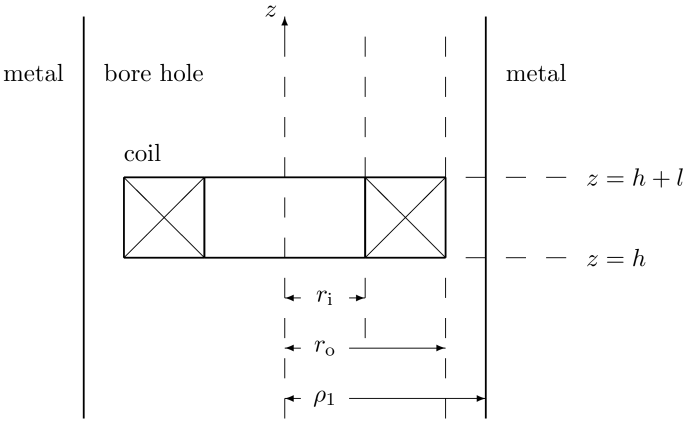

Fig. 6.26 Cross section through the axis of a circular bobbin coil coaxial with the bore of the test-piece

Since the bobbin coil is primarily applied in tube inspection, rather than in borehole inspection, a detailed discussion of the impedance calculation for the bobbin coil is deferred to Sect. 7.2.6 where test-pieces with more than one interface (in this case the interior and exterior surfaces of the tube) are considered. Example impedance-plane plots for a bobbin coil internal to a tube are given in Fig. 7.6 for a tube with fixed ratio of wall thickness to outer diameter, and in Fig. 7.7 for a bobbin coil internal to a tube with varying ratio of wall thickness to outer diameter. The curves plotted in those figures are also applicable to coils encircling tube-like test samples.

6.6.1 Sources of Uncertainty

For the configuration of a bobbin probe inserted into a tube or a borehole, a source of noise in the measurement may be probe "wobble". This is a type of geometrical noise, caused by the movement of the probe. Ideally, the coil is coaxial with the tube, but wobble of the probe may cause the coil axis to shift a finite distance from the tube axis, as shown in Fig. 6.27. Some of the effects of probe wobble on the impedance-plane plot are shown in Fig. 6.28, at three distinct frequencies. For comparison, the effects of 10% inner diameter (ID) or outer diameter (OD) wall thinning of the tubular test-piece are also shown. Noting that the "f_{90}" frequency is defined as the frequency that provides approximately 90° phase separation between shallow ID and OD defects, the three frequencies for which comparisons are plotted in Fig. 6.28 are $f_{90}/2$, f_{90} and $2f_{90}$. The frequency f_{90} and may be computed using the empirical expression

$$f_{90} = \frac{516\sigma}{T^2} \tag{6.133}$$

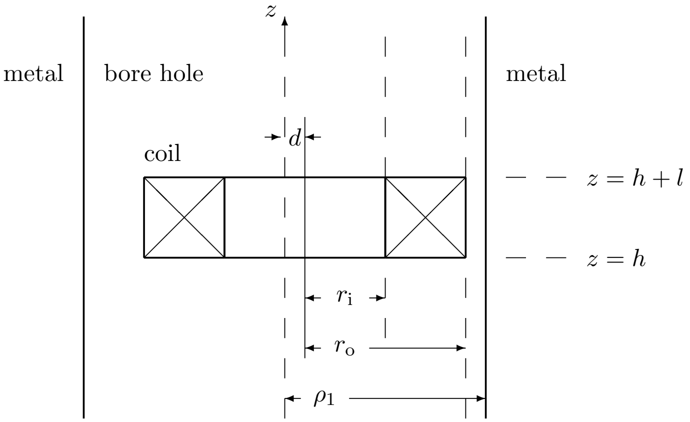

Fig. 6.27 Cross section through the axis of a circular bobbin coil that is offset by distance d from the axis of the test-piece bore

where σ is in %IACS, T is the tube wall thickness in mm and the result is in kHz.

Also shown in Fig. 6.28 is the sum of the ID and OD signals with the signal due to wobble at maximum axis offset. It can be seen that the phase angle between ID and OD thinning increases as frequency increases and that the amplitude of the OD signal decreases with increasing frequency due to the skin effect. For OD wall thinning the deleterious effect of wobble on the flaw signal can be seen clearly at frequency $2f_{90}$, for which the signal due to probe wobble overwhelms that due to the flaw.

6.7 Summary

This chapter has dealt with classical solutions to canonical problems in the theory of eddy-current nondestructive evaluation and has examined sources of uncertainty in EC NDE. The impedance of an EC coil was expressed for test-pieces with half-space (Cartesian) and rod or borehole (cylindrical) geometries. Upon this foundation, the effect of introducing additional boundaries to the test-piece is considered in Chap. 7. Following this approach, the EC inspection of plates, tubes, surface coatings or material under surface coatings can be modeled. A method for modeling the effect of test-piece edges on the EC signal is also introduced. The ability to model the effect of such geometrical features on the EC signal provides a pathway for separating such effects from a flaw signal.

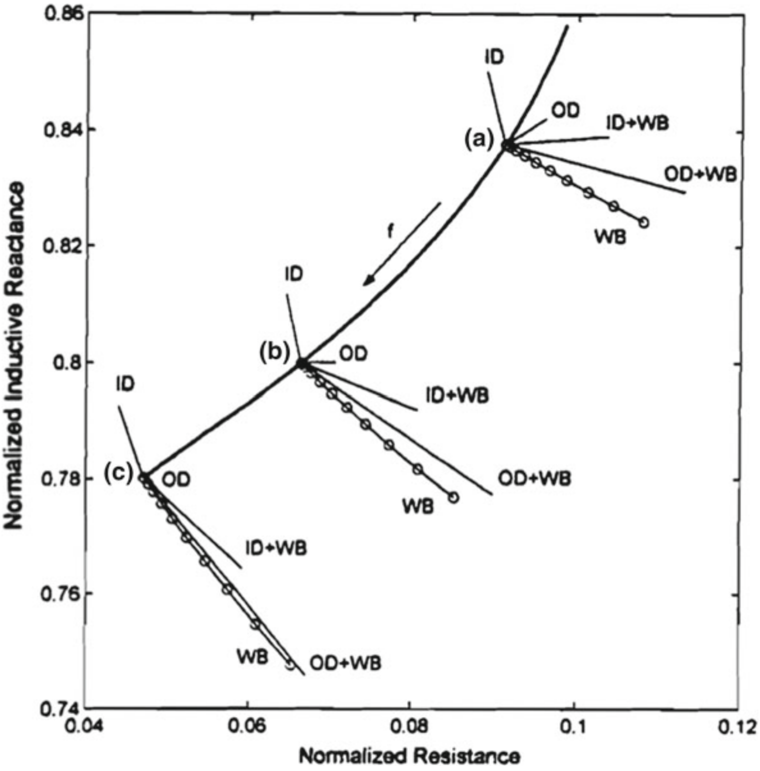

Fig. 6.28 ΔZ due to 10% inner diameter (ID) and 10% outer diameter (OD) uniform thinning, wobble (WB), and their superposition for maximum offset, at three frequencies: **a** $f_{90}/2$, f_{90} and $2f_{90}$ [19]. With kind permission from Springer Science and Business Media: *Res. Nondestruct. Eval.*, vol. 4, 2002, p. 120, Analytical modeling of wobble in eddy-current tube testing with bobbin coils, T. P. Theodoulidis, Fig. 2. Original caption: Impedance changes due to 10%ID and 10%OD uniform thinning, wobble, and their superposition for maximum offset, at three frequencies: **(a)** $f_{90}/2$; **(b)** f_{90}; **(c)** $2f_{90}$

6.8 Exercises

1. Show that the magnetic field in a region of space that contains a phasor current source $\mathbf{J}_s$ (varying as the real part of $e^{j\omega t}$) and a conductor carrying induced eddy-current density $\mathbf{J}_{ec} = \sigma\mathbf{E}$, where σ is the conductivity of the metal, obeys the following governing equation

$$\left(\nabla^2 - j\omega\mu\sigma\right)\mathbf{H} = -\nabla \times \mathbf{J}_s.$$

Hint: Follow a method similar to that used to determine (6.10), but now begin by taking the curl of (6.6) rather than of (6.5).

2. Apply the Biot–Savart Law to obtain the following expression for B_z along the axis of a circular current loop with radius a carrying current I, whose axis coincides with that of a cylindrical coordinate system.

$$B_z = \frac{\mu_0 I}{2} \frac{a^2}{(a^2 + z^2)^{3/2}} \tag{6.134}$$

3. A long solenoid consists of n similar loops of wire, per unit length, each with radius a. The axis of the solenoid coincides with the z-axis of a cylindrical co-ordinate system. The magnetic field inside the solenoid is uniform over its cross-sectional area and is given by

$$H_z = nI, \tag{6.135}$$

where I is the magnitude of the current flowing in the wire. Show that the inductance per unit length of a solenoid filled with a ferromagnet whose permeability is μ is given by

$$L = \mu\pi(na)^2 \tag{6.136}$$

and that the normalized impedance of the coil per unit length is given by

$$\frac{Z}{X_0} = \frac{R_0}{\omega\mu_0\pi(na)^2} + j\mu_\mathrm{r} \tag{6.137}$$

where R_0 is the DC resistance of the coil. Plot Z/X_0 on an impedance-plane plot.
4. Take the curl of the vector potential given in (6.36) to obtain the expressions for B_r and B_z given in (6.42) and (6.43).[1] Show that, on the axis, the result for B_z of (6.43) reduces to that obtained by the Biot–Savart Law, Exercise 2.
5. We know from interface conditions (Sect. 5.6) that the tangential component of the electric field must be continuous at a boundary. Show that $E_\phi(r, z)$ for the filamentary coil above a half-space conductor in (6.64)–(6.66) is continuous at $z = h$ and $z = 0$.
6. Suppose the conductive half-space interrogated by a filamentary current loop, as in Sect. 6.3.3, now has a surface layer with depth d and conductivity σ_3 (region 3, $-d \le z \le 0$). The substrate conductivity is now σ_4 (region 4, $z \le -d$). Hence $\gamma_i = \sqrt{\kappa^2 + j\omega\mu_0\sigma_i}$ with $i = 3, 4$. In this case,

---

[1] Hint: In definitions (6.37) and (6.38), k is known as the *modulus* of these integrals. The following functional relations between elliptic integrals are given in Eqs. 8.123.2 and 8.123.4 of [20].

$$\frac{dK(k)}{dk} = \frac{E(k)}{kk'^2} - \frac{K(k)}{k}$$
$$\frac{dE(k)}{dk} = \frac{E(k) - K(k)}{k}$$

In these relations, k' is known as the complementary modulus and $k' = \sqrt{1 - k^2}$; $k^2 < 1$.

$$E_\phi^1(\rho, z) = -\frac{1}{2} j\omega\mu_0 I a \int_0^\infty J_1(\kappa a) J_1(\kappa r) e^{-\kappa(h+z)} \times \left\{ e^{2\kappa h} + \frac{(\kappa+\gamma_3)(\gamma_3-\gamma_4)+(\kappa-\gamma_3)(\gamma_3+\gamma_4)e^{2\gamma_3 d}}{(\kappa-\gamma_3)(\gamma_3-\gamma_4)+(\kappa+\gamma_3)(\gamma_3+\gamma_4)e^{2\gamma_3 d}} \right\} d\kappa. \tag{6.138}$$

Identify two limits in which this result should reduce to the result for the half-space conductor and show that (6.138) does indeed reduce to (6.64) in these limits.

7. Show how the factor μ_r appears in relation (6.70), in the case of a ferromagnetic test-piece.

References

1. Hugo, G.R.: Impedance changes in a coil due to a nearby small conducting sphere. J. Phys. D: Appl. Phys. **21**, 33–38 (1988)
2. Kolyshkin, A.A., Vaillancourt, R.: Impedance of a single-turn coil due to a double-layered sphere with varying properties. IEEE T. Magn. **31**, 2274–2280 (1995)
3. Theodoulidis, T.P., Kriezis, E.E.: Coil impedance due to a sphere of arbitrary radial conductivity and permeability profiles. IEEE T. Magn. **38**, 1452–1460 (2002)
4. Moore, P.O. (ed.), Udpa, S.S. (tech. ed.): Nondestructive Testing Handbook: Electromagnetic Testing, vol. 5, 3rd edn. American Society for Nondestructive Testing, Columbus (2004)
5. Badics, Z., Matsumoto, Y., Aoki, K., Nakayasu, F., Kurokawa, A.: Finite element models of stress corrosion cracks (SCC) in 3-D eddy current NDE problems. In: Collins, R., Dover, W.D., Bowler, J.R., Miya, K. (eds.) Nondestructive Testing of Materials. Studies in Applied Electromagnetics and Mechanics, vol. 8, pp. 21–30. IOS Press, Amsterdam (1995)
6. Grimberg, R., Savin, A., Radu, E., Mihalache, O.: Nondestructive evaluation of the severity of discontinuities in flat conductive materials by an eddy-current transducer with orthogonal coils. IEEE T. Magn. **36**, 299–307 (2000)
7. Van Bladel, J.: Electromagnetic Fields. Hemisphere Publishing Corporation, Washington (1985)
8. Dodd, C.V., Deeds, W.E.: Analytical solutions to eddy-current probe-coil problems. J. Appl. Phys. **39**, 2829–2838 (1968)
9. Dodd, C.V., Cheng, C.C., Deeds, W.E.: Induction coils coaxial with an arbitrary number of cylindrical conductors. J. Appl. Phys. **45**, 638–647 (1974)
10. Theodoulidis, T.P., Kriezis, E.E.: Eddy Current Canonical Problems (with Applications to Nondestructive Evaluation). Tech Science Press, Forsyth (2006)
11. Ferroxcube product web pages
12. Theodoulidis, T.P.: Model of ferrite-cored probes for eddy current nondestructive evaluation. J. Appl. Phys. **93**, 3071–3078 (2003)
13. Lu, Y., Bowler, J.R., Theodoulidis, T.P.: An analytical model of a ferrite-cored inductor used as an eddy current probe. J. Appl. Phys. **111**, 103907 (2012)
14. Harrison, D.J., Jones, L.D., Burke, S.K.: Benchmark problems for defect size and shape determination in eddy-current nondestructive evaluation. J. Nondestruct. Eval. **15**, 21–34 (1996)
15. Bowler, N., Huang, Y.: Electrical conductivity measurement of metal plates using broadband eddy-current and four-point methods. Meas. Sci. Technol. **16**, 2193–2200 (2005)
16. Theodoulidis, T.P.: Analytical model for tilted coils in eddy current nondestructive evaluation. IEEE T. Magn. **41**, 2447–2454 (2005)

17. McMaster, R.C., McIntire, P. (eds.), Mester, L.M. (tech. ed.): Nondestructive Testing Handbook: Electromagnetic Testing, vol. 4, 2nd edn. American Society for Nondestructive Testing, Columbus (1986)
18. Theodoulidis, T.P., Skarlatos, A.: Eddy current interaction of an arbitrarily positioned probe coil with a conductive cylinder. IEEE T. Magn. **48**, 2392–2394 (2012)
19. Theodoulidis, T.P.: Analytical modeling of wobble in eddy current tube testing with bobbin coils. Res. Nondestruct. Eval. **14**, 111–126 (2002)
20. Gradshteyn, I.S., Ryzhik, I.M. (eds.): Table of Integrals, Series and Products, 6th edn. Academic, London (2000)

Chapter 7
Layered and Truncated Conductors

Abstract The subject of this chapter is the eddy-current inspection of test-pieces that are coated, layered, or truncated. It is presumed that various surfaces of the test-piece significantly perturb the induced eddy currents and that the effect of those surfaces must be taken into account to properly interpret the observed eddy-current probe coil impedance. The discussion includes a description of impedance-plane diagrams for surface coils, encircling coils, and bobbin coils in relation to coated, layered, or truncated test-pieces with planar or cylindrical surfaces. The effect of the test-piece edge on the observed probe coil impedance is also described.

7.1 Introduction

In this chapter, the effect on the impedance of the eddy-current coil of a test-piece with multiple physical boundaries or interfaces is discussed. In Chap. 6, the discussion was limited to fundamental cases described by one physical boundary—either flat or cylindrical—at the surface of a homogeneous conductor. Generally, coil impedance can be expressed for an arbitrary number of layers in the sample, each with its particular material properties σ_i and μ_i. Such expressions of impedance are presented here for a multilayered test-piece, whose interfaces are all (i) parallel planes and (ii) concentric cylinders. Impedance expressions are also presented for cases that are important in practical terms, i.e., for simplified geometries in which the test-piece has two layers. One of these cases is that of the coated conductor; a half-space or cylinder with a coating which may or may not be conductive, and the other case is that of the plate or tube; a conductor of finite thickness. It is worth acknowledging that no conductor is truly a half-space, i.e., infinitely thick, but in the context of EC NDE a half-space is a conductor with a planar inspection surface, whose other surfaces (sides and back-plane) are sufficiently remote that they do not disturb the eddy currents significantly. As in Chap. 6, the spherical test-piece geometry is not discussed explicitly here. Readers interested in a treatment of eddy-current probe response to layered spheres are directed to [1, 2].

In Sect. 7.2, expressions are provided for the impedance of coils that exhibit cylindrical symmetry in relation to these test-pieces. In Sect. 7.3, a description is

N. Bowler, *Eddy-Current Nondestructive Evaluation*,
Springer Series in Measurement Science and Technology,
https://doi.org/10.1007/978-1-4939-9629-2_7

provided of methods that can be applied to analyze inspection scenarios in which the conductors are truncated in some manner; a plate edge or the end of a tube, for example. Impedance-plane plots are presented in several cases.

For geometries yet more complex than these, such as a coil interacting with a rivet in a layered aircraft skin, full numerical modeling in the form of finite- or boundary-element approaches are applicable. Numerous approaches to computational electromagnetics in the context of EC NDE are discussed by Sabbagh et al. [3].

7.2 Layered Conductors

The important work of Dodd and Deeds published in 1968 [4] involves analyses of the impedance of a surface coil positioned above a half-space conductor, discussed in Sect. 6.3.4, and of a coil encircling a rod conductor, discussed in Sect. 6.5.2. In both configurations, the treatment presented in [4] accommodates a single surface layer of a different material coating the test-piece. In fact, since the material properties assigned to the surface layer or substrate are entirely arbitrary in the analysis, the impedance of a surface coil positioned above a plate or of a coil encircling a tube conductor can also be computed by assigning the conductivity of the substrate to be zero. Extending this work to test-pieces with an arbitrary number of layers, co-author Cheng joined Dodd and Deeds and published analyses in 1971 and 1974 concerning the impedance of an eddy current surface coil above a planar conductor composed of an arbitrary number of layers [5] and of an eddy current coil coaxial with an arbitrary number of cylindrical conductors [6]. The former, [5], is useful not only for studying the impedance of a surface coil in the vicinity of a layered planar conductor, discussed in Sect. 7.2.1, but also of a plate sufficiently thin for its back surface to influence the value of measured coil impedance, which itself might be composed of multiple layers. The latter, [6], is applicable to a coil encircling a solid circular cylindrical conductor, discussed in Sect. 6.5.2, and to a coil internal to and coaxial with a borehole in a conductor. The fact that an arbitrary number of cylindrical conductors is treated, Sect. 7.2.4, allows the analysis to be applied also to a coil external to a layered cylindrical rod, Sect. 7.2.5, to a coil coaxial with a tube (either internal or external), Sect. 7.2.6, and to a coil internal to a layered borehole, not discussed explicitly in this text.

7.2.1 Planar Conductor with an Arbitrary Number of Layers

The impedance of a surface coil positioned above a planar conductor with an arbitrary number of layers, shown schematically in Fig. 7.1, is given by

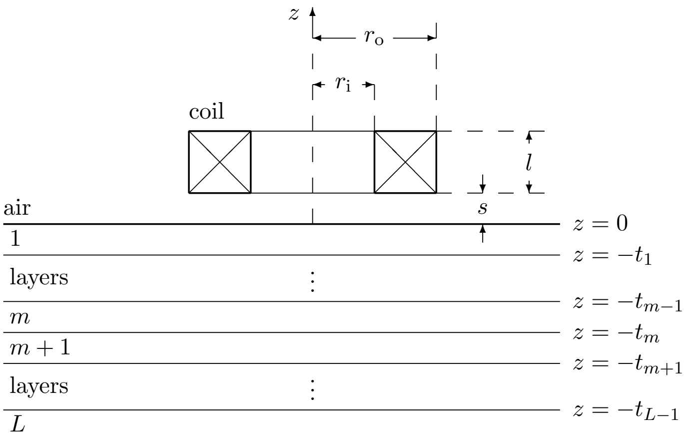

Fig. 7.1 Cross-section through the axis of a circular, air-cored, eddy-current surface coil, positioned above a layered half-space

$$
\begin{aligned}
Z = \frac{j\omega\mu_0\pi n^2}{l^2(r_o - r_i)^2} \int_0^\infty \frac{J^2(\kappa r_i, \kappa r_o)}{\kappa^6} \Big\{ 2\kappa l + 2e^{-\kappa l} - 2 + \left[e^{-\kappa s} - e^{-\kappa(s+l)}\right]^2 \\
\times \left[\frac{(\kappa\mu_{r(m+1)} - \gamma_1)V_{11}(1) + (\kappa\mu_{r(m+1)} + \gamma_1)V_{21}(1)}{(\kappa\mu_{r(m+1)} + \gamma_1)V_{11}(1) + (\kappa\mu_{r(m+1)} - \gamma_1)V_{21}(1)} \right] \Big\} d\kappa \quad (7.1)
\end{aligned}
$$

where $\gamma_i = \sqrt{\kappa^2 + j\omega\mu_0\mu_{ri}\sigma_i}$ and μ_{ri} is the relative permeability of the ith layer. The first three terms in curly brackets $2\kappa l + 2e^{-\kappa l} - 2$, in (7.1) give the impedance of the isolated coil (6.88). The remainder of the expression represents the additional effect of the conductor on the coil impedance. In (7.1), the function $J(\kappa r_i, \kappa r_o)$ defined in (6.78) is related to the coil dimensions. The matrix elements $V_{kl}(k, l = 1, 2)$ have argument m, where m is an integer denoting the position of the layer relative to the coil. Then,

$$
\overline{V}(m) = \overline{T}(m, m+1)\overline{T}(m+1, m+2)\ldots\overline{T}(L-2, L-1)\overline{T}(L-1, L) \quad (7.2)
$$

where the $\overline{T}(m, m+1)$ are 2 × 2 transformation matrices

$$
\overline{T}(m, m+1) = \begin{bmatrix} T_{11}(m, m+1) & T_{12}(m, m+1) \\ T_{21}(m, m+1) & T_{22}(m, m+1) \end{bmatrix} \quad (7.3)
$$

whose elements are

$$
T_{11}(m, m+1) = \frac{1}{2} e^{(-\gamma_{m+1}+\gamma_m)t_m} \left[1 + \frac{\mu_{rm}}{\mu_{r(m+1)}} \frac{\gamma_{m+1}}{\gamma_m} \right]
$$

$$
T_{12}(m, m+1) = \frac{1}{2} e^{(\gamma_{m+1}+\gamma_m)t_m} \left[1 - \frac{\mu_{rm}}{\mu_{r(m+1)}} \frac{\gamma_{m+1}}{\gamma_m} \right]
$$

$$T_{21}(m, m+1) = \frac{1}{2} e^{(-\gamma_{m+1}-\gamma_m)t_m} \left[1 - \frac{\mu_{rm}}{\mu_{r(m+1)}} \frac{\gamma_{m+1}}{\gamma_m} \right]$$

$$T_{22}(m, m+1) = \frac{1}{2} e^{(\gamma_{m+1}-\gamma_m)t_m} \left[1 + \frac{\mu_{rm}}{\mu_{r(m+1)}} \frac{\gamma_{m+1}}{\gamma_m} \right]. \tag{7.4}$$

7.2.2 *Coated Half-Space Conductor*

The case of the half-space conductor with a surface coating of another material, or with a surface that has been modified by a particular treatment process (e.g., surface hardening), is commonly encountered in practice. Such a test-piece can often be considered as having a step-function change in material properties at the interface between the two media. The impedance change of an air-cored surface coil positioned above a coated half-space can be deduced from (7.1) by putting $L = 2$:

$$Z = \frac{2j\omega\mu_0\pi n^2}{l^2(r_o - r_i)^2} \int_0^\infty \frac{J^2(\kappa r_i, \kappa r_o)}{\kappa^6} \Big\{ \kappa l + e^{-\kappa l} - 1 + \left[e^{-\kappa s} - e^{-\kappa(s+l)} \right]^2 \times \left[\frac{(\gamma_1\mu_{r2} + \gamma_2\mu_{r1})(\kappa\mu_{r1} - \gamma_1) + e^{-2\gamma_1 t_1}(\gamma_1\mu_{r2} - \gamma_2\mu_{r1})(\kappa\mu_{r1} + \gamma_1)}{(\gamma_1\mu_{r2} + \gamma_2\mu_{r1})(\kappa\mu_{r1} + \gamma_1) + e^{-2\gamma_1 t_1}(\gamma_1\mu_{r2} - \gamma_2\mu_{r1})(\kappa\mu_{r1} - \gamma_1)} \right] \Big\} d\kappa \tag{7.5}$$

The normalized impedance plane diagram Fig. 7.2 illustrates how the impedance of an air-cored coil changes as a function of the thickness of a conductive coating on a half-space substrate of different conductivity.

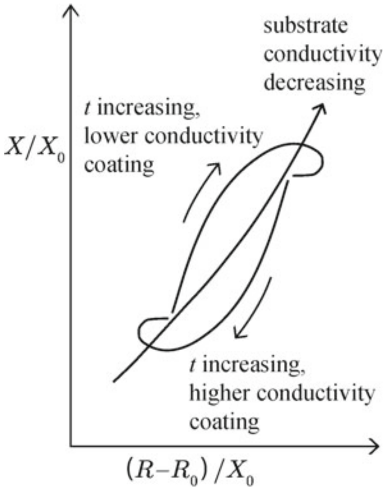

Fig. 7.2 Normalized impedance plane diagram for an air-cored surface coil positioned above a coated half-space. The normalized impedance depends upon the coating thickness, its conductivity, and the conductivity of the half-space substrate. Both the substrate and coating are non-ferromagnetic in this example

7.2.3 Plate Conductor

The impedance of an air-cored surface coil positioned above a layered plate can be deduced from (7.1) by putting $\sigma_L = 0$ and $\mu_{rL} = 1$. With these parameters, the second-line term in (7.1) in square brackets becomes simply $[V_{21}(1)/V_{11}(1)]$.

The impedance of a coil in the presence of a homogeneous plate is a special case that combines the conditions $L = 2$, $\sigma_L = \sigma_2 = 0$ and $\mu_{rL} = \mu_{r2} = 1$. Imposing these values in (7.1) or (7.5) gives

$$Z = \frac{2j\omega\mu_0\pi n^2}{l^2(r_\mathrm{o}-r_\mathrm{i})^2}\int_0^\infty \frac{J^2(\kappa r_\mathrm{o},\kappa r_\mathrm{i})}{\kappa^6}\left\{\kappa l + e^{-\kappa l} - 1 + \left[e^{-\kappa s} - e^{-\kappa(s+l)}\right]^2 \times \right.$$
$$\left.\left[\frac{(\gamma_1+\kappa\mu_{r1})(\kappa\mu_{r1}-\gamma_1) + e^{-2\gamma_1 t_1}(\gamma_1-\kappa\mu_{r1})(\kappa\mu_{r1}+\gamma_1)}{(\gamma_1+\kappa\mu_{r1})(\kappa\mu_{r1}+\gamma_1) + e^{-2\gamma_1 t_1}(\gamma_1-\kappa\mu_{r1})(\kappa\mu_{r1}-\gamma_1)}\right]\right\} d\kappa. \quad (7.6)$$

An impedance plane plot showing the effect of changing the thickness of various metal plates on the impedance of a surface coil is given in Fig. 7.3. It is noticeable that the resistance of the coil passes through a maximum value as the thickness of the test-piece increases, whereas the coil reactance passes through a minimum, before the coil impedance converges to a constant complex value equal to its impedance in the presence of a half-space conductor. Convergence occurs as the conductor becomes sufficiently thick that its back wall no longer disturbs the eddy-current distribution significantly. The way in which increasing conductivity or lift-off affects the impedance is marked in Fig. 7.3 and has already been discussed in the context of Fig. 6.2.

7.2.4 Cylindrical Conductor with an Arbitrary Number of Layers

The impedance of a coil coaxial with an arbitrary number of conductive layers that may be located exterior and/or interior to it, shown schematically in Fig. 7.4, is given by

$$Z = Z_0 + \frac{2j\omega\mu_0 n^2}{l^2(r_\mathrm{o}-r_\mathrm{i})^2}\int_0^\infty \frac{2(1-\cos\kappa l)}{\kappa^6} \times$$
$$\left[\frac{U_{12}V_{11}I^2(\kappa r_\mathrm{i},\kappa r_\mathrm{o}) + U_{22}V_{21}K^2(\kappa r_\mathrm{i},\kappa r_\mathrm{o}) + 2U_{12}V_{21}I(\kappa r_\mathrm{i},\kappa r_\mathrm{o})K(\kappa r_\mathrm{i},\kappa r_\mathrm{o})}{U_{22}V_{11} - U_{12}V_{21}}\right] d\kappa \quad (7.7)$$

where Z_0 represents the impedance of the isolated coil, (6.88), and the second term represents the effect of the conductor on the coil impedance. The function $K^2(x_1, x_2)$ is defined in (6.130) and $I^2(x_1, x_2)$ can be obtained from it by substituting I for K.

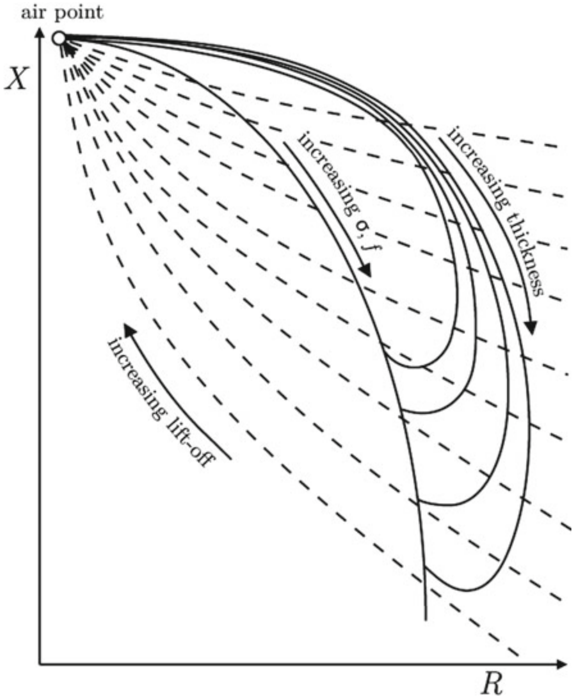

Fig. 7.3 Z for several different non-ferromagnetic metals as a function of plate thickness [7]

The matrix elements V_{ij} and U_{ij} have arguments m and m', respectively, where m and m' are integers denoting the layers adjacent to the coil, on the interior and exterior, respectively. Then,

$$\overline{V}(m) = \overline{T}(m, m-1)\overline{T}(m-1, m-2)\ldots\overline{T}(3, 2)\overline{T}(2, 1) \tag{7.8}$$

$$\overline{U}(m') = \overline{T}(m', m'-1)\overline{T}(m'-1, m'-2)\ldots\overline{T}(3', 2')\overline{T}(2', 1'), \tag{7.9}$$

where the $\overline{T}(i, j)$ are 2 × 2 transformation matrices

$$\overline{T}(m+1, m) = \begin{bmatrix} T_{11}(m+1, m) & T_{12}(m+1, m) \\ T_{21}(m+1, m) & T_{22}(m+1, m) \end{bmatrix}, \tag{7.10}$$

whose elements are

$$\begin{aligned} T_{11}(m+1, m) &= \gamma_{m+1}\rho_m[K_0(\gamma_{m+1}\rho_m)I_1(\gamma_m\rho_m) \\ &\qquad + (\gamma_m/\gamma_{m+1})I_0(\gamma_m\rho_m)K_1(\gamma_{m+1}\rho_m)] \\ T_{12}(m+1, m) &= \gamma_{m+1}\rho_m[K_0(\gamma_{m+1}\rho_m)K_1(\gamma_m\rho_m) \\ &\qquad + (\gamma_m/\gamma_{m+1})K_0(\gamma_m\rho_m)K_1(\gamma_{m+1}\rho_m)] \end{aligned}$$

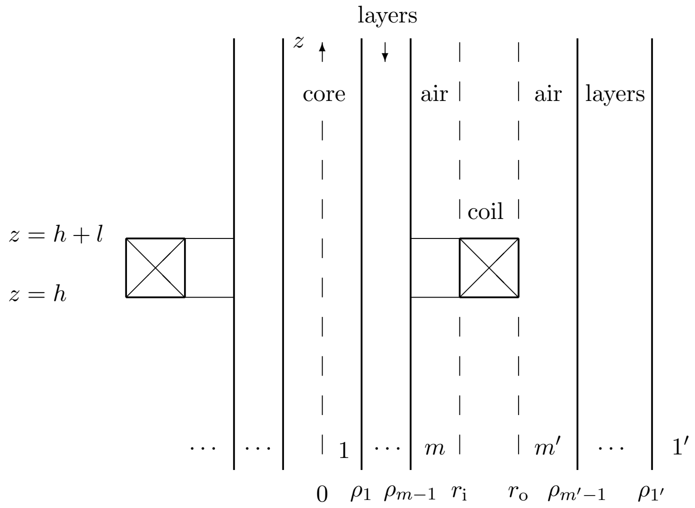

Fig. 7.4 Cross-section through the axis of a circular coil with finite cross-section, coaxial with a cylindrical conductor with an arbitrary number of layers, that may be interior (m layers) and/or exterior (m' layers) to the coil. Note that the system is circularly symmetric about the z-axis although the m' exterior layers are shown only on the right in this diagram, for clarity. $\cdots$ indicate multiple layers. Further, $r_\mathrm{i} \equiv \rho_m$ and $r_\mathrm{o} \equiv \rho_{m'}$

$$\begin{aligned}
T_{21}(m+1,m) &= \gamma_{m+1}\rho_m[I_0(\gamma_{m+1}\rho_m)I_1(\gamma_m\rho_m) \\
&\qquad +(\gamma_m/\gamma_{m+1})I_0(\gamma_m\rho_m)I_1(\gamma_{m+1}\rho_m)] \\
T_{22}(m+1,m) &= \gamma_{m+1}\rho_m[I_0(\gamma_{m+1}\rho_m)K_1(\gamma_m\rho_m) \\
&\qquad +(\gamma_m/\gamma_{m+1})K_0(\gamma_m\rho_m)I_1(\gamma_{m+1}\rho_m)]. \qquad (7.11)
\end{aligned}$$

Note that $\overline{V}(2) = \overline{T}(2, 1)$ so that $V_{11}(2)$ is simply $T_{11}(2, 1)$ and $V_{21}(2)$ is $T_{21}(2, 1)$, etc.

7.2.5 Coated Cylindrical Conductor

The case of the coated cylindrical conductor is useful for analyzing several configurations of practical importance such as case-hardened steel shafts, for which the surface-hardened layer has a different conductivity and permeability than the unhardened core, and metal coatings applied to rods of other metal types, for various purposes. Note that a *non*conductive (and non-ferromagnetic) coating on a cylindrical metal test-piece behaves, from the point of view of eddy-current inspection, merely as nonresponsive filler between the coil and the metal. Assuming that the outer diameter of the test-piece can be measured, the thickness of the nonconductive coating can be determined by measuring the impedance of an encircling coil and establishing the fill-factor (and therefore radius) of the conductive core within the coil, from an impedance-plane plot such as that shown in Fig. 6.23.

For a coil encircling a coated cylinder such as that shown schematically in Fig. 7.5, the impedance is given by setting $m = 3$ and $m' = 1$ in (7.7). Noting that the following hold, in the special case of no conductive layers exterior to the coil,

$$\overline{U} = 1, \qquad \text{i.e.} \qquad U_{12} = 0 \ \text{ and } \ U_{22} = 1, \tag{7.12}$$

then

$$Z = Z_0 + \frac{2j\omega\mu_0 n^2}{l^2(r_\mathrm{o} - r_\mathrm{i})^2} \int_0^\infty \frac{2(1-\cos\kappa l)}{\kappa^6} \frac{V_{21}(3)}{V_{11}(3)} K^2(\kappa r_\mathrm{i}, \kappa r_\mathrm{o}) d\kappa \tag{7.13}$$

in which, explicitly,

$$\begin{aligned} V_{11}(3) &= T_{11}(3,2)T_{11}(2,1) + T_{12}(3,2)T_{21}(2,1) \\ V_{12}(3) &= T_{21}(3,2)T_{11}(2,1) + T_{22}(3,2)T_{21}(2,1) \end{aligned}$$

and expressions for the $T_{ij}(m+1, m)$ are given in (7.11). Note, some simplification occurs for the case shown in Fig. 7.5 due to the fact that $\gamma_3 = \kappa$.

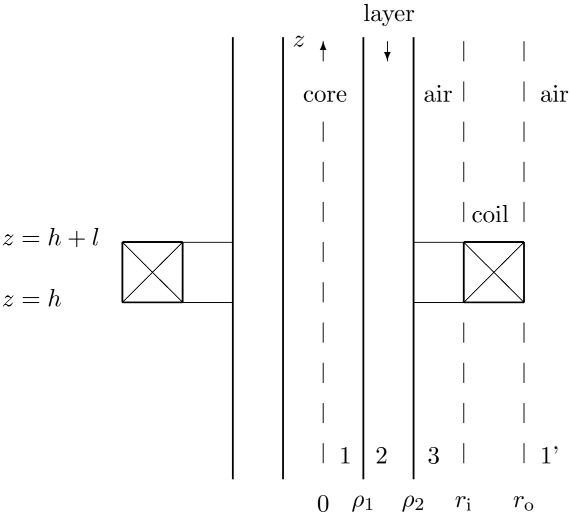

Fig. 7.5 Cross-section through the axis of a circular coil with finite cross-section, coaxial with a coated cylindrical conductor

7.2.6 *Tube Conductor*

Encircling Coil

For an introductory discussion on the role of the encircling coil, the reader is referred to Sect. 6.5. There, the impedance of a coil encircling a solid cylindrical rod is discussed. Here, the discussion is extended to the coil encircling a hollow cylindrical rod (cylindrical tube). As with the rod, the tube test-piece geometry was studied extensively by Friedrich Förster and a summary of his work relevant to the encircling coil and tube is given in [8, Sect. 4: Theory of Encircling Coil and Internal Axial Coil Tests of Tubes]. The definition of fill-factor given in (6.97) for the solid rod conveys the same meaning in the case of the tube but is modified according to the nomenclature of Fig. 7.5, by replacing ρ_1 in (6.97) with ρ_2, which is the outer radius of the tube indicated in Fig. 7.5:

$$\eta = \left(\frac{\rho_2}{r_\mathrm{i}}\right)^2 . \tag{7.14}$$

The tube inspected by an encircling coil is a special case of the coated cylindrical conductor shown in Fig. 7.5, in which the core, region 1, takes the parameter values of air; $\sigma_1 = 0$ and $\mu_{\mathrm{r}1} = 1$ so that $\gamma_1 = \gamma_3 = \kappa$ in the equations of Sect. 7.2.5.

The normalized impedance plane diagram shown in Fig. 7.6 illustrates the effect of changing fill-factor, frequency of inspection, and test-piece conductivity for the encircling coil inspection of a conductive, non-ferromagnetic tube assuming that the coil and tube are coaxial with one another [8]. Figure 7.7 illustrates the effect on the impedance-plane plot of changing the tube wall thickness.

Bobbin Coil

For discussions on the role of the bobbin probe, the reader is referred to Sects. 6.6 and 8.3 of this text and again to the detailed work of Friedrich Förster [8, Sect. 4: Theory of Encircling Coil and Internal Axial Coil Tests of Tubes]. The definition of fill-factor given in (6.132) is modified for this case by replacing ρ_1 in (6.132) with $\rho_{m'-1}$ that denotes the inner radius of the tube shown in Fig. 7.4:

$$\eta_b = \left(\frac{r_\mathrm{o}}{\rho_{m'-1}}\right)^2 . \tag{7.15}$$

The tube inspected by a bobbin coil is a special case of the coated cylindrical conductor shown in Fig. 7.4, in which there is no conductor interior to the coil and, exterior to the coil, $m' = 3$, $\sigma_{1'} = \sigma_{3'} = 0$ and $\mu_{\mathrm{r}1'} = \mu_{\mathrm{r}3'} = 1$ so that $\gamma_{1'} = \gamma_{3'} = \kappa$ in the equations of Sect. 7.2.5.

The normalized impedance-plane diagram shown in Fig. 7.6 illustrates the effect of changing fill-factor, frequency of inspection, and test-piece conductivity for the bobbin coil inspection of a conductive, non-ferromagnetic tube assuming that the

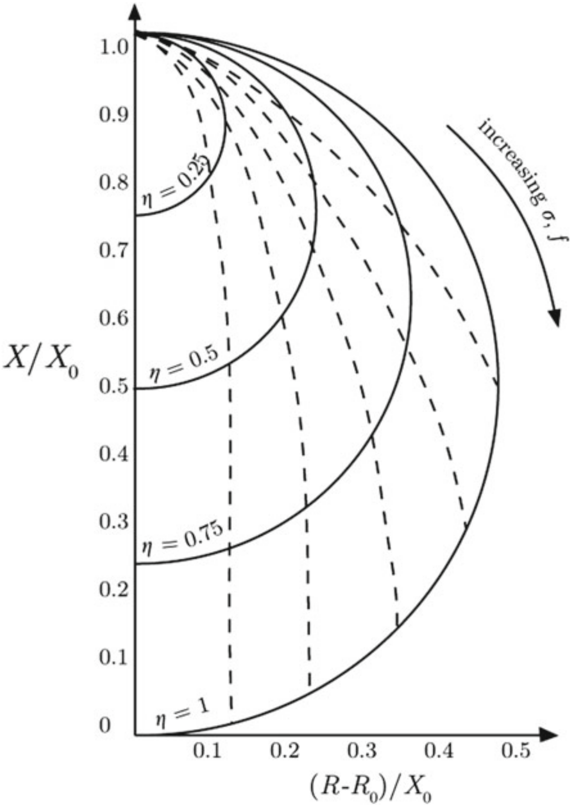

Fig. 7.6 Normalized impedance-plane plot for a coil with inner radius $r_{\rm i}$ encircling a tubular, non-ferromagnetic, test-piece with outer radius ρ_2 and constant ratio of wall thickness to ρ_2, i.e., $(\rho_2 - \rho_1)/\rho_2 = \text{constant}$, Fig. 7.5. Solid lines (——) represent the complex impedance of the probe as a function of rod conductivity, σ, or frequency of coil operation, f. Broken lines (- - -) represent the effect of changing η, (7.14). The same curves are obtained for a bobbin coil with outer radius $r_{\rm o}$ internal to and coaxial with a tube with inner diameter $\rho_{m'-1}$, Fig. 7.4 and (7.15) [8]

coil and tube are coaxial with one another [8]. Figure 7.7 illustrates the effect on the impedance-plane plot of changing the tube wall thickness.

7.3 Truncated Conductors

An eddy current probe may be viewed as ‘small’ relative to the dimensions of a test-piece if the eddy current density induced by the coil is negligible in the vicinity of any sharp geometrical changes in the test-piece. This condition may be satisfied if the geometrical variations of the test-piece take place over a length scale much larger than the dimensions of the probe coil, but the distribution of the eddy-current density also depends on the frequency at which the coil is operating. Looking back at Fig. 2.8 it can be seen that not only does the depth of penetration of the eddy currents decline as the frequency increases, by the skin effect, but the lateral spread of the eddy-current density declines as the probe frequency increases, as well. This

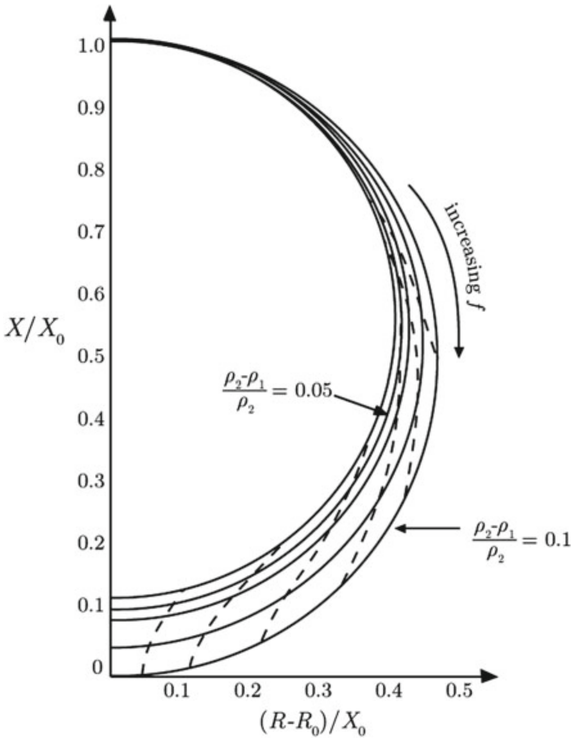

Fig. 7.7 Normalized impedance-plane plot for a coil with inner radius r_1 encircling a cylindrical test-piece with varying outer radius ρ_2, constant conductivity, and constant inner diameter, for various ratios of wall thickness to outside tube radius $(\rho_2 - \rho_1)/\rho_2$, Fig. 7.5. Solid lines (——) represent the complex impedance of the probe as a function of frequency, f. Broken lines (- - -) represent the effect of changing $(\rho_2 - \rho_1)/\rho_2$. The outermost solid curve applies for $\eta = 1$ and the innermost curve for $\eta = 0.9$, (7.14). Similar curves are obtained for a bobbin coil internal to a tube, Fig. 7.4 and (7.15) [8]

means that geometrical variations in a test-piece will be less noticeable to a probe operating at higher frequency, if all other parameters are equal.

Eddy-current inspection commonly needs to be done in regions where the geometrical variation of the test-piece is noticeable, however. Examples of such variations include edge effects. As a surface probe approaches the edge of a plate, as a bobbin probe emerges from a tube, or as a rotary probe emerges from a borehole, for example, there is a sharp transition in the eddy current density in the vicinity of the coil due to the truncation of the test-piece. The impedance changes in the eddy-current probe that result from changes in local test-piece geometry are often larger than impedance changes due to defects in those regions. The inspector therefore faces the problem of needing to separate a defect signal from a potentially masking signal due to geometrical variations of the test-piece.

This section offers a review of quasi-analytical solutions to problems that have been solved in relation to EC NDE of conductors with relatively sharp geometrical variations. Many of the solutions employ the truncated region eigenfunction expansion (TREE) method, introduced by Theodoulidis [9] and mentioned in Sect. 6.3.5 with reference to modeling the effect of a ferrite probe core on the probe impedance.

7.3.1 Truncated Region Eigenfunction Expansion Method

The TREE method is a quasi-analytical method of solving the electromagnetic equations governing probe coil behavior in the environs of conductive test-pieces of various geometries. The homogeneous and layered flat and cylindrical test-pieces treated in Chap. 6 and Sect. 7.2 were tractable by the traditional method of separation of variables, as employed by Dodd, Deeds, and Cheng [4–6]. The TREE method also relies upon separation of variables to express a general solution for the electromagnetic field in analytic form but, additionally, employs truncation of the solution domain in one or more coordinates. Truncation of the solution domain allows expression of the solution in the truncated coordinate as a series summation rather than as an integral of infinite extent. The primary advantage of this approach is that the interface conditions on the electromagnetic fields can be satisfied at several interfaces simultaneously, allowing analytical treatment of the eddy-current inspection of truncated conductors such as the ends of tubes or rods, and the edges of plates. The development of the TREE method and its application to several problems in EC NDE that were previously intractable analytically was a significant breakthrough in the field, carrying the additional benefit of highly efficient numerical solvers with easier error control than afforded by the numerical evaluation of integrals [10].

7.3.2 Wedge and Plate Edge

In a series of articles published in 2005 [11], 2010 [12], and 2014 [13], the problem of EC inspection of a thick conductor with an abrupt edge has been examined in different aspects. This test-piece geometry is also termed a *wedge* conductor or, in the case of a wedge with a right-angled vertex, a *quarter-space* conductor. The first of these articles was concerned with calculating the impedance of an eddy-current surface coil, whose axis is perpendicular to one of the faces of a conductive quarter space [11], Fig. 7.8. The second solved a similar problem but for a surface coil whose axis may adopt any of the three orthogonal directions relative to the faces of the quarter-space [12]. In a new departure, the focus of [13] was computation of the impedance of an EC coil in the vicinity of a conductive wedge of arbitrary angle. The assumptions adopted were that the wedge is perfectly conducting and that the coil axis is parallel to the line defining the vertex of the wedge. For this arrangement, the problem reduces to that of a tangent coil (Sect. 6.4) above a half-space conductor as the wedge angle tends to 180°.

In 2006, the TREE method calculation of eddy-current coil impedance for a coil with axis perpendicular to the surface of a truncated plate was published [14], Fig. 7.9. This result is particularly useful for understanding the contribution made by the edge of a plate to the EC coil impedance. Figure 7.10 shows a normalized impedance plane plot calculated as the coil is moved from the surface of a plate, over its edge, and to a point remote from it. The normalized impedance is plotted as a difference

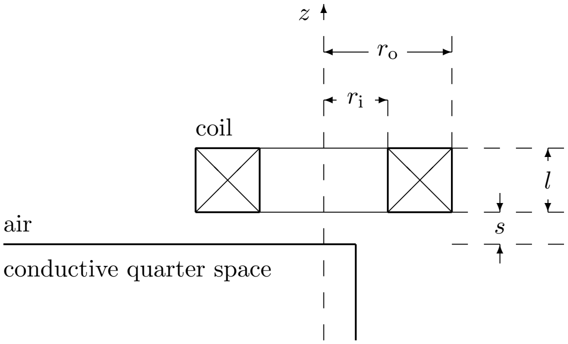

Fig. 7.8 Cross-section through the axis of a circular, air-cored, eddy-current coil, positioned horizontally above a conductive quarter-space

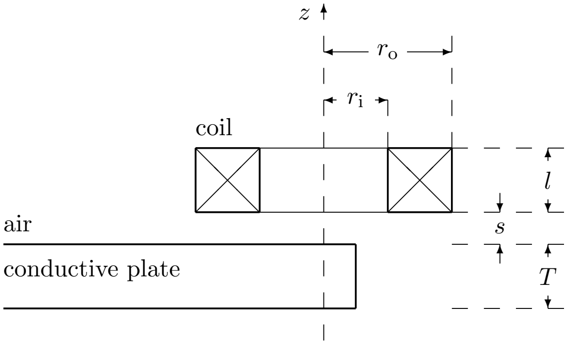

Fig. 7.9 Cross-section through the axis of a circular, air-cored, eddy-current coil, positioned horizontally above a conductive plate

relative to the free-space (isolated coil) value, with the maximum difference revealed when the coil is over the plate, at the lower end of each curve in the figure. Five plate thicknesses are considered in Fig. 7.10 and parameters of the calculation are given in Table 7.1.

Together, these solutions for EC coil interaction with wedge and plate-edge geometries represent a significant advance in the analysis of EC coil impedance due to sharp geometrical features for the reasons mentioned in Sec. 7.3.1.

7.3.3 End Effects and Cylindrical Conductors

The earliest application of the TREE method in the context of EC NDE was to the analysis of impedance of a surface coil with a ferrite core in the vicinity of a layered conductive half-space, Sect. 6.3.5, published in 2003 [9]. The core was treated as a truncated ferromagnetic cylinder. Building on this approach, a series of publications have treated a variety of test-pieces with truncated circular cylindrical geometry.

A quasi-analytical solution for the impedance of a bobbin coil emerging from the end of a tube, and coaxial with it, was published in 2004 [15]. The effects of wall-thinning near the tube end and the difficulty of detecting a small defect close

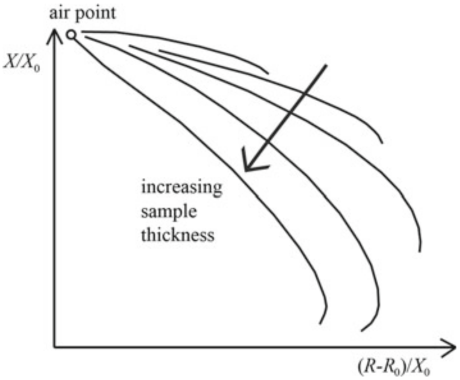

Fig. 7.10 Normalized impedance-plane plot for a coil with axis perpendicular to the surface of a plate, thickness T, as the coil scans from the plate to free space, over the plate edge (Fig. 7.9). Normalized impedance is plotted as a difference relative to the free-space (isolated coil) value, with the maximum difference revealed when the coil is over the plate, at the lower end of each curve [14]

Table 7.1 Parameters for the numerical calculations whose data are presented in Fig. 7.10 [14]

Coil parameters		Value
r_o	Outer radius (mm)	11.43
r_i	Inner radius (mm)	4.04
l	Length (mm)	8.02
s	Stand-off (mm)	1.08
n	Number of turns	1,858
Test-piece parameters		Value
σ	Conductivity (MSm^{-1})	17.5
μ_r	Relative permeability	1

to the tube end were demonstrated in this paper. The complementary problem, of an encircling coil coaxial with a truncated circular conducting rod, layered rod or tube, was treated in 2005 [16, 17].

A solution published in 2008 accommodated a greater degree of uncertainty in the position of the coil in relation to a borehole [18], modeling the impedance of both a rotary coil interior to the borehole, Fig. 6.5, and of a bobbin coil whose axis is offset from the axis of the borehole, Fig. 6.27.

The interested reader is invited to pursue these solutions through the original literature cited here.

7.4 Summary

This chapter has collected together analytical expressions for the impedance of a coil in the presence of layered, coated, or thin flat and cylindrical test-pieces. Impedance plane plots that show how the impedance varies as a function of various geometrical, physical, and probe parameters have been presented. Further, the Truncated Region Eigenfunction Expansion method has been mentioned as having been successfully applied to model the impedance of EC coils in the vicinity of test-pieces with sharp geometrical discontinuities.

Building upon the discussion of signals, coils, and the impedance responses to various types of test piece, covered in Chap. 6 and this chapter, the next chapter considers the ways in which coils and other sensors are put together in various configurations to form probes that are optimized for different inspection needs.

7.5 Examples

1. Identify *two* limiting cases in which the expression for the impedance of an EC surface coil positioned above a coated half-space conductor (7.5) should reduce to the result for the half-space conductor (given in (6.87) and reproduced below for convenience):

$$Z = \frac{j\omega\mu_0\pi n^2}{l^2(r_\text{o}-r_\text{i})^2}\int_0^\infty \frac{J^2(\kappa r_\text{i},\kappa r_\text{o})}{\kappa^5}\left(2l+\frac{1}{\kappa}\left\{2e^{-\kappa l}-2\right.\right.$$
$$\left.\left.+[e^{-2\kappa(l+s)}+e^{-2\kappa s}-2e^{-\kappa(l+2s)}]\left(\frac{\gamma-\kappa}{\gamma+\kappa}\right)\right\}\right)d\kappa$$

   and show that (7.5) does indeed reduce correctly in those limits.
2. Identify one limiting case in which the expression for the impedance of an EC surface coil positioned above a plate conductor (7.6) should reduce to the result for the half-space conductor given above, and show that (7.6) does indeed reduce correctly in that limit.

References

1. Kolyshkin, A.A., Vaillancourt, R.: Impedance of a single-turn coil due to a double-layered sphere with varying properties. IEEE T. Magn. **31**, 2274–2280 (1995)
2. Theodoulidis, T.P., Kriezis, E.E.: Coil impedance due to a sphere of arbitrary radial conductivity and permeability profiles. IEEE T. Magn. **38**, 1452–1460 (2002)
3. Sabbagh, H.A., Murphy, R.K., Sabbagh, E.H., Aldrin, J.C., Knopp, J.S.: Computational Electromagnetics and Model-Based Inversion: A Modern Paradigm for Eddy-Current Nondestructive Evaluation. Springer, New York (2013)

4. Dodd, C.V., Deeds, W.E.: Analytical solutions to eddy-current probe-coil problems. J. Appl. Phys. **39**, 2829–2838 (1968)
5. Cheng, C.C., Dodd, C.V., Deeds, W.E.: General analysis of probe coils near stratified conductors Int. J. NDT **3**, 109–130 (1971)
6. Dodd, C.V., Cheng, C.C., Deeds, W.E.: Induction coils coaxial with an arbitrary number of cylindrical conductors. J. Appl. Phys. **45**, 638–647 (1974)
7. Cartz, L.: Nondestructive Testing: Radiography, Ultrasonics, Liquid Penetrant, Magnetic Particle. Eddy Current. ASM International, Materials Park, OH (1995)
8. McMaster, R.C., McIntire, P. (eds.), Mester, L.M. (tech. ed.): Nondestructive Testing Handbook: Electromagnetic Testing, vol. 4, 2nd edn. American Society for Nondestructive Testing, Columbus (1986)
9. Theodoulidis, T.P.: Model of ferrite-cored probes for eddy current nondestructive evaluation. J. Appl. Phys. **93**, 3071–3078 (2003)
10. Theodoulidis, T.P., Kriezis, E.E.: Eddy Current Canonical Problems (with Applications to Nondestructive Evaluation). Tech Science Press, Forsyth (2006)
11. Theodoulidis, T.P., Bowler, J.R.: Eddy current coil interaction with a right-angled conductive wedge. P. Roy. Soc. A-Math. Phy. **461**, 3123–3139 (2005)
12. Interaction of an eddy-current coil with a right-angled conductive wedge. IEEE T. Magn. **46**, 1034–1042 (2010)
13. Trampel, C.P., Bowler, J.R.: Eddy-current coil interaction with a perfectly conducting wedge of arbitrary angle. Res. Nondestruct. Eval. **25**, 186–202 (2014)
14. Bowler, J.R., Theodoulidis, T.P.: Coil impedance variation due to induced current at the edge of a conductive plate. J. Phys. D: Appl. Phys. **39**, 2862–2868 (2006)
15. Theodoulidis, T.: End effect modeling in eddy current tube testing with bobbin coils. Int. J. Appl. Electrom. **19**, 207–212 (2004)
16. Bowler, J.R., Theodoulidis, T.P.: Eddy currents induced in a conducting rod of finite length by a coaxial encircling coil. J. Phys. D: Appl. Phys. **38**, 2861–2868 (2005)
17. Sun, H.Y., Bowler, J.R., Theodoulidis, T.P.: Eddy currents induced in a finite length layered rod by a coaxial coil. IEEE T. Magn. **41**, 2455–2461 (2005)
18. Theodoulidis, T.P., Bowler, J.R.: Impedance of an induction coil at the opening of a borehole in a conductor. J. Appl. Phys. **103**, 024905 (2008)

Chapter 8
Probes

Abstract In this chapter, various probe configurations are discussed in the context of particular applications for which they are well suited. Common and more exotic configurations are included. Practically speaking, probes are often composed of more than one coil either for differential operation that is particularly effective in defect detection or so that each coil may be individually optimized for its role as drive or pick up coil. Some probes are of hybrid design, in which a drive coil induces eddy currents in the test-piece yet the signal is measured by another type of sensor, e.g., a Hall device or a giant magnetoresistive (GMR) sensor. Thin, flexible coils designed for in situ structural health monitoring, and array probes designed for rapid wide-area inspection, are also presented.

8.1 Introduction

Eddy-current inspection can be optimized, to achieve the best sensitivity to a certain defect in a certain test-piece, by the correct choice of probe and operating frequency. In this chapter, common and emerging types of eddy-current probe are introduced and their uses are discussed. The simplest configuration is that of the *absolute probe* in which the probe is formed with a single coil that acts as both the *driver* and the *pick up*. Current flowing in a drive coil induces eddy currents in the test-piece, whereas a pick up coil senses the magnetic field produced by the eddy currents. In the absolute probe, one coil performs both of these functions. An *absolute surface coil* has axis perpendicular to the test-piece, whereas an *absolute encircling coil* is wound on a hollow former through which the test-piece is passed, during an inspection. In some probe configurations (*driver pick up* or *reflection probes*), the driver and pick up roles are performed by separate coils, Sect. 8.4.

Differential probes, which employ two similar coils wound oppositely to each other, form another important class of probe, Sect. 8.3. They are particularly useful for defect detection because they are designed to reduce noise in the signal that may

N. Bowler, *Eddy-Current Nondestructive Evaluation*,
Springer Series in Measurement Science and Technology,
https://doi.org/10.1007/978-1-4939-9629-2_8

arise due to a number of factors such as probe lift-off variations, large-scale variations in material properties, or temperature variations of the part under test. Contributions to the impedance of multi-coil probes may be deduced from theoretical results for the single coil by the principle of linear superposition. This means that multi-coil probe fields, in the presence of materials with linear electromagnetic properties, may be obtained by the vector sum of fields due to the individual coils that constitute the multi-coil probe. The impedance of a differential probe has a null value in the absence of a defect because the fields of the two oppositely wound coils that constitute the differential probe cancel each other out unless a defect is present.

A coil oriented such that its axis lies tangential to the surface of the test-piece is known as a *tangent coil*. Two tangent coils operating in differential mode and combined in such a way that their axes are perpendicular to each other, while being tangential to the surface of the test-piece as well, form the *plus-point probe*. Plus-point probes find application in detection of surface cracks in ferromagnetic materials because they are less sensitive to permeability variation than a surface coil with axis perpendicular to the surface of the test-piece. Plus-point probes are discussed in Sect. 8.5.

Probes formed from arrays of coils are discussed in Sect. 8.6. Such probes have the advantage of covering a wide inspection area in a single pass, serving to reduce inspection time when compared with multiple passes required of a single coil to cover the same area.

Flexible coils, whose copper windings are traced on flexible polymer substrate materials by printed circuit technology, offer the advantage of conformability to curved surfaces, improving the coupling between the probe and the test-piece. A summary of the developments in theory and experiment of flexible spiral coils is given in Sect. 8.7.

Discussion of a hybrid driver pick up probe, that employs a Hall sensor instead of a pick up coil, is given in Sect. 8.8. The Hall sensor measures the magnetic induction field directly, rather than impedance as measured by a conventional pick up coil. Their small size permits Hall sensors to be formed into arrays, offering measurements with fine spatial resolution. The chapter concludes with discussion of a similar hybrid probe, that employs a giant magnetoresistive sensor as the pick up device, in Sect. 8.9.

8.2 Absolute Probe

Surface probes often operate in *absolute mode*, meaning that the signal obtained in a measurement is simply the value of the coil impedance itself. The configuration of a typical surface probe is shown in Fig. 8.1. A pencil probe is shown in Fig. 8.2 with an absolute coil configuration detailed in the tip enlargement at left. The tip enlargement at right shows a differential coil configuration, described in Sect. 8.3.

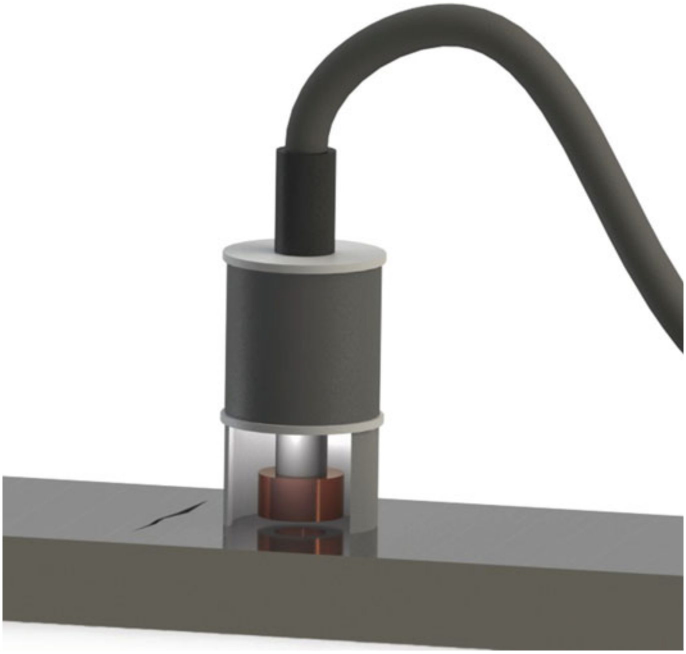

Fig. 8.1 An eddy-current surface probe scanning a cracked metal test-piece. This type of probe would typically be held by hand. In the figure, part of the probe casing is cut away to reveal the coil

Fig. 8.2 A pencil probe. Enlargements of the tip area show either an absolute coil configuration (left) or a differential coil configuration (right)

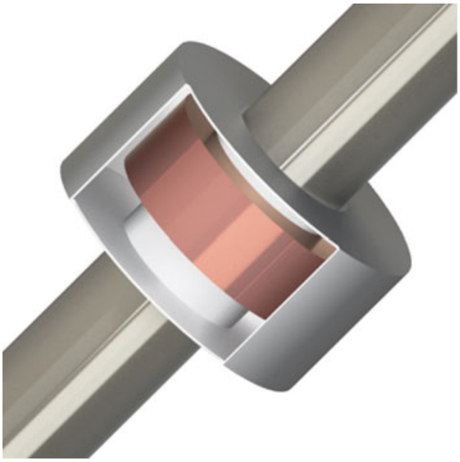

Fig. 8.3 An eddy-current probe encircling a metal rod test-piece. The coil is wound on a plastic former and housed in protective plastic casing which has been cut away in the image, to show the coil

Pencil probes may be either straight or with a bend near the tip as shown in Fig. 8.2. The probe configuration can be chosen to provide the best access to the inspection surface, subject to any geometrical constraints of the region to be inspected.

An absolute probe with encircling geometry is shown in Fig. 8.3. An encircling coil is wound on a hollow former so that the test-piece can pass through it. This probe is sometimes known as an outside diameter (OD) probe.

Absolute probes are useful for material property measurements as well as for defect detection. Their sensitivity to material properties can be a disadvantage when being used for defect detection, however, since any changes in material properties then act as noise sources that interfere with the defect signal. Absolute probes also suffer from noise due to probe lift-off variations and tilt, in the case of the surface coil, or due to wobble and tilt in the case of an encircling coil. These problems have been discussed in Sect. 6.3.6.

8.3 Differential Probe

A differential probe is one in which two nominally identical coils are connected in series in the same probe, but are wound in opposition to one another, so that the sum of their impedances is zero when no defect is present. A differential surface probe is shown in Fig. 8.2 (tip enlargement at right). The differential coil in that figure is known as a "split-D" coil, also shown in Fig. 8.4. Another example of a differential probe is shown in Fig. 8.5, in which two coils that are nominally the same are wound as opposing encircling coils for inspecting a cylindrical specimen. An example of a differential bobbin probe is shown in Fig. 8.6. This type of probe is commonly used for the detection of defects in tubes, such as steam-generator tubes in nuclear power plants.

Fig. 8.4 A differential surface probe is commonly formed from two nominally identical "D"-shaped coils, which are formed from multiple figure-of-eight loops like the one illustrated. The resulting coil is known as a "split-D" coil

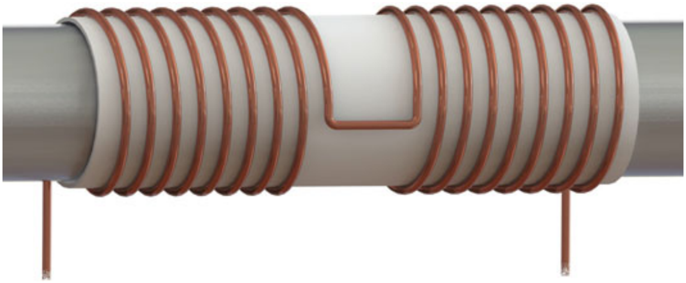

Fig. 8.5 A differential encircling probe may be formed from two nominally identical encircling coils connected in "tandem" and in electrical opposition, indicated schematically in this diagram

Fig. 8.6 Differential bobbin probe formed from two nominally identical but oppositely wound coils connected in series

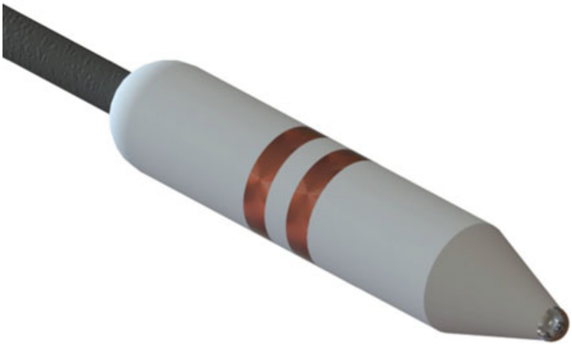

The impedance of a differential probe is obtained by summing the impedance of the two individual coils, according to the principle of linear superposition. One statement of this principal is that the total electromagnetic field due to multiple sources, in a region where material properties are linear, may be obtained by the vector sum of the fields due to the individual sources. Hence, the impedance of a differential probe, Z_{diff}, formed from two nominally identical coils wound in opposition and distinguished by the labels 1 and 2, gives

$$Z_{\mathrm{diff}} = Z_1 + Z_2 = Z_1 + (-Z_1) = 0 \tag{8.1}$$

when both coils are near an unflawed region of the test-piece. When the two probe coils are not symmetrically placed with respect to a defect, a change in the impedance of the probe ΔZ_{diff} is obtained. Then,

$$\Delta Z_{\mathrm{diff}} = \Delta Z_1 + \Delta Z_2 \tag{8.2}$$

and ΔZ_{diff} can be calculated by calculating ΔZ_1 and ΔZ_2 due to a particular flaw, perhaps according to the theoretical methods outlined in Chap. 6.

The major advantage of the differential probe configuration is that an impedance change in the probe is produced only when the impedances of the two individual coils are different. This means that noise due to lift-off, in the differential configuration of Fig. 8.2, or due to wobble, in the configurations of Figs. 8.5 and 8.6, is largely eliminated. The probe is also insensitive to slow changes in the geometry of the test-piece (changes on a length scale somewhat greater than the dimensions of the probe). This means, however, that a differential probe is *not* suitable for measurements of specimen properties such as thickness and conductivity. Differential probes are ideally suited to defect detection.

A typical signal due to a differential surface coil as it scans over a surface crack is illustrated in Fig. 8.7. The point in the center of the impedance-plane plot is the *null point*, representing the signal measured by the probe as it rests on an unflawed region of the test-piece. As the probe is moved toward the flaw (to the right in this figure), first only one of the coils senses the presence of the defect (coil 2, Fig. 8.7(a)) and the total impedance of the probe changes because $Z_1 \neq Z_2$. Approximately, $\Delta Z_1 \approx 0$ and $\Delta Z_{\mathrm{diff}} \approx \Delta Z_2$. When the probe moves farther to the right, symmetry is recovered when the crack is positioned centrally between the two coils, Fig. 8.7(b). Here, both coils are influenced by the presence of the crack to an equal but opposite extent so that $\Delta Z_{\mathrm{diff}} = \Delta Z_1 + \Delta Z_2 = \Delta Z_1 - \Delta Z_1 = 0$. As the probe moves yet farther to the right, only coil 1 senses the defect. Since coil 1 is wound oppositely to coil 2, the impedance change resulting at Fig. 8.7(c) is opposite to that shown in Fig. 8.7(a). Finally, as the probe moves away from the defect altogether the "figure-of-eight" impedance-plane response that is characteristic of the differential probe comes to completion.

Example signals due to a differential bobbin probe as it is pulled through a tube with exterior defects of different depth is shown in Fig. 8.8. Note that the double loops forming the signal from each of the three example defects are similar to that illustrated in the case of the differential surface coil, Fig. 8.7. Further points of note are (i) qualitatively, the size of the signal increases as the defect size increases, and (ii) the phase angle of the signal increases as the ligand thickness increases. The ligand is the unflawed material that exists between the tube bore and the bottom of the defect. The ligand thickness decreases as the defect becomes deeper.

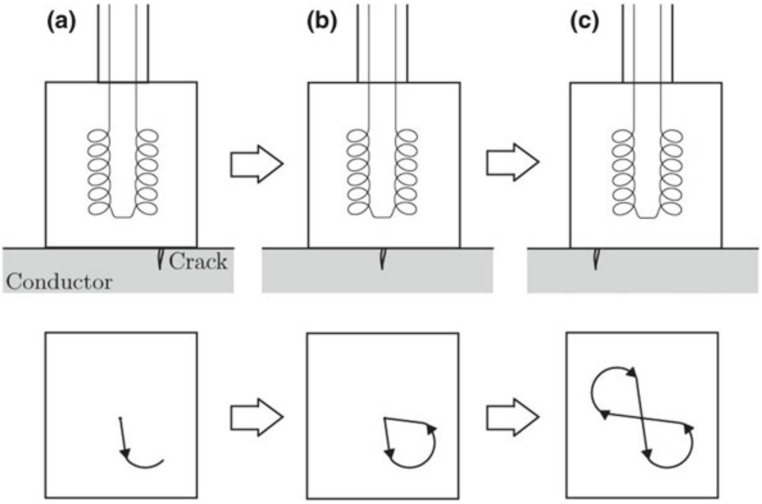

Fig. 8.7 A differential surface probe formed from two nominally identical but oppositely wound coils connected in series, above, and the impedance-plane (Z-plane) response of the probe, below, as the probe moves over a surface defect

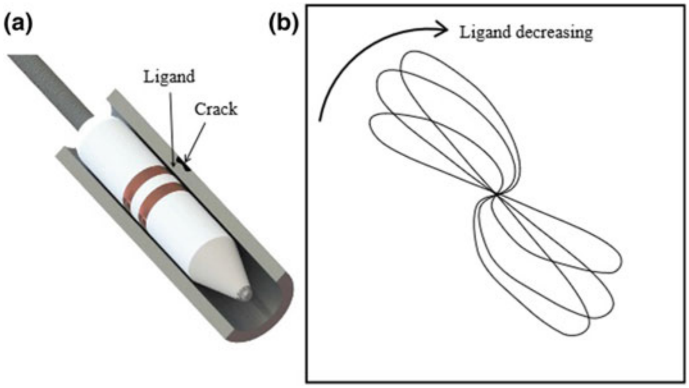

Fig. 8.8 **(a)** A differential bobbin probe is pulled through a tube with an exterior defect, and **(b)** the Z-plane response as a differential bobbin probe encounters three exterior defects, of the type shown in **(a)**, of different depth

Signals from differential probes are difficult to interpret for more complex defects or rapid changes in surrounding structure. For example, steam-generator tubes in nuclear power plants are threaded through metal plates for support. In a tube inspection, the support plates may give rise to a strong signal in an eddy current bobbin coil and, in order to identify defects in the support-plate region, the signal from the support plate itself must be understood. The theoretical analysis of the influence of the tube support-plate on the eddy current bobbin coil impedance has been presented in [1, Chap. 5], and the interested reader is referred to that publication for further information.

8.4 Driver Pick Up Probe

A driver pick up probe is one in which the current is induced in the test-piece by one of a pair of coils that are electrically *separate* from one another. The inducing coil is known as the *driver* coil. Impedance changes are recorded by the other coil, which is known as the *pick up* coil. Such a configuration is shown schematically in Fig. 8.9 for a surface probe. A driver pick up probe is sometimes known as a reflection probe. The major advantage of this arrangement is that both the driver and pick up coils can be separately optimized for the inspection at hand. In crack detection work this may mean, for example, that the pick up coil is much smaller than the driver coil, to improve spatial resolution in the measurements, and the pick up coil is positioned very near to the test-piece, to increase the magnitude of the measured signal. In a driver pick up encircling probe, the pick up coil may be wound inside the driver coil using many turns of fine wire, to increase its sensitivity.

If a driver pick up probe is used in absolute mode, the impedance measured by the pick up coil can be calculated by dividing the voltage across the pick up coil (coil 2) by the current flowing in the driver coil (coil 1):

$$Z_{2,1} = \frac{\mathcal{V}_2}{\mathcal{I}_1}. \tag{8.3}$$

Compare with definition (4.25).

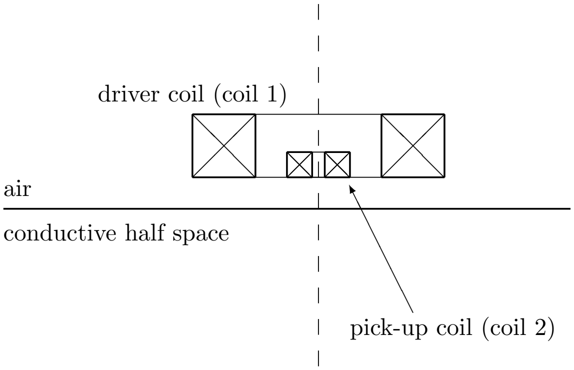

Fig. 8.9 Cross-section through the axis of a driver pick up (reflection) eddy-current probe, positioned horizontally above a conductive half-space

8.5 Plus-Point Probe

The plus-point probe consists of two orthogonally wound tangent coils operating in differential mode (the tangent coil was discussed in Sect. 6.4 and is shown in the schematic diagram of Fig. 6.21). The plus-point probe is so named for the reason that the two coils are oriented at 90° to one another, forming a plus sign (+) when viewed from certain angles. The coil windings in a plus-point probe may have square or circular cross-section, the latter being illustrated in Fig. 8.10.

The plus-point probe offers the same advantages as any differential probe, discussed in Sect. 8.3; suppressing noise due to lift-off variations or gradual changes in material conductivity or permeability. In addition to these advantages, the plus-point probe offers bidirectional sensitivity. Recalling that the eddy-current density induced in a test-piece by a tangent coil does not display circular symmetry but displays directionality, as shown by the lowest pair of images in Fig. 6.20, it can be inferred by superposition of the two plus-point coil fields that the probe displays bidirectional sensitivity. Remember, however, that the coupling between a surface coil (whose axis is perpendicular to the surface of the test-piece) is much stronger than that between a tangent coil and the test-piece so, overall, the signal strength is lower in the case of a plus-point (or tangent) coil compared with what it would be if the same coils were oriented with their axes perpendicular to the test-piece surface. This latter point is illustrated in Fig. 6.19, where we see more than 90% reduction in $\Delta X/X_0$ as the coil axis tilt angle increases from 0° (surface coil) to 90° (tangent coil).

The plus-point probe was developed first for detection of surface-breaking cracks "in the weldment region of steel components while effectively reducing signal responses generated by variations in conductivity or permeability" [2, p. 4.2]. It

Fig. 8.10 Two tangent coils wound orthogonally to form a plus-point probe

has also been employed for the inspection of welds in structural steels for bridges [3]. In a report of the United States Nuclear Regulatory Commission [2, p. 4.2], the plus-point probe was evaluated for its effectiveness for the inspection of the inner surface of cast stainless steel piping; for detecting, localizing and sizing surface cracks. Some variation in background noise was observed, relating to orientation of the grain distribution and microstructure of the material, but the background noise level was not significantly changed by reorienting the probe. On the other hand, it was noted that the probe is more sensitive to cracks that align with either of the coil planes but less sensitive to off-angle cracks especially those that may be oriented at 45° to the coil planes.

8.6 Array Probes

Array probes comprise several sensing coils in one probe head. Examples are shown in Figs. 8.11 and 8.12. Their primary benefit is the ability to cover a larger test-piece area in one pass of the probe than is possible with a single-coil probe. The array of

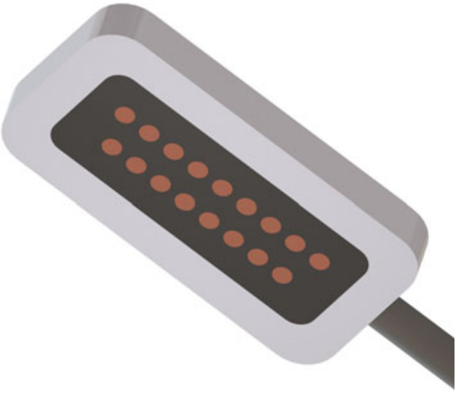

Fig. 8.11 A surface probe formed from a spatial array of multiple eddy-current surface coils, for wide-area surface inspection. Note that the two rows of coils are offset from one another to provide full coverage

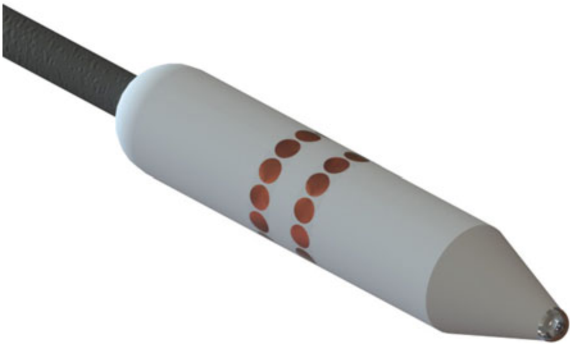

Fig. 8.12 A bobbin probe incorporating a spatial array of multiple eddy-current surface coils, for full inspection of a tube interior without rotation the probe head. Note that the two rows of coils are offset from one another, azimuthally, to provide full surface coverage

surface coils designed for wide-area surface inspection shown in Fig. 8.11 illustrates the principle of using a double row of coils, offset from one another, to achieve full coverage of the test-piece without any blind spots that might be evident if only a single row of coils were used. Similarly, the bobbin array-probe designed for tube or borehole inspection shown in Fig. 8.12 provides for full-angle inspection of the tube or borehole by the array of surface coils, removing the need to rotate the probe head as in the case of a rotating probe head in which a single surface coil is mounted, Fig. 6.5.

8.7 Flexible Probes

Flexible coils offer the advantage of being able to conform to a curved inspection surface, which is helpful for improving the coupling between the coil and the test-piece. If a coil is thin as well as flexible, it could be mounted permanently on a structure, e.g., under paint, to provide in situ inspection for structural health monitoring [4]. An example of a ten-turn spiral coil etched on 25-micron-thick polyimide film is shown in Fig. 8.13. A challenge arising in the practical application of a thin probe with only one layer of windings relates to the fact that only a relatively small number of turns is possible. The achievable signal is, therefore, weaker than for a coil with a larger number of turns. In the case of the coil pictured in Fig. 8.13, the DC resistance and inductance of the coil are merely 2.32 Ω and 0.28 μH, respectively.

The theory of spiral coils has been studied by Burke, Ditchburn, and Theodoulidis, appearing in the literature since 2003. Theoretical calculations of impedance and benchmark experiments are compared in [4] for flat circular–spiral coils such as the one shown in Fig. 8.13 and others like it, with up to 100 turns. The mutual impedance of a pair of such coils is presented in [5]. Closed-form expressions for the impedance of flat rectangular-spiral coils were developed in [6], 2005, wherein

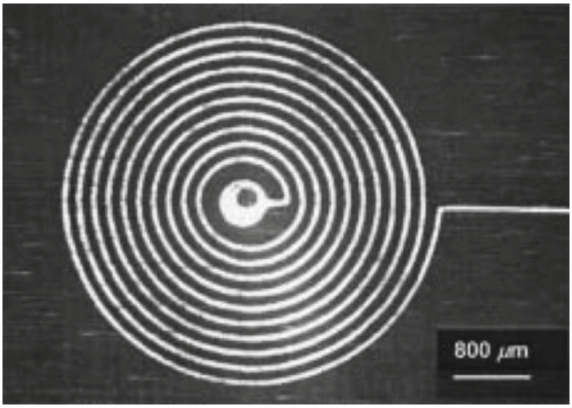

Fig. 8.13 Photomicrograph of a ten-turn circular spiral coil ©Commonwealth of Australia [4]

the impedance change in response to a surface crack as a function of coil aspect ratio and orientation were investigated. The rectangular–spiral coil was studied further in a 2008 publication that focused on the curved rectangular coil, conformed to the surface of a conductive cylinder [7]. The rectangular coil in this configuration has the theoretical advantage that its windings align with either the ϕ- or the z-direction. Both self-impedance of a single coil and mutual impedance of a pair of coils were studied and theoretical impedance calculations were compared with experimental data measured on aluminum alloy samples. Most recently, closed-form expressions for the impedance of a curved circular–spiral coil have been developed [8], addressing the challenge of mixing coordinate systems by a second-order vector potential formalism.

8.8 Hall Sensor Probes

Hall devices are solid-state magnetic field sensors that offer numerous advantages: they exhibit linear response to the magnetic induction field B, they are compact, highly sensitive, and can operate over a wide range of frequency, temperature, and field amplitude.

Hall devices have been explored as pick up sensors for transient or pulsed eddy-current NDE [9–12] and as arrays of pick up sensors to accompany eddy-current drive coils [10, 13–16]. Such probes can be termed *hybrid* probes because the field excitation is provided by eddy-current induction, whereas the sensing technology relies upon the Hall effect measurement of the magnetic induction field.

A brief overview of the Hall effect is given in Sect. 8.8.1 followed by a description of ways in which Hall sensor technology can enhance eddy-current NDE in Sects. 8.8.2–8.8.5.

8.8.1 The Hall Effect

If a conductor such as the one illustrated in Fig. 4.1 is placed into a magnetic induction field, there is a resulting force on the moving charge carriers that is expressed as

$$\mathbf{F} = Q\mathbf{v} \times \mathbf{B}. \tag{8.4}$$

This force is known as the Lorentz force and **v** is the velocity of the charge carriers. The Lorentz force acts to push the charge carriers toward one side of the conductor. As the charge carriers accumulate, equilibrium is reached when the Lorentz force is balanced by the force due to the electric field, expressed in (4.1), that results from the separation of charge across the conductor, in a direction perpendicular to both **v** and **B**. The separation of moving charge carriers across a conductor under the influence of an external perpendicular **B**-field is known as the *Hall effect* after Edwin Herbert

Fig. 8.14 Edwin Herbert Hall, American physicist, 1855–1938 [17]

Hall who discovered it in 1879. The Hall effect gives rise to a measurable voltage across the conductor, named the Hall voltage.

Hall (1855–1938, Fig. 8.14) was an American physicist who conducted thermoelectric research at Harvard University. He did his undergraduate work at Bowdoin College, Brunswick, and obtained a Ph.D. from Johns Hopkins University, Baltimore, in 1880. His seminal experiments were performed during the course of his graduate studies and were published, eventually, in his doctoral thesis. Hall passed an electric current through thin gold leaf supported on a glass plate and measured a potential difference (now known as the Hall voltage) *across* the sheet when it was placed in a magnetic field perpendicular to it. Hall's success in measuring the effect was related to the fact that the Hall voltage is inversely proportional to the thickness of the conductor and Hall's gold leaf samples were sufficiently thin. The Hall effect can be observed in all conductors and the Hall voltage and current are material- and geometry-dependent, as follows.

Consider a Hall device as shown schematically in Fig. 8.15. Charge carriers that are positively charged flow in the direction of conventional current I shown in the figure. With $\mathbf{B} = B_z\hat{z}$, (8.4) leads to

$$\mathbf{F} = Q\, v_x\hat{x} \times B_z\hat{z} = -Qv_x B_z\hat{y}. \tag{8.5}$$

In other words, the Lorentz force acts on the moving positive charge carriers to push them in the negative y-direction. Perhaps unexpectedly, negative charge carriers (electrons) flowing in the direction opposite to that of conventional current I are also forced in the negative y-direction by $B_z\hat{z}$:

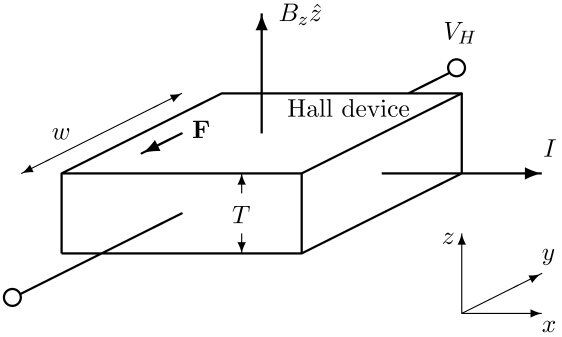

Fig. 8.15 Schematic diagram illustrating the Hall effect. The magnetic induction field **B** gives rise to the Lorentz force **F** that acts on the moving charge carriers I in the Hall device, pushing them in the negative y-direction and creating a potential difference known as the Hall voltage, V_H. Note that V_H is measured in the direction perpendicular to both **B** and the flow of I

$$\mathbf{F} = -|e|\,(-v_x)\hat{x} \times B_z\hat{z} = -|e|v_x B_z\hat{y}, \tag{8.6}$$

where $e = 1.602 \times 10^{-19}$ C is the charge on an electron. At equilibrium, the electric field resulting from positive charge accumulation at the nearest face in Fig. 8.15 is y-directed. Hence

$$-\,Qv_x B_z\hat{y} + QE_y\hat{y} = 0 \tag{8.7}$$

and

$$v_x B_z = \frac{V_H}{w} \tag{8.8}$$

since $V_H = E_y w$. Noting that $v_x = I/(QwTn)$ where n is the charge carrier density, an expression for the Hall voltage is obtained:

$$V_H = \frac{IB_z}{QTn}. \tag{8.9}$$

The Hall voltage is proportional to the control current I and the magnetic induction field B_z, and is inversely proportional to the device thickness T, as mentioned before. One great advantage of the Hall device as a magnetic field sensor is this simple relationship between the Hall voltage, which can be easily measured, and the magnetic induction field component perpendicular to it. In the case of negative charge carriers, the electric field whose force balances the Lorentz force is now oppositely directed. Consequently, the Hall voltage changes sign:

$$V_H = -\frac{IB_z}{|e|Tn}. \tag{8.10}$$

Table 8.1 Charge carrier mobility in typical Hall device materials [13]

Material	Mobility ($cm^2V^{-1}S^{-1}$)
GaAs	8.50×10^3
InAs	2.26×10^4
InSb	7.50×10^4

Practically speaking, both V_H and the sensitivity of a Hall sensor are proportional to the mobility of the charge carriers, which is material dependent. Electron mobilities in some typical Hall device materials are listed in Table 8.1 [13]. Sensitivity of a Hall sensor is also inversely proportional to the thickness of the Hall element, T, but there is a design trade-off between sensitivity and resistance of a Hall device, resistance increasing as T decreases. High resistance leads to undesirable device characteristics such as increased power consumption and self-heating so, practically speaking, the extent to which T may be reduced to increase V_H and sensitivity is constrained by corresponding increase in device resistance. Further details are available in [13].

8.8.2 *Defect Detection with the Hall Sensor*

To understand the signal measured by a Hall Sensor in the vicinity of a defective conductor excited by eddy currents, it is necessary to understand the distribution of the vector magnetic induction field at the surface of the conductor. Let's adapt Fig. 1.7 to indicate **B** in the vicinity of a surface crack. Using the right-hand rule, we can discover that the magnetic induction field associated with the perturbation of the eddy-current density **J** as it flows around a surface crack, Fig. 8.16, is directed up at one end of the crack mouth and down at the other. There is a null point in the center of the crack where $B_z \approx 0$, with z being the direction normal to the conductor surface. A Hall sensor that is set up to detect B_z in the region just above the surface of the test-piece will therefore give a signal that changes sign as the sensor scans along the crack.

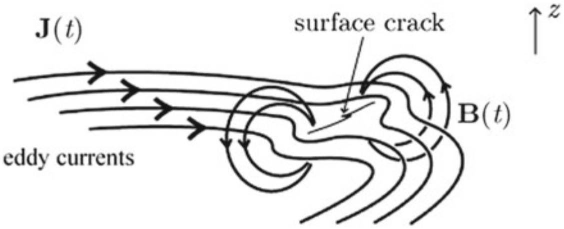

Fig. 8.16 Eddy currents **J** disrupted by a surface defect and the associated magnetic induction field **B**. A Hall sensor can be set up to detect the vertical (z) component of the magnetic induction field, for example

8.8.3 Hall Sensors and Transient EC NDE

Hall sensor technology has been applied in the context of transient eddy current NDE by several different groups in works published in [9–12, 18]. Transient EC NDE (also known as pulsed EC NDE) is a method, whereby the eddy currents are induced in the test-piece by a step-like change in the current in the exciting coil, rather than by a sinusoidal current excitation. The method offers enhanced performance in the detection and characterization of flaws significantly below the surface of the test-piece, in principle allowing a continuum of frequency information to be captured from a single transient measurement [9, 10]. More information on this method is available in [19, Chap. 2]. The works of [9, 12] employ a single Hall sensor pick up centered within a single exciting coil, Fig. 8.17, whereas dual Hall sensor pick up elements operated differentially are employed in [11], Fig. 8.18. By employing time-gate methods of image reconstruction, Harrison developed some impressive images of multilayered, riveted aircraft structures [9]. Lebrun et al. detected artificial

Fig. 8.17 A surface probe employing a single Hall pick up sensor [9, 12]

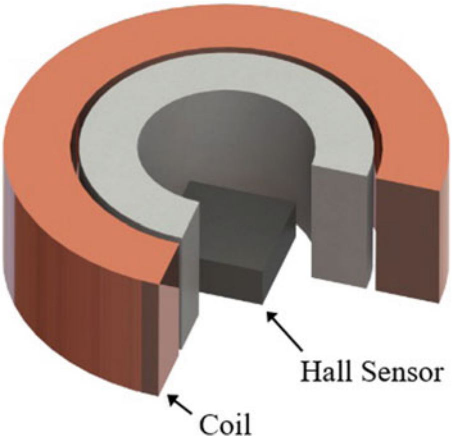

Fig. 8.18 A differential surface probe employing dual Hall pick up sensors [11]

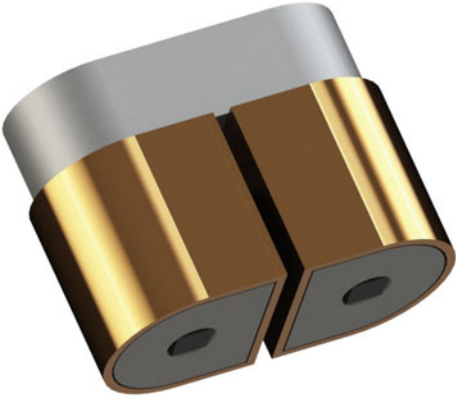

cracks only 1 mm in radial extent, adjacent to fasteners, and under 5 mm of material, by using a pulsed excitation and four Hall sensors arranged around the fastener head.

The method proposed in [10] is discussed in Sect. 8.8.4 in the context of Hall sensor arrays.

8.8.4 Hall Sensor Arrays

At least as early as 2004, Hall sensor arrays were proposed as pick up arrays for eddy current NDE. In [10, 13], linear arrays of Hall sensors were demonstrated with rectangular and "race-track" exciting coils, respectively. A sparse array of nine Hall sensor elements, separation 4 mm, presented in [10] allowed rapid scanning of relatively large test-piece areas. Local image resolution was enhanced by "over-scanning" areas of interest at finer resolution. A calibration procedure was developed to correct for variation in the precise position of each Hall sensor within its encapsulated integrated circuit. The race-track exciting coil with a linear array of Hall sensors is depicted in Fig. 8.19.

In 2007, an 8 × 8 planar array of Hall sensors, coupled with an eddy current excitation, was demonstrated to determine the dimensions of machined notches of various sizes in austenitic stainless steel [14]. The array was mounted on a rigid circuit board substrate and occupied an area of approximately 28 × 28 mm^2 corresponding to a linear spatial resolution of approximately 3.5 mm. Building on this concept, flexible substrate technology was employed in a paper published in 2013 that demonstrated the combination of a Hall sensor array and an eddy current bobbin coil for inspection of piping, Fig. 8.20 [15]. This technology also overcomes difficulties with knowing the precise position of encapsulated Hall devices, encountered in [10]. The best linear spatial resolution achieved in [15] was 0.52 mm. Taking this concept even further, a flexible array of Hall sensors based on graphene as the Hall element was proposed in [16].

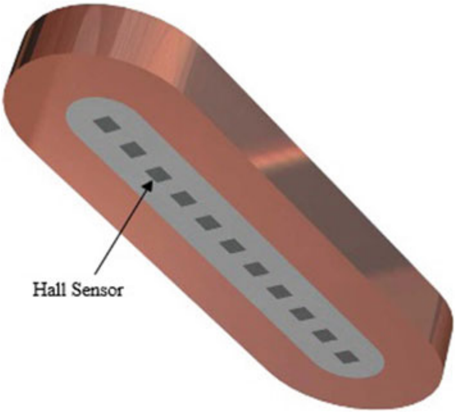

Fig. 8.19 A 'race-track' surface probe employing multiple Hall pick up sensors [13]

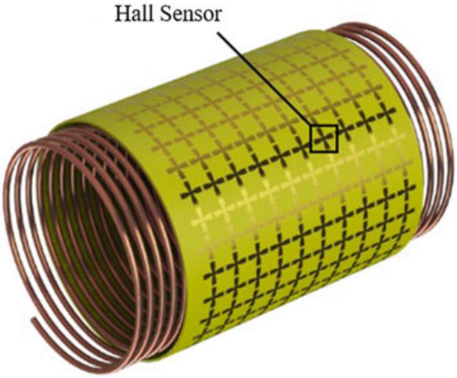

Fig. 8.20 Multiple Hall sensors arranged on a flexible substrate form the array of pick up sensors for this bobbin coil designed for inspecting the interior of holes or tubes

8.8.5 Conclusion

It is appropriate to make some concluding remarks concerning the relative merits of Hall devices and induction coils for magnetic field sensing. A review article published in [20] mentions the important advantages of induction coils: "simplicity of operation and design, wide frequency bandwidth and large dynamics." Further, a pick up coil contains no magnetic elements or excitation currents and the magnetic field is not disturbed, therefore, by the measurement of it. On the other hand, the output signal of an induction coil depends not simply on B but on $\partial B/\partial t$, which means that it is frequency dependent and less simple to handle than the Hall sensor in this regard. As mentioned above, linear spatial resolution achievable with an array of Hall sensors is 0.52 mm or better whereas micro-coils prepared through the use of thin-film techniques offer dimensions of approximately 1 mm. Considering dynamic range, Tumanski [20] points out that the measurable field range of the induction coil is the largest of any magnetic sensor—from less than 1 nT to greater than 1 T—but it must be borne in mind that this is true only if sensor size is not limited. By contrast, the Hall effect sensor is effective for measuring fields over less than one-third of this range; from around 1 mT to 1 T. Considering the limit of resolution between measured values of the magnetic induction field, the practical limit of resolution yielded by most sensors is dependent on achieving the noise floor. This has been estimated to be 100 fT $\text{Hz}^{-1/2}$ for the induction coil and much worse ($\approx$10 nT $\text{Hz}^{-1/2}$, 10^5 times larger!) for Hall sensors [21].

A more narrowly focused comparative study was published in [22] in which the performance of a ferrite-cored eddy current two-coil probe was compared with that of a hybrid probe with eddy current exciting coil and Hall sensor pick up. All three coils employed in the study comprised 100 turns of 0.08-mm-diameter wire wrapped on 1.6-mm-diameter ferrite core material. The two-coil probe comprised one exciting coil and one compensating coil held at fixed position in relation to the surface of the test-piece and wound in opposition to the primary coil, for the purpose of increasing the dynamic range of the probe. The Hall sensor was a Honeywell

Sensing and Control SS94A1 device with area approximately 7 × 15 mm^2. A series of experiments was constructed in which, firstly, the signal-to-noise ratio (SNR) of the two probes was compared in the task of detecting through-holes with diameter 1, 1.5, 2, and 2.5 mm in 1-mm-thick aluminum plate. It was concluded that, in these tests, the differential eddy current probe achieved higher SNR than the hybrid eddy current–Hall probe. Second, it was shown that the signal amplitude is linear as a function of probe lift-off, for the hybrid probe, whereas the rate of change of signal amplitude as a function of probe lift-off decreases with increasing lift-off in the case of the two-coil probe. Hence, the hybrid eddy current-Hall probe showed greater sensitivity in measuring lift-off values greater than 1.5 mm whereas the two-coil eddy current probe was more sensitivity for such measurements smaller than 1 mm. This result is applicable to measurement accuracy of the thickness of a nonconductive layer coating the metal test-piece, for example.

From this brief survey, it could be concluded that Hall sensor technology has yet to find its niche in hybrid eddy-current probes since pick up coils remain competitive for most applications. A niche may be emerging for arrays of miniaturized Hall devices on flexible substrates because of the high-resolution imaging capability that they can offer, but the cost and complexity of such a device may keep the uptake by industry slow in the short term.

8.9 Giant Magnetoresistor (GMR) Probes

The magnetoresistive (MR) effect is a phenomenon, whereby the resistance of a material changes in response to its magnetization. The MR phenomenon is described in standard texts on magnetism by Jiles, by Cullity, and by O'Handley [23–25] for example. Of these, O'Handley [25] gives the most thorough treatment of this topic. The so-called giant magnetoresistive (GMR) effect relies upon a magnetoresistive mechanism that occurs in certain multilayer materials and gives larger signal strength and sensitivity than the ordinary MR effect. The signal strength and sensitivity offered by a GMR sensor suggests construction of a hybrid probe that utilizes a GMR pick up in conjunction with an eddy-current excitation coil. In the context of NDE, GMR sensors have been explored primarily for detection of deep-lying flaws in aerospace structures.

Research articles and presentations on the use of GMR sensors for enhanced eddy-current flaw detection started to appear in the mid-1990s. The key improvement offered by GMR sensing in relation to eddy-current testing is the ability of the GMR sensor to respond to low-magnetic induction field amplitudes *at low frequency*. While a suitably designed search coil can measure smaller magnetic induction field amplitudes with better resolution than a GMR sensor, the fact that the Faraday effect relies upon time-variation of the induction field whereas the GMR sensor measures B directly is what gives the GMR sensor the advantage at low frequencies. An EC coil operating at low frequency or excited by a transient current induces eddy currents that penetrate deeply into the test material according to the skin effect (penetration depth

$\delta \propto f^{-1/2}$, Sect. 2.9) and the GMR sensor is capable of detecting the low-magnitude field perturbations associated with deep-lying flaws. As with the Hall sensor, relatively small physical dimensions of the GMR sensor also offer the possibility of fabricating sensor arrays to reduce inspection times.

In the following sections, a brief overview of the GMR effect is given in Sect. 8.9.1. The theme of deep-flaw detection will be discussed with reference to several key publications utilizing low-frequency time-harmonic and transient EC excitations, in Sects. 8.9.2 and 8.9.3, respectively. GMR array probes and a few specialist application areas are also mentioned.

8.9.1 The Giant Magnetoresistive Effect

Magnetoresistance is often quoted as fractional change in resistance and is typically a few percent in magnitude, for the ordinary and anisotropic MR effects that are observed in ferromagnetic materials at low temperatures. Details of these mechanisms are discussed in [25, pp. 573–584], for example. By contrast, the GMR effect relies upon antiferromagnetic coupling in a multilayer material that can result in MR ratios an order of magnitude larger than those observed for the ordinary and anisotropic MR effects.

The so-called giant magnetoresistive effect was first observed in 1988 in a material comprising FeCr multilayers, when an MR ratio of 50% was reported for measurements made at 4.2 K [26]. In this type of magnetoresistor, the Fe layers are coupled antiferromagnetically through the Cr layers and the application of an external magnetic field acts to align the magnetic dipole moments in the different Fe layers. As those moments become more closely aligned, there are fewer scattering events for conduction electrons and the resistivity declines.

Measuring the GMR effect for varying thicknesses of Cr, it was observed that the "magnetoresistance maxima occur at Cr layer thicknesses for which the magnetic layers are coupled antiferromagnetically" [27]. Experiments were performed in 1992 whose results suggest that the interfaces *between* the layers are predominant in controlling the electron scattering that leads to the alteration of resistance in response to the magnetic field applied to the material [28].

Two conventions exist for the definition of the GMR ratio. These refer the change in resistance ΔR either to its high-field value or to its low-field value. The former has the advantage of being bounded by 100% but the state for which there is zero applied external magnetic field ($\mathbf{H} = \mathbf{0}$) may not always correspond to complete antiferromagnetic coupling, for which $\mathbf{M} = \mathbf{0}$. This definition is often used in describing experimental data. The latter, where

$$\text{GMR ratio} = \frac{\Delta R}{R_0} \tag{8.11}$$

and R_0 is the resistance in the absence of an applied magnetic field, is more often used in calculations.

8.9.2 Defect Detection with the GMR Sensor

The primary advantages of the GMR sensor—its high sensitivity as a pick up device for measurement of subtle magnetic field perturbations at low magnitude—are emphasized in its role in the field of EC NDE. It appears in conjunction with an EC exciting coil as a hybrid EC-GMR probe often operating at low frequency for the detection of deep-lying flaws. The GMR sensor makes possible the detection of flaws situated beneath multiple layers of material, that were previously not detectable using conventional EC methods.

Several researchers have considered the inspection limits of EC-GMR probes in multilayered structures of relevance to aviation; in generic aluminum test-pieces [29–32], in particular wing-splice structures [33], and in the vicinity of fasteners or fastener holes [34, 35]. Others have considered various specialist applications such as for mechanical stress measurement of steel reinforcing bars in concrete [36], the detection of disconnects or short-circuits in printed circuit boards [37], the detection of conductive microbeads with radius ranging from 125 to 300 μm [38], and for real-time shrapnel detection in the medical context of key-hole surgery [39].

In a sequence of two papers, Wincheski and Namkung examined the detection capabilities of a commercially available GMR sensor incorporated into a self-nulling probe [29, 30]. The incorporation of the GMR sensor showed good performance but a limiting factor was increasing background noise with decreasing frequency for flaws deeper than approximately 5 mm [29]. Subsequently, active feedback was incorporated into the probe design in order to reduce the background field levels in the interior of the probe, in the vicinity of the GMR sensor [30]. With this modification, an EDM through-notch 14 mm long and 0.127 mm wide in an aluminum plate 1 mm thick was clearly detected beneath a stack of nine other 1-mm-thick aluminum plates, by the EC-GMR self-nulling probe operating at 185 Hz.

In 2001, Dogaru and Smith published work in which a GMR sensor was used as the pick up device in a hybrid EC-GMR probe. The paper demonstrated that GMR-based probes are capable of accurately sizing surface cracks, due in part to the fact that in this particular probe design the signal detected by the sensor was not heavily influenced by the applied field. The GMR sensor detected components of magnetic induction field tangential to the inspection surface.

Nair et al. presented work in 2006 that investigated the capability of EC-GMR probes for rapid, real-time inspection of aircraft structures [32]. The probe exhibited inspection rates comparable with magneto-optic imaging systems with the advantage of providing quantitative information about the magnetic induction field.

In the context of a particular aviation concern, Avrin developed a hybrid EC-GMR probe for crack and corrosion detection in wing-splice structures [33]. A narrow slot of length 6.3 mm was detected in the lowest of three aluminum plates, total thickness 25 mm, the slot being buried under 19 mm of aluminum. The probe was designed with a differential configuration to minimize background errors due to lift-off, edge effects, and the presence of steel fasteners in the structure. It was operated at 35 Hz.

Several authors have approached the difficult problem of detecting cracks in the immediate vicinity of fasteners in aircraft structures by using GMR sensors. Cracks under fasteners can grow in any of the metal layers—often three or more—that the fasteners hold together. The inspection scenario is complex geometrically, because it includes multiple layers and fasteners holding those layers together, and materially, because fasteners are made from various metals and may be ferromagnetic.

In work published in 2004, EC-GMR probes with specially shaped excitation coils, and judicious positioning and orientation of the GMR sensors, were shown capable of detecting 2.5-mm-long corner cracks in a two-layer aluminum structure with 13 mm of overlying material [34]. The probe was operated at 100 Hz. In 2010, feature extraction and image classification schemes were applied to response signals collected by GMR sensors, for the automatic detection of third-layer cracks at rivet sites in aircraft [35]. A 1-mm-long crack adjacent to the fastener in the lowest of three aluminum layers was detected under 10 mm of overlying material. In this case, a 100 Hz square waveform excitation current was used.

8.9.3 GMR Sensors and Transient EC NDE

It has already been mentioned that the ability of the GMR sensor to detect subtle perturbations in the magnetic induction field make it attractive for detecting deep-lying flaws. Similarly, transient EC NDE, in which eddy currents are excited by a near step-function change in current in the exciting coil, is suitable for detection of deep-lying flaws due to its exciting a quasi-continuum of frequencies in the induced eddy currents, meaning that their long-time response conveys information from deep within the test-piece. Putting transient EC excitation together with GMR sensing makes sense, therefore, for enhancing deep-lying flaw detection.

In 2010, a transient EC-GMR system was developed as an approach to detecting deep cracks at the sites of fasteners in multilayered aircraft structures [35]. This work was mentioned in the previous section in the context of automatic detection of third-layer cracks at rivet sites. Here, it is noted that the EC excitation was in the form of a square waveform, and that the method exploited the advantages of a transient current excitation as well as the ability of the GMR sensor to measure the magnetic flux density directly.

8.9.4 GMR Arrays

Developing the 2010 work of Kim et al. [35], Postolache et al. [40] in 2013 formed a probe from two planar exciting coils, a rectangular magnetic field biasing coil, and a linear array of five GMR sensors for speeding up the process of defect detection.

8.9.5 Conclusion

The relative merits of the induction coil and the Hall device as magnetic field sensors were discussed in Sect. 8.8.5. Considering similar characteristics of GMR sensors [20], it is found that the range of the magnetic induction field measurable using GMR sensors is from around 10 nT to well over 1 T. This range is outperformed by the induction coil if its design parameters are unconstrained (<1 nT to >1 T), but not by the Hall sensor (≈ 1 mT to 1 T). In terms of induction field resolution, magnetoresistive sensors perform at around 100 pT $\text{Hz}^{-1/2}$, again poorer than the induction coil (≈ 100 fT $\text{Hz}^{-1/2}$) but better than the Hall sensor (≈ 10 nT $\text{Hz}^{-1/2}$).

8.10 Summary

In this chapter, many different kinds of probes have been discussed that optimize the EC measurement of material properties or the detection of defects of various types. The absolute coil, which acts as both driver and pick up, is the foundational unit from which probes can be formed by adding further coils or solid state magnetometers. In the next and final chapter of this book, the physics and mathematics describing the interaction between the coil's excitation field (or induced eddy currents) and defects of various kinds are considered. Analytic expressions are derived that describe the impedance change in the probe that occurs when the induced eddy currents encounter a crack or other defect.

8.11 Exercises

1. List five sources of error, uncertainty, or noise in EC impedance measurements made with an absolute probe.
2. List three reasons why the current density is not uniform over the cross-section of a real (non-ideal) EC coil.
3. Which of the following probe types—absolute probe, differential probe, single encircling coil, differential bobbin probe, reflection surface probe—would be best for each application listed? Justify your claims.
    i. Conductivity measurement of a metal rod;
    ii. detection of a surface crack much smaller than the probe drive coil;
    iii. detection of a metal support structure on the outside of a metal tube;
    iv. thickness measurement of an insulating layer on a flat metal sheet;
    v. reflection surface probe.
4. On the same impedance-plane plot, sketch lift-off curves produced by a surface coil as it is moved from air to (i) the surface of an aluminum plate and (ii) the

surface of a ferromagnetic steel plate. Explain the physics underlying the difference between the two curves, with reference to Faraday's Law of electromagnetic induction.

5. Edwin Hall's experimental demonstration of what became known as the Hall effect was made on gold leaf. Given that the charge carrier density in gold at 20 °C is 5.90×10^{28} electrons/m^3 and that the charge on an electron is 1.60×10^{-19} C, evaluate the Hall voltage generated across a gold film 10 μm thick carrying current 0.01 A in the presence of a normal **B**-field of magnitude 10 T.
6. List four advantages of using a giant magnetoresistor pick up, rather than a pick up coil, in conjunction with an eddy-current excitation coil. Are there any disadvantages?

References

1. Lu, Y.: Potential drop and eddy current nondestructive evaluation problems. Ph.D. thesis, Iowa State University (2012)
2. Diaz, A.A., Mathews, R.A., Hixon, J., Doctor, S.R., Jackson, D.A., Norris, W.E.: Assessment of eddy current testing for the detection of cracks in cast stainless steel reactor piping components. U.S. Nuclear Regulatory Commission, NUREG/CR-6929 (2007)
3. Lamtenzan, D., Washer, G., Lozev, M.: Detection and sizing of cracks in structural steel using the eddy current method. U.S. Department of Transportation Federal Highway Administration, FHWA-RD-00-018 (2000)
4. Ditchburn, R.J., Burke, S.K., Posada, M.: Eddy-current nondestructive inspection with thin spiral coils: long cracks in steel. J. Nondestruct. Eval. **22**, 63–77 (2003)
5. Burke, S.K., Ditchburn, R.J.: Mutual impedance of planar eddy-current driver-pickup spiral coils. Res. Nondestruct. Eval. **19**, 1–19 (2008)
6. Ditchburn, R.J., Burke, S.K.: Planar rectangular spiral coils in eddy-current non-destructive inspection. NDT&E Int. **38**, 690–700 (2005)
7. Burke, S.K., Ditchburn, R.J., Theodoulidis, T.P.: Impedance of curved rectangular spiral coils around a conductive cylinder. J. Appl. Phys. **104**, 014912 (2008)
8. Burke, S.K., Ditchburn, R.J., Theodoulidis, T.P.: Impedance of a curved spiral coil around a conductive cylinder. NDT&E Int. **64**, 1–6 (2014)
9. Harrison, D.J.: The detection of corrosion in layered structures using transient eddy currents. In: Collins, R., Dover, W.D., Bowler, J.R., Miya, K. (eds.) Nondestructive Testing of Materials, 1st International Workshop on Electromagnetic Nondestructive Evaluation, London, September 1995. Studies in Applied Electromagnetics and Mechanics, vol. 8, pp. 115–124. IOS Press, Amsterdam (1995)
10. Smith, R.A., Harrison, D.J.: Hall sensor arrays for rapid large-area transient eddy current inspection. Insight **46**, 142–146 (2004)
11. Park, D.-G., Angani, C.S., Rao, B.C.P., Vértesy, G., Lee, D.-H., Kim, K.-H.: Detection of the subsurface cracks in a stainless steel plate using pulsed eddy current. J. Nondestruct. Eval. **32**, 350–353 (2013)
12. Angani, C.S., Ramos, H.G., Ribeiro, A.L., Rocha, T.J., Prashanth, B.: Transient eddy current oscillations method for the inspection of thickness change in stainless steel. Sens. Actuators A **233**, 217–223 (2015)
13. Sun, H.: Electromagnetic methods for measuring material properties of cylindrical rods and array probes for rapid flaw inspection Ph.D. thesis, Iowa State University (2005)

14. Jun, J., Hwang, J., Lee, J.: Quantitative nondestructive evaluation of the crack on the austenite stainless steel using the induced eddy current and the Hall sensor array. In: Paper Presented at the Instrumentation and Measurement Technology Conference - IMTC 2007, Warsaw, Poland, 1–3 May 2007
15. Jun, J., Lee, J., Kim, J., Le, M., Lee, S.: Eddy current imager based on bobbin-type Hall sensor arrays for nondestructive evaluation in small-bore piping system. In: Thompson, D.O., Chimenti, D.E. (eds.) 39th Annual Review of Progress in Quantitative Nondestructive Evaluation, Denver, CO, USA, July 2012. AIP Conference Proceedings, vol. 1511, pp. 502–509. American Institute of Physics, Melville (2013)
16. Wang, Z., Shaygan, M., Otto, M., Schall, D., Neumaier, D.: Flexible Hall sensors based on graphene. Nanoscale **8**, 7683–7687 (2016)
17. Public domain image. https://commons.wikimedia.org/wiki/File:Edwin_Herbert_Hall_(1855-1938).jpg. Accessed 30 Jan 2019
18. Lebrun, B., Jayet, Y., Baboux, J.-C.: Pulsed eddy current signal analysis: application to the experimental detection and characterization of deep flaws in highly conductive materials. NDT&E Int. **30**, 163–170 (1997)
19. Huang, S., Wang, S.: New Technologies in Electromagnetic Non-destructive Testing. Springer, Singapore (2016)
20. Tumanski, S.: Induction coil sensors-a review. Meas. Sci. Technol. **18**, R31–R46 (2007)
21. Prance, R.J., Clark, T.D., Prance, H.: Room temperature induction magnetometers. In: Grimes, C.A., Dickey, E.C., Pishko, M.V. (eds.) Encyclopedia of Sensors, vol. 10, pp. 1–12. American Scientific Publishers, Valencia (2006)
22. Garcia-Martin, J., Gomez-Gil, J.: Comparative evaluation of coil and Hall probes in hole detection and thickness measurement on aluminum plates using eddy current testing. Russ. J. Nondestruct. Test. **49**, 482–491 (2013)
23. Jiles, D.C.: Introduction to the Principles of Materials Evaluation. CRC Press/Taylor & Francis Group, Boca Raton (2008)
24. Cullity, B.D., Graham, C.D.: Introduction to Magnetic Materials, 2nd edn. IEEE Press, Hoboken (2009)
25. O'Handley, R.C.: Modern Magnetic Materials. Wiley, New York (2000)
26. Baibich, M.N., Broto, J.M., Fert, A., Nguyen Van Dau, f., Petroff, F., Etienne, P., Creuzet, G., Friedrich, A., Chazelas, J.: Phys. Rev. Lett. **61**, 2472–2475 (1988)
27. Parkin, S.S.P., More, N., Roche, K.P.: Oscillations in exchange coupling and magnetoresistance in metallic superlattice structures - Co/Ru, Co/Cr, and Fe/Cr. Phys. Rev. Lett. **64**, 2304–2307 (1990)
28. Parkin, S.S.P.: Dramatic enhancement of interlayer exchange coupling and giant magnetoresistance in $Ni_{81}Fe_{19}$/Cu multilayers by addition of thin Co interface layers. Appl. Phys. Lett. **61**, 1358–1360 (1992)
29. Wincheski, B., Namkung, M.: Development of very low frequency self-nulling probe for inspection of thick layered aluminum structures. In: Thompson, D.O., Chimenti, D.E. (eds.) 25th Annual Review of Progress in Quantitative Nondestructive Evaluation, Snowbird, UT, USA, July 1998, vol. 18A, pp. 1177–1184. Springer, USA (1999)
30. Wincheski, B., Namkung, M.: Deep flaw detection with giant magnetoresistive (GMR) based self-nulling probe. In: Thompson, D.O., Chimenti, D.E. (eds.) 26th Annual Review of Progress in Quantitative Nondestructive Evaluation, Montreal, Canada, July 1999. AIP Conference Proceedings, vol. 509, pp. 465–472. American Institute of Physics, Melville (2000)
31. Dogaru, T., Smith, S.T.: Giant magnetoresistance-based eddy-current sensor. IEEE T. Magn. **37**, 3831–3838 (2001)
32. Nair, N.V., Melapudi, V.R., Jimenez, H.R., Liu, X., Deng, Y., Zeng, Z., Udpa, L., Moran, T.J., Udpa, S.S.: A GMR-based eddy current system for NDE of aircraft structures. IEEE T. Magn. **42**, 3312–3314 (2006)
33. Avrin, W.F.: Eddy current measurements with magneto-resistive sensors: third-layer flaw detection in a wing-splice structure 25 mm thick. In: Mal, A.K. (ed.) Nondestructive Evaluation of Aging Aircraft, Airports, and Aerospace Hardware IV. Proceedings of SPIE, vol. 3994, pp. 29-36. SPIE (2000)

34. Dogaru, T., Smith, C.H., Schneider, R.W., Smith, S.T.: Deep crack detection around fastener holes in airplane multi-layered structures using GMR-based eddy current probes. In: Thompson, D.O., Chimenti, D.E., (eds.) 30th Annual Review of Progress in Quantitative Nondestructive Evaluation, Green Bay, WI, USA, July 2003, vols. 23A and 23B, pp. 398–405. American Institute of Physics, Melville (2004)
35. Kim, J., Yang, G., Udpa, L., Udpa, S.: Classification of pulsed eddy current GMR data on aircraft structures. NDT&E Int. **43**, 141–144 (2010)
36. Ricken, W., Liu, J., Becker, W.-J.: GMR and eddy current sensor in use of stress measurement. Sens. Actuators A **91**, 42–45 (2001)
37. Yamada, S., Chomsuwan, K., Fukuda, Y., Iwahara, M., Wakiwaka, H., Shoji, S.: Eddy-current testing probe with spin-valve type GMR sensor for printed circuit board inspection. IEEE T. Magn. **40**, 2676–2678 (2004)
38. Yamada, S., Chomsuwan, K., Hagino, T., Tian, H., Minamide, K., Iwahara, M.: Conductive microbead array detection by high-frequency eddy-current testing technique with SV-GMR sensor. IEEE T. Magn. **41**, 3622–3624 (2005)
39. Sakthivel, M., George, B., Sivaprakasam, M.: A novel GMR-based eddy current sensing probe with extended sensing range. IEEE T. Magn. **52**, 4000512 (2016)
40. Postolache, O., Ribeiro, A.L., Ramos, H.G.: GMR array uniform eddy current probe for defect detection in conductive specimens. Measurement **46**, 4369–4378 (2013)

Chapter 9
Flaw Models

Abstract The focus of this chapter is the effect of defects on the impedance of an eddy-current probe coil. Simple flaw shapes are considered, initially, for the purpose of showing how the various characteristics of a defect (its size, shape, location, and filler material, etc.) influence the observed change in impedance of the eddy-current coil. Two regimes are considered: the “small flaw” regime, when the flaw is significantly smaller than the electromagnetic skin depth of the eddy currents in the material, and the “thin-skin’ regime, when a surface crack is significantly deeper than the electromagnetic skin depth. In these regimes, analytic solutions for the impedance change due to the defect can be derived. The analytic solutions give clear insight into the way in which the coil impedance changes due to these and similar flaws.

9.1 Introduction

The first part of this chapter is dedicated to Michael Leonard Burrows, who laid out so beautifully in his Ph.D. thesis of 1964 [1] the theory in which the response of a small flaw, due to eddy currents incident on it, is approximated as that of a Hertzian dipole. Indeed, the development in Sect. 9.4 of this chapter closely follows that of Burrows [1]. This chapter begins with a presentation of a theorem that is very useful in the calculation of impedance changes in EC NDE, the *reciprocity theorem* originally proposed by Rumsey [2]. Following that is a discussion of electric dipoles, current dipoles, and magnetic dipoles, their scalar potentials and associated electric or magnetic fields. In the following section it is revealed, by following Burrows, how a small inclusion in a test-piece may behave as a current–dipole source that perturbs the applied electric field, or as a magnetic–dipole source that perturbs the applied magnetic field. A “small” flaw is defined as one which is somewhat smaller than the electromagnetic skin depth in the test-piece, δ. The impedance change due to the presence of these defects and various other small, surface defects is expressed analytically.

Following the treatment of the small flaw, it is shown how the impedance change in an eddy-current coil may be calculated from an integral of the complex Poynting vector over the surface of the flaw. This approach is then used to derive expressions

N. Bowler, *Eddy-Current Nondestructive Evaluation*,
Springer Series in Measurement Science and Technology,
https://doi.org/10.1007/978-1-4939-9629-2_9

for ΔZ due to various surface cracks in the high-frequency (thin-skin) regime, in which the defect size is assumed much larger than δ.

The chapter concludes with a short discussion of the way in which ΔZ in an EC coil due to a crack may be modeled in general by populating the crack with a surface distribution of current dipoles whose strength varies over the surface of the crack according to certain boundary conditions.

9.2 Reciprocity Theorem and ΔZ

The reciprocity theorem shows that, in a probe formed from two coils, it does not matter which of the coils plays the role of the energizing coil, and which the role of the pick up coil. In either case, the measured impedance is the same. In addition, the reciprocity theorem may be used to derive an expression for the impedance change in a coil due to the presence of a defect, in cases where the defect may be represented as the source of a perturbation to the induced eddy-current density. In some cases, such a source is appropriately represented by a current dipole.

An expression of the reciprocity theorem will be derived by starting with the time-harmonic forms of Faraday's Law and Ampère's Law, (6.5) and (6.7), respectively, reproduced here for convenience;

$$\nabla \times \mathbf{E} = -j\omega \mathbf{B}, \tag{9.1}$$

$$\nabla \times \mathbf{H} = \mathbf{J}_\mathrm{s} + \mathbf{J}_\mathrm{ec}, \tag{9.2}$$

where $\mathbf{J}_\mathrm{s}$ is the current density in the source coil and $\mathbf{J}_\mathrm{ec}$ the eddy-current density induced in the test-piece. Note that $\mathbf{J}_\mathrm{s}$ and $\mathbf{J}_\mathrm{ec}$ are spatially confined—within the windings of the source coil and within the test-piece, respectively—whereas $\mathbf{H}$ exists in all space. Now consider two distinct sets of externally-imposed current densities, $\mathbf{J}_\mathrm{s}^{(i)}$, $i = 1, 2$, and their corresponding induced eddy current densities, $\mathbf{J}_\mathrm{ec}^{(i)}$. Then,

$$\nabla \times \mathbf{E}^{(1)} = -j\omega \mathbf{B}^{(1)}, \qquad \nabla \times \mathbf{H}^{(1)} = \mathbf{J}_\mathrm{s}^{(1)} + \mathbf{J}_\mathrm{ec}^{(1)} \tag{9.3}$$

$$\nabla \times \mathbf{E}^{(2)} = -j\omega \mathbf{B}^{(2)}, \qquad \nabla \times \mathbf{H}^{(2)} = \mathbf{J}_\mathrm{s}^{(2)} + \mathbf{J}_\mathrm{ec}^{(2)} \tag{9.4}$$

Take the scalar products of (9.3a) (the left-hand equation) with $\mathbf{H}^{(2)}$, and of (9.3b) (the right-hand equation) with $\mathbf{E}^{(2)}$. Similarly, take the scalar product of (9.4a) with $-\mathbf{H}^{(1)}$ and of (9.4b) with $-\mathbf{E}^{(1)}$, respectively. Summing all four resulting equations gives

$$\begin{aligned} \left[\mathbf{H}^{(2)} \cdot \nabla \times \mathbf{E}^{(1)} - \mathbf{E}^{(1)} \cdot \nabla \times \mathbf{H}^{(2)}\right] - \left[\mathbf{H}^{(1)} \cdot \nabla \times \mathbf{E}^{(2)} - \mathbf{E}^{(2)} \cdot \nabla \times \mathbf{H}^{(1)}\right] = \\ -j\omega \left[\mathbf{H}^{(2)} \cdot \mathbf{B}^{(1)} - \mathbf{H}^{(1)} \cdot \mathbf{B}^{(2)}\right] + \left[\mathbf{E}^{(2)} \cdot \mathbf{J}_\mathrm{ec}^{(1)} - \mathbf{E}^{(1)} \cdot \mathbf{J}_\mathrm{ec}^{(2)}\right] \\ +\mathbf{E}^{(2)} \cdot \mathbf{J}_\mathrm{s}^{(1)} - \mathbf{E}^{(1)} \cdot \mathbf{J}_\mathrm{s}^{(2)} \end{aligned} \tag{9.5}$$

Due to the relations $\mathbf{B}^{(i)} = \mu\mathbf{H}^{(i)}$ and $\mathbf{J}^{(i)} = \sigma\mathbf{E}^{(i)}$, the two bracketed terms on the second line of (9.5) are each zero. Applying the vector identity (10.47) to the terms in the first line of (9.5) then gives

$$\nabla \cdot \left[\mathbf{E}^{(1)} \times \mathbf{H}^{(2)} - \mathbf{E}^{(2)} \times \mathbf{H}^{(1)}\right] = \mathbf{E}^{(2)} \cdot \mathbf{J}_\mathrm{s}^{(1)} - \mathbf{E}^{(1)} \cdot \mathbf{J}_\mathrm{s}^{(2)}. \tag{9.6}$$

Now integrate over all space (volume V) and apply the divergence theorem (10.48) to the term arising from the left-hand side of (9.6) to obtain

$$\int_S \left[\mathbf{E}^{(1)} \times \mathbf{H}^{(2)} - \mathbf{E}^{(2)} \times \mathbf{H}^{(1)}\right] \cdot d\mathbf{S} = \int_V \mathbf{E}^{(2)} \cdot \mathbf{J}_\mathrm{s}^{(1)} dV - \int_V \mathbf{E}^{(1)} \cdot \mathbf{J}_\mathrm{s}^{(2)} dV. \tag{9.7}$$

If the sources $\mathbf{J}_\mathrm{s}^{(i)}$ are bounded in space, then the integral on the left-hand side of (9.7) can be made zero by taking the surface S to be infinitely remote. The null result emerges because the electric and magnetic fields decay at least as fast as r^{-2} for quasi-static, bounded sources. Further, the integrals on the right-hand side of (9.7) can be written more particularly by specifying the volume over which they yield a nonzero result, $V^{(i)}$, to be the volume of the ith source $\mathbf{J}_\mathrm{s}^{(i)}$. At last, the following statement of the reciprocity theorem is obtained:

$$\int_{V^{(1)}} \mathbf{E}^{(2)} \cdot \mathbf{J}_\mathrm{s}^{(1)} dV = \int_{V^{(2)}} \mathbf{E}^{(1)} \cdot \mathbf{J}_\mathrm{s}^{(2)} dV. \tag{9.8}$$

Clearly, this expression is invariant under the transformation $1 \leftrightarrow 2$, hence the term "reciprocity".

9.2.1 Coil and Flaw

Now consider the reciprocity relation in the context of impedance change in an eddy current coil due to a defect. First, make $\mathbf{J}_\mathrm{s}^{(1)}$ in (9.8) the source due to current flowing in the energizing coil. Next, note that in the quasi-static regime $\mathbf{J}_\mathrm{s} = \mathcal{I} d\mathbf{l}$ for a time-harmonic current, so that the left-hand side of (9.8) may be written in terms of a line integral over the coil windings. The left-hand side of (9.8) then becomes

$$\int_{V^{(1)}} \mathbf{E}^{(2)} \cdot \mathbf{J}_\mathrm{s}^{(1)} dV = \mathcal{I}^{(1)} \int_{C^{(1)}} \mathbf{E}^{(2)} \cdot d\mathbf{l}^{(1)}, \tag{9.9}$$

for a coil whose current $\mathcal{I}^{(1)}$ flows along path $C^{(1)}$.

It is necessary to make a conceptual jump at this point, to consider a flaw as a *source* of eddy-current density. How can a flaw be a source of eddy currents? It is certainly true that a defect does not, in and of itself, *generate* eddy currents. The concept is more subtle. A flaw *perturbs* the eddy currents that are induced in a test-piece by the exciting coil, and it can be conceived that the *perturbed part* of the eddy currents are the source of impedance *change* in the pick-up coil. In this conception, the perturbed eddy currents can be regarded as a secondary current source that can be handled by (9.8).

Allowing this to be the case, the mathematics proceeds by letting $\mathbf{J}_\mathrm{s}^{(2)}$ represent the part of the eddy current density perturbed by the presence of a defect. This means that $\mathbf{J}_\mathrm{s}^{(2)}$ represents that part of the eddy current density that is due to the presence of the defect only, *not* including the eddy-current density that is induced in the absence of the defect.

Applying this reasoning to the right-hand side of (9.8) and replacing the left-hand side of (9.8) according to (9.9), the following re-expression of (9.8) is obtained.

$$\mathcal{I}^{(1)} \int_{C^{(1)}} \mathbf{E}^{(2)} \cdot d\mathbf{l}^{(1)} = \int_{V^{(2)}} \mathbf{E}^{(1)} \cdot \mathbf{J}_\mathrm{s}^{(2)} dV. \tag{9.10}$$

The left-hand side of (9.10) is the product of the current in the energizing coil $\mathcal{I}^{(1)}$ and the voltage induced in that same coil due to perturbation of the current density in the vicinity of the flaw, represented by the integral over $C^{(1)}$. To obtain the impedance change in the coil due to the perturbation of the current density by the flaw, (4.25) is applied to obtain

$$\Delta Z = \frac{1}{\left[\mathcal{I}^{(1)}\right]^2} \int_{V^{(2)}} \mathbf{E}^{(1)} \cdot \mathbf{J}_\mathrm{s}^{(2)} dV. \tag{9.11}$$

In (9.11), it is clear that ΔZ may be computed by representing the defect as a source of current density, $\mathbf{J}_\mathrm{s}^{(2)}$.

Sometimes, adopting terminology used to describe light scattering due to objects with dimension similar to the wavelength of the light, $\mathbf{J}_\mathrm{s}^{(2)}$ has been termed the "scattered" eddy current density. In this chapter, the term "perturbed" is used to refer to that part of the eddy-current density (or other field) that arises due to the presence of the flaw. Further discussion of this point is given around (9.27).

9.2.2 Two Coils

The reciprocity relation is also illuminating on the interaction of two coils. Consider the case in which the current sources in (9.8) are both coils of wire. Then, in the quasi-static regime, $\mathbf{J}_\mathrm{s} = I d\mathbf{l}$ and (9.8) becomes

$$\mathcal{I}^{(1)} \int_{C^{(1)}} \mathbf{E}^{(2)} \cdot d\mathbf{l}^{(1)} = \mathcal{I}^{(2)} \int_{C^{(2)}} \mathbf{E}^{(1)} \cdot d\mathbf{l}^{(2)}, \tag{9.12}$$

where the $C^{(i)}, i = 1, 2$, indicate the path of integration around the wire loops forming the coils. With reference to (4.3), it can be seen that the integral terms represent the electromotance $\mathcal{V}^{(i,j)}$ induced in coil i due to the current flowing in coil j or vice versa. Hence, (9.12) may be written as

$$\mathcal{I}^{(1)}\mathcal{V}^{(1,2)} = \mathcal{I}^{(2)}\mathcal{V}^{(2,1)} \tag{9.13}$$

and these terms represent electrical power. Writing the electromotance in terms of impedance via the relation

$$\mathcal{V}^{(i,j)} = \mathcal{I}^{(j)}Z^{(i,j)} \tag{9.14}$$

gives

$$\mathcal{I}^{(1)}\mathcal{I}^{(2)}Z^{(1,2)} = \mathcal{I}^{(2)}\mathcal{I}^{(1)}Z^{(2,1)}$$

and hence

$$Z^{(1,2)} = Z^{(2,1)}. \tag{9.15}$$

In (9.15) the $Z^{(i,j)}$ represent *trans*impedance, the impedance of the ith coil due to the source current in the jth coil. Equation (9.15) is another expression of the reciprocity relation, showing that “it is immaterial which of two coils plays the part of the energizing coil and which the pick-up coil” [1].

9.3 The Dipole

As mentioned at the beginning of this chapter, Burrows showed in his Ph.D. thesis of 1964 [1] that the perturbation of eddy currents incident upon a small volumetric flaw can often be modeled as a current dipole of appropriate strength. Other flaws can be modeled as a distribution of current dipoles, Sect. 9.4.2. For this reason, it is useful to review the electric and magnetic field distributions associated with the electric and magnetic dipoles. I begin with the classic derivation of the electric field due to an electric dipole and then show how the current density distribution associated with a current dipole may be deduced from it. Similarly, the form of the magnetic field distribution due to a magnetic dipole is given.

9.3.1 Electric Dipole

An electric dipole consists of two equal and opposite charges separated by vector $\mathbf{l}$. The vector is directed from the negative to the positive of the two charges. The electrostatic potential V_P due to the dipole at an arbitrary point P in space can be determined by summing potentials due to the two charges. Considering the configuration shown in Fig. 9.1, the potential at P is given by

$$V_P = \frac{Q}{4\pi\epsilon r_2} - \frac{Q}{4\pi\epsilon r_1} = \frac{Q(r_1 - r_2)}{4\pi\epsilon r_1 r_2} \tag{9.16}$$

where ϵ is the permittivity of the medium. But, from trigonometry,

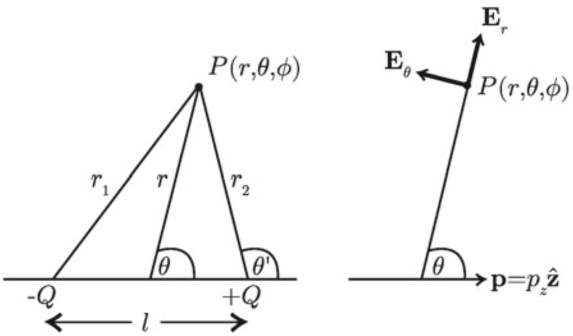

Fig. 9.1 Configuration for calculating the potential due to the electrostatic dipole at arbitrary field point $P(r, \theta, \phi)$, at left, and showing the components of the electric field due to a dipole directed along the z-axis, at right

$$r_1^2 = r_2^2 + l^2 + 2r_2 l \cos\theta'$$

which can be rearranged to show that

$$r_1 - r_2 = \frac{l(l + 2r_2\cos\theta')}{r_1 + r_2}.$$

When this relation is substituted into (9.16), V_P becomes

$$V_P = \frac{Ql(l + 2r_2\cos\theta')}{4\pi\epsilon r_1 r_2(r_1 + r_2)}. \tag{9.17}$$

This is an exact expression, but it can be simplified in the case of an ideal dipole for which $l \ll r$. Under these circumstances, $r_1 \to r$, $r_2 \to r$ and $\theta' \to \theta$. Taking these limits, (9.17) becomes

$$V_P = \frac{Ql\cos\theta}{4\pi\epsilon r^2} = \frac{p^Q\cos\theta}{4\pi\epsilon r^2} \tag{9.18}$$

where $p^Q = Ql$ is the electric dipole moment with unit Coulomb meter (Cm). From (9.18), the electric field of the dipole can be obtained from the relation $\mathbf{E} = -\nabla V$, yielding

$$\mathbf{E}(r,\theta) = \frac{p^Q}{4\pi\epsilon r^3}(2\cos\theta\,\hat{r} + \sin\theta\,\hat{\theta}) \tag{9.19}$$

and then

$$\mathbf{D}(r,\theta) = \epsilon\mathbf{E}(r,\theta) = \frac{p^Q}{4\pi r^3}(2\cos\theta\,\hat{r} + \sin\theta\,\hat{\theta}) \tag{9.20}$$

for a dipole at the origin of coordinates, directed in the z-direction ($\mathbf{p} = p_z\hat{z}$). Note, there is no $\hat{\phi}$-component of $\mathbf{E}$ for a z-directed dipole, due to symmetry, and $\mathbf{E}$ is independent of ϕ, because the dipole field is invariant with respect to rotation about the z-axis.

9.3.2 *Current Dipole*

The well-known development leading to (9.19) and (9.20) is for an electrostatic dipole embedded in a dielectric material of permittivity ϵ [3]. A similar field distribution, for the current density **J**, arises from the dipole-like behavior of a small defect in a conductor with conductivity σ. In the latter case, the current density **J** in the conductor is identified with the electric displacement **D** in (9.20), and σ identified with ϵ, so that the current density distribution due to current dipole p^J is given by

$$\mathbf{J}(r,\theta) = \sigma\mathbf{E}(r,\theta) = \frac{p^J}{4\pi r^3}(2\cos\theta\,\hat{r} + \sin\theta\,\hat{\theta}). \tag{9.21}$$

In (9.21), $p^J = Il$ now represents a current dipole and has unit Ampère-meter (Am). As before, (9.21) holds for a dipole at the origin of coordinates, directed in the z-direction.

9.3.3 *Magnetic Dipole*

The magnetic dipole moment of a current loop, **m**, is defined to be the product of the current flowing in the loop, I, and the vector area of the loop, **S**, such that $\mathbf{m} = I\mathbf{S}$ as discussed in Sect. 3.2 and shown schematically in Fig. 3.2. The units of **m** are Ampère-meter-squared (Am^2). Note that the magnetic dipole moment of a long bar magnet can also be defined in terms of the product of the pole strength and the length of the magnet, see (3.1) [4], which is analogous with the definition of the electric dipole moment $p^Q = Ql$ but is not useful in general. The definition given in (3.2) connects the magnetic dipole with its fundamental source—charge in motion.

By analogy with the derivation of the current density **J** associated with the current dipole in a conductor, it can be shown that the magnetic field **H** associated with a magnetic dipole $\mathbf{m} = m_z\hat{z}$ is given by

$$\mathbf{H}(r,\theta) = \frac{m}{4\pi r^3}(2\cos\theta\,\hat{r} + \sin\theta\,\hat{\theta}). \tag{9.22}$$

9.4 Small Flaws

Certain simple calculations of the impedance change due to a flaw ΔZ can be made under the "small flaw" approximation. A small flaw is defined as one whose dimension Δ is

1. Small compared with the electromagnetic skin depth, $\delta = [2/(\omega\mu\sigma)]^{1/2}$, in both the flaw and the surrounding metal;

2. Sufficiently small that the incident field is approximately uniform over the flaw—this means that the magnitude and direction of the eddy-current density incident upon a volume similar to that occupied by the flaw does not change appreciably in magnitude or direction from point to point within that volume;
3. Small compared with the distance between the flaw and the nearest discontinuity in the specimen. A discontinuity may be another flaw, a joint with another piece of material or the surface of the test-piece, etc.

The first and second of these "small flaw" conditions may be connected. One way of satisfying both of them is to impose the condition that the flaw dimension Δ must be less than, say, one-tenth of the electromagnetic skin depth, i.e., $\delta/\Delta > 10$. This condition usually gives good accuracy in applying solutions obtained under the approximation of a small flaw. If the flaw is as large as one-third of the skin depth, or $\delta/\Delta > 3$, accuracy will likely still be tolerable. For smaller δ/Δ, the full solution to Maxwell's equations needs to be determined. Similar conditions can be stated in relation to the third item listed above.

If δ is assumed large with respect to the flaw size, it is implied that the frequency is low. In fact, within the small flaw approximation it is assumed that the static form of Maxwell's equations may be applied. Taking the limit $\omega \to 0$ in the set of equations given in Table 5.2 gives the relations shown in Table 9.1. This means that, unlike at arbitrary frequency, **E** and **H** are *decoupled* in the static regime. Taking Gauss' Law for both electric and magnetic fields, it is clear that **E** and **H** may both be written as the gradient of different scalar potentials;

$$\mathbf{E} = -\nabla V \tag{9.23}$$

$$\mathbf{H} = -\nabla \Phi. \tag{9.24}$$

From the mathematical point of view, this formulation is beneficial because then the governing equations for the system are simply Laplace equations of the scalar potentials:

$$\nabla^2 V = 0 \tag{9.25}$$

$$\nabla^2 \Phi = 0, \tag{9.26}$$

Table 9.1 The static form of Maxwell's equations. The general form is given in the central column. The form obtained by applying constitutive relations (2.25) and (2.33), and noting that there is no volume charge distribution in a metal, is given in the right-hand column

Law	Differential form	In a metal
Faraday's law	$\nabla \times \mathbf{E} = 0$	$\nabla \times \mathbf{E} = 0$
Maxwell–Ampère law	$\nabla \times \mathbf{H} = \mathbf{J}$	$\nabla \times \mathbf{H} = \mathbf{J}$
Gauss' law	$\nabla \cdot \mathbf{D} = \rho_v$	$\nabla \cdot \mathbf{E} = 0$
Gauss' law for magnetic fields	$\nabla \cdot \mathbf{B} = 0$	$\nabla \cdot \mathbf{H} = 0$

obtained by inserting (9.25) and (9.26) into the static form of Gauss' Law and Gauss' Law for magnetic fields, Table 9.1, respectively. When appropriate boundary conditions are specified, (9.25) and (9.26) can be solved and then the electric and magnetic fields determined through relations (9.23) and (9.24).

I now introduce terminology that shall be used in the solution of (9.25) and (9.26). Consider a flaw or inclusion of conductivity σ_f in a metal of conductivity σ so that the flaw is defined by a discontinuity in the conductivity of the test-piece. The eddy current density induced by the coil is assumed to be uniform at the flaw, according to assumption 2 in the small flaw approximation. The incident current density will be denoted $\mathbf{J}^{(i)}$. When $\mathbf{J}^{(i)}$ encounters the flaw, it is perturbed. The perturbed field will be denoted $\mathbf{J}^{(s)}$. The total field is the sum of both the incident and the perturbed fields so that

$$\mathbf{J}^{(t)} = \mathbf{J}^{(i)} + \mathbf{J}^{(s)}. \tag{9.27}$$

Note, $\mathbf{J}^{(s)}$ has associated with it a perturbed magnetic field due to Ampère's Law. In the case of a discontinuity in the conductivity of the test-piece, this is the magnetic field whose changing flux is detected by the EC pick up coil.

Now consider the case in which a flaw or inclusion in a metal test-piece also has permeability μ_f that is different from that of the host, so that $\mu_\mathrm{f} \neq \mu$. In this case, there is an additional component to the perturbed magnetic field that satisfies

$$\nabla \times \mathbf{H}' = 0, \qquad \nabla \cdot \mathbf{H}' = 0, \qquad \mathbf{B}' = \mu \mathbf{H}'. \tag{9.28}$$

There is no current source of $\mathbf{H}'$ because it arises due to contrast in permeability between the inclusion and the host, rather than due to a perturbation of the current.

So we see that there are two mechanisms by which field perturbations by a flaw or inclusion may occur. Both give rise to a perturbation in the magnetic field that can be detected by an EC coil. The first is due to conductivity contrast, and the second due to permeability contrast, between the inclusion and host. Note that these mechanisms can exist independently of one another but in practice it is common that either the first ($\sigma_\mathrm{f} \neq \sigma$) exists alone, as in the case of nonmagnetic metals, or that both mechanisms exist together, as in the case of ferromagnetic metals.

9.4.1 Subsurface Sphere

Current Dipole In accordance with assumption 2 in Sect. 9.4, consider a uniform current density directed along the z-axis, $\mathbf{J}^{(i)} = J_z^{(i)}\hat{z} = \sigma E_z^{(i)}\hat{z}$, incident on a sphere with conductivity σ_f and radius a, centered on the origin of a system of spherical-polar coordinates, Fig. 9.2. Assume that there is good electrical contact between the spherical inclusion and the test-piece so that, if the inclusion is conductive and $\sigma_\mathrm{f} \neq 0$, current can freely enter the inclusion.

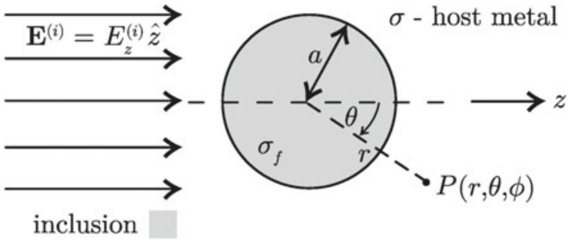

Fig. 9.2 Uniform electric field $\mathbf{E}^{(i)} = E_z^{(i)}\hat{z}$ in a metal test-piece with conductivity σ, incident on a small spherical inclusion with conductivity σ_f

Boundary Conditions To determine the perturbed part of the electric field, that arises due to the presence of the flaw, and eventually the impedance measured in an eddy current coil due to the flaw, Laplace equation (9.25) will be solved subject to certain boundary conditions on the surface of the sphere. The first of these is obtained from (5.19) which states that the tangential component of the electric field at an interface is continuous. In this case, write

$$[(\mathbf{E}^{(i)} + \mathbf{E}^{(s)} - \mathbf{E}^{(f)}) \times \hat{r}]_{r=a} = 0 \tag{9.29}$$

where the superscripts (i), (s), and (f) represent the incident field in the metal external to the inclusion, the perturbed part of the field external to the inclusion due to the presence of the flaw, and the total field within the flaw, respectively. In this spherical geometry,

$$[E_\theta^{(i)} + E_\theta^{(s)} - E_\theta^{(f)}]_{r=a} = 0. \tag{9.30}$$

Writing condition (9.30) in terms of the scalar potential V now gives

$$[V^{(i)} + V^{(s)} - V^{(f)}]_{r=a} = 0. \tag{9.31}$$

Normal to the surface of the sphere, the current density is continuous:

$$[(\mathbf{J}^{(i)} + \mathbf{J}^{(s)} - \mathbf{J}^{(f)}) \cdot \hat{r}]_{r=a} = 0 \tag{9.32}$$

and, equivalently,

$$[J_r^{(i)} + J_r^{(s)} - J_r^{(f)}]_{r=a} = 0. \tag{9.33}$$

In terms of the scalar potential V,

$$\left[\sigma\left(\nabla V^{(i)} + \nabla V^{(s)}\right) - \sigma_\mathrm{f}\nabla V^{(f)}\right]_{r=a} \cdot \hat{r} = 0. \tag{9.34}$$

Solution The incident field defined above is z-directed, which means that the system is rotationally invariant in the azimuthal (ϕ) direction. In spherical-polar coordinates, $\mathbf{E}^{(i)} = E_z^{(i)}\hat{z}$ which means that

$$V^{(i)} = -E_z^{(i)} z = -E_z^{(i)} r\cos\theta.$$

Under this circumstance, the general solution of the Laplace equation is given by

$$V = \sum_{n=0}^{\infty} \left(\frac{a_n}{r^{n+1}} + b_n r^n \right) P_n(\cos\theta), \tag{9.35}$$

where $P_n(x)$ is the Legendre polynomial of order n. In the case of the embedded sphere, no source of the electromagnetic field exists in the interior of the sphere. This means that the a_n vanish inside the sphere and the b_n vanish outside the sphere.

$$V^{(s)} = \sum_{n=0}^{\infty} \frac{a_n}{r^{n+1}} P_n(\cos\theta), \qquad r \geq a \tag{9.36}$$

$$V^{(f)} = \sum_{n=0}^{\infty} b_n P_n(\cos\theta) r^n, \qquad r \leq a \tag{9.37}$$

To this general solution the boundary conditions (9.31) and (9.34) are applied, in order to determine the values of the coefficients a_n and b_n. It is found that all coefficients vanish apart from a_1 and b_1, which have the following forms,

$$\begin{aligned} a_1 &= -\left(\frac{\sigma - \sigma_\mathrm{f}}{2\sigma + \sigma_\mathrm{f}} \right) a^3 E^{(i)} \\ b_1 &= -\left(\frac{3\sigma}{2\sigma + \sigma_\mathrm{f}} \right) E^{(i)}. \end{aligned}$$

In order to eventually obtain an expression for the impedance change due to the flaw, the perturbed field external to the flaw is needed. Substituting a_1 into (9.36) and taking the negative gradient according to (9.23) gives

$$\mathbf{J}^{(s)} = -J^{(i)} \left(\frac{\sigma - \sigma_\mathrm{f}}{2\sigma + \sigma_\mathrm{f}} \right) \frac{a^3}{r^3} \left(2\cos\theta\, \hat{r} + \sin\theta\, \hat{\theta} \right). \tag{9.38}$$

Comparing this expression with that of the field of an electrostatic dipole, (9.20), it can be seen that $\mathbf{J}^{(s)}$ may be written

$$\mathbf{J}^{(s)} = \frac{p}{4\pi r^3} \left(2\cos\theta\, \hat{r} + \sin\theta\, \hat{\theta} \right) \tag{9.39}$$

where we identify a current dipole $\mathbf{p}$ with

$$\mathbf{p} = -4\pi a^3 \left(\frac{\sigma - \sigma_\mathrm{f}}{2\sigma + \sigma_\mathrm{f}} \right) \mathbf{J}^{(i)}. \tag{9.40}$$

It should be emphasized that $\mathbf{p}$ is not an electrostatic dipole formed by separation of electrostatic charge. Rather, $\mathbf{p}$ is a current dipole, whose field resembles that of the electrostatic dipole. The current dipole **p** has unit Ampère-meter (Am) rather than Coulomb meter (Cm) as in the case of the electrostatic dipole.

Following Burrows [1], I now write **p** in terms of the volume of the sphere, $v = 4\pi a^3/3$, and a dimensionless current-scattering parameter α, defined

$$\alpha = 2\left(\frac{\sigma - \sigma_\mathrm{f}}{2\sigma + \sigma_\mathrm{f}}\right). \tag{9.41}$$

Then the following compact expression for **p** pertains,

$$\mathbf{p} = -\frac{3}{2}v\alpha\mathbf{J}^{(i)}. \tag{9.42}$$

There are several points that should be noted regarding the form of **p**.

1. Dipole strength p is proportional to the volume of the sphere, v;
2. p is proportional to the magnitude of the incident current density $J^{(i)}$, but has the opposite direction (see Fig. 9.3);
3. p is strongest for greatest contrast between σ and σ_f, that is, for $\sigma_\mathrm{f} = 0$; in this case, the defect is a void and $\mathbf{p} = -(3/2)v\,\mathbf{J}^{(i)}$;
4. as $\sigma_\mathrm{f} \to \sigma$, the dipole strength weakens because $\alpha \to 0$ and $p \to 0$.

Note, these expressions were derived under the assumption of good electrical contact between the test-piece and the inclusion. In the case that an insulating oxide layer, for example, exists at the interface between the inclusion and the test-piece, then

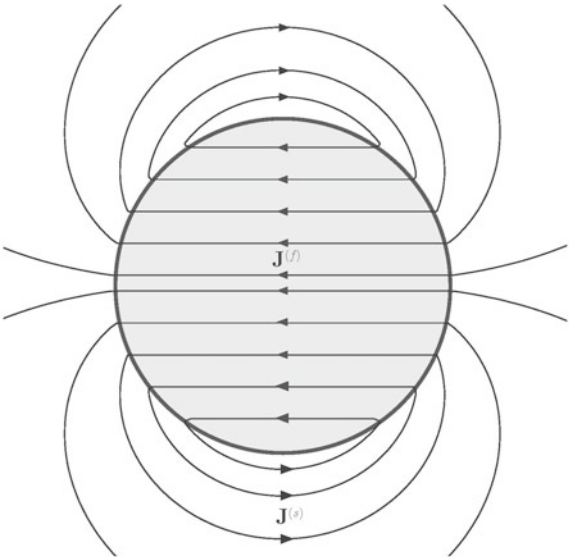

Fig. 9.3 Current density vector field $\mathbf{J}^{(f)}$ inside and $\mathbf{J}^{(s)}$ exterior to a spherical inclusion with conductivity $\sigma_\mathrm{f} \neq 0$. The incident current density $\mathbf{J}^{(i)}$ is uniform over the dimension of the sphere and is directed from left to right

current is not able to enter the material of the inclusion and it will appear as a void, even if $\sigma_\mathrm{f} \neq 0$.

Current Dipole Contribution to ΔZ due to a Subsurface Spherical Inclusion The computation of ΔZ due to an inclusion that can be represented as a current dipole-like source of perturbed current density can be simplified by invoking the "small flaw" approximation. Under this approximation, the incident electric field associated with the current density induced by the energizing coil, superscript (1), is assumed uniform over the flaw, superscript (2). Under this circumstance, (9.11) can be written as

$$\left[\mathcal{I}^{(1)}\right]^2 \Delta Z = \mathbf{E}^{(1)} \cdot \left[\int_{V^{(2)}} \mathbf{J}_\mathrm{s}^{(2)} dV\right] = \mathbf{E}^{(1)} \cdot \mathbf{p} = \mathbf{E}^{(i)} \cdot \mathbf{p}, \tag{9.43}$$

where the current dipole $\mathbf{p}$ has been identified with $\int_{V^{(2)}} \mathbf{J}_\mathrm{s}^{(2)} dV$. This is the scalar product of the current dipole moment $\mathbf{p}$ with the incident electric field produced by the energizing coil at the position of the dipole. Substituting the form of $\mathbf{p}$ given in (9.42) into (9.43) gives

$$\left[\mathcal{I}^{(i)}\right]^2 \Delta Z = \frac{3}{2} \upsilon \alpha \sigma \left[\mathbf{E}^{(i)} \cdot \mathbf{E}^{(i)}\right]_{\mathbf{r}=\mathbf{r}_p} = \frac{3}{2} \upsilon \alpha \sigma \left[\mathbf{E}^{(i)}\right]^2_{\mathbf{r}=\mathbf{r}_p}, \tag{9.44}$$

where the superscript (i) denotes the current in the energizing coil or the field originating from it and $\mathbf{r}_p$ denotes the position of the current dipole associated with the flaw response.

For a spherical inclusion whose center is at depth D below the surface of a conductive half-space that is excited by a uniform current sheet such as shown in Fig. 2.5, the magnetic and electric fields at the surface $z = 0$ are given by $\mathbf{H} = H_0 \hat{y}$ and $\mathbf{E} = E_0 \hat{x} = (-jkH_0/\sigma)\hat{x}$ respectively. Inserting these expressions into (9.44), the following equation for the impedance change due to the defect can be found;

$$\Delta Z_\mathrm{s} = -\frac{2\pi\alpha}{\sigma} \left[\frac{H_0}{\mathcal{I}^{(i)}}\right]^2 k^2 a^3 e^{-2jkD}. \tag{9.45}$$

Note that there is a phase shift in ΔZ_s as a function of flaw depth D. The term

$$\exp(-2jkD) = \exp[-2j(1-j)D/\delta] = \exp(-2jD/\delta)\exp(-2D/\delta)$$

shows that

$$\arg(\Delta Z_\mathrm{s}) = -2D/\delta.$$

In other words, the phase of ΔZ_s is proportional to D/δ. The phase change as a function of depth is illustrated in Fig. 8.8.

Note, while the field perturbed by the flaw is obtained under the small flaw approximation, that is effectively a quasi-static approximation leading to governing Laplace equations (9.25) and (9.26), the frequency reappears in the impedance change expression (9.45)—embedded in k—due to the fact that the incident field, which is frequency dependent, is inserted into the impedance formula (9.44) in order to obtain (9.45). There is no conflict in the fact that frequency variation is dropped when determining the equivalent dipole response of the flaw but then reinstated to calculate the impedance change, because the small flaw approximation describes the negligible variation of the field with respect to the flaw dimensions; an assumption that can hold even while the field varies in time, as it must for there to be induction of eddy currents at all according to Faraday's Law.

Magnetic Dipole A parallel development to that given in (9.29)–(9.42), wherein the perturbation of $\mathbf{J}^{(i)}$ by a flaw was recognized as equivalent to a perturbation due to the presence of an equivalent current dipole $\mathbf{p}$, can be followed to show that the perturbation of $\mathbf{B}^{(i)}$ by a flaw can be expressed as that due to the presence of an equivalent magnetic dipole $\mathbf{m}$, where

$$\mathbf{m} = -\frac{3}{2} v \beta \mathbf{H}^{(i)} \tag{9.46}$$

and

$$\beta = 2\left(\frac{\mu - \mu_\mathrm{f}}{2\mu + \mu_\mathrm{f}}\right). \tag{9.47}$$

As with $\mathbf{p}$, there are several points that should be noted regarding the form of $\mathbf{m}$.

1. Dipole strength m is proportional to the volume of the sphere, v;
2. m is proportional to the magnitude of the incident magnetic field $H^{(i)}$, but has the opposite direction;
3. m is strongest for greatest contrast between μ and μ_f although, unlike σ_f, μ_f cannot be zero but in the case of a void or nonmagnetic inclusion in a ferromagnetic material $\mu \gg \mu_\mathrm{f}$ which implies that $\beta \to 1$ and $\mathbf{m} = -(3/2)v\,\mathbf{H}^{(i)}$;
4. as $\mu_\mathrm{f} \to \mu$, the dipole strength weakens because $\beta \to 0$ and $m \to 0$;
5. the magnetic dipole strength is weak (usually negligible) in any non-ferromagnetic test-piece.

Magnetic Dipole Contribution to ΔZ due to a Subsurface Spherical Inclusion To account for a magnetic dipole contribution to the impedance change of an EC coil that arises due to permeability contrast between a subsurface spherical inclusion and its surrounding material, an additional term ΔZ_m is needed that originates in the electromotance induced in a pick-up loop by a magnetic dipole. A suitable form for ΔZ_m can be obtained by manipulating (9.11) in the following way. First taking $\mathbf{J}_\mathrm{s}^{(2)} = \mathcal{I}^{(2)} d\mathbf{l}$ where current $\mathcal{I}^{(2)}$ flows along circular path $C^{(2)}$, (9.11) becomes

$$\Delta Z = \frac{\mathcal{I}^{(2)}}{\left[\mathcal{I}^{(1)}\right]^2} \int_{C^{(2)}} \mathbf{E}^{(1)} \cdot d\mathbf{l} \tag{9.48}$$

to which Stokes' theorem (10.49) may be applied to give

$$\Delta Z = \frac{\mathcal{I}^{(2)}}{\left[\mathcal{I}^{(1)}\right]^2} \int_{S^{(2)}} [\nabla \times \mathbf{E}^{(1)}] \cdot d\mathbf{S} \tag{9.49}$$

where $S^{(2)}$ is an open surface bounded by $C^{(2)}$ that we can take to be a circular disk. By Faraday's Law and remembering from (3.2) that $\mathbf{m} = I\mathbf{S}$ in general, (9.49) becomes

$$\Delta Z = j\omega \frac{\mathcal{I}^{(2)}}{\left[\mathcal{I}^{(1)}\right]^2} \int_{S^{(2)}} \mathbf{B}^{(1)} \cdot d\mathbf{S} = \frac{j\omega}{\left[\mathcal{I}^{(1)}\right]^2} \mathbf{B}^{(1)} \cdot \mathbf{m}^{(2)}. \tag{9.50}$$

The last step can be taken under the small flaw approximation where $\mathbf{B}^{(1)}$ due to the energizing coil does not vary significantly over the volume of the flaw. Then, in the case of a small flaw,

$$\Delta Z = \Delta Z_{\mathrm{p}} + \Delta Z_{\mathrm{m}} = \frac{1}{\left[\mathcal{I}^{(1)}\right]^2} \left[\mathbf{E}^{(1)} \cdot \mathbf{p}^{(2)} + j\omega \mathbf{B}^{(1)} \cdot \mathbf{m}^{(2)}\right] \tag{9.51}$$

where the subscripts p and m represent current dipole and magnetic dipole contributions to ΔZ, respectively. Substituting the forms of $\mathbf{p}$ and $\mathbf{m}$ given in (9.42) and (9.46), respectively, into (9.51) gives, for the impedance change in a coil due to a small flaw that behaves as a current dipole and magnetic dipole source,

$$\left[\mathcal{I}^{(i)}\right]^2 \Delta Z = \frac{3}{2} v \left\{ \alpha\sigma [E^{(i)}]^2_{\mathbf{r}=\mathbf{r}_p} - j\omega\beta\mu [H^{(i)}]^2_{\mathbf{r}=\mathbf{r}_m} \right\} \tag{9.52}$$

where the superscript (i) denotes the current in the energizing coil or fields originating from it, and $\mathbf{r}_p$ and $\mathbf{r}_m$ indicate the positions of the current and magnetic dipoles associated with the flaw response, respectively, which would usually be the same.

Note that the first term on the right-hand side of (9.52) is the same as that studied in Sect. 9.4.1. It is the contribution to ΔZ_{s} due to the equivalent electric current dipole representation of the flaw.

For a spherical inclusion whose center is at depth D below the surface of a conductive half-space that is excited by a uniform current sheet such as shown in Fig. 2.5, the magnetic and electric fields at the surface $z = 0$ are given by $\mathbf{H} = H_0\hat{y}$ and $\mathbf{E} = E_0\hat{x} = (-jkH_0/\sigma)\hat{x}$, respectively. Inserting these expressions into (9.52), it is found that

$$\Delta Z_{\mathrm{p}} = -\frac{2\pi\alpha}{\sigma} \left[\frac{H_0}{\mathcal{I}^{(i)}}\right]^2 k^2 a^3 e^{-2jkD}, \tag{9.53}$$

which is the same as (9.45), and

$$\Delta Z_{\mathrm{m}} = \frac{2\pi\beta}{\sigma} \left[\frac{H_0}{\mathcal{I}^{(i)}}\right]^2 k^2 a^3 e^{-2jkD}. \tag{9.54}$$

Combining these according to (9.51) yields

$$\Delta Z_{\mathrm{s}} = \Delta Z_{\mathrm{p}} \left(1 - \frac{\beta}{\alpha} \right) \tag{9.55}$$

which shows, interestingly, that $\Delta Z_{\mathrm{s}} \to 0$ as $\beta \to \alpha$.

Nonspherical Subsurface Flaws More generally, inclusions of other shapes may also be modeled under the approximation of being "small flaws". Canonical shapes such as an ellipsoid or spheroids may be modeled as a single-dipole source of perturbed current density, as exemplified here in the limiting case of the sphere. Expressions for **p** due to oblate and prolate spheroids are given by Burrows [1]. Oblate spheroids may be used to approximate disc-like defects, whereas prolate spheroids may approximate needle-like inclusions. In these cases the scattering parameters α or β must include the semi-axes lengths of the spheroid, as well as the conductivity or permeability values of the test-piece and the inclusion. Inclusions of arbitrary shape can in principle be modeled by including higher order multipoles to represent the perturbed current density.

9.4.2 *Surface Defects*

Representation of Surface Defects as a Current Dipole Distribution The perturbation of eddy currents by *surface* defects may also be described theoretically by representing the defect in terms of equivalent current dipoles. This representation can be adopted regardless of the relative size of the crack and the skin depth but, in the low-frequency regime, simple asymptotic expressions are available for the current dipole distribution that represents various defects. In the high-frequency, or "thin-skin" regime, other methods may be applied as discussed in Sect. 9.5. At intermediate frequencies or flaw sizes, for which the defect size is similar to the value of δ, it is possible to determine a two-dimensional dipole density distribution over the crack surface by numerical means [5], from which ΔZ can be computed. Similar comments apply for the perturbation of the incident magnetic field by magnetic dipoles whose effect is equivalent to that of a surface flaw. The remaining examples given in this Sect. 9.4.2, give explicit forms for the contribution to the impedance change due to the conductivity contrast between the flaw and the test-piece, i.e., due to the current dipole contribution, whereas any contribution due to permeability contrast is left to the interested reader to determine.

Hemispherical Indentation The impedance change ΔZ_{h} due to a hemispherical surface indentation with radius a in a uniform incident field can be obtained from ΔZ_{s} for a subsurface sphere by setting $\sigma_{\mathrm{f}} = 0$ and taking the limit $D \to 0$ (which means that $\alpha \to 1$), and halving the dipole strength because the flaw now has only half of the volume of a sphere. Applying these operations to (9.45) yields

$$\Delta Z_{\mathrm{h}} = -\pi \frac{1}{\sigma} \left[\frac{H_0}{\mathcal{I}^{(i)}} \right]^2 k^2 a^3 . \tag{9.56}$$

Consideration of this expression reveals that ΔZ_{h} is purely inductive (because $k^2 = -j\omega\mu\sigma$). This is in contrast with ΔZ_{s} for the subsurface spherical inclusion, for which the phase of ΔZ_{s} changes as a function of the depth of the inclusion below the conductor surface, as discussed in Sect. 9.4.1.

Semicircular Crack In 1996, Harfield, Yoshida, and Bowler [6] published low-frequency perturbation theory solutions for the impedance change in an EC coil due to (i) a semicircular surface crack and (ii) a long, surface crack with uniform depth. The cracks occupy a plane normal to the plane of the conductor surface and normal to the direction of the uniform incident current density. Several terms in a series expansion for ΔZ in these cases were obtained analytically, the first of which are reproduced here.

In the case of a semicircular surface crack, radius a, the current dipole contribution to the impedance change is given by

$$\Delta Z_{\mathrm{s-c}} = -\frac{4}{3\sigma}\left[\frac{H_0}{\mathcal{I}^{(i)}}\right]^2 k^2 a^3. \tag{9.57}$$

As in the case of the hemispherical indentation, the impedance change due to this surface defect is purely imaginary (inductive).

Long Crack For a long, surface crack with depth d that occupies a plane normal to the plane of the conductor surface and normal to the direction of the uniform incident current density [6],

$$\Delta Z_{\infty} = -\frac{\pi}{2\sigma}\left[\frac{H_0}{\mathcal{I}^{(i)}}\right]^2 (kd)^2. \tag{9.58}$$

As in the cases of the hemispherical indentation and the semicircular surface crack, the impedance change due to the long surface crack is purely imaginary (inductive).

9.5 High-Frequency "Thin-Skin" Treatment of Surface Cracks

The "small flaw" regime, dealt with in Sect. 9.4, arises naturally when low-frequency excitations are used, because then the electromagnetic skin depth, δ, is often significantly larger than the defect that is sought. The opposite regime arises naturally when a higher frequency excitation is used for the interrogation of surface defects. This regime is known as the "thin-skin" regime because at higher frequencies the induced eddy-current density can be thought of as occupying a relatively thin layer (skin) near the surface of the metal test-piece. Then, it is often the case that $\delta \ll \Delta$, where Δ is a relevant dimension of the surface defect.

In this discussion of thin-skin theory, a new method of calculating ΔZ will be introduced, Sect. 9.5.1, and a detailed solution given for a two-dimensional system in which a long, surface crack with depth $d \gg \delta$ is interrogated by a uniform incident current density, Sect. 9.5.4. This simplified geometry permits solution in the context of this textbook. Other thin-skin solutions for the impedance change in an eddy-current coil due to surface cracks with finite length and several different profiles are summarized in Sects. 9.5.6–9.5.9. For details of these solutions the reader is referred to the series of articles [7–9] in which Harfield and Bowler published a theory of thin-skin eddy current interaction with surface cracks that has the ability to describe ΔZ in various coils due to various cracks. The impedance calculation relies on evaluation of an integral along the line of the crack mouth, with the incident magnetic field due to the eddy-current coil being an input of the integrand. Calculated and experimentally measured values of ΔZ were compared for an eddy current surface coil interacting with long [7], rectangular [8], semielliptical [9] and epicyclic [9] artificial defects that were fabricated by electro-discharge machining.

9.5.1 Poynting Vector and Z

We are now familiar with the circuit-theory approach by which Z or ΔZ may be calculated in an eddy-current coil as the ratio of phasor voltage to phasor current, via (4.25). Here, it will be shown that Z or ΔZ may be calculated in an alternative way, that relies on knowledge of the electric and magnetic fields in the vicinity of the metal or defect. In the context of thin-skin theory, this latter approach is more convenient for determination of the impedance.

Recall the definition of the Poynting vector (2.19) and the average power that can be calculated from it when fields are time-harmonic (2.21). From circuit theory, power is also given by the product $\mathcal{V}\mathcal{I} = \mathcal{I}^2 Z$ which allows us to identify

$$\mathcal{I}^2 Z = \int_S \overline{\mathcal{P}} \cdot d\mathbf{S} = \frac{1}{2}\mathrm{Re} \int_S \left(\mathbf{E} \times \mathbf{H}^*\right) \cdot d\mathbf{S}. \tag{9.59}$$

Hence, the impedance of an eddy-current coil may be determined by integrating $\mathbf{E} \times \mathbf{H}^*$ over a relevant surface:

$$Z = \frac{1}{2[\mathcal{I}^{(i)}]^2}\mathrm{Re} \int_S \left(\mathbf{E} \times \mathbf{H}^*\right) \cdot d\mathbf{S}. \tag{9.60}$$

9.5.2 Current-Sheet Excitation of an Unflawed Half-Space

As an example of the application of (9.60), first consider the impedance due to current-sheet excitation of an unflawed half-space conductor, Fig. 9.4.

The current sheet excitation gives rise to an x-directed electric field $\mathbf{E} = E_x \hat{x}$ and a y-directed magnetic field $\mathbf{H} = H_y \hat{y}$, which both decay in the conductor according to e^{jkz}, (6.22). Denote the magnetic field at the conductor surface by H_0. Then,

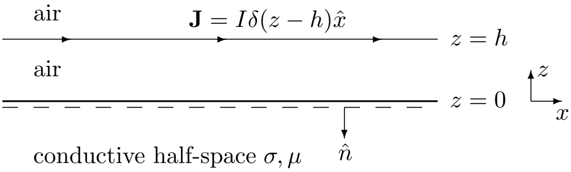

Fig. 9.4 Conductive half-space excited by a uniform current sheet **J**. The surface of integration S is depicted as the dashed line, with $d\mathbf{S} = \hat{n}dS$

$$H_y^*(z=0) = H_y(z=0) = H_0 \qquad \text{and} \qquad E_x(z=0) = -\frac{jkH_0}{\sigma}, \tag{9.61}$$

where the expression for $E_x(z=0)$ can be obtained by applying Faraday’s Law. Therefore, over a square with side length L at the conductor surface, the impedance of the conductor is given by

$$Z = \frac{1}{2[\mathcal{I}^{(i)}]^2}\int_{-L/2}^{L/2}\int_{-L/2}^{L/2}(E_x\hat{x} \times H_y^*\hat{y}) \cdot (-\hat{z})dxdy = \frac{jkL^2}{2\sigma}\left[\frac{H_0}{\mathcal{I}^{(i)}}\right]^2, \tag{9.62}$$

and the impedance per unit surface area is

$$Z' = \frac{jk}{2\sigma}\left[\frac{H_0}{\mathcal{I}^{(i)}}\right]^2. \tag{9.63}$$

This method of calculating the impedance will be employed, in the next section, in determining ΔZ due to a long, surface crack.

9.5.3 Definition of an Ideal Crack

An *ideal crack* is a mathematical construct in which a crack is represented as a closed surface (this means that the crack has infinitesimal width) which nonetheless forms a perfect barrier to the flow of electrical current across it. This second condition may be expressed as

$$\mathbf{J}(\mathbf{r}) \cdot \hat{n} = 0, \qquad \mathbf{r} \in S_\mathrm{c} \tag{9.64}$$

in which S_c is the crack surface and $\hat{n}$ is the unit vector normal to that surface.

9.5.4 Long Crack in a Uniform Field

Add a surface crack with depth d to the conductor shown in Fig. 9.4, to give the configuration shown in Fig. 9.5. This problem was tackled by Kahn, Spal, and Feldman in [10] by breaking it down into three distinct parts. The impedance change

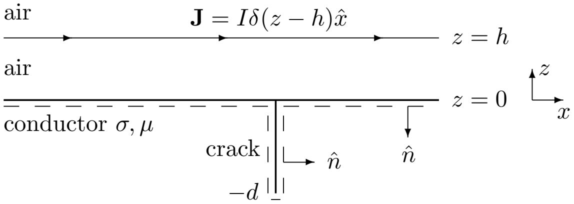

Fig. 9.5 Conductive half-space excited by a uniform current sheet $\mathbf{J}$, containing a long surface crack with depth d. The surface of integration S is depicted as the dashed line, with $d\mathbf{S} = \hat{n}dS$

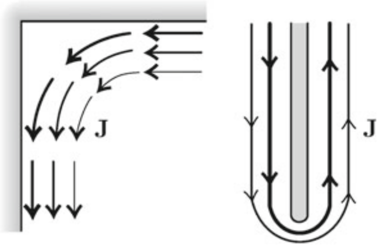

Fig. 9.6 Current path in the conductive corner at one side of the mouth of a long, surface crack (left) and flowing around its buried edge (right)

due to the crack was constructed as primarily a contribution from the crack faces, with correction terms due to the shortened current path at the crack mouth, where essentially the current may "cut the corners", Fig. 9.6 (left), and due to the flow of the current density around the buried crack tip or edge, Fig. 9.6 (right). At the faces of a crack located in the plane $x = 0$, the electromagnetic field has the form $e^{-jk|x|}$ in the thin-skin regime, much like its form at the air–conductor interface, where it depends upon e^{jkz}. This essentially defines the thin-skin regime; the crack is sufficiently deep that the current flow over its surface is mostly like a thin-skin, as it is at the air–conductor interface. Corrections to ΔZ were then made to account for the departure of the current path from its thin-skin behavior, at the crack edge and mouth. A similar approach was adopted by Harfield and Bowler [11] in 1994, and in this paper all terms were evaluated analytically, whereas the correction terms in [10] had been evaluated numerically. Note that Harfield and Bowler erroneously integrated over the instantaneous power density—Poynting's vector—(2.19) rather than the average power per unit area (2.20) in their calculation of impedance [11], leading to the omission of a factor of $\frac{1}{2}$ in their result. The lowest order contribution to ΔZ, from the crack faces, will be derived here and results for the correction terms will be stated.

Integrating the average power per unit area over the surface shown in Fig. 9.5, that has been extended to include the surfaces of the crack, now yields Z_{flaw}, the impedance of the conductor and crack. The impedance change due to the crack, ΔZ, can be obtained by integrating the average power per unit area over a surface that encloses the crack alone. Comparing Figs. 9.4 and 9.5 we can see that application of (6.4) gives rise to the surface shown in Fig. 9.7. Hence,

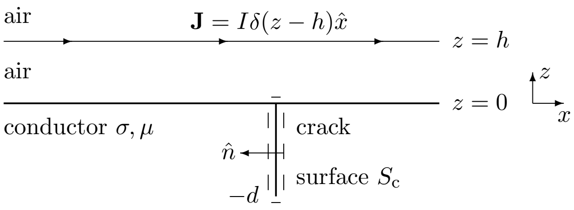

Fig. 9.7 Conductive half-space excited by a uniform current sheet **J**, containing a long surface crack with depth d. The surface of integration S_c, depicted as the dashed line, now tightly encloses the crack, with $d\mathbf{S} = \hat{n} dS$

$$\Delta Z = \frac{1}{2[\mathcal{I}^{(i)}]^2} \mathrm{Re} \int_{S_c} \left(\mathbf{E} \times \mathbf{H}^*\right) \cdot d\mathbf{S}. \tag{9.65}$$

Lowest Order Solution for ΔZ The lowest order solution for ΔZ due to a long, surface crack excited by a uniform field may be obtained by making the approximation that the magnetic and electric fields in the vicinity of the crack decay exponentially as a function of distance from the crack. In other words, it is assumed that the functional form of the fields near the ideal (nonconducting) crack is the same as that near the air–conductor interface. This means that, close to a crack in the plane $x = 0$, the fields decay as $e^{-jk|x|}$. By analogy with expressions (9.61),

$$H_y^*(x=0) = H_y(x=0) = H_0 \qquad \text{and} \qquad E_z(x=0) = -\frac{jkH_0}{\sigma}. \tag{9.66}$$

These expressions allow us to perform the integration of (9.65). Replace S_c by integrating twice over the crack face at $x = 0+$. This gives

$$\Delta Z = \frac{1}{[\mathcal{I}^{(i)}]^2} \int_{-d}^{0} \int_{-L/2}^{L/2} (E_z\hat{z} \times H_y\hat{y}) \cdot (-\hat{x}) dy dz = -\frac{jkdL}{\sigma} \left[\frac{H_0}{\mathcal{I}^{(i)}}\right]^2, \tag{9.67}$$

or, per unit length of the crack,

$$\Delta Z = Z_f = -\frac{jkd}{\sigma} \left[\frac{H_0}{\mathcal{I}^{(i)}}\right]^2. \tag{9.68}$$

This result differs in sign from that of [11] due to the different definition of ΔZ adopted in (6.4) of this text and by a factor of $\frac{1}{2}$ which was erroneously omitted from [11]. In (9.68), the notation Z_f is introduced, representing the impedance due to the current flowing uniformly over the crack faces. Comparing this result with that for the unflawed conductor, it can be seen that the effect of the crack is to change the impedance in proportion with the length of the current path around the defect, which is $2d$, to lowest order. For (9.68) to be accurate to within about 10% of a measured value, the condition $d > 8\delta$ must hold. For 1% accuracy, $d > 80\delta$ must hold! In the derivation of Z_f the perturbing effects of the crack edge and corners on the path of the eddy-current density, Fig. 9.6, have been neglected. If these perturbations are taken into account, as described in the next section, then a simple modification to (9.68) achieves good accuracy even for $d \approx 3\delta$.

Higher Order Solution for ΔZ An analytic form for the electromagnetic field in the vicinity of the crack edge, Fig. 9.6, may be deduced from that for electromagnetic scattering at an insulating half-plane in a conductive medium. A famous solution of this problem was derived originally by Sommerfeld in the context of optical scattering [12, Sect. 38] and its adaptation for this context of EC NDE is described in [11]. Analysis of the electromagnetic field near the crack edge, and computation of the resulting contribution to impedance from it, gives

$$Z_\mathrm{f} + Z_\mathrm{e} = -\frac{1}{2\sigma}\left[\frac{H_0}{\mathcal{I}^{(i)}}\right]^2 (2jkd + 1)\,, \tag{9.69}$$

where Z_e is the impedance contribution due to the field perturbation at the crack edge. The impedance contribution due to the form of the field in the conductive corners near the crack mouth, Fig. 9.6, was determined in [10, 11] by using the method of images [13, Chap. 7]. The analysis gives rise to

$$Z_\mathrm{c} = \frac{4}{\pi\sigma}\left[\frac{H_0}{\mathcal{I}^{(i)}}\right]^2 . \tag{9.70}$$

Combining (9.69) and (9.70) yields the impedance change due to a long, surface crack excited by a uniform field, in the thin-skin regime:

$$\Delta Z = -\frac{1}{2\sigma}\left[\frac{H_0}{\mathcal{I}^{(i)}}\right]^2 \left(2jkd + 1 - \frac{8}{\pi}\right). \tag{9.71}$$

In the analysis of [11] it was shown that this result is accurate for configurations in which $d \geq 3\delta$.

Considering these results, it is clear that Z_e and Z_c are both real (resistive) terms, whereas Z_f has real and imaginary parts with equal magnitude. Explicitly,

$$\mathrm{Re}(\Delta Z) = -\frac{1}{\sigma}\left[\frac{H_0}{\mathcal{I}^{(i)}}\right]^2 \left(\frac{d}{\delta} + \frac{1}{2} - \frac{4}{\pi}\right) \tag{9.72}$$

$$\mathrm{Im}(\Delta Z) = -\frac{1}{\sigma}\left[\frac{H_0}{\mathcal{I}^{(i)}}\right]^2 \frac{d}{\delta} \tag{9.73}$$

This means that the perturbations to the current flow at the crack edge and corners effectively reduce the crack depth in $\mathrm{Re}(\Delta Z)$ by 0.77δ:

$$d' = d + \left(\frac{1}{2} - \frac{4}{\pi}\right)\delta = d - 0.77\delta. \tag{9.74}$$

Hence, the correction terms are more significant as d decreases, but may be negligible for $d \gg \delta$.

9.5.5 Semicircular Crack in a Uniform Field

As a limiting case of the more complex problem of determining the impedance change in an EC coil due to a semicircular surface crack, the following elegant solution was obtained for the impedance change due to a semicircular surface crack excited by a uniform field, in the thin-skin regime [9]. The crack occupies the plane normal to both the conductor surface and the current sheet excitation, similar to the geometry shown in Fig. 9.7, with d replaced by a, the crack radius.

$$\Delta Z = -\frac{2jk}{\sigma}\left[\frac{H_0}{\mathcal{I}^{(i)}}\right]^2 a^2 \left(\frac{\pi}{2} - \frac{2}{\pi}\right). \tag{9.75}$$

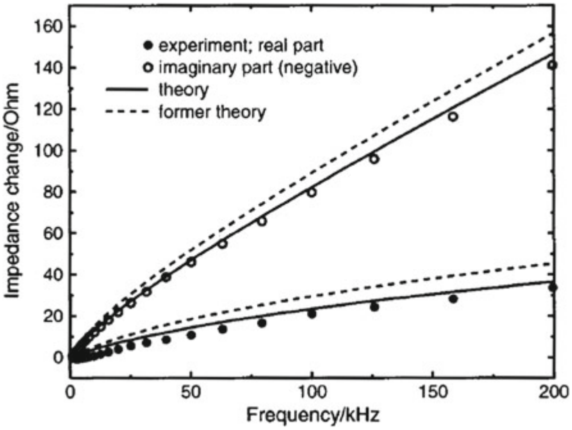

Fig. 9.8 Calculated impedance and experimental data taken using coil C9, Table 9.2, centered over long slot L1, Table 9.3, in aluminum [7]. The broken lines represent calculations made using Auld’s prior assumption that the tangential magnetic field at the conductor surface is undisturbed by a surface defect [14]. Reproduced with permission from American Institute of Physics: *J. Appl. Phys.*, vol. 82, 1997, p. 4599, Theory of thin-skin eddy-current interaction with surface cracks, N. Harfield and J. R. Bowler, Fig. 7. Original caption: Impedance predictions and experimental data for a coil centered over a long slot in aluminum. The broken lines represent predictions made using Auld’s assumption that the tangential magnetic field at the conductor surface is undisturbed by a surface defect

9.5.6 Long Crack in a Coil Field

The impedance change in an EC coil due to thin-skin eddy-current interaction with a surface crack can be calculated by evaluation of an integral along the line of the crack mouth, wherein the magnetic field generated by the EC coil is an input of the integrand [7]. In Fig. 9.8, calculated impedance is compared with experimental data from frequency scans for a coil centered over a long slot in aluminum [7]. The experimental parameters are given in Tables 9.2 and 9.3.

9.5.7 Rectangular Crack in a Coil Field

In Figs. 9.9, 9.10 and 9.12, impedance calculations are compared with experimental data as a coil is scanned along the mouth of rectangular slots in aluminum [8]. Two cracks are studied. Crack R1 is similar in length to the diameter of the interrogating coil, C7, whereas crack R2 is much longer than the coil diameter. The signals exhibit various characteristic features. In Figs. 9.9 and 9.10, “shoulders” are clearly visible at coil positions approximately ±22 mm. These occur when the current density induced

Table 9.2 Coil parameters for the data shown in Figs. 9.8 to 9.16, with reference to the dimensional parameters defined in Fig. 1.9; n is the number of wire turns on the coil, L_0 its DC inductance and f_0 its resonance frequency, Sect. 4.10

Coil	C7	C9	C11
r_i (mm)	6.95	3.015	2.51
r_o (mm)	9.35	5.46	7.50
l (mm)	6.70	2.94	4.99
h (mm)	2.07	1.32	0.10
n	335	900	4,000
L_0 (mH)	1.752	6.027	
f_0 (kHz)		850	
References	[8]	[7]	[9]

Table 9.3 Material and defect parameters for the data shown in Figs. 9.8 to 9.16. Note that the conductivity of aluminum varies considerably, according to the alloy

Defect	L1	R1	R2	D1	D2
Depth (mm), maximum	12.0	5.0	2.9	8.6	8.9
Length (mm), maximum	n/a	12.6	47.1	22.1	49.8
Gape (mm), maximum	0.41	0.28	0.64	0.33	0.37
Aluminum σ (MS/m)	16.7	30.6	16.7	22.5	22.4
References	[7]	[8]	[8]	[9]	[9]

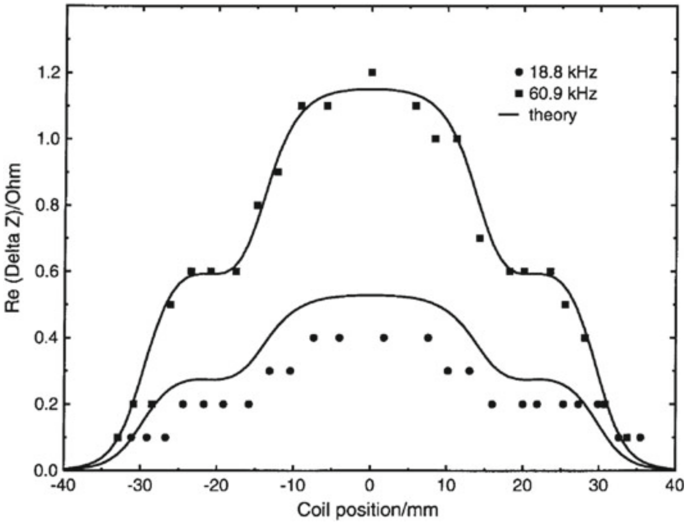

Fig. 9.9 Calculated real impedance Re(ΔZ) and experimental data taken using coil C7, Table 9.2, as it is scanned along the mouth of rectangular slot R2, Table 9.3, in aluminum [8]. Reproduced with permission from IEEE: *IEEE Trans. Magn.*, vol. 34, 1998, p. 521, Evaluation of Probe Impedance Due to Thin-Skin Eddy-Current Interaction with Surface Cracks, J. R. Bowler and N. Harfield, Fig. 5. Original caption: The real part of the impedance change in coil C7 as it is scanned along the mouth of rectangular slot 2 (aluminum)

by *one* side of the coil is fully engaged with the crack. The distance between the shoulders provides an estimate of the surface length of the crack. The central peak in ΔZ appears when the current density induced by *both* sides of the coil interacts with the crack. Note that the peak ΔZ is approximately twice the magnitude of the shoulder signal. The signal shape shown in Figs. 9.9 and 9.10 is typical for a coil with diameter somewhat less than the maximum crack length. Figure 9.11 displays the data of Figs. 9.9 and 9.10 in the form of a Z-plane plot. While Z-plane plots give a ready view of the complex impedance signal, note that the position information cannot be seen explicitly in the Z-plane plot, as it can be in Figs. 9.9 and 9.10. In contrast, Re(ΔZ) is shown in Fig. 9.12 for a crack with maximum length somewhat shorter than the coil diameter. In this case, the separation of the peaks in the signal provides nothing more than an indication of the coil diameter, although the width of each peak gives an indication of the flaw size. The signal exhibits a minimum when the coil is centered over the crack because there is a minimum in the eddy-current density below the center of a coil with large aperture, as can be seen in Fig. 6.18. Comparing Figs. 9.12 and 9.9, one can deduce that in order to size a crack by observing ΔZ, a coil with diameter somewhat smaller than the crack is preferable.

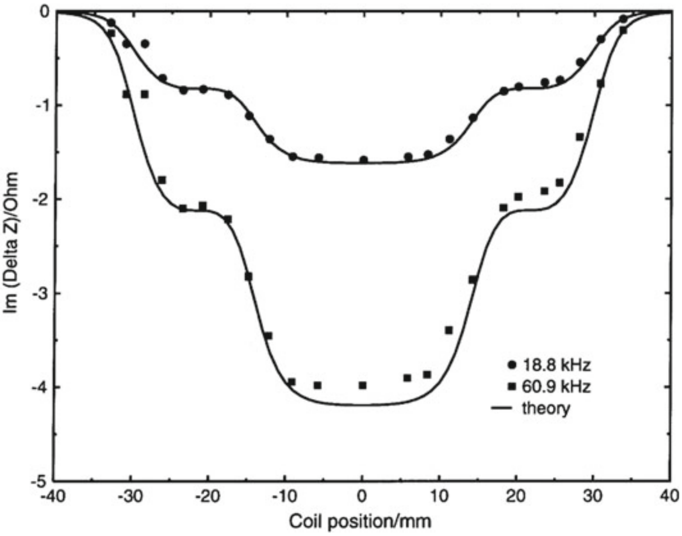

Fig. 9.10 Calculated imaginary impedance Im(ΔZ) and experimental data taken using coil C7, Table 9.2, as it is scanned along the mouth of rectangular slot R2, Table 9.3, in aluminum [8]. Reproduced with permission from IEEE: *IEEE Trans. Magn.*, vol. 34, 1998, p. 521, Evaluation of Probe Impedance Due to Thin-Skin Eddy-Current Interaction with Surface Cracks, J. R. Bowler and N. Harfield, Fig. 6. Original caption: The imaginary part of the impedance change in coil C7 as it is scanned along the mouth of rectangular slot 2 (aluminum)

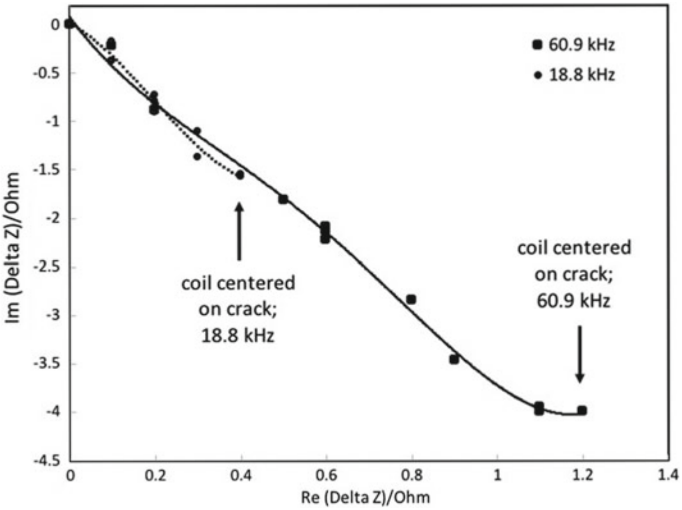

Fig. 9.11 Impedance-plane plot constructed from experimental data shown in Figs. 9.9 and 9.10 taken using coil C7, Table 9.2, as it is scanned along the mouth of rectangular slot R2, Table 9.3, in aluminum [8]. The solid and dotted lines are, in this case, fourth-order polynomial fits to the data and serve as a guide to the eye, rather than theoretical curves as shown in Figs. 9.9 and 9.10

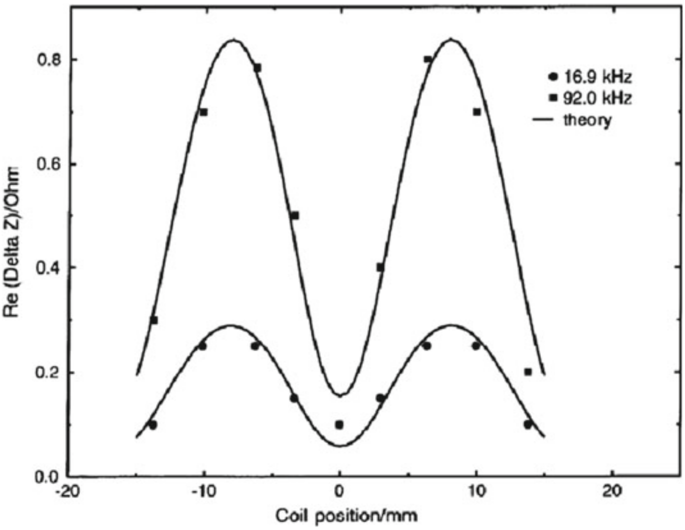

Fig. 9.12 Calculated real impedance Re(ΔZ) and experimental data taken using coil C7, Table 9.2, as it is scanned along the mouth of rectangular slot R1, Table 9.3, in aluminum [8]. Reproduced with permission from IEEE: *IEEE Trans. Magn.*, vol. 34, 1998, p. 520, Evaluation of Probe Impedance Due to Thin-Skin Eddy-Current Interaction with Surface Cracks, J. R. Bowler and N. Harfield, Fig. 3. Original caption: The real part of the impedance change in coil C7 as it is scanned along the mouth of rectangular slot 1 (aluminum)

9.5.8 Semielliptical Crack in a Coil Field

Real surface cracks do not grow with a rectangular profile (of course!) but often grow with a semi-elliptical profile. Following an approach in which the thin-skin field at the surface of a crack is represented as a transverse-magnetic (TM) potential that satisfies the Laplace equation on the crack, solutions of the Laplace problem for semi-elliptical cracks were obtained by conformal mapping to a rectangular region [9]. A semi-elliptical defect with depth profile shown in Fig. 9.13 was fabricated and experiments conducted in order to verify calculated impedance values. Calculated and measured values of ΔZ are shown in Fig. 9.14 and good agreement between them is observed. The impedance signal resembles that of Figs. 9.9 and 9.10 but is smoother, reflecting the absence of sharp corners in the defect profile.

9.5.9 Epicyclic Crack in a Coil Field

A more elaborate example, designed to simulate two conjoined surface cracks of different size, is shown in Fig. 9.15 [9]. The impedance change due to this defect was calculated in a manner similar to that for the semi-ellipse; by exploiting a conformal

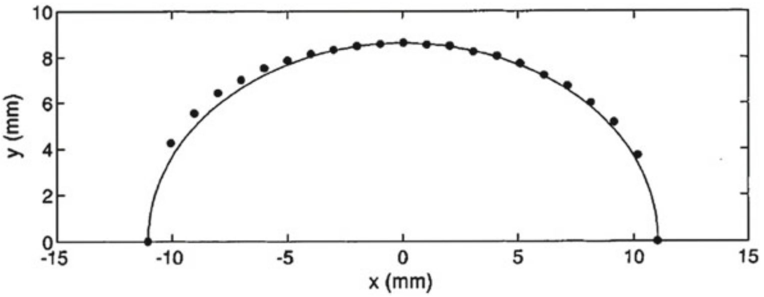

Fig. 9.13 Semi-elliptical profile of slot D1, Table 9.2 [9]. Reproduced with permission from IEEE: *IEEE Trans. Magn.*, vol. 36, 2000, p. 287, Thin-Skin Eddy-Current Interaction with Semielliptical and Epicyclic Cracks, J. R. Bowler and N. Harfield, Fig. 5a. Original caption: Comparison of crack edge coordinates with the profile representation used for mapping. **(a)** Slot D1 is approximated in the calculation as a semiellipse

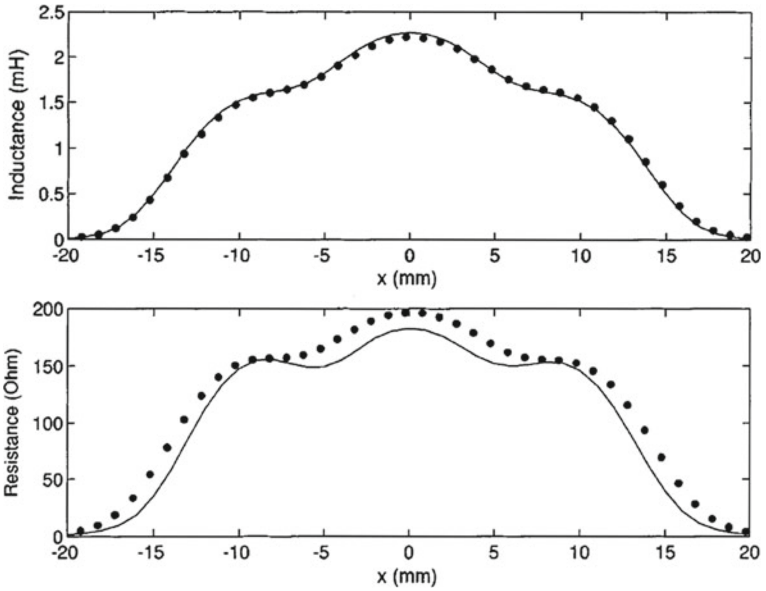

Fig. 9.14 Comparison of calculated probe impedance with experimental data for coil C11, Table 9.2, and slot D1, Table 9.3, approximated as a semi-ellipse [9]. Reproduced with permission from IEEE: *IEEE Trans. Magn.*, vol. 36, 2000, p. 289, Thin-Skin Eddy-Current Interaction with Semielliptical and Epicyclic Cracks, J. R. Bowler and N. Harfield, Fig. 7. Original caption: Comparison of probe impedance predictions with experimental measurements for slot D1, approximated as a semiellipse

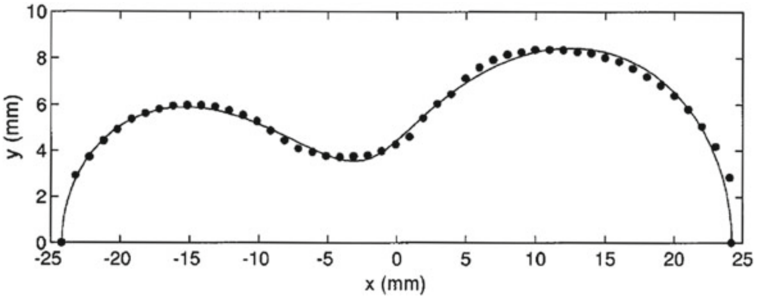

Fig. 9.15 Epicyclic profile of slot D2, Table 9.2 [9]. Reproduced with permission from IEEE: *IEEE Trans. Magn.*, vol. 36, 2000, p. 287, Thin-Skin Eddy-Current Interaction with Semielliptical and Epicyclic Cracks, J. R. Bowler and N. Harfield, Fig. 5b. Original caption: Comparison of crack edge coordinates with the profile representation used for mapping. **(b)** Slot D2 is approximated as a fifth-order elliptical epi-cycle

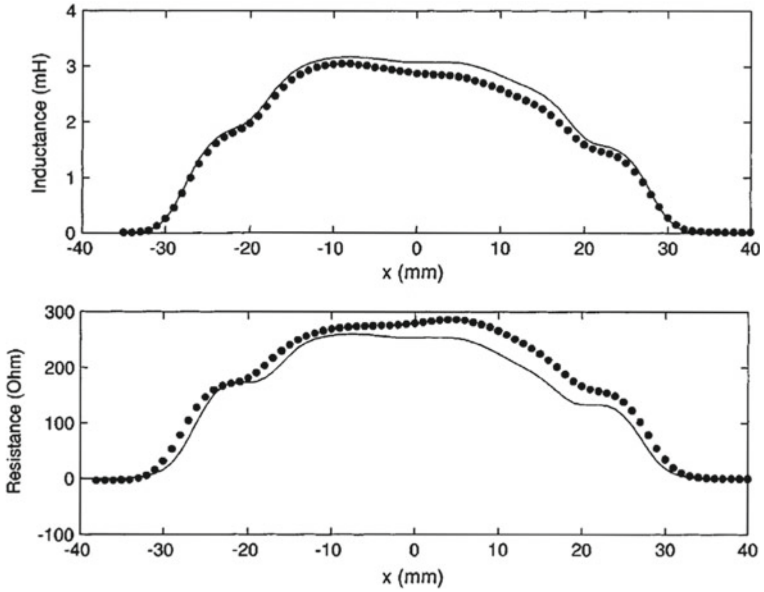

Fig. 9.16 Comparison of calculated probe impedance with experimental data for coil C11, Table 9.2, and slot D2, Table 9.3 [9]. Reproduced with permission from IEEE: *IEEE Trans. Magn.*, vol. 36, 2000, p. 289, Thin-Skin Eddy-Current Interaction with Semielliptical and Epicyclic Cracks, J. R. Bowler and N. Harfield, Fig. 8. Original caption: Comparison of probe impedance predictions with experimental measurements for slot D2

mapping from the crack domain shown to a rectangular domain. To do this, the crack profile was approximated by a series of nested elliptical epicycles. Despite the relative complexity of the profile of this defect, the impedance measurements still match the calculated values quite well, Fig. 9.16.

9.6 Other Regimes

For inspections whose frequencies fall between the “small flaw” and “thin-skin” regimes examined in this chapter, more generalized computer modeling approaches can be employed to model the coil impedance change due to various types of defect. For a detailed exposition of computational electromagnetics with specific application to the field of EC NDE, the reader is referred to [15].

9.7 Summary

In this chapter, some analytical forms for leading terms in the impedance change that would be observed due to various defects in a metal have been presented. The discussion has been divided into two regimes that can be treated analytically: a “low-frequency” regime and a “thin-skin” regime. For purposes of comparison, some results that have been presented are gathered in Table 9.4. From the table, it can be seen that leading terms in the impedance change due to these defects in the low-frequency regime are of order k^2, purely inductive. In the thin-skin regime the leading terms in the impedance change are of order k, contributing to real and imaginary parts of ΔZ in equal magnitude. It is important to note that the leading terms are of order k in the thin-skin regime only when the crack is closed, i.e., ‘ideal’ according to the definition presented in Sect. 9.5.3. A discussion of the way in which the leading contribution to ΔZ becomes purely inductive, of the form k^2dg where d is the depth and g the gape or opening of the crack, is given in [16]. An algorithm for determining the depth and opening of a long crack in the thin-skin regime, that recognizes this term, is given in [17] and references therein.

This chapter concluded with a review of articles and results comparing thin-skin theoretical calculations of coil impedance with experimental data taken on narrow cracks with rectangular, semi-elliptical, and epicyclic profiles.

Table 9.4 Leading terms in impedance change due to various defects, in low-frequency and thin-skin regimes. Multiply by $-\frac{1}{\sigma}\left[\frac{H_0}{\mathcal{I}^{(i)}}\right]^2$ to obtain ΔZ

Defect	Low-frequency regime		Thin-skin regime	
Hemispherical indentation	$\pi k^2 a^3$	(9.56)	–	
Semicircular crack	$\frac{4}{3}k^2a^3$	(9.57)	$2jka^2\left(\frac{\pi}{2}-\frac{2}{\pi}\right)$	(9.75)
Long crack	$\frac{\pi}{2}(kd)^2$	(9.58)	$jkd+\frac{1}{2}-\frac{4}{\pi}$	(9.71)

9.8 Exercises

1. Sketch the magnitude of the radial and polar components of $\mathbf{J}$ due to a dipole p, given by

$$\mathbf{J}(r,\theta) = \frac{p}{4\pi r^3}(2\cos\theta\,\hat{r} + \sin\theta\,\hat{\theta}),$$

   as a function of polar angle θ, for $r = a$. At what value of θ is $|\mathbf{J}|$

   (i) weakest?
   (ii) strongest?

2. Sketch the form of the dimensionless scattering parameter α that appears in the dipole representation of a small flaw

$$\alpha = 2\left(\frac{\sigma - \sigma_\mathrm{f}}{2\sigma + \sigma_\mathrm{f}}\right)$$

   as a function of σ_f for $0 \leq \sigma_\mathrm{f} \leq \sigma$. Comment on the meaning of α and it's maximum and minimum values.
3. Evaluate ΔZ for an ideal, semicircular, surface crack in chromium with radius $a = 1$ mm. At the surface of the test-piece the magnitude of the magnetic field is given by $H_0 = 10^4$ A/m. It is produced by a horizontal current sheet carrying current 0.1 A and located above the test-piece, oscillating at 1 kHz. Justify the use of the formula that you choose and explain the role of the metal conductivity in your calculation.
4. The center of a spherical void, radius 1 mm, is located 2 mm below the surface of a steel test-piece. In the steel, $\sigma = 10\%$ IACS and $\mu_\mathrm{r} = 80$. The uniform magnetic field at the surface of the test-piece is $\mathbf{H} = H_0\hat{y} = 10^6\hat{y}$ A/m, the electric field at the surface is $\mathbf{E} = -jkH_0\hat{x}/\sigma$, the exciting current is 0.1 A, and the excitation frequency is 1 kHz.

   (i) Evaluate ΔZ due to the defect.
   (ii) What are the relative contributions of the current dipole term and the magnetic dipole term to ΔZ in terms of their magnitude and phase?

5. (i) Plot $|\mathrm{Re}(\Delta Z)|$ for a long, surface breaking crack excited by a uniform incident field, as a function of d/δ where d is the crack depth and δ the electromagnetic skin depth, according to (9.72).
   (ii) For what value of d/δ are the higher order correction terms $<1\%$ of $|\mathrm{Re}(\Delta Z)|$?
   (iii) Hence, evaluate the frequencies at which the higher order terms are negligible ($<1\%$) in aluminum with $\sigma = 43$ MS/m for surface cracks (i) 2 mm deep (ii) 2 μm deep.
   (iv) Are the frequencies you have found in part (iii) commonly used in EC NDE?
6. Consider a spherical void, radius $a = 0.1$ mm, whose center is located 2 mm below the surface of a titanium specimen, for which $\sigma = 0.58$ MS/m. The test-piece is

excited by a current sheet excitation, with $I = 0.1$ A and the value of the magnetic field at the conductor surface is $H_0 = 10^6$ A/m.

(i) Evaluate the frequency f for which $\delta = 10a$, where δ is the electromagnetic skin depth.
(ii) For an excitation at 1 kHz, evaluate ΔZ due to the void, expressing your answer in the form $|\Delta Z|e^{j\phi}$.
(iii) Now consider a different defect, a hemispherical indentation at the conductor surface. The signal due to this defect has $|\Delta Z|$ the same as that you obtained for the subsurface defect in part (ii). With all other quantities being equal, what is the radius of the hemispherical indentation? Does this defect satisfy the criterion defining a "small flaw"?
(iv) Given that the subsurface sphere of part (ii) and the hemispherical indentation of part (iii) have the same $|\Delta Z|$, how could you distinguish between them in an eddy-current inspection?

References

1. Burrows, M.L.: A theory of eddy current flaw detection. Ph.D. thesis, University of Michigan (1964)
2. Harrington, R.F.: Time Harmonic Electromagnetic Fields. McGraw-Hill, New York (1961)
3. Duffin, W.J.: Electricity and Magnetism. McGraw-Hill, London (1980)
4. Spaldin, N.: Magnetic Materials: Fundamentals and Device Applications. Cambridge University Press, Cambridge (2003)
5. Bowler, J.R.: Eddy-current interaction with an ideal crack I: The forward problem. J. Appl. Phys. **12**, 8128–8137 (1994)
6. Harfield, N., Yoshida, Y., Bowler, J.R.: Low-frequency perturbation theory in eddy-current non-destructive evaluation. J. Appl. Phys. **80**, 4090–4100 (1996)
7. Harfield, N., Bowler, J.R.: Theory of thin-skin eddy-current interaction with surface cracks. J. Appl. Phys. **82**, 4590–4603 (1997)
8. Bowler, J.R., Harfield, N.: Evaluation of probe impedance due to thin-skin eddy-current interaction with surface cracks. IEEE Trans. Magn. **34**, 515–523 (1998)
9. Bowler, J.R., Harfield, N.: Thin-skin eddy-current interaction with semi-elliptical and epicyclic cracks. IEEE Trans. Magn. **36**, 281–291 (2000)
10. Kahn, A.H., Spal, R., Feldman, A.: Eddy-current losses due to a surface crack in conducting material. J. Appl. Phys. **48**, 4454–4459 (1977)
11. Harfield, N., Bowler, J.R.: Analysis of eddy-current interaction with a surface-breaking crack. J. Appl. Phys. **76**, 4853–4856 (1994)
12. Sommerfeld, A.: Optics. Academic, New York (1964)
13. Morse, E.M., Feshbach, H.: Methods of Theoretical Physics. McGraw-Hill, New York (1953)
14. Auld, B.A., Jefferies, S.R., Moulder, J.C.: Eddy-current signal analysis and inversion for semielliptical surface cracks. J. Nondestruct. Eval. **7**, 79–94 (1988)
15. Sabbagh, H.A., Murphy, R.K., Sabbagh, E.H., Aldrin, J.C., Knopp, J.S.: Computational Electromagnetics and Model-Based Inversion: A Modern Paradigm for Eddy-Current Nondestructive Evaluation. Springer, New York (2013)
16. Harfield, N.: Analytical Methods in Eddy-Current Non-Destructive Evaluation. Ph.D. thesis, University of Surrey, United Kingdom (1994)
17. Burke, S.K.: Eddy-current inversion in the thin-skin limit: Determination of depth and opening for a long crack. J. Appl. Phys. **76**, 3072–3080 (1994)

Chapter 10
Appendices

Abstract This Appendix introduces and defines mathematical tools that are of particular usefulness in the analysis of eddy-current impedance signals. Complex numbers, certain trigonometric functions, important operators, and identities of vector analysis in Cartesian, cylindrical, and spherical coordinate systems are presented. Due to their importance in analysis of eddy-current probe coil fields, Bessel functions are defined and described in some detail.

10.1 Complex Numbers

A complex number z has the Cartesian form

$$z = x + jy \tag{10.1}$$

where x and y are *real* numbers and $j = \sqrt{-1}$. x is known as the *real part* of z, $\mathrm{Re}\{z\}$, and y the *imaginary part* of z, $\mathrm{Im}\{z\}$. A complex-plane plot of z is shown in Fig. 10.1. Be careful about the fact that, although y is known as the imaginary part of z, y itself is a real number. The *complex conjugate* of c is c^* where

$$c^* = x - jy. \tag{10.2}$$

In polar coordinates $x = |z|\cos\phi$ and $y = |z|\sin\phi$ from which it follows that

$$z = |z|(\cos\phi + j\sin\phi) \tag{10.3}$$

where $|z| = \sqrt{x^2 + y^2}$ is the *modulus* of z and $\phi = \arctan(y/x)$ is its *argument* or *phase*. From the following relation (Euler's Formula),

$$e^{j\phi} = \cos\phi + j\sin\phi, \tag{10.4}$$

z can be written in polar form as follows, also shown in Fig. 10.1,

$$z = |z|e^{j\phi}. \tag{10.5}$$

N. Bowler, *Eddy-Current Nondestructive Evaluation*,
Springer Series in Measurement Science and Technology,
https://doi.org/10.1007/978-1-4939-9629-2_10

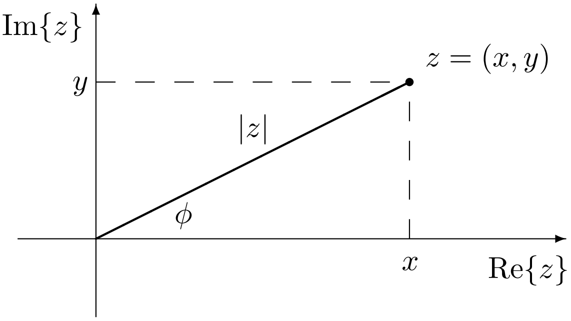

Fig. 10.1 Complex-plane representation of complex number $z = x + jy = |z|e^{j\phi}$

10.2 Trigonometry

The following useful relations are extracted from [1]. Noting that $j = \sqrt{-1}$,

$$e^{\pm jx} = \cos x \pm j \sin x, \qquad \text{Euler's theorem} \tag{10.6}$$

$$\cos x = \frac{e^{jx} + e^{-jx}}{2}, \qquad \sin x = \frac{e^{jx} - e^{-jx}}{2j} \tag{10.7}$$

$$\cos^2 x + \sin^2 x = 1 \tag{10.8}$$

$$\sin(A \pm B) = \sin A \cos B \pm \cos A \sin B \tag{10.9}$$

$$\cos(A \pm B) = \cos A \cos B \mp \sin A \sin B \tag{10.10}$$

$$\sin A + \sin B = 2 \sin\left(\frac{A+B}{2}\right) \cos\left(\frac{A-B}{2}\right) \tag{10.11}$$

$$\sin A - \sin B = 2 \cos\left(\frac{A+B}{2}\right) \sin\left(\frac{A-B}{2}\right) \tag{10.12}$$

$$\cos A + \cos B = 2 \cos\left(\frac{A+B}{2}\right) \cos\left(\frac{A-B}{2}\right) \tag{10.13}$$

$$\cos A - \cos B = -2 \sin\left(\frac{A+B}{2}\right) \sin\left(\frac{A-B}{2}\right) \tag{10.14}$$

10.3 Vector Analysis

The relationships in this section are extracted from [2, Appendix 1], [3, Chaps. 4 and 6] and [4, Part 1].

10.3.1 Continuity and Differentiability

First note the following definition of continuity of a scalar function. A scalar function $f(x)$ is *continuous* at x if

$$\lim_{\Delta x \to 0} f(x + \Delta x) = f(x).$$

Equivalently, $f(x)$ is continuous at x if for each positive number ϵ we can find some positive number η such that

$$|f(x + \Delta x) - f(x)| < \epsilon \qquad \text{whenever} \qquad |\Delta x| < \eta.$$

Equivalent definitions can be formulated for a vector field $\mathbf{a}(x)$ and for scalar and vector fields in three dimensions; $f(x, y, z)$ and $\mathbf{a}(x, y, z)$.

A scalar or vector function of x is *differentiable of order n* if its nth derivative exists. A function which is differentiable is necessarily continuous (but a continuous function is *not* necessarily differentiable).

10.3.2 Differential Operators

The vector differential operator *del*, written ∇ and also known as *nabla*, is defined by

$$\nabla \equiv \frac{\partial}{\partial x}\hat{x} + \frac{\partial}{\partial y}\hat{y} + \frac{\partial}{\partial z}\hat{z} \equiv \hat{x}\frac{\partial}{\partial x} + \hat{y}\frac{\partial}{\partial y} + \hat{z}\frac{\partial}{\partial z}. \tag{10.15}$$

This vector operator is useful in defining three quantities which arise in analysis of three-dimensional field quantities, including the electromagnetic field. These are the *gradient*, *divergence* and *curl*.

The Gradient

Let $f(x, y, z)$ be defined and differentiable at each point (x, y, z) in a certain region of space (this means that f is a differentiable scalar field). The *gradient* of f is then

$$\nabla f = \frac{\partial f}{\partial x}\hat{x} + \frac{\partial f}{\partial y}\hat{y} + \frac{\partial f}{\partial z}\hat{z}. \tag{10.16}$$

Note that ∇f defines a *vector* field.

The component of ∇f in the direction of a unit vector $\hat{u}$ is given by $\nabla f \cdot \hat{u}$ and is known as the directional derivative of f in the direction $\hat{u}$. Physically, this is the rate of change of f at (x, y, z) in the direction $\hat{u}$.

The Divergence

Let $\mathbf{a}(x, y, z) = a_x\hat{x} + a_y\hat{y} + a_z\hat{z}$ be defined and differentiable at each point (x, y, z) in a certain region of space (this means that $\mathbf{a}$ is a differentiable vector field). The *divergence* of $\mathbf{a}$ is then

$$\begin{aligned}\nabla\cdot\mathbf{a} &= \left(\frac{\partial}{\partial x}\hat{x} + \frac{\partial}{\partial y}\hat{y} + \frac{\partial}{\partial z}\hat{z}\right)\cdot(a_x\hat{x} + a_y\hat{y} + a_z\hat{z}) \\ &= \frac{\partial a_x}{\partial x} + \frac{\partial a_y}{\partial y} + \frac{\partial a_z}{\partial z}. \end{aligned} \tag{10.17}$$

Note that $\nabla\cdot\mathbf{a}$ defines a *scalar* field. Note also that $\nabla\cdot\mathbf{a} \neq \mathbf{a}\cdot\nabla$. A vector field $\mathbf{a}$ is said to be *divergenceless* or *solenoidal* if $\nabla\cdot\mathbf{a} = 0$.

The Curl

If $\mathbf{a}$ is a differentiable vector field, then the *curl* (or rotation) of $\mathbf{a}$ is defined by

$$\begin{aligned}\nabla\times\mathbf{a} &= \left(\frac{\partial}{\partial x}\hat{x} + \frac{\partial}{\partial y}\hat{y} + \frac{\partial}{\partial z}\hat{z}\right)\times(a_x\hat{x} + a_y\hat{y} + a_z\hat{z}) \\ &= \begin{vmatrix} \hat{x} & \hat{y} & \hat{z} \\ \frac{\partial}{\partial x} & \frac{\partial}{\partial y} & \frac{\partial}{\partial z} \\ a_x & a_y & a_z \end{vmatrix} \\ &= \left(\frac{\partial a_z}{\partial y} - \frac{\partial a_y}{\partial z}\right)\hat{x} + \left(\frac{\partial a_x}{\partial z} - \frac{\partial a_z}{\partial x}\right)\hat{y} + \left(\frac{\partial a_y}{\partial x} - \frac{\partial a_x}{\partial y}\right)\hat{z}. \end{aligned} \tag{10.18}$$

A vector field $\mathbf{a}$ is said to be *irrotational* or *conservative* if $\nabla\times\mathbf{a} = 0$.

The Laplacian

If f is a differentiable scalar field, then the *Laplacian* of f is the divergence of the gradient of f;

$$\begin{aligned}\nabla^2 f &= \nabla\cdot\nabla f \\ &= \left(\frac{\partial}{\partial x}\hat{x} + \frac{\partial}{\partial y}\hat{y} + \frac{\partial}{\partial z}\hat{z}\right)\cdot\left(\frac{\partial f}{\partial x}\hat{x} + \frac{\partial f}{\partial y}\hat{y} + \frac{\partial f}{\partial z}\hat{z}\right) \\ &= \frac{\partial^2 f}{\partial x^2} + \frac{\partial^2 f}{\partial y^2} + \frac{\partial^2 f}{\partial z^2}\end{aligned}$$

The Laplacian of a scalar field is a scalar field. A scalar field f is said to be *harmonic* in a given region if its Laplacian vanishes in that region ($\nabla^2 f = 0$). On the other hand, the Laplacian of a vector field $\mathbf{a}$ results in a vector field.

$$\begin{aligned}\nabla^2\mathbf{a} &= \nabla(\nabla\cdot\mathbf{a}) - \nabla\times\nabla\times\mathbf{a} \\ &= (\nabla^2 a_x)\hat{x} + (\nabla^2 a_y)\hat{y} + (\nabla^2 a_z)\hat{z}.\end{aligned}$$

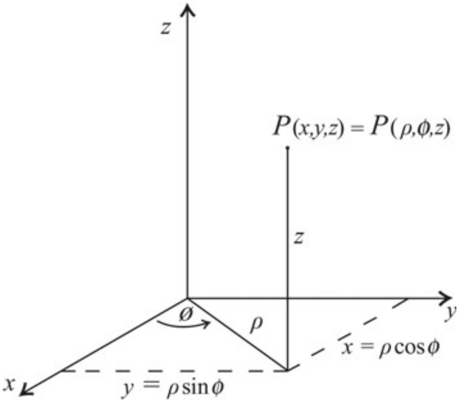

Fig. 10.2 Relationship between rectangular coordinates (x, y, z) and circular–cylindrical coordinates (ρ, ϕ, z)

10.3.3 Circular–Cylindrical Coordinates

The relationship between rectangular coordinates (x, y, z) and circular–cylindrical coordinates (ρ, ϕ, z) is written as follows and shown in Fig. 10.2.

$$x = x(\rho, \phi, z) = \rho\cos\phi \tag{10.19}$$

$$y = y(\rho, \phi, z) = \rho\sin\phi \tag{10.20}$$

$$z = z(\rho, \phi, z) = z \tag{10.21}$$

$$\rho = \rho(x, y, z) = \sqrt{x^2 + y^2}, \qquad 0 \le \rho < \infty \tag{10.22}$$

$$\phi = \phi(x, y, z) = \arctan(y/x), \qquad 0 \le \phi < 2\pi \tag{10.23}$$

The differential operators in circular cylindrical coordinates are reproduced below. f and $\mathbf{a}$ are differentiable scalar and vector fields, respectively.

$$\nabla \equiv \frac{\partial}{\partial\rho}\hat{\rho} + \frac{1}{\rho}\frac{\partial}{\partial\phi}\hat{\phi} + \frac{\partial}{\partial z}\hat{z} \tag{10.24}$$

$$\nabla f = \frac{\partial f}{\partial\rho}\hat{\rho} + \frac{1}{\rho}\frac{\partial f}{\partial\phi}\hat{\phi} + \frac{\partial f}{\partial z}\hat{z} \tag{10.25}$$

$$\nabla \cdot \mathbf{a} = \frac{1}{\rho}\frac{\partial}{\partial\rho}(\rho a_\rho) + \frac{1}{\rho}\frac{\partial a_\phi}{\partial\phi} + \frac{\partial a_z}{\partial z} \tag{10.26}$$

$$\nabla \times \mathbf{a} = \left(\frac{1}{\rho}\frac{\partial a_z}{\partial\phi} - \frac{\partial a_\phi}{\partial z}\right)\hat{\rho} + \left(\frac{\partial a_\rho}{\partial z} - \frac{\partial a_z}{\partial\rho}\right)\hat{\phi} + \left(\frac{1}{\rho}\frac{\partial}{\partial\rho}(\rho a_\phi) - \frac{1}{\rho}\frac{\partial a_\rho}{\partial\phi}\right)\hat{z} \tag{10.27}$$

$$\nabla^2 f = \frac{1}{\rho}\frac{\partial}{\partial\rho}\left(\rho\frac{\partial f}{\partial\rho}\right) + \frac{1}{\rho^2}\frac{\partial^2 f}{\partial\phi^2} + \frac{\partial^2 f}{\partial z^2} \tag{10.28}$$

$$\nabla^2\mathbf{a} = \left(\nabla^2 a_\rho - \frac{a_\rho}{\rho^2} - \frac{2}{\rho^2}\frac{\partial a_\phi}{\partial\phi}\right)\hat{\rho} + \left(\nabla^2 a_\phi - \frac{a_\phi}{\rho^2} + \frac{2}{\rho^2}\frac{\partial a_\rho}{\partial\phi}\right)\hat{\phi} + \nabla^2 a_z\hat{z} \tag{10.29}$$

10.3.4 Spherical-Polar Coordinates

The relationship between rectangular coordinates (x, y, z) and spherical-polar coordinates (r, θ, ϕ) is written as follows and shown in Fig. 10.3.

$$x = x(r, \theta, \phi) = r\sin\theta\cos\phi \tag{10.30}$$

$$y = y(r, \theta, \phi) = r\sin\theta\sin\phi \tag{10.31}$$

$$z = z(r, \theta, \phi) = r\cos\theta \tag{10.32}$$

$$r = r(x, y, z) = \sqrt{x^2 + y^2 + z^2}, \qquad 0 \le r < \infty \tag{10.33}$$

$$\theta = \theta(x, y, z) = \arccos(z/r), \qquad 0 \le \theta \le \pi \tag{10.34}$$

$$\phi = \phi(x, y, z) = \arctan(y/x), \qquad 0 \le \phi < 2\pi \tag{10.35}$$

The differential operators in spherical-polar coordinates are reproduced below. f and $\mathbf{a}$ are differentiable scalar and vector fields, respectively.

$$\nabla \equiv \frac{\partial}{\partial r}\hat{r} + \frac{1}{r}\frac{\partial}{\partial\theta}\hat{\theta} + \frac{1}{r\sin\theta}\frac{\partial}{\partial\phi}\hat{\phi} \tag{10.36}$$

$$\nabla f = \frac{\partial f}{\partial r}\hat{r} + \frac{1}{r}\frac{\partial f}{\partial\theta}\hat{\theta} + \frac{1}{r\sin\theta}\frac{\partial f}{\partial\phi}\hat{\phi} \tag{10.37}$$

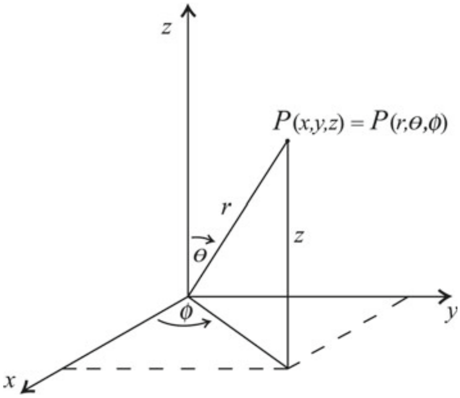

Fig. 10.3 Relationship between rectangular coordinates (x, y, z) and spherical-polar coordinates (ρ, θ, ϕ)

$$\nabla \cdot \mathbf{a} = \frac{1}{r^2}\frac{\partial}{\partial r}(r^2 a_r) + \frac{1}{r\sin\theta}\frac{\partial}{\partial\theta}(\sin\theta\, a_\theta) + \frac{1}{r\sin\theta}\frac{\partial a_\phi}{\partial\phi} \tag{10.38}$$

$$= \frac{\partial a_r}{\partial r} + \frac{2a_r}{r} + \frac{1}{r}\frac{\partial a_\theta}{\partial\theta} + \frac{a_\theta}{r\tan\theta} + \frac{1}{r\sin\theta}\frac{\partial a_\phi}{\partial\phi} \tag{10.39}$$

$$\begin{aligned}\nabla \times \mathbf{a} = {} & \frac{1}{r\sin\theta}\left[\frac{\partial}{\partial\theta}(\sin\theta\, a_\phi) - \frac{\partial a_\theta}{\partial\phi}\right]\hat{r} + \frac{1}{r}\left[\frac{1}{\sin\theta}\frac{\partial a_r}{\partial\phi} - \frac{\partial}{\partial r}(r a_\phi)\right]\hat{\theta} \\ & + \frac{1}{r}\left[\frac{\partial}{\partial r}(r a_\theta) - \frac{\partial a_r}{\partial\theta}\right]\hat{\phi}\end{aligned} \tag{10.40}$$

$$\nabla^2 f = \frac{1}{r^2}\frac{\partial}{\partial r}\left(r^2\frac{\partial f}{\partial r}\right) + \frac{1}{r^2\sin\theta}\frac{\partial}{\partial\theta}\left(\sin\theta\frac{\partial f}{\partial\theta}\right) + \frac{1}{r^2\sin^2\theta}\frac{\partial^2 f}{\partial\phi^2} \tag{10.41}$$

$$\begin{aligned}\nabla^2\mathbf{a} = {} & \left(\nabla^2 a_r - \frac{2a_r}{r^2} - \frac{2\cot\theta}{r^2}a_\theta - \frac{2}{r^2}\frac{\partial a_\theta}{\partial\theta} - \frac{2}{r^2\sin\theta}\frac{\partial a_\phi}{\partial\phi}\right)\hat{r} \\ & + \left(\nabla^2 a_\theta + \frac{2}{r^2}\frac{\partial a_r}{\partial\theta} - \frac{a_\theta}{r^2\sin^2\theta} - \frac{2\cos\theta}{r^2\sin^2\theta}\frac{\partial a_\phi}{\partial\phi}\right)\hat{\theta} \\ & + \left(\nabla^2 a_\phi + \frac{2}{r^2\sin\theta}\frac{\partial a_r}{\partial\phi} - \frac{a_\phi}{r^2\sin^2\theta} + \frac{2\cos\theta}{r^2\sin^2\theta}\frac{\partial a_\theta}{\partial\phi}\right)\hat{\phi}\end{aligned} \tag{10.42}$$

10.3.5 Differential Relationships

These general relationships, or *identities*, hold true in all coordinate systems. Let f, **a** and **b** be defined and differentiable at each point in a certain region of space. Then,

$$\nabla \times \nabla f = 0 \tag{10.43}$$

$$\nabla \cdot \nabla \times \mathbf{a} = 0 \tag{10.44}$$

$$\nabla \times (\mathbf{ab}) = (\nabla \times \mathbf{a})\mathbf{b} - \mathbf{a} \times \nabla\mathbf{b} \tag{10.45}$$

$$\nabla \times \nabla \times \mathbf{a} = \nabla\nabla \cdot \mathbf{a} - \nabla^2\mathbf{a} \tag{10.46}$$

$$\nabla \cdot (\mathbf{a} \times \mathbf{b}) = \mathbf{b} \cdot \nabla \times \mathbf{a} - \mathbf{a} \cdot \nabla \times \mathbf{b} \tag{10.47}$$

10.3.6 Integral Theorems

Gauss' Divergence Theorem may be stated as follows. If V is the volume bounded by a closed surface S and **a** is a vector function of position with continuous derivatives, then the divergence of **a** integrated over the volume V is equivalent to the integral of **a** over closed surface S. Mathematically,

$$\int_V \nabla \cdot \mathbf{a}\, dV = \oint_S \mathbf{a} \cdot \hat{n}\, dS = \oint_S \mathbf{a} \cdot d\mathbf{S}, \tag{10.48}$$

where $\hat{n}$ is the positive (outward drawn) normal to S.

Note, in rectangular coordinates the elemental volume dV is $dxdydz$. The range of each of the coordinates x, y, and z is from $-\infty$ to ∞. In circular cylindrical coordinates, $dV = d\rho \times \rho d\phi \times dz = \rho\, d\rho\, d\phi\, dz$. The range of ρ is from 0 to ∞, that of ϕ is from 0 to 2π and that of z is again from $-\infty$ to ∞.

Stokes' Theorem states that if S is an open, two-sided surface bounded by a closed, nonintersecting curve C (simple closed curve) and if **a** has continuous derivatives, then the integral of **a** around the closed loop C is equivalent to the integral of the curl of **a** over surface S. Mathematically,

$$\oint_C \mathbf{a} \cdot d\mathbf{l} = \int_S (\nabla \times \mathbf{a}) \cdot \hat{n}\, dS = \int_S (\nabla \times \mathbf{a}) \cdot d\mathbf{S}, \tag{10.49}$$

where C is traversed in the positive direction. The direction of C is called positive if an observer, walking on the boundary of S in this direction, with their head pointing in the direction of the positive normal to S, has the surface on their left.

10.4 Bessel Functions

Bessel functions arise in the analysis of systems with cylindrical geometry. In Cartesian coordinates, solutions are expressed in terms of sine, cosine, sinh, cosh, and exponential functions. To describe the radial dependence of a field or potential in cylindrical-polar coordinates, on the other hand, Bessel functions are used.

The properties of Bessel functions were not discovered by mathematicians but by scientists who became famous for solving basic practical problems. Examples of these are Bernoulli's solutions for the motion of heavy hanging chains, Fourier's description of the flow of heat in cylinders and Bessel's theory describing the motion of the planets. Solutions of these problems are all expressed in terms of Bessel functions.

In this section, Bessel functions are introduced by solving the Laplace equation for an axially symmetric system. This is closely related to the solution for the electric field due to a circular current loop developed in Sect. 6.3.2, which involves the solution of the Helmholtz equation, but is also axially symmetric. Next, higher order Bessel functions are introduced via solution of the general three-dimensional Laplace equation in which azimuthal variation is accounted for.

10.4.1 Separation of Variables

The Laplace equation for an axially symmetric, two-dimensional scalar field Φ is

$$\nabla^2\Phi = \frac{\partial^2\Phi}{\partial\rho^2} + \frac{1}{\rho}\frac{\partial\Phi}{\partial\rho} + \frac{\partial^2\Phi}{\partial z^2} = 0. \tag{10.50}$$

Axial symmetry implies that there is no variation of Φ with azimuthal variable ϕ. This means that derivatives with respect to ϕ vanish and terms in (10.50) depend only on ρ and z. Proceeding to solve the Laplace equation of (10.50) by the method of separation of variables, a solution in the form of a product of functions that each depend on only one variable is sought: $\Phi(\rho, z) = R(\rho)Z(z)$. Inserting this product into (10.50) and dividing throughout by the same product gives

$$\left[\frac{1}{R(\rho)}\frac{\partial^2 R(\rho)}{\partial\rho^2} + \frac{1}{\rho R(\rho)}\frac{\partial R(\rho)}{\partial\rho}\right] + \left[\frac{1}{Z(z)}\frac{\partial^2 Z(z)}{\partial z^2}\right] = 0 \tag{10.51}$$

Now, the bracketed terms [ ] each depend on only one variable. The first bracketed term depends on ρ and the second on z. Note that the first term cannot change as ρ changes because there is no other term in (10.51) that can balance the effect of a change in the first term. This means that the first bracketed term must be constant even when ρ changes. Similarly, the second bracketed term must remain constant even when z changes.

Let the constant with respect to changes in z be written β^2 where β is a positive real number. (In general, β may be a complex number.) Then

$$\frac{\partial^2 Z(z)}{\partial z^2} - \beta^2 Z(z) = 0 \tag{10.52}$$

with solution

$$A(\beta)\exp(\beta z) + B(\beta)\exp(-\beta z). \tag{10.53}$$

Consequently, substituting (10.52) into (10.51) yields

$$\frac{\partial^2 R(\rho)}{\partial\rho^2} + \frac{1}{\rho}\frac{\partial R(\rho)}{\partial\rho} + \beta^2 R(\rho) = 0. \tag{10.54}$$

Equation (10.54) is Bessel's equation of zero order. It is a second-order differential equation with two independent solutions. One of these solutions is regular at the origin (has a value) and the other is singular (infinite) as $\rho \to 0$. The solution that is regular can be expressed as a power series in ρ. Starting with a power series expansion with arbitrary coefficients, one can insert the series into Bessel's equation and equate terms of the same power in the variable to determine the coefficients. This procedure then defines one of the solutions of (10.54); $J_0(\beta\rho)$, the Bessel function of the first kind of order zero.[1] The singular solution, $Y_0(\beta\rho)$, is also a zero-order Bessel function, but contains a logarithmic singularity $\log\rho$ as well as power series terms.[2] Including both Bessel functions forms a general solution of (10.54) [1]:

$$C(\beta)J_0(\beta\rho) + D(\beta)Y_0(\beta\rho).$$

$Y_0(\beta\rho)$ is the zero-order Bessel function of the second kind.

In an alternative development, the second bracketed term in (10.51) is written as, say, $-\kappa^2$. This is particularly convenient where κ is a real number. In this case,

$$\frac{\partial^2 Z(z)}{\partial z^2} + \kappa^2 Z(z) = 0, \tag{10.55}$$

the solution of which is

$$A(\kappa)\cos(\kappa z) + B(\kappa)\sin(\kappa z), \tag{10.56}$$

in contrast with (10.53). Then,

$$\frac{\partial^2 R(\rho)}{\partial \rho^2} + \frac{1}{\rho}\frac{\partial R(\rho)}{\partial \rho} - \kappa^2 R(\rho) = 0 \tag{10.57}$$

and the part of the solution representing the radial dependence is

$$C(\kappa)I_0(\kappa\rho) + D(\kappa)K_0(\kappa\rho) \tag{10.58}$$

where $I_0(\kappa\rho)$ is the modified Bessel function of the first kind of order zero, and $K_0(\kappa\rho)$ is the modified Bessel function of the second kind of order zero. Note that $I_0(\kappa\rho)$, like $J_0(\beta\rho)$, is regular whereas $K_0(\kappa\rho)$, like $Y_0(\beta\rho)$, exhibits a logarithmic singularity as $\rho \to 0$.

---

[1] The Bessel function of the first kind of order zero is regular, with the power series form

$$J_0(z) = 1 - \frac{x^2}{2^2} + \frac{x^4}{2^2 4^2} - \ldots = \sum_{m=0}^{\infty} \frac{\left(-\frac{1}{4}z^2\right)^m}{(m!)^2}.$$

[2] It can be shown that

$$Y_0(z) = \frac{2}{\pi}\left\{ J_0(z)[\log\left(\frac{z}{2}\right) + \gamma] + \sum_{k=1}^{\infty}(-1)^{k+1} H_k \frac{\left(\frac{1}{4}z^2\right)^k}{(k!)^2} \right\}$$

where $\gamma \approx 0.577215665$ is Euler's constant and

$$H_k = 1 + \frac{1}{2} + \frac{1}{3} + \ldots \frac{1}{k}$$

is a harmonic number.

10.4.2 Higher Order Bessel Functions

In a system without axial symmetry, the three-dimensional Laplace equation accounts for an azimuthal dependence;

$$\nabla^2\Phi = \frac{\partial^2\Phi}{\partial\rho^2} + \frac{1}{\rho}\frac{\partial\Phi}{\partial\rho} + \frac{1}{\rho^2}\frac{\partial^2\Phi}{\partial\phi^2} + \frac{\partial^2\Phi}{\partial z^2} = 0. \tag{10.59}$$

In this case, solution via separation of variables begins by writing $\Phi(\rho, \phi, z) = R(\rho)P(\phi)Z(z)$. Inserting this product into (10.59) and dividing throughout by the same product yields

$$\left[\frac{1}{R(\rho)}\frac{\partial^2 R(\rho)}{\partial\rho^2} + \frac{1}{\rho R(\rho)}\frac{\partial R(\rho)}{\partial\rho}\right] + \left[\frac{1}{\rho^2 P(\phi)}\frac{\partial^2 P(\phi)}{\partial\phi^2}\right] + \left[\frac{1}{Z(z)}\frac{\partial^2 Z(z)}{\partial z^2}\right] = 0. \tag{10.60}$$

As in the previous treatment of (10.52), equate the z-dependent term in (10.60) with β^2. This gives rise to a general solution with exponential z-dependence as expressed in (10.53). Next proceed by acknowledging that the ϕ-dependence of Φ is periodic. This means that the second bracketed term in (10.60) can be equated with $-n^2/\rho^2$ to give

$$\frac{\partial^2 P(\phi)}{\partial\phi^2} + n^2 P(\phi) = 0. \tag{10.61}$$

This ensures azimuthal dependence of the form

$$P(\phi) = L_n \cos(n\phi) + M_n \sin(n\phi), \tag{10.62}$$

which allows a general azimuthal dependence to be written as a Fourier series. Consequently, for arbitrary order, the radial dependence of Φ is governed by

$$\frac{\partial^2 R(\rho)}{\partial\rho^2} + \frac{1}{\rho}\frac{\partial R(\rho)}{\partial\rho} + (\beta^2 - n^2)R(\rho) = 0, \tag{10.63}$$

whose solutions are

$$C(\beta)J_n(\beta\rho) + D(\beta)Y_n(\beta\rho) \tag{10.64}$$

Figures 10.4 and 10.5 show, respectively, the variation of $J_n(x)$ and $Y_n(x)$ for orders from zero to 5.

Proceeding in the same way but now using $-\kappa^2$ in place of β^2 does not change the Fourier expansion for the azimuthal dependence (10.62), but it does mean that the z-dependence is trigonometric as in (10.56) and the radial function satisfies

$$\frac{\partial^2 R(\rho)}{\partial\rho^2} + \frac{1}{\rho}\frac{\partial R(\rho)}{\partial\rho} - (\kappa^2 + n^2)R(\rho) = 0 \tag{10.65}$$

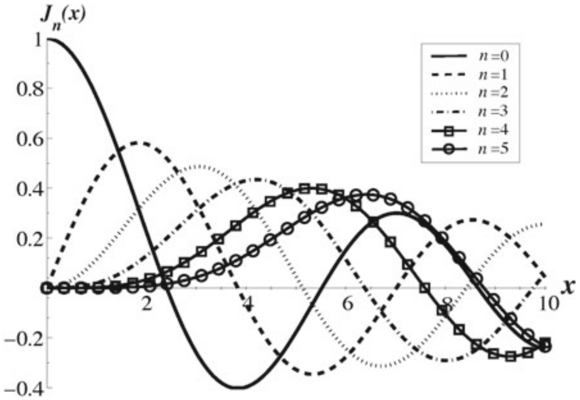

Fig. 10.4 Bessel functions of the first kind of order n, J_n

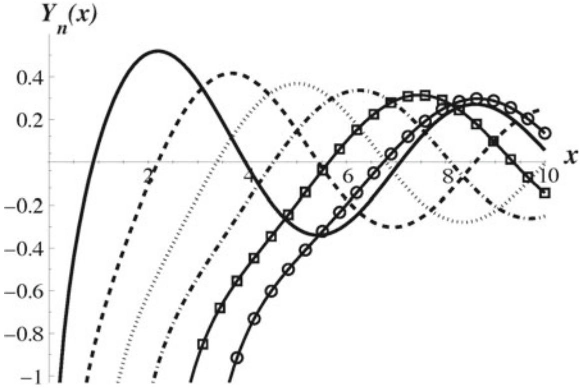

Fig. 10.5 Bessel functions of the second kind of order n, Y_n. The $Y_n(x)$ exhibit a logarithmic singularity as $x \to 0$

with solution

$$C(\kappa)I_n(\kappa\rho) + D(\kappa)K_n(\kappa\rho). \tag{10.66}$$

Figures 10.6 and 10.7 show, respectively, the variation of $I_n(x)$ and $K_n(x)$ for orders from 0 to 5.

10.5 Exercises

1. A complex number c is defined $c = 6 + j13$. Evaluate

   (i) the real part of c,
   (ii) the imaginary part of c,
   (iii) the magnitude of c,
   (iv) the phase of c.

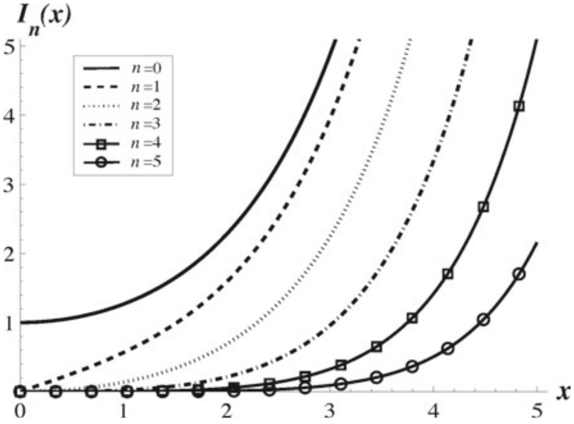

Fig. 10.6 Modified Bessel functions of the first kind of order n, I_n

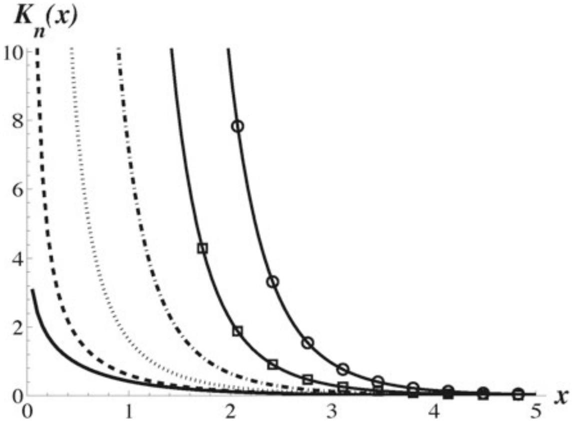

Fig. 10.7 Modified Bessel functions of the second kind of order n, K_n. The $K_n(x)$ exhibit a logarithmic singularity as $x \to 0$

If c^* is the complex conjugate of c, evaluate the following. You may give your answers in *either* the form $z = a + jb$ *or* $z = |z|e^{j\phi}$.

(v) $c + c^*$,
(vi) $c - c^*$,
(vii) $c\,c^*$, and
(viii) c/c^*.

2. Find the two values of z that satisfy the equation $z^2 = 3 - 2j$. Draw your results on a diagram where the real axis is horizontal and the imaginary axis is vertical.
3. Given $\mathbf{a} = x^2 y\hat{x} - yz\hat{y} + yz^2\hat{z}$, evaluate

(i) the magnitude of vector $\mathbf{a}$ at point T, $(2, -1, 3)$;
(ii) the distance vector from point T to point S if S is 5.6 units away from T in the same direction as vector $\mathbf{a}$ at T;
(iii) the position vector of S.

4. **E** and **F** are vector fields given by $\mathbf{E} = 2x\hat{x} + \hat{y} + yz\hat{z}$ and $\mathbf{F} = xy\hat{x} - y^2\hat{y} + xyz\hat{z}$. Determine
   - (i) the magnitude of **E** at $(1, 2, 3)$;
   - (ii) the component of **E** along **F** at $(1, 2, 3)$;
   - (iii) a vector perpendicular to both **E** and **F** at $(0, 1, -3)$ whose magnitude is unity.
5. Find the gradient of these scalar fields.
   (a) $U = 4xz^2 + 3yz$
   (b) $W = 2\rho(z^2 + 1)\cos\phi$
6. Determine the divergence of the following vector fields.
   (a) $\mathbf{a} = xy\hat{x} + y^2\hat{y} - xz\hat{z}$
   (b) $\mathbf{b} = \rho z^2\hat{\rho} + \rho\sin^2\phi\,\hat{\phi} + 2\rho z\sin^2\phi\hat{z}$
7. Show that $\nabla\ln\rho = \nabla\times\phi\hat{z}$.
8. For a differentiable vector field **a** show that $\nabla\cdot\nabla\times\mathbf{a} = 0$.
9. If $\mathbf{F} = 2\rho z\hat{\rho} + 3z\sin\phi\,\hat{\phi} - 4\rho\cos\phi\,\hat{z}$, verify Stokes' Theorem for the open surface defined by $z = 1, 0 < \rho < 2, 0 < \phi < 45°$.
10. (i) From a suitable reference find an expression for $K_0(z)$ and deduce a first approximation for $K_0(z)$ when z is very small.
    (ii) What is the electrostatic potential due to a line charge varying as $q\cos(az)$?

References

1. Abramowitz, M., Stegun, I.A. (eds.): Handbook of Mathematical Functions with Formulas, Graphs and Mathematical Tables. Dover, New York (1972)
2. Van Bladel, J.: Electromagnetic Fields. Hemisphere Publishing Corporation, Washington (1985)
3. Spiegel, M.R.: Schaum's Outline Series Theory and Problems of Vector Analysis and an Introduction to Tensor Analysis. McGraw-Hill Book Company, New York (1974)
4. Sadiku, M.N.O.: Elements of Electromagnetics, 4th edn. Oxford University Press, New York (2007)

Index

N. Bowler, *Eddy-Current Nondestructive Evaluation*,
Springer Series in Measurement Science and Technology,
https://doi.org/10.1007/978-1-4939-9629-2